KfK 3202/2
UWFDM-450
Dezember 1981

HIBALL — A Conceptual Heavy Ion Beam Driven Fusion Reactor Study

Volume 2

Institut für Neutronenphysik und Reaktortechnik

Kernforschungszentrum Karlsruhe

KERNFORSCHUNGSZENTRUM KARLSRUHE

Institut für Neutronenphysik und Reaktortechnik

KfK 3202

UWFDM-450

HIBALL - A Conceptual Heavy Ion Beam Driven Fusion Reactor Study

Volume 2

B. Badger[a]
F. Arendt[b]
K. Becker[c]
K. Beckert[d]
R. Bock[d]
D. Böhne[d]
I. Bozsik[e]
J. Brezina[c]
M. Dalle Donne[f]
L. El-Guebaly[a]
R. Engelstad[a]
W. Eyrich[f]
R. Fröhlich[f]
N. Ghoniem[g]
B. Goel[f]
A. Hassanein[a]
D. Henderson[f]
W. Höbel[f]
I. Hofmann[e]
E. Hoyer[h]
R. Keller[d]
G. Kessler[f]
A. Klein[a]
R. Kreutz[i]
G. Kulcinski[a]
E. Larsen[a]
K. Lee[a]
K. Long[f]
E. Lovell[a]
N. Metzler[j]
J. Meyer-ter-Vehn[j]
U. von Möllendorff[f]
N. Moritz[f]
G. Moses[a]
R. Müller[d]
K. O'Brien[a]
R. Peterson[a]
K. Plute[a]
L. Pong[a]
R. Sanders[a]
J. Sapp[k]
M. Sawan[a]
K. Schretzmann[f]
T. Spindler[a]
I. Sviatoslavsky[a]
K. Symon[a]
D. Sze[a]
N. Tahir[f]
W. Vogelsang[a]
A. White[a]
S. Witkowski[j]
H. Wollnik[c]

[a]University of Wisconsin, Madison
[b]KfK, Institut für Technische Physik
[c]Universität Gießen, II. Physikalisches Institut
[d]Gesellschaft für Schwerionenforschung, Darmstadt
[e]Max-Planck-Institut für Plasmaphysik, Garching
[f]KfK, Institut für Neutronenphysik und Reaktortechnik
[g]University of California, Los Angeles
[h]Lawrence Berkeley Laboratory, Berkeley
[i]Interatom, Bergisch Gladbach
[j]Max-Planck-Institut für Quantenoptik, Garching
[k]McDonnell-Douglas

Kernforschungszentrum Karlsruhe GmbH, Karlsruhe

Kernforschungszentrum Karlsruhe GmbH
und University of Wisconsin-Madison
ISSN 0303-4003

Abstract

HIBALL - A Conceptual Heavy Ion Beam Driven Fusion Reactor Study

A preliminary concept for a heavy-ion beam driven inertial confinement fusion power plant is presented. The high repetition rate of the RF accelerator driver is utilized to serve four reactor chambers alternatingly. In the chambers a novel first-wall protection scheme is used. At a target gain of 83 the total net electrical output is 3.8 GW. The recirculating power fraction is below 15%.

The main goal of the comprehensive HIBALL study (which is continuing) is to demonstrate the compatibility of the design of the driver, the target and the reactor chambers. Though preliminary, the present design is essentially self-consistent. Tentative cost estimates are given. The costs compare well with those found in similar studies on other types of fusion reactors.

Zusammenfassung

HIBALL - Eine Konzeptstudie für einen durch Schwerionenstrahlen getriebenen Fusionsreaktor

Es wird ein vorläufiges Konzept für ein Trägheitsfusionskraftwerk mit Schwerionenstrahltreiber vorgestellt. Die hohe Pulsfolgefrequenz des Treibers vom HF-Beschleuniger-Typ wird ausgenutzt, um vier Reaktorkammern abwechselnd zu bedienen. In den Kammern wird eine neuartige Technik zum Schutz der ersten Wand eingesetzt. Bei einem Target-Energiegewinn von 83 beträgt die elektrische Netto-Gesamtleistung 3.8 GW. Der rezirkulierende Leistungsanteil liegt unter 15%.

Hauptziel der umfassenden HIBALL-Studie (die fortgesetzt wird) ist es, die Verträglichkeit der Entwürfe für Treiber, Target und Reaktorkammern nachzuweisen. Obwohl vorläufig, ist der vorliegende Entwurf im wesentlichen konsistent. Es werden vorläufige Kostenschätzungen angegeben. Die Kosten sind gut vergleichbar mit denen, die in ähnlichen Studien für andere Typen von Fusionsreaktoren gefunden wurden.

TABLE OF CONTENTS
VOLUME 1

References are found after each subchapter (e.g., III.1) or chapter (e.g., I).

VI Cavity Design

VI.1 General Requirements, Description, and Reference Parameters

VI.1.1 Requirements

The requirements imposed on the design of the cavity for HIBALL are determined by a number of sometimes conflicting considerations. A strict definition of the cavity is that part of the chamber inside the first material wall. For the purposes of this section the definition is expanded to include the entire chamber including reflectors, shields, and the top and bottom portions. The basic requirements are: (1) the cavity be able to dissipate the energy from the target in a coolant operating at temperatures consistent with material requirements and the necessity to produce steam suitable for operation of a steam turbine driven generator, (2) the atmosphere in the cavity be such that the heavy ion beam can be focussed on the target, (3) the system be maintainable in a reasonable fashion, (4) the system be able to breed tritium at a breeding ratio greater than or equal to unity, (5) the tritium be recoverable without undue accumulation of tritium in the breeding material, and (6) the dose rate outside the shielding be at an acceptable level.

The two requirements which have the greatest impact are the need to dissipate the target energy and propagate the beam through the chamber to the target. The fusion yield of the HIBALL target is 400 MJ and the repetition rate is 5 Hz, yielding a fusion power of 2000 MW per chamber. The time dependent neutronics studies reported in section VI.3.4 indicate that because of endothermic reactions in the target the actual energy available is slightly less, i.e. 396 MJ/shot. Of these 396 MJ, 285 MJ is carried by neutrons of average energy of 12 MeV, 90 MJ is contained in X-rays emitted from the target, and 21 MJ by the target debris, i.e. He, unburned D and T, Pb, and Li. A very small amount appears as high energy gamma radiation. This means that al-

though the greatest part of the energy is carried by the neutrons and therefore is volumetrically deposited in the blanket materials, a significant amount, viz. 111 MJ, is in a form that would be deposited on or very near the surface of any material surrounding the target.

VI.1.2 INPORT Concept

A persistant technical problem in the Inertial Confinement Fusion (ICF) field has been the protection of the first load bearing walls from target debris, x-rays, and neutrons. Various schemes have been proposed in the past: swirling liquid metal pools[1], wetted walls[2,3,4,5], magnetic protection[6], gaseous protection[7], dry wall ablative shields[8-11], and free falling sheets of liquid metals[12-15]. None of these schemes have been completely satisfactory, but the liquid metal protection scheme, HYLIFE[15], seems to be the best developed thus far.

One disadvantage with the HYLIFE scheme is the disassembly of the liquid metal columns after each shot and the need to reestablish the stream before the next target can be injected. This results in small ΔT, high recirculation rates, and large pumping powers, especially for the Pb-Li alloys. Ideally, one would like to develop a scheme which would slow down the flow of liquid metal so that it can absorb the energy of several shots before exiting the reactor.

Such a scheme was developed in late 1979 for the HIBALL project. The basis of this new design is the use of woven SiC tubes which are flexible, sufficiently strong, compatible with Pb-Li alloys used in HIBALL, and porous enough to allow liquid to cover the surface while the bulk of the fluid flows down the center of the tube (Fig. VI.1-1). This idea is called the INPORT concept, standing for the Inhibited Flow - Porous Tube Concept. The film thickness of roughly 1 mm is sufficient to absorb the energy from x-rays and

Figure VI.1-1

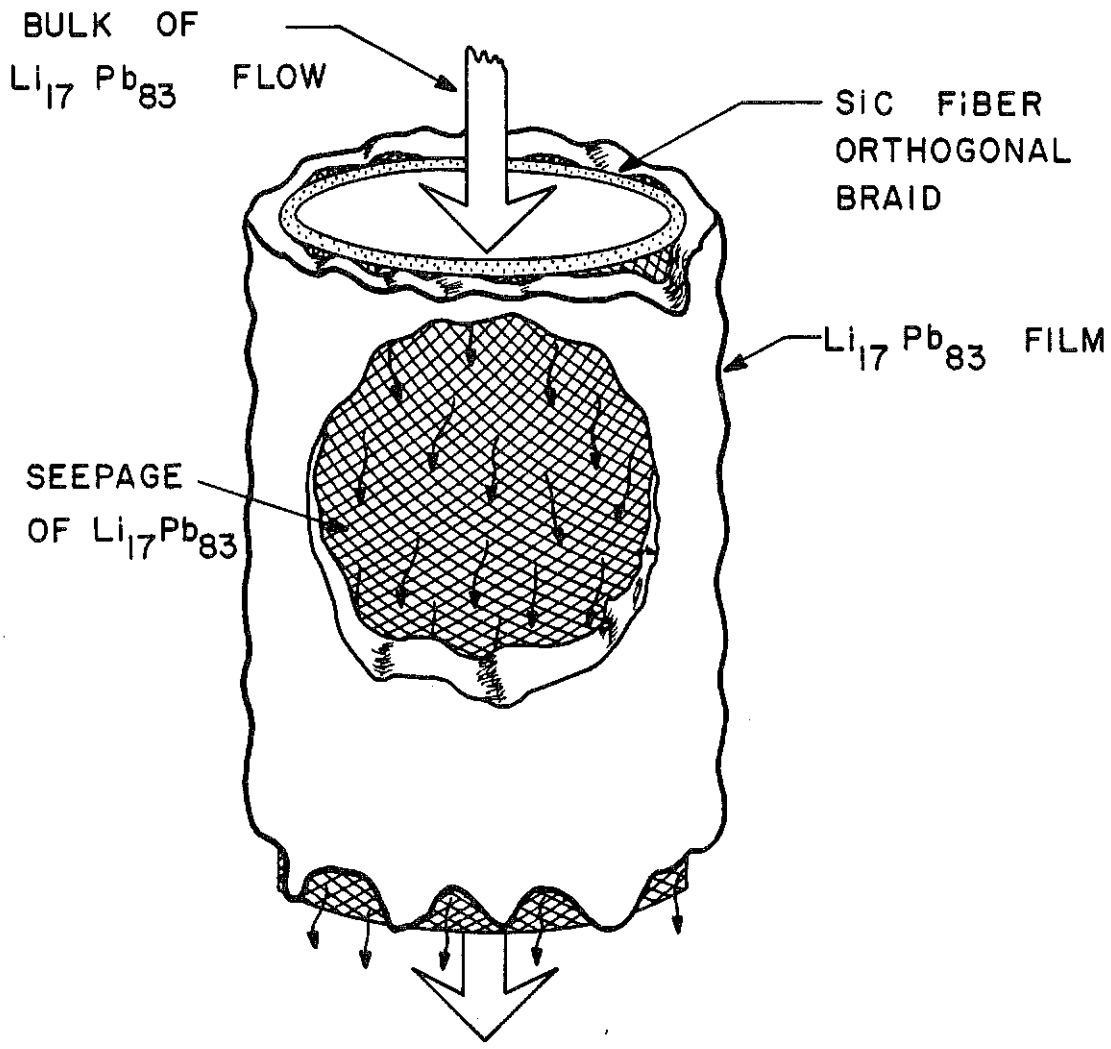
BULK OF
Li_{17} Pb_{83} FLOW
SiC FiBER
ORTHOGONAL
BRAID
Li_{17} Pb_{83} FILM
SEEPAGE
OF $Li_{17}Pb_{83}$

target debris while several banks of tubes provide enough Pb-Li alloy to considerably moderate the neutron flux and reduce the total damage and damage rate in the first wall (Fig. VI.1-2).

A schematic of how the porous tube structure fits into the HIBALL chamber design is given in Fig. VI.1-3 and the overall chamber design is shown in Fig. VI.1-4. A few of the major operating parameters are given below:

Tube radius, cm (Number) - inner rows	1.5/(1230)
- outer rows	5/(3070)
Inlet/outlet temp. of $Pb_{83}Li_{17}$	330/500°C
Max. flow velocity (front tube)	5 m/s
Target yield x frequency of shots	400 MJ x 5 Hz
Energy flux to first Pb-Li surface	35 J/cm^2
Condensation time to 10^{-5} torr (at RT)	0.15 sec
dpa in HT-9 FW per FPY w/o INPORT units	21
dpa in HT-9 FW per FPY with INPORT units	2.7

It is clear that the INPORT concept enhances the promise of ICF reactors and it should remedy one of the more serious drawbacks of the HYLIFE concept, the disassembly after each shot. The rest of this section will discuss, in more detail, how the INPORT concept fits into the HIBALL design.

VI.1.3 Mechanical Description of Cavity

The cavity is an upright cylinder with internal dimensions of 11.5 m height on axis and 10 m in diameter, Fig. VI.1-4. From the center and outward in all directions, the cavity is characterized by three distinct zones, the blanket, reflector and shield. In the vertical sides of the cavity, the blanket consists of a 2 m thick zone of SiC tubes through which $Li_{17}Pb_{83}$ is

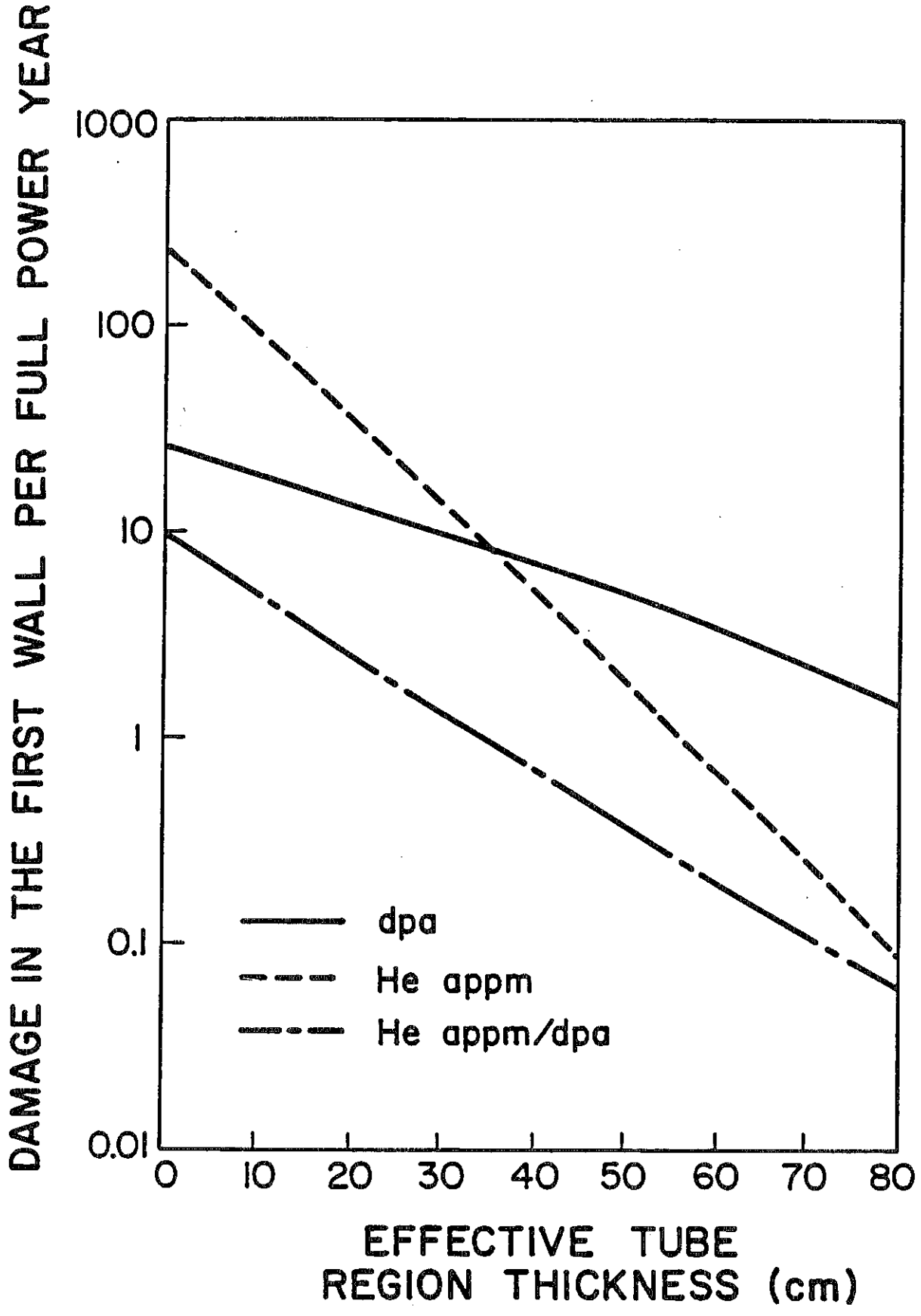

Fig. VI·1-2 Effect of INPORT tubes on Damage in HT-9 first wall.

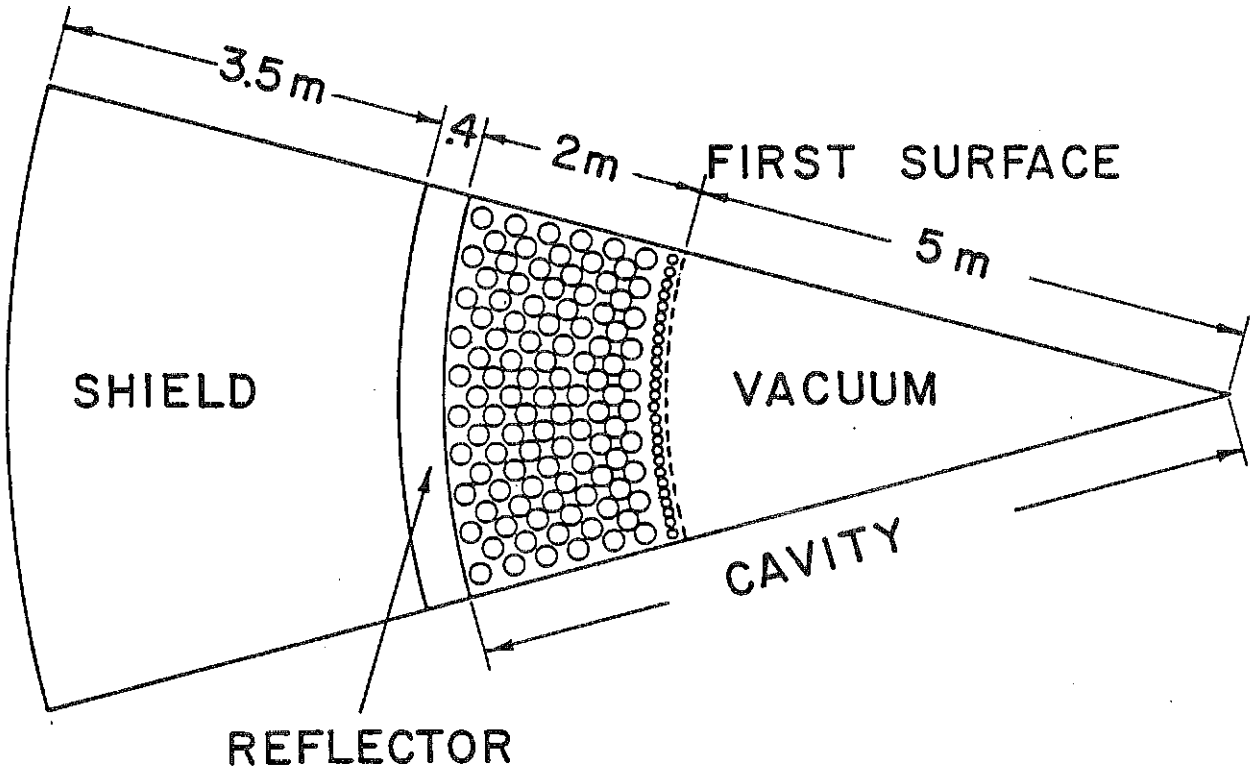

Fig. VI.1-3

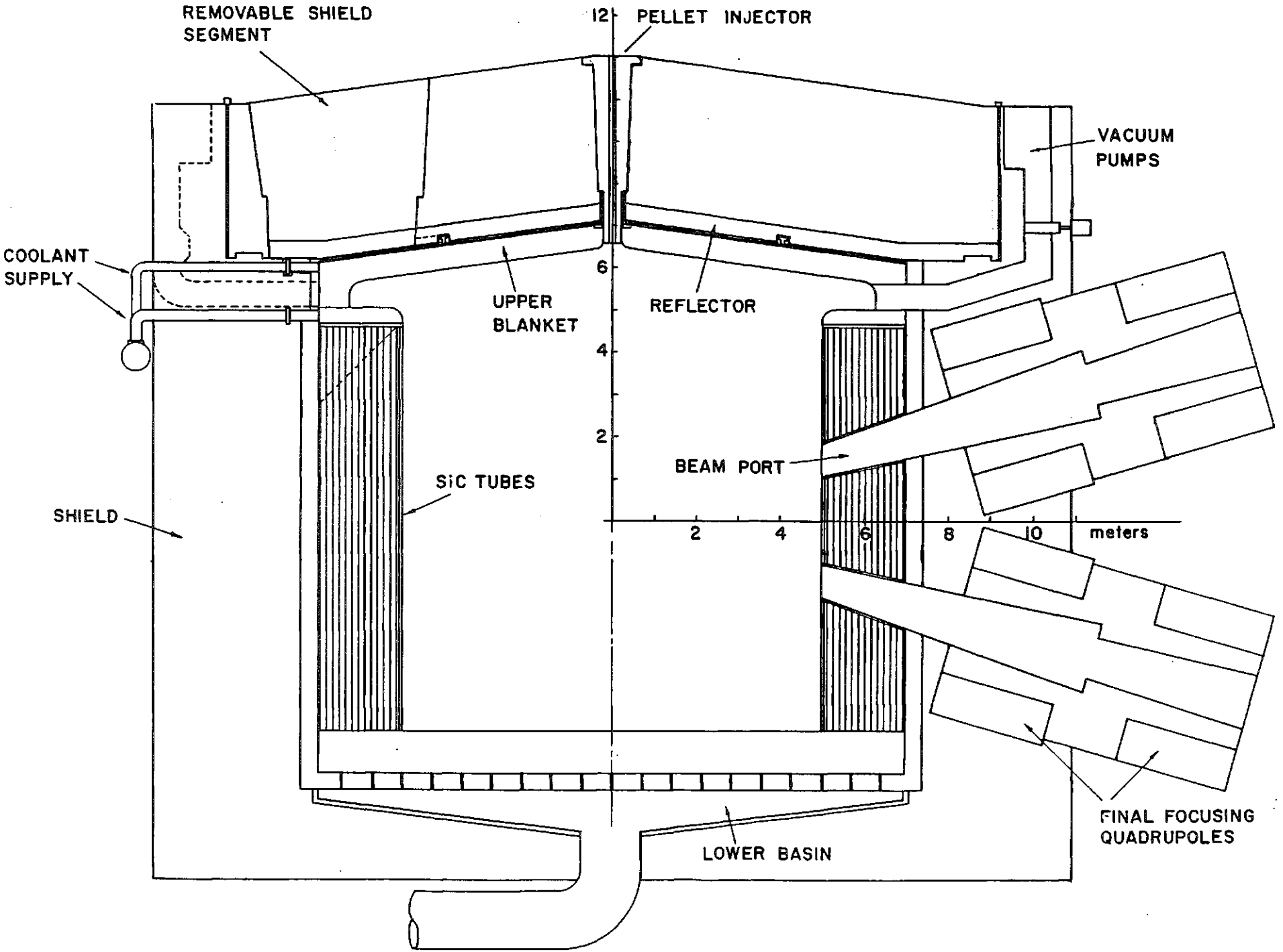
REMOVABLE SHIELD SEGMENT
12
PELLET INJECTOR
VACUUM PUMPS
COOLANT SUPPLY
UPPER BLANKET
REFLECTOR
6
4
2
BEAM PORT
SiC TUBES
SHIELD
2
4
6
8
10
meters
FINAL FOCUSING QUADRUPOLES
LOWER BASIN

Fig. VI.1-4

circulated, Fig. VI.1-3. It is followed by a reflector zone made of HT-9 which is 40 cm thick and finally by the shield, which is primarily concrete and is 3.5 m thick. The top of the cavity has wedge shaped blanket modules, 50 cm thick which are also filled with $Li_{17}Pb_{83}$. They too are followed by 40 cm of HT-9 reflector and a 3.5 m concrete shield. The bottom of the cavity has a pool of $Li_{17}Pb_{83}$ one meter thick, followed by a 40 cm thick reflector which has holes in it to allow the coolant to drain out. A catch basin then directs the flow to an outlet tube through which it is pumped to the steam generator. The rest of the material that follows is a concrete shield.

The top of the cavity has a unique design. Although the blanket modules are designed to stay stationary, the reflector and shield is capable of being rotated about the central axis. This is needed to provide access to the blanket modules for replacement and will be discussed further in Chapter IX. The upper blanket modules are locked to the reflector by means of studs which fit in milled slots. During reactor operation when the modules are filled with $Li_{17}Pb_{83}$, the stud latches are actuated and the modules are locked to the reflector. However, during servicing when the modules are drained of all the breeding material, the stud latches are de-activated. At this time the blanket modules are only supported on the outer periphery and in the center of the cavity, where they are attached to a central hub. This makes it possible to rotate the reflector and shield while the blanket modules remain stationary.

The cavity is sealed to the outside by a liner which is welded to the reflector at the upper end of the cavity. A circumferential weld (or seal) between the liner on the stationary part of the top shield and the rotatable part maintains the cavity atmosphere during operation.

At the junction between the top blanket modules and the SiC tubes, there are 30 apertures, 65 cm high and 1.2 m wide. These are the vacuum system ports. The vacuum ducts which are concealed from direct line of sight of neutrons lead to pumping stations located in the upper corner of the reactor cavity. These pumps are used to evacuate the cavity prior to operation and to pump the non-condensable gases, such as the hydrogen species and the helium. The pumping system is discussed further in section VI.5.

There are 20 beam ports in each cavity. Each two beams come in at ± 16° to the horizontal, spaced at 36° circumferentially. The blanket is divided in such a way that every third module has two beam ports built in. At the first surface (5 m radius) the beam ports are 23 cm wide and 74 cm high. Distribution manifolds surround the beam tubes such that the SiC tubes are attached to them on the top and bottom. Each beam transport line is attached to the cavity at the point of entry and constitutes the vacuum interface between the cavity and the beam handling system.

VI.1.4 Chamber Parameters

Table VI.1-1 presents reference parameters which have been used as a basis for the calculations in the following sections of this chapter. These values were chosen on the basis of: (1) defining the nature and role of the system, (2) consistency with known materials characteristics of various parts of the system, or (3) as a result of previous calculations. A more detailed parameter set is given in Appendix A.

Table VI.1-1

Cavity and INPORT Region	
Neutron energy/shot (MJ)	285
X-ray energy/shot (MJ)	90
Debris energy/shot (MJ)	21
Gamma energy/shot (MJ)	< 1
Cavity shape	cylindrical
Cavity diameter to vacuum wall (m)	14
Cavity height at center (m)	11.5
Coolant and breeding material	$Pb_{83}Li_{17}$ (natural)
INPORT tube structural material	SiC
INPORT region support structure	HT-9
First surface radius (m)	5
INPORT tube region packing fraction	0.33
INPORT tube length (m)	10
INPORT tube diameter (cm)	
First two rows	3
Remainder	10
Number of first row tubes	1230
Number of remaining tubes	3060
Number of Beam penetrations	20
Total area of beam penetrations at the first surface (m^2)	3.6
Pb atom density (x 10^{-10} atom/cm^3) just before shot	4
Noncondensible atom density at 500°C (x 10^{-10} atoms/cm^3)	0.13
Chamber top thickness (m)	0.5
Coolant volume fraction	0.97
Bottom region thickness (m)	1
Coolant volume fraction	1
Vacuum Wall (first material wall)	
Structural material	HT-9
Inside diameter (m)	14
Thickness (m)	0.01

Table VI.1-1 (continued)

Reflector	
Structural material	HT-9
Coolant	$Pb_{83}Li_{17}$
Coolant volume fraction	0.9
Inside diameter (m)	14.02
Thickness (m)	0.4
Shield	
Structural Material	Concrete (unreinforced)
Coolant	H_2O
Coolant volume fraction	0.05
Inside diameter (m)	14.82
Thickness (m)	3.5
$Pb_{83}Li_{17}$ Coolant	
Inlet temperature (°C)	330
Outlet temperature (°C)	500
Pressure (MPa)	0.2

References for Section VI.1

1. A.P. Fraas, "The BLASCON - An Exploding Pellet Fusion Reactor," Oak Ridge National Laboratory, Oak Ridge, TN, TM-3231 (July 1971).

2. L.A. Booth, "Central Station Power Generation by Laser Driven Fusion," Nucl. Eng. and Design 24, 263, North-Holland Publishing Co. (1973).

3. J. Hovingh, J.A. Maniscalco, M. Peterson, R.W. Werner, "The Preliminary Design of a Suppressed Ablation Laser Induced Fusion Reactor," Proc. 1st Top. Mtg. on the Tech. of Controlled Nucl. Fusion, I, 96, San Diego, CA (1974).

4. J.K. Baird and V.E. Anderson, "Combination First Wall and Parabolic Lithium Mirror for a Laser-Driven Pellet Fusion Reactor," Proc. 6th Symp. on Eng. Prob. of Fusion Research, 1015, San Diego, CA (1976).

5. R.R. Holman and W.P. Kovacki, "Conceptual Approach to Laser Fusion Hybrid Reactor," Trans. ANS 1977 Summer Mtg., 56, New York, NY (1977).

6. T. Frank, D. Freiwald, T. Merson, J. Devaney, "A Laser Fusion Reactor Concept Utilizing Magnetic Fields for Cavity Protection," Proc. 1st Top. Mtg. Tech. of Controlled Nucl. Fusion, I, 83, San Diego, CA (1974).

7. B. Badger et al., "SOLASE, A Laser-Fusion Reactor Study," University of Wisconsin Fusion Design Memo UWFDM-220, (Dec. 1977).

8. F.H. Bohn, H. Conrads, J. Darvas, and S. Forster, "Some Design Aspects of Inertially Confined Fusion Reactors," Proc. 5th Symp. of Eng. Prob. of Fusion Research, 107, Princeton, NJ (1973).

9. J.M. Williams, F.T. Finch, T.G. Frank, and J.S. Gilbert, "Engineering Design Considerations for Laser Controlled Thermonuclear Reactors," Proc. 5th Symp. of Eng. Prob. of Fusion Research, 102, Princeton, NJ (1973).

10. S.G. Varnado and G.A. Carlson, "Considerations in the Design of Electron-Beam-Induced Fusion Reactor Systems," Nucl. Tech. 29, 415 (June 1976).

11. J. Hovingh, "First Wall Studies of a Laser Fusion Hybrid Reactor Design," Proc. 2nd Top. Mtg. on the Tech. of Controlled Nucl. Fusion, II, 765, Richland, WA (1976).

12. R.J. Burke, "Outline for a Large-Pulse Electron-Beam-Ignited Fusion Reactor," Argonne National Laboratory, Argonne, IL, CTR/TM-31 (1974).

13. W. Seifritz and H. Naegel, "Uranium and Thorium Shells Serving as Tampers of DT-Fuel Pellets for the Electron-Beam-Induced Fusion Approach," Trans. ANS 21, 18 (1975).

14. J.R. Powell, O. Lazareth and J. Fillo, "A Liquid Wall Boiler and Moderator (BAM) for Heavy Ion-Pellet Fusion Reactors," Brookhaven National Laboratory, Long Island, NY, BNL-50744 (Nov. 1977).

15. W.R. Meier and J.A. Maniscalco, "Reactor Concepts for Laser Fusion," Lawrence Livermore National Laboratory, Livermore, CA, UCRL-79694 (1977).

VI.2 Impulse Response of INPORT Tubes

VI.2.1 Impulse Characterization

When the PbLi is vaporized by the target generated X-rays, a reactive impulse imparts radial acceleration to the first two rows of the tube bank. One can conservatively estimate the bulk kinetic energy of the vaporized fluid to be equal to the thermal energy of the gas.

$$(3/2)\ (M_{gas}/m_{ion})\ k_B T_{gas} \doteq (1/2)\ M_{gas}\ V^2 \qquad \text{(VI.2-1)}$$

Here the left-hand-side represents the thermal energy of the gas which is equal to the deposited X-ray energy less the energies of ionization and vaporization. The bulk velocity of the gas is denoted by V while m_{ion} represents the average mass of ions in the gas. For the case of 87.6 MJ of X-ray energy and 13.3 kg of vaporized PbLi, T_{gas} = 1.26 eV. The reactive impulse equals $M_{gas}V$.

$$\Delta I = M_{gas}\ (3k_B T_{gas}/m_{ion})^{1/2} \qquad \text{(VI.2-2)}$$

$$= 1.89 \times 10^9 \text{ dyne-sec.}$$

This can also be expressed as an impulsive pressure per unit surface area.

$$\Delta P = 600 \text{ dyne-sec/cm}^2 \qquad \text{(VI.2-3)}$$

The preceding estimate is conservative since it is assumed that all vaporized atoms are initially moving towards the center of the cavity with their thermal velocity. This will clearly overestimate the reactive impulse.

VI.2.2 Stiffened INPORT Tubes

VI.2.2.1 General Characterization

Both stiffened and unstiffened silicon carbide tubes were considered for the INPORT units. In the former case the woven tubes are rigidized with a SiC binder or matrix but with a porous wall. Such members resist transverse loading by flexural action, not unlike structural beams. A general formulation is developed for stresses, deflections and frequencies. For uniform impulsive pressure, design data is presented which identifies the basic mechanical characteristics of these elements.

VI.2.2.2 Dynamic Analysis

The principle equation of motion governing the transverse vibration of the tube is given by

$$EI\ \partial^4 y(x,t)/\partial x^4 + \bar{m}\ \partial^2 y(x,t)/\partial t^2 = p(x,t) \qquad \text{(VI.2-4)}$$

where E = elastic modulus

I = cross section moment of inertia

$\bar{m}$ = mass per unit length

$p(x,t)$ = dynamic pressure (force per unit length)

t = time

$y(x,t)$ = transverse displacement.

The coordinate system and loading are shown on a typical span of tubing in Fig. VI.2-1.

To determine the natural frequencies of the tube, the external load is set equal to zero, resulting in the differential equation for free vibration. A solution of the form

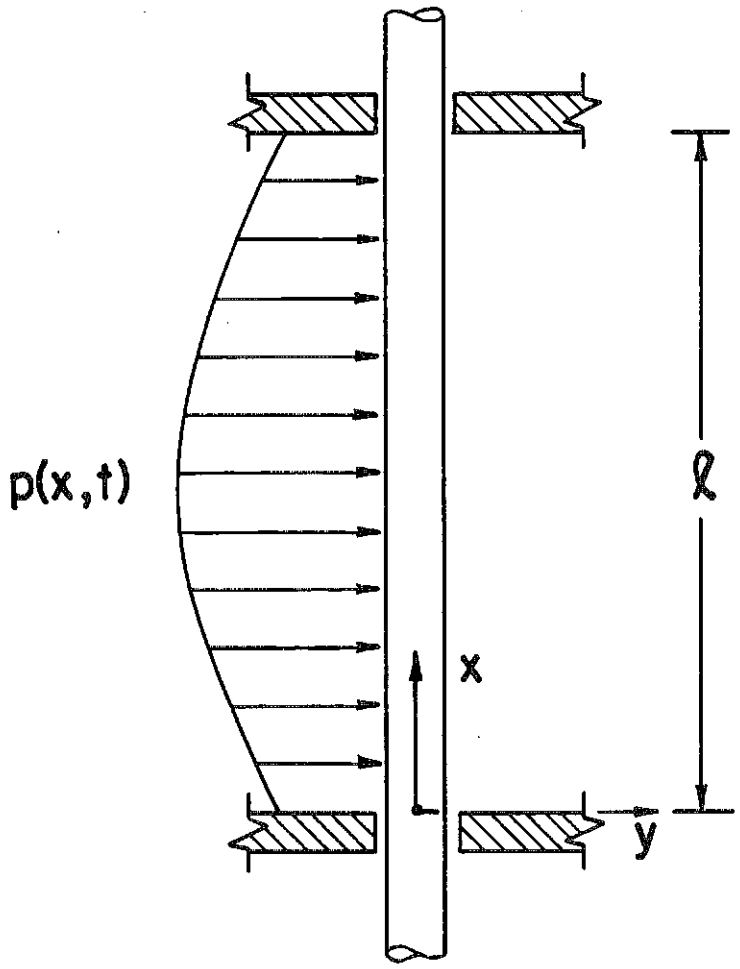

Fig. VI.2-1

$$y(x,t) = \Phi(x)\, Y(t) \qquad \text{(VI.2-5)}$$

is substituted into Eq. VI.2-4, leading to

$$\frac{EI}{\bar{m}\,\Phi(x)} \frac{d^4\Phi(x)}{dx^4} = \frac{1}{Y(t)} \frac{d^2Y(t)}{dt^2} \,. \qquad \text{(VI.2-6)}$$

With x and t being independent variables, the preceding equation can be satisfied only if both sides are set equal to a constant, producing two ordinary differential equations. Choosing ω^2 for this constant, these equations will have solutions of the form

$$Y(t) = C_1 \sin \omega t + C_2 \cos \omega t \qquad \text{(VI.2-7)}$$

$$\Phi(x) = A \sin ax + B \cos ax + C \sinh ax + D \cosh ax \qquad \text{(VI.2-8)}$$

where

$$a^4 = \bar{m}\, \omega^2/EI \,.$$

The tubes would be continuous through any intermediate support, if provided, with the deformed shape for any span characterized by zero slope change and zero deflection at each end. Thus, the boundary conditions are

$$y(o,t) = y\,(\ell,t) = 0$$

$$\partial y(o,t)/\partial x = \partial y(\ell,t)/\partial x = 0 \,. \qquad \text{(VI.2-9)}$$

With these and Eq. VI.2-8 the following transcendental equation is obtained.

$$\cos a\ell \cosh a\ell = 1 \qquad \text{(VI.2-10)}$$

This equation generates an infinite number of discrete eigenvalues, $a_n (n=1,2,3,...)$, which are obtained numerically and are related to the natural frequencies ω_n by

$$\omega_n = a_n^2 (EI/\bar{m})^{1/2} \qquad n = 1,2,3, \ldots \qquad \text{(VI.2-11)}$$

Corresponding to each natural frequency is a characteristic shape or eigenfunction

$$\Phi_n(x) = C_n[(A_n/B_n)(\sinh a_n x - \sin a_n x) + \cosh a_n x - \cos a_n x] \qquad \text{(VI.2-12)}$$

where

$$A_n/B_n = (\cos a_n \ell - \cosh a_n \ell)/(\sinh a_n \ell - \sin a_n \ell)$$

and C_n is an arbitrary constant.

After the mode shapes and frequencies have been determined, a modal-superposition method of analysis can be used to solve for the dynamic response of the forced vibration. Thus, any displacement can be expressed by superimposing appropriate amplitudes of the vibration mode shapes for the structure. This can be written as

$$y(x,t) = \sum_n \Phi_n(x)\, Y_n(t) \qquad \text{(VI.2-13)}$$

Using an energy solution, Lagrange's equation is applied to the system

$$d[\partial K/\partial \dot{Y}_n(t)]/dt + \partial U/\partial Y_n(t) = \partial \Omega_e/\partial Y_n(t) \qquad \text{(VI.2-14)}$$

where K = total kinetic energy

U = total flexural strain energy

Ω_e = external work

and $(\cdot)$ denotes differentiation with respect to time, t. The kinetic energy for the entire system is given by

$$\begin{aligned} K &= (1/2)\ \bar{m} \int_0^{\ell} \dot{y}(x,y)^2\ dx \\ &= (1/2)\ \bar{m} \int_0^{\ell} [\sum_n \Phi_n(x)\ \dot{Y}_n(t)]^2\ dx \\ &= (1/2)\ \bar{m} \sum_n \dot{Y}_n^2(t) \int_0^{\ell} \Phi_n^2(x)\ dx \end{aligned} \qquad \text{(VI.2-15)}$$

where $\bar{m}$ is considered to be constant over the span and orthogonality of the mode shapes has been utilized.

The work done by external forces is

$$\begin{aligned} \Omega_e &= \int_0^{\ell} p(x,t)\ y(x,t)\ dx \\ &= \int_0^{\ell} p(x,t)\ [\sum_n \Phi_n(x)\ Y(t)]\ dx\ . \end{aligned} \qquad \text{(VI.2-16)}$$

Considering $p(x,t) = P(x)\ f(t)$, where $P(x)$ is the spatial load distribution and $f(t)$ is the time function, the external work becomes

$$\Omega_e = f(t) \sum_n Y_n(t) \int_0^{\ell} P(x)\ \Phi_n(x)\ dx\ .$$

Substituting into Eq. VI.2-14 yields

$$\tilde{m}\,\ddot{Y}_n(t)\int_o^\ell \Phi_n^2(x)\,dx = \partial U/\partial Y_n(t) = f(t)\int_o^\ell P(x)\,\Phi_n(x)\,dx$$

or (VI.2-17)

$$\ddot{Y}_n(t) = \omega_n^2\,Y_n(t) = f(t)\int_o^\ell P(x)\,\Phi_n(x)\,dx/\bar{m}\int_o^\ell \Phi_n^2(x)\,dx\ .$$

Eliminating the time dependency, the modal static deflection can be defined as follows.

$$Y_{n\ st} = \int_o^\ell P(x)\,\Phi_n(x)\,dx/\bar{m}\,\omega_n^2\int_o^\ell \Phi_n^2(x)\,dx\ . \qquad \text{(VI.2-18)}$$

To determine the dynamic response, the static response is multiplied by the dynamic load factor (DLF). More descriptively this could be identified as a dynamic load function, representing the time function of the loading for an equivalent single degree of freedom system. Additional details on this can be found in Reference (1). The total deflection at any point is given by

$$y(x,t) = \sum_n \Phi_n(x)\,Y_{n\ st}\,(DLF)_n\ . \qquad \text{(VI.2-19)}$$

The dynamic bending moment can be determined from

$$M(x,t) = EI\,\partial^2 y(x,t)/\partial x^2 = EI\sum_n Y_{n\ st}\,d^2\Phi_n(x)/dx^2\,DLF_n\ . \qquad \text{(VI.2-20)}$$

The flexural stess in the tube is

$$\sigma(x,t) = M(x,t)\,R_o/I = ER_o\sum_n Y_{n\ st}\,d^2\,\Phi_n(x)/dx^2\,(DLF)_n\ . \qquad \text{(VI.2-21)}$$

Here R_0 represents the outer radius and the stress is associated with points at the outer surface.

VI.2.2.3 Quantitative Results

The preceding work identifies principle equations for stiffened tube response. Complete details were incorporated into a computer program for the determination of numerical values.

The fundamental frequency curves are shown as functions of tube length for various radii and thicknesses in Figs. VI.2-2, 2-3 and 2-4. These include the mass of the PbLi. It can be seen that for lengths greater than 800 cm, frequencies are very low and relatively constant. For lengths less than 200 cm, the fundamental frequencies rise very quickly. To avoid resonance, these results indicate that the effective length (between supports) should be considerably less than the full length of 10 m. Figure VI.2-5 shows deflection results based upon a dynamic load factor of unity for a single impulse, i.e., resonance is not considered. As the tube thickness and inner radius decrease, e.g., 1 mm x 1.5 cm, the transverse displacements rise very rapidly. Similar effects can be expected for flexural stresses. In Fig. VI.2-6, the value predicted for an INPORT unit with a radius, thickness and length of 1.5 cm, 1 mm, and 10 m is unacceptably high.

Natural frequencies can be raised substantially above the repetition rate while deflections and stresses are reduced if an intermediate support mechanism is employed. Figure VI.2-7 is a conceptual representation for a ring support which sustains the radial impulsive forces by self-equilibrated circumferential tensile stresses. Such a design precludes the necessity to transmit thrust to the outer wall. Small radial dimensions, as implied by the sketch, would generally be important to reduce thermal stresses caused by

Fig. VI.2-2

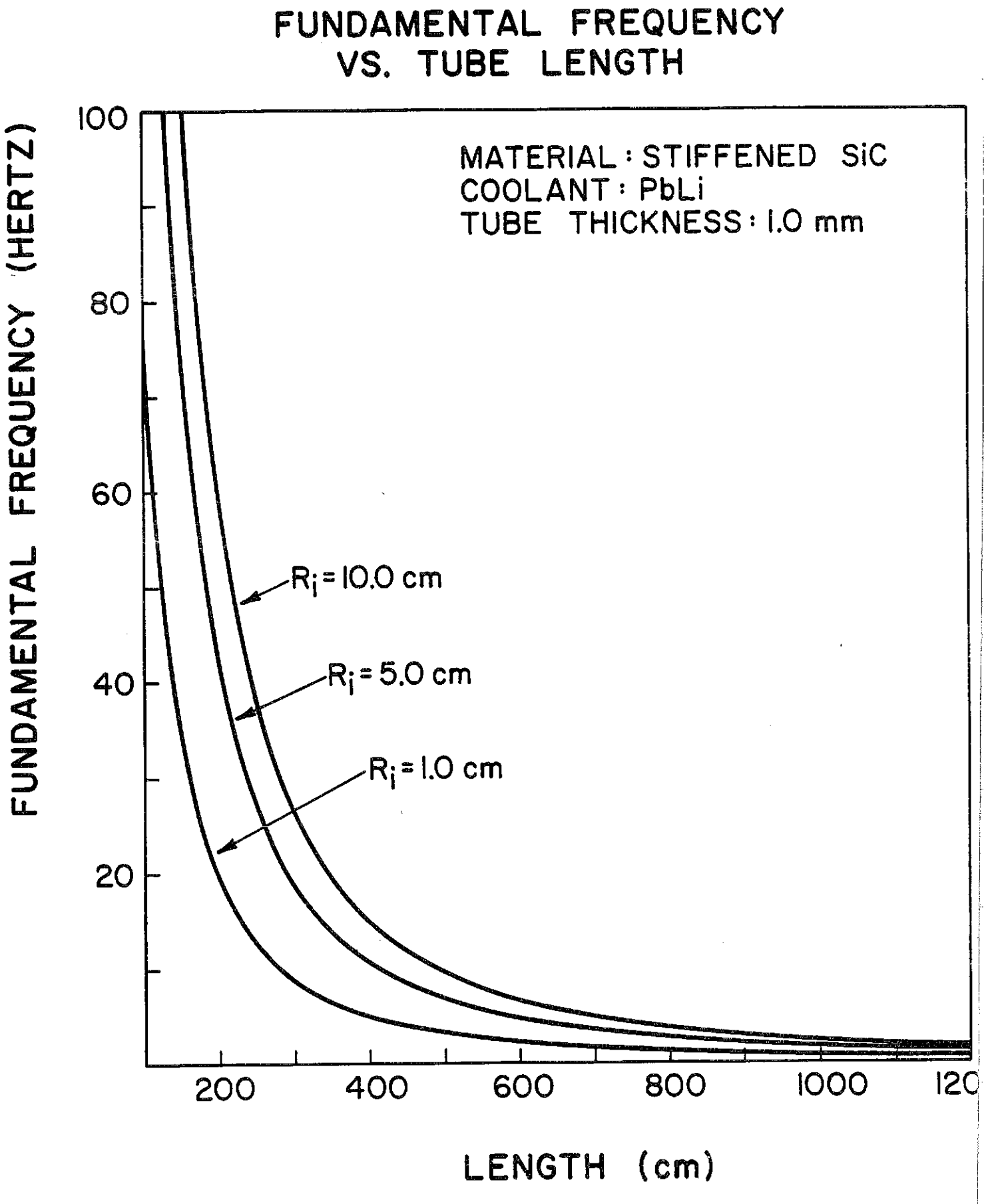
FUNDAMENTAL FREQUENCY
VS. TUBE LENGTH
MATERIAL : STIFFENED SiC
COOLANT : PbLi
TUBE THICKNESS : 1.0 mm
R_i = 10.0 cm
R_i = 5.0 cm
R_i = 1.0 cm
FUNDAMENTAL FREQUENCY (HERTZ)
100
80
60
40
20
200
400
600
800
1000
120
LENGTH (cm)

Fig. VI.2-3

FUNDAMENTAL FREQUENCY VS. TUBE LENGTH

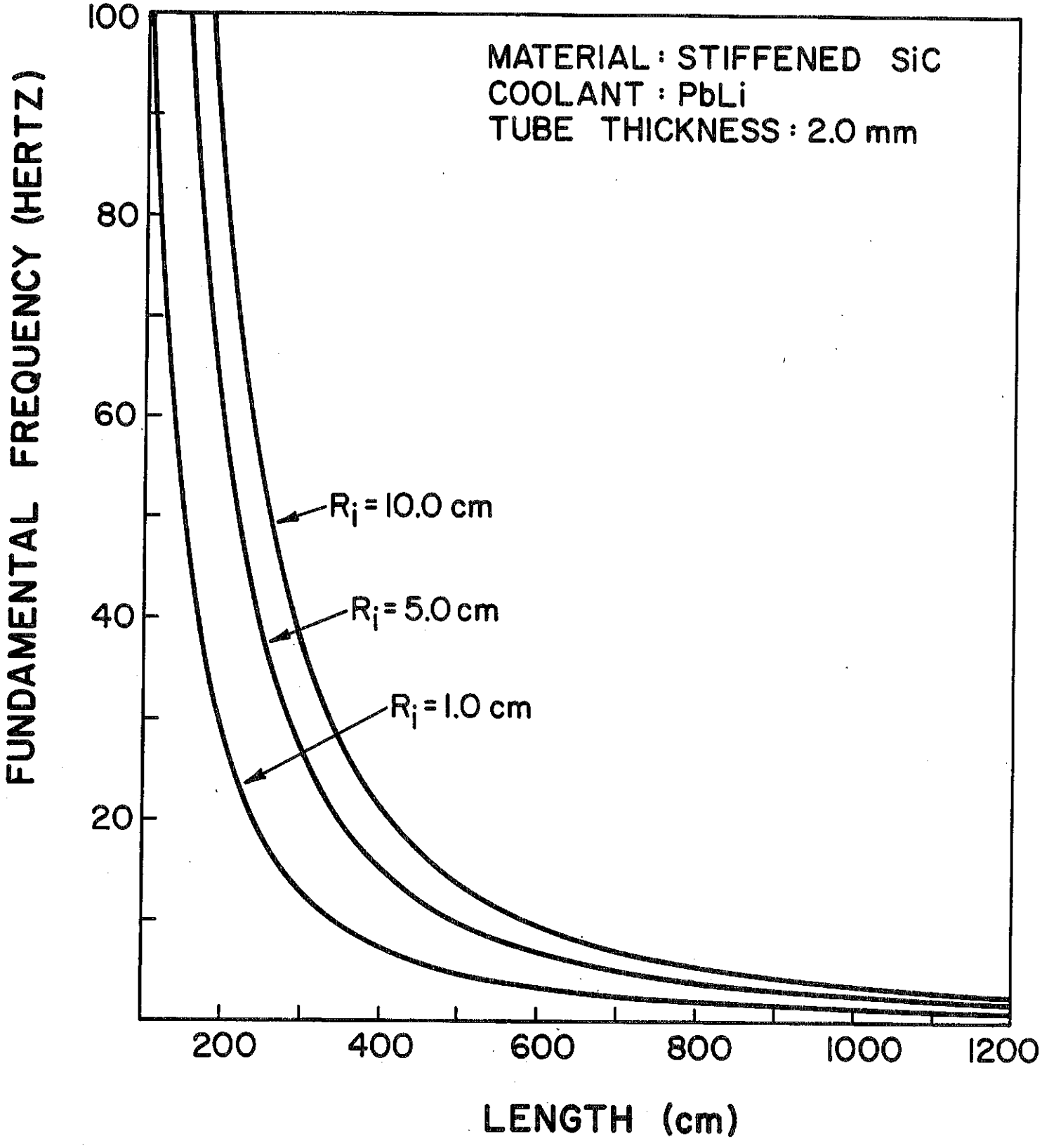

Fig. VI.2-4

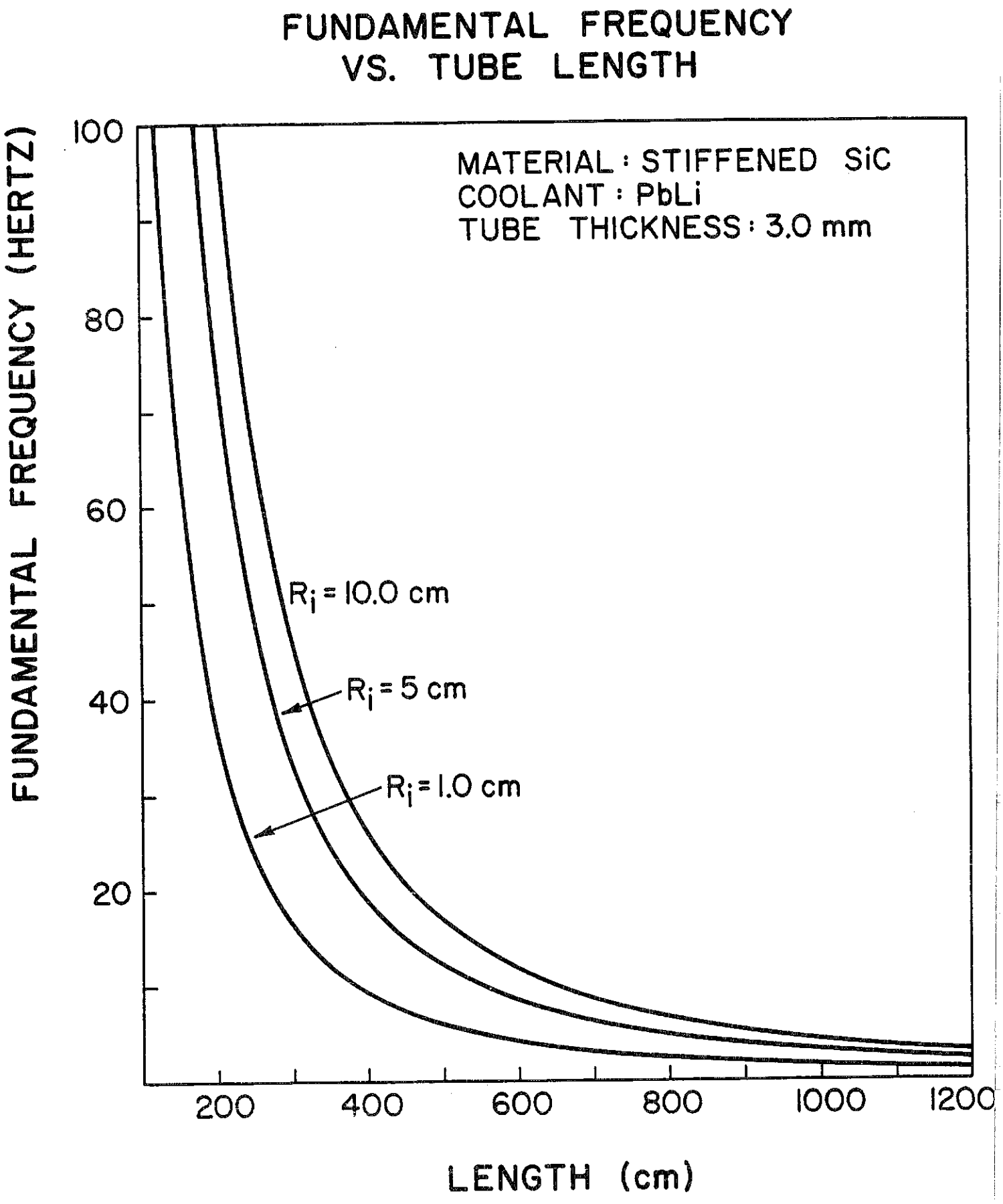
FUNDAMENTAL FREQUENCY
VS. TUBE LENGTH
MATERIAL : STIFFENED SiC
COOLANT : PbLi
TUBE THICKNESS : 3.0 mm
R_i = 10.0 cm
R_i = 5 cm
R_i = 1.0 cm
FUNDAMENTAL FREQUENCY (HERTZ)
100
80
60
40
20
200
400
600
800
1000
1200
LENGTH (cm)

Fig. VI.2-5

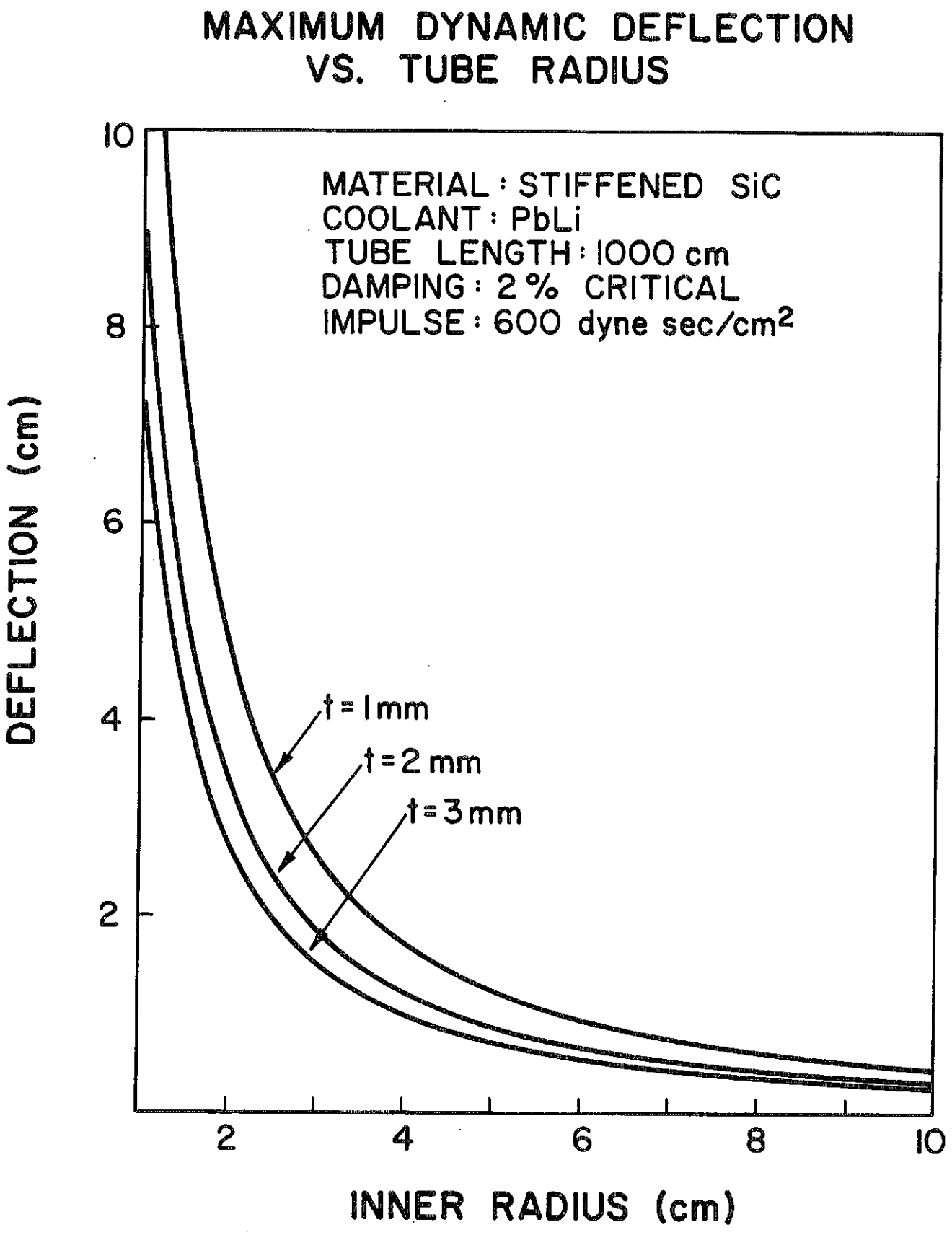
MAXIMUM DYNAMIC DEFLECTION
VS. TUBE RADIUS
MATERIAL : STIFFENED SiC
COOLANT : PbLi
TUBE LENGTH : 1000 cm
DAMPING : 2 % CRITICAL
IMPULSE : 600 dyne sec/cm²
t = 1 mm
t = 2 mm
t = 3 mm
DEFLECTION (cm)
INNER RADIUS (cm)
2
4
6
8
10

VI.2-13

Fig. VI.2-6

MAXIMUM DYNAMIC FLEXURAL STRESS VS. TUBE RADIUS

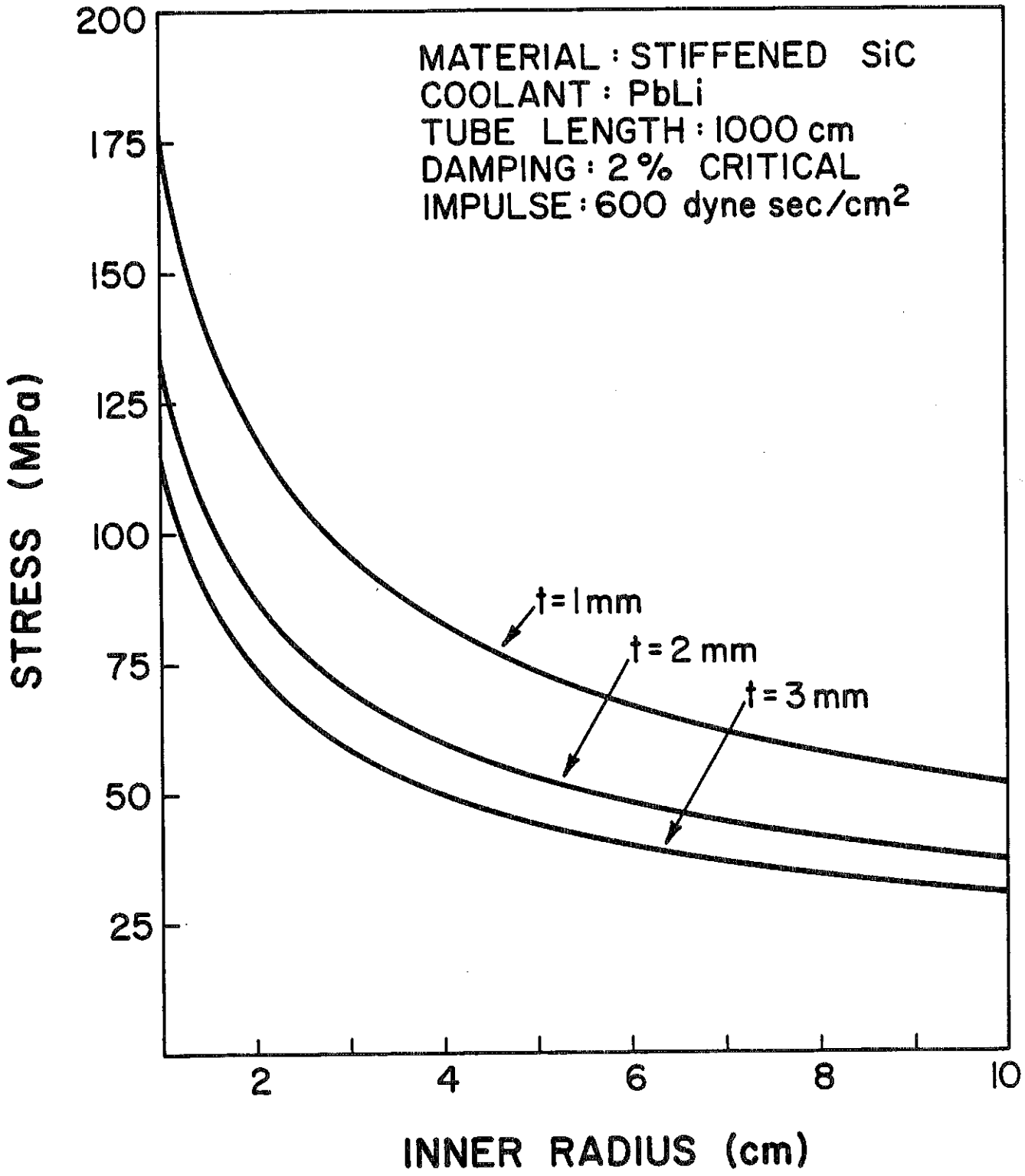

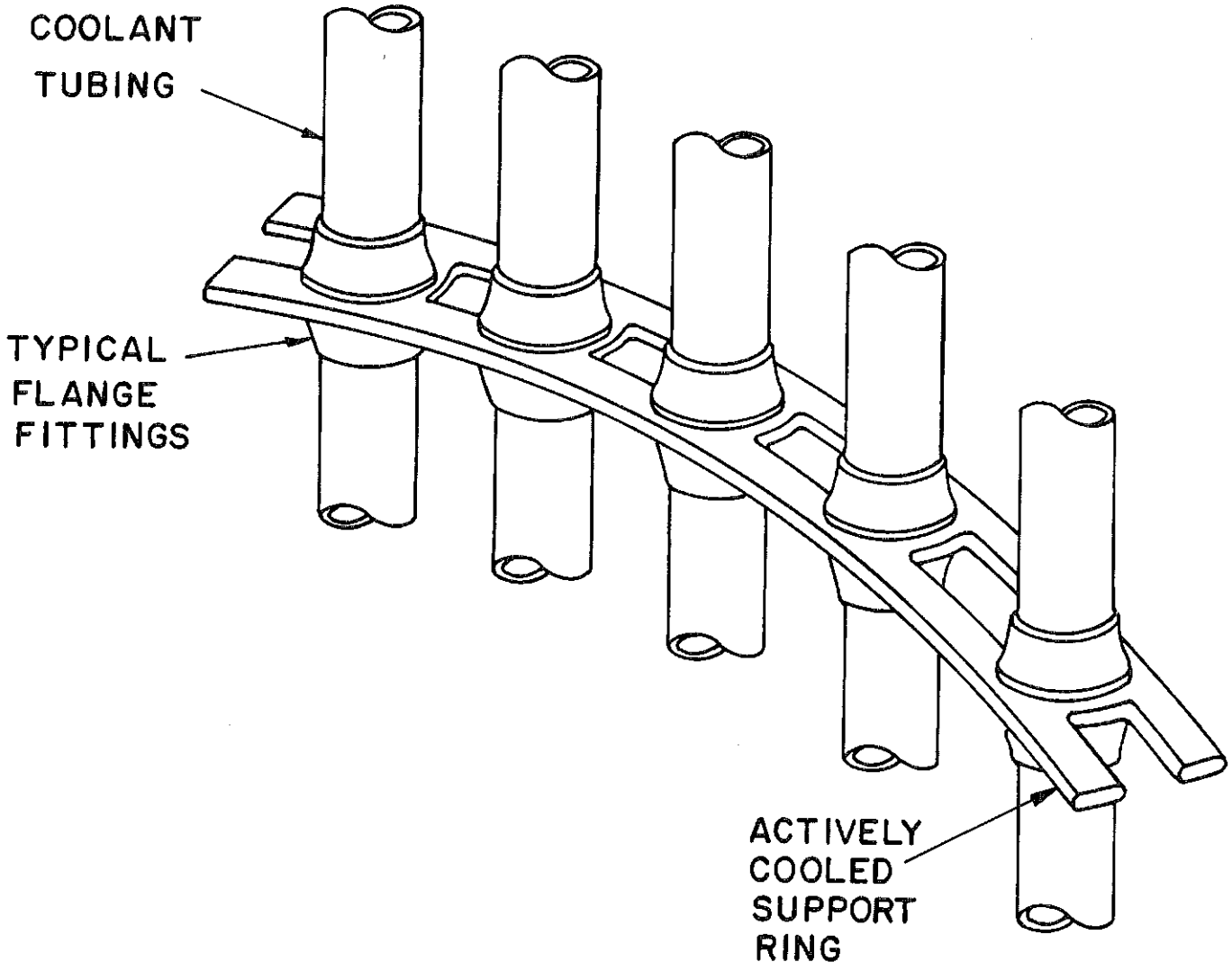
COOLANT
TUBING
TYPICAL
FLANGE
FITTINGS
ACTIVELY
COOLED
SUPPORT
RING

Fig. VI.2-7

radial temperature gradients. Active protective cooling would still be essential.

A combination of reasons led the decision to use unstiffened rather than stiffened SiC tubes for the INPORT units. In the latter case, the geometry is that of a somewhat delicate structure requiring extra care in fabrication and handling. The analysis has shown that resonance, large deflections and stresses are potential problems without supplementary structural support which of course is another addition to complexity. The stiffened tubes also involve untested manufacturing techniques and unknown additional expenses as well. By comparison, unstiffened tubes do not appear to have such disadvantages while possessing inherent desirable features. Their mechanical response characteristics are discussed in the work which follows.

VI.2.3 Mechanical Response of Unstiffened INPORT Tubes

VI.2.3.1 General Characteristics

The term "unstiffened" used here denotes a tube woven from silicon carbide fibers alone. The wall is pliable and porous, essentially cloth-like. A small percentage of fibers will run axially in the wall to enhance the tensile load carrying capacity.

As structural members, such units resist lateral loading by tensile force action alone, i.e., having negligible shear and bending resistance. For the dynamic response, dissipation is accounted for by including viscous damping in the system. In the work which follows, two support modes are considered separately. The first involves suspension from the upper end with the lower free to move while the second has the bottom end constrained in addition.

VI.2.3.2 Equilibrium Equations and Vibration Modes-One Point Suspension

The notation and coordinate system for the equilibrium equations is shown in Fig. VI.2-8. On the element, T represents the tension while ρ and g denote

INPORT TUBE EQUILIBRIUM NOTATION

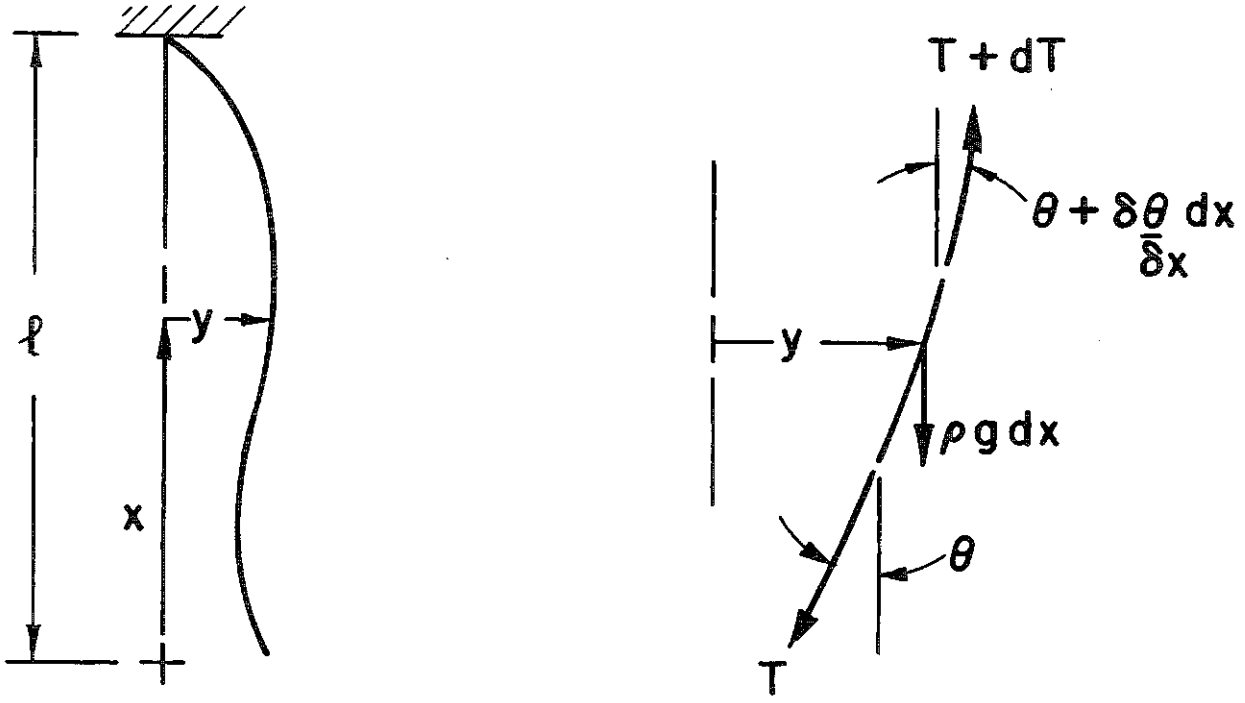

Fig. VI.2-8

the mass density per unit length and the gravitational constant, respectively. At a generic location x, the lateral displacement component is taken to be y. For response characterized by small slope changes, equilibrium in the axial direction requires the tension gradient to be equal to the weight per unit length,

$$dT/dx = \rho g$$

or

$$T = \rho g x \qquad \text{(VI.2-22)}$$

from the condition that the tension is zero at the lower end. In the transverse direction, the equilibrium statement can be reduced to

$$T\ \partial\Theta/\partial x + \rho g \Theta = \rho\ \partial^2 y/\partial t^2 \qquad \text{(VI.2-23)}$$

in which t denotes time. The two preceding equations can be combined into

$$x\ \partial^2 y/\partial x^2 + \partial y/\partial x = \partial^2 y/g\partial t^2\ . \qquad \text{(VI.2-24)}$$

Characteristic solutions may be developed by taking the displacement as a product of functions in the variables: X(x) T(t). Thus

$$\ddot{T}/gT = xX''/X + X'/X = -\lambda^2\ . \qquad \text{(VI.2-25)}$$

It follows that the solution for the time-dependent component is

$$T = A \cos \lambda\sqrt{g}t + B \sin \lambda\sqrt{g}t \qquad \text{(VI.2-26)}$$

where λ, A and B are constants. The equation for the spatial component is of the form

$$(x^r y')' + (ax^s + bx^{r-2})\, y = 0$$

the solution of which can be expressed in terms of Bessel Functions of the first and second kind, J_ν and Y_ν. In general the parameters and solution are

$$\alpha = (1-r)/2 \qquad \gamma = (2-r+s)/2$$

$$k = 2|a|^{1/2}/(2-r+s)$$

$$\nu = [(1-r)^2 - 4b]^{1/2}/(2-r+s)$$

$$y = x^\alpha [CJ_\nu(kx^\gamma) + DY_\nu(kx^\gamma)]$$

where C and D are arbitrary constants. For this specific case

$r = 1$ $\quad b = 0$ $\quad a = \lambda^2$ $\quad s = 0$

$\alpha = 0$ $\quad \gamma = 1/2$ $\quad k = 2\lambda$ $\quad \nu = 0$.

Thus

$$X = CJ_0(2\lambda x^{1/2}) + DY_0(2\lambda x^{1/2}) \qquad \text{(VI.2-27)}$$

Since Y_0 becomes arbitrarily large as x tends to zero, it is necessary to delete this component, or simply set D equal to zero. Satisfaction of the

boundary condition at the upper support is also necessary.

$$y(\ell,t) = 0 \qquad \therefore J_0 (2\lambda\ell^{1/2}) = 0 .$$

The roots are

$$2\lambda\ell^{1/2} = 2.4048,\ 5.5201,\ 8.6537,\ \text{etc.}$$

However, the natural frequencies can be defined as

$$\omega_n = \lambda g^{1/2}$$

and thus, for example, the fundamental is

$$\omega_1 = 1.2024\ (g/\ell)^{1/2}\ \text{(rad/sec)}$$

From this it can be seen that system frequencies are determined essentially by the unsupported length. For a length of 10m, the fundamental frequency is

$$\omega_1 = 0.1877\ \text{Hz}$$

The first ten natural frequencies are listed with Fig. VI.2-9. The mode shapes corresponding to the first three natural frequencies are also shown.

VI.2.3.3 Forced Response - One Point Suspension

The general form for the transverse displacement can be obtained using superposition of characteristic solutions.

Fig. VI.2-9

NATURAL VIBRATION MODES OF 3 cm × 10 m INPORT TUBES

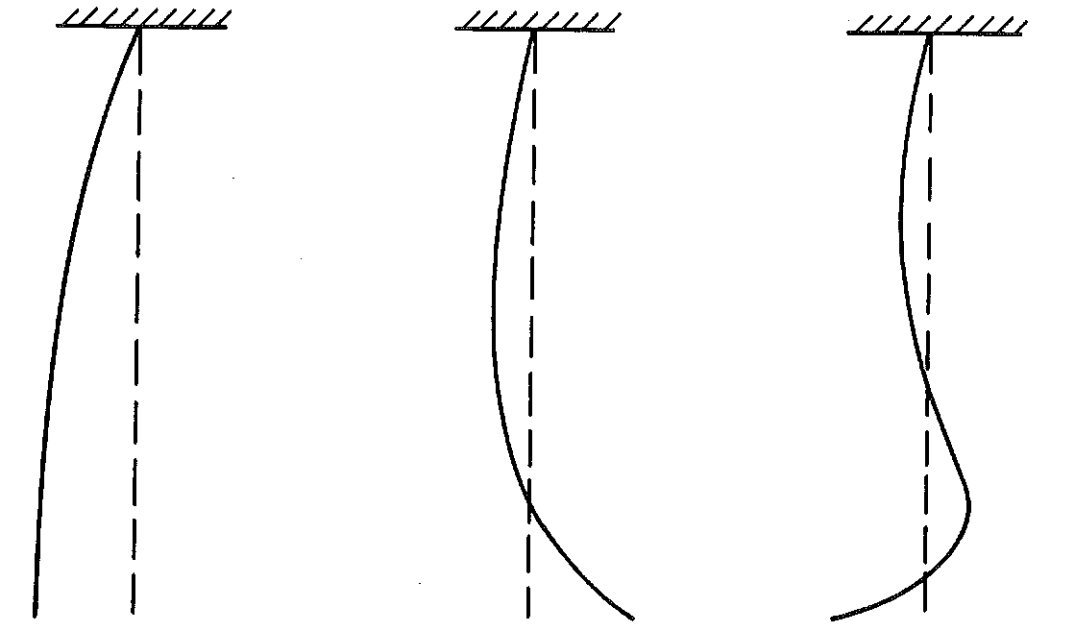

0.1877 Hz 0.4309 Hz 0.6756 Hz

MODE NO.	NATURAL FREQUENCY (Hz)
1	0.1877
2	0.4309
3	0.6756
4	0.9205
5	1.1656
6	1.4519
7	1.7042
8	1.9566
9	2.2089
10	2.4613

$$y(x,t) = \sum_{m=1}^{\infty} J_o(2\lambda_m x^{1/2})[A_m \cos(\lambda_m g^{1/2} t) + B_m \sin(\lambda_m g^{1/2} t)] \quad \text{(VI.2-28)}$$

For a single impulse the initial conditions are

$$y(x,o) = 0 \qquad \partial y(x,o)/\partial t = f(x) \quad \text{(VI.2-29)}$$

With these and orthogonality of the solutions,

$$A_m = 0 \quad B_m = \int_o^{\ell} f(x)\, J_o(2\lambda_m x^{1/2})dx / g^{1/2}\lambda_m \int_o^{\ell} J_o^2(2\lambda_m x^{1/2})dx \quad \text{(VI.2-30)}$$

In this work, $f(x)$ is taken as a uniform initial velocity $\dot{y}_o$. Then after evaluating the integrals in Eq. VI.2-30, the result is

$$B_m = \dot{y}_o/\lambda_m^2 (g\ell)^{1/2} J_1(2\lambda_m \ell^{1/2}) \quad \text{(VI-2-31)}$$

Thus the formal solution is complete for the initial impulse problem. Numerical results are obtained from a computer program based upon the preceding analysis. Calculations include the weight of the PbLi, the SiC and the outer surface film.

The displacement profile following an impulse at rest is initially very uniform. A typical result is shown in Fig. VI.2-10 at a time of 0.20 sec. This is the instant at which a second impulse would occur in operation. However if the excitation is limited to a single shot, and motion allowed to develop for larger values of time, the shapes become somewhat complex as shown qualitatively in Fig. VI.2-11. The quantitative time histories of Figs. VI.2-12 and VI.2-13 correspond to this case also. The maximum midpoint and tip deflections are approximately 16 and 55 cm, respectively. It was felt

Fig. VI.2-10

DEFLECTION PROFILE OF 3 cm TUBE AT t = 0.20 sec

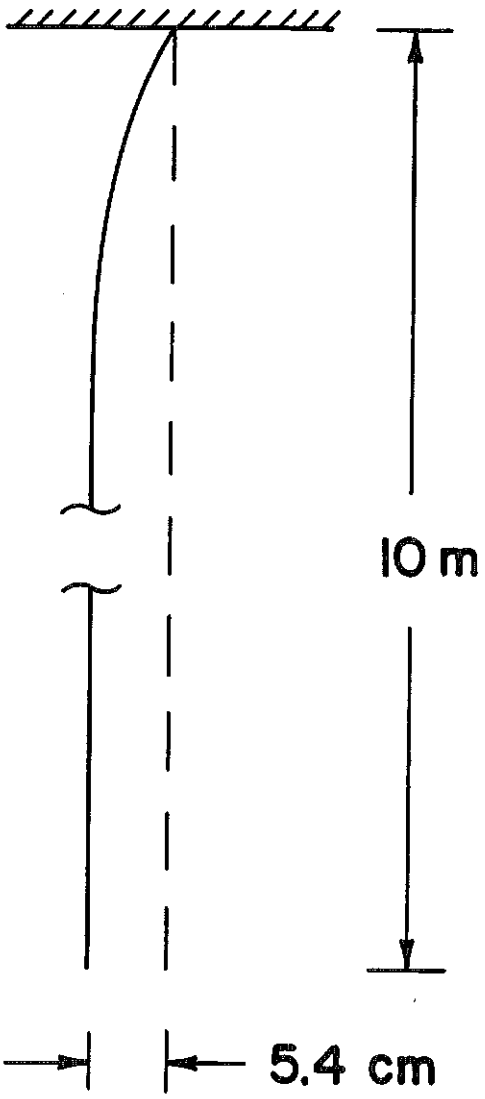

VI.2-23
Fig. VI.2-11

DEFLECTED SHAPES OF 3 cm TUBES AT VARIOUS TIMES AFTER UNIFORM IMPULSE

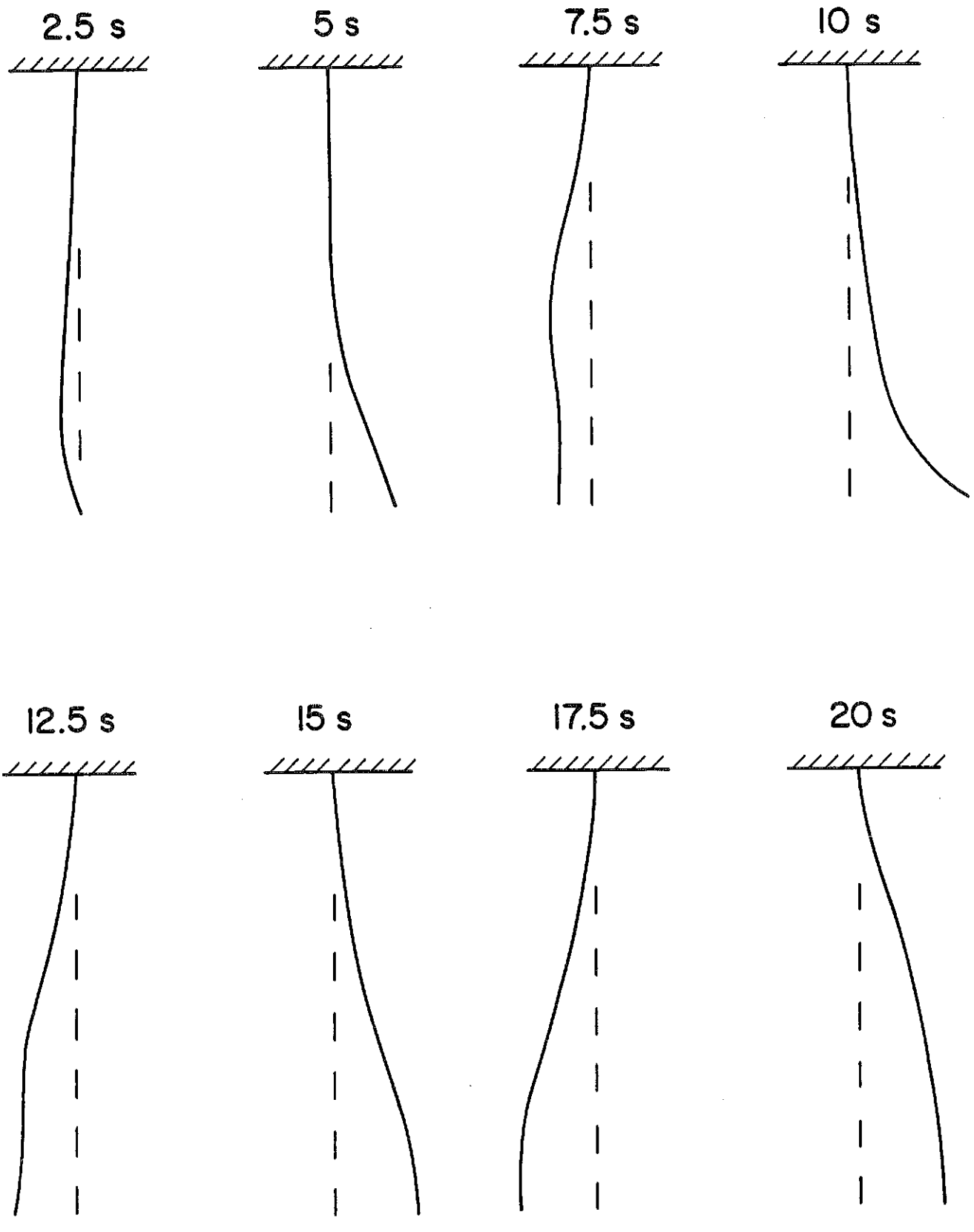

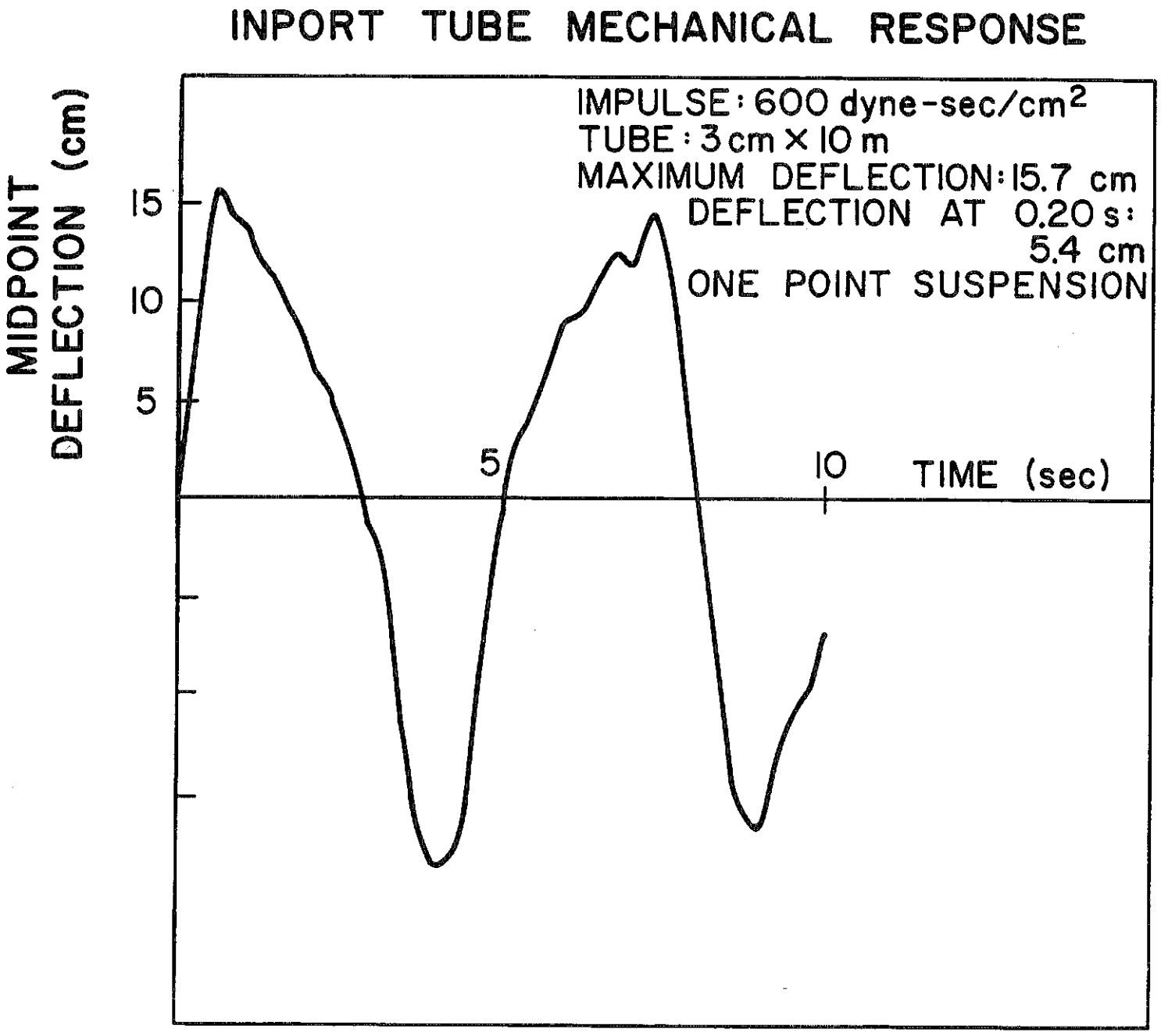
INPORT TUBE MECHANICAL RESPONSE
MIDPOINT DEFLECTION (cm)
15
10
5
5
10
TIME (sec)
IMPULSE: 600 dyne-sec/cm²
TUBE: 3 cm × 10 m
MAXIMUM DEFLECTION: 15.7 cm
DEFLECTION AT 0.20 s: 5.4 cm
ONE POINT SUSPENSION

Fig. VI.2-12

Fig. VI.2-13

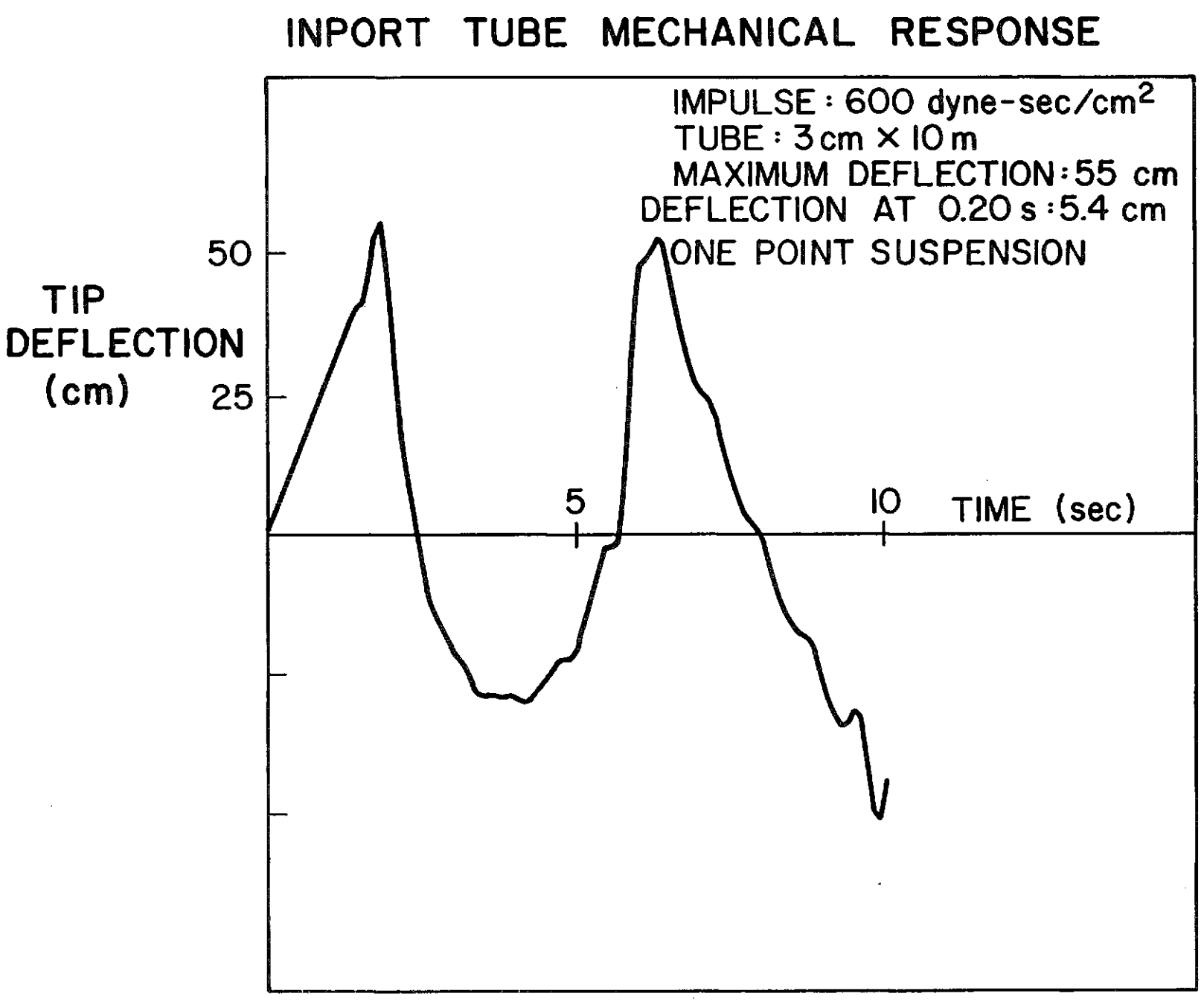
INPORT TUBE MECHANICAL RESPONSE
IMPULSE : 600 dyne-sec/cm2
TUBE : 3 cm × 10 m
MAXIMUM DEFLECTION : 55 cm
DEFLECTION AT 0.20 s : 5.4 cm
ONE POINT SUSPENSION
TIP DEFLECTION (cm)
50
25
5
10
TIME (sec)

that as typical values, these displacements were excessive, particularly on a single shot basis.

VI.2.3.4 Analytical Outline - Two Point Suspension

In order to control deflections, it has been proposed to constrain the bottom as well as the top of the INPORT tubes. The background analysis for this case is briefly outlined in the work which follows.

The principle equation of motion is

$$\partial^2 y/\partial t^2 - (T/\rho)\, \partial^2 y/\partial x^2 + 2b\partial y/\partial t = 0 \qquad \text{(VI.2-32)}$$

in which b is a viscous damping coefficient. The initial conditions and boundary conditions are

$$y(x,o) = f(x) \qquad \partial y(x,o)/\partial t = g(x)$$

$$y(o,t) = o \qquad y(\ell,t) = o \qquad \text{(VI.2-33)}$$

The solution form is taken as

$$y(x,t) = \sum b_n(t) \sin n\pi x/\ell$$

with

$$f(x) = \sum f_n \sin n\pi x/\ell = \sum b_n(o) \sin nx/\ell$$

$$g(x) = \sum g_n \sin n\pi x/\ell = \sum \dot{b}_n(o) \sin n\pi x/\ell \qquad \text{(VI.2-34)}$$

i.e., $b_n(o)$ and $\dot{b}_n(o)$ are the Fourier coefficients of f(x), g(x). With the preceding, the solution to Eq. VI.2-32 can be expressed as

$$y(x,t) = e^{-bt} \sum [f_n \cos \bar{\omega}_n t + (g_n + bf_n)/(\sin \bar{\omega}_n t)/\bar{\omega}_n] \sin n\pi x/\ell \ . \quad \text{(VI.2-35)}$$

For a single impulse, with no initial displacement

$$f_n = o$$

$$\partial y(x,o)/\partial t = g(x) = I(x)/\rho$$

where I(x) is the impulse per unit length. Thus Eq. VI-2-35 becomes

$$y(x,t) = (2e^{-bt}/\rho\ell) \sum [\int_o^\ell I(u) \sin(n\pi u/\ell)du] \frac{\sin\bar{\omega}_n t}{\bar{\omega}_n} \sin \frac{n\pi x}{\ell} \ . \quad \text{(VI-2-36)}$$

If a more general force is imposed, F(x,t) per unit length,

$$y(x,t) = \frac{2e^{-bt}}{\rho\ell} \sum \int_o^\ell \int_o^t F(u,\tau) \sin \frac{n\pi u}{\ell} \sin \frac{n\pi x}{\ell} \sin \frac{\bar{\omega}_n(t-\tau)}{\bar{\omega}_n} d\tau du \ .$$

VI.2.3.5 Numerical Results - Two Point Suspension

The response of the INPORT tubes was first determined for a single impulse, uniformly distributed along the length. Figures VI.2-14 - VI.2-17 show the time histories of the midspan displacement for various levels of damping. The amount of damping is expressed as a fraction of the so-called critical value, i.e., the damping coefficient which would produce non-oscillatory response. The peak values shown for a single pulse appear acceptable.

The program was extended to determine INPORT tubes response under repetitive impulses at 5 Hz. Figure VI.2-18 corresponds to "start up", with the initial velocity and displacement zero. At the end of 0.20 sec the velocity

Fig. VI.2-14

INPORT TUBE MECHANICAL RESPONSE

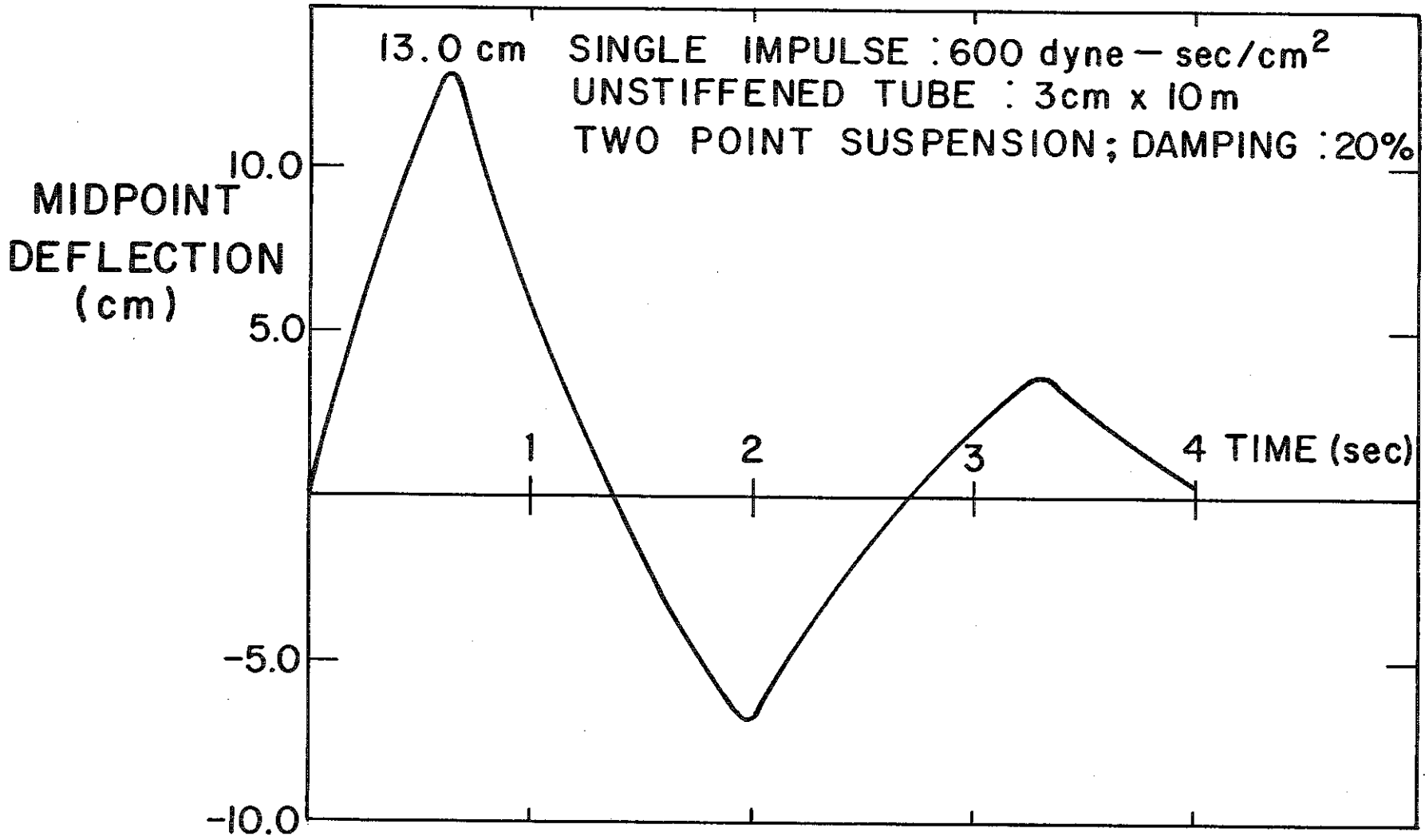

Fig. VI.2-15

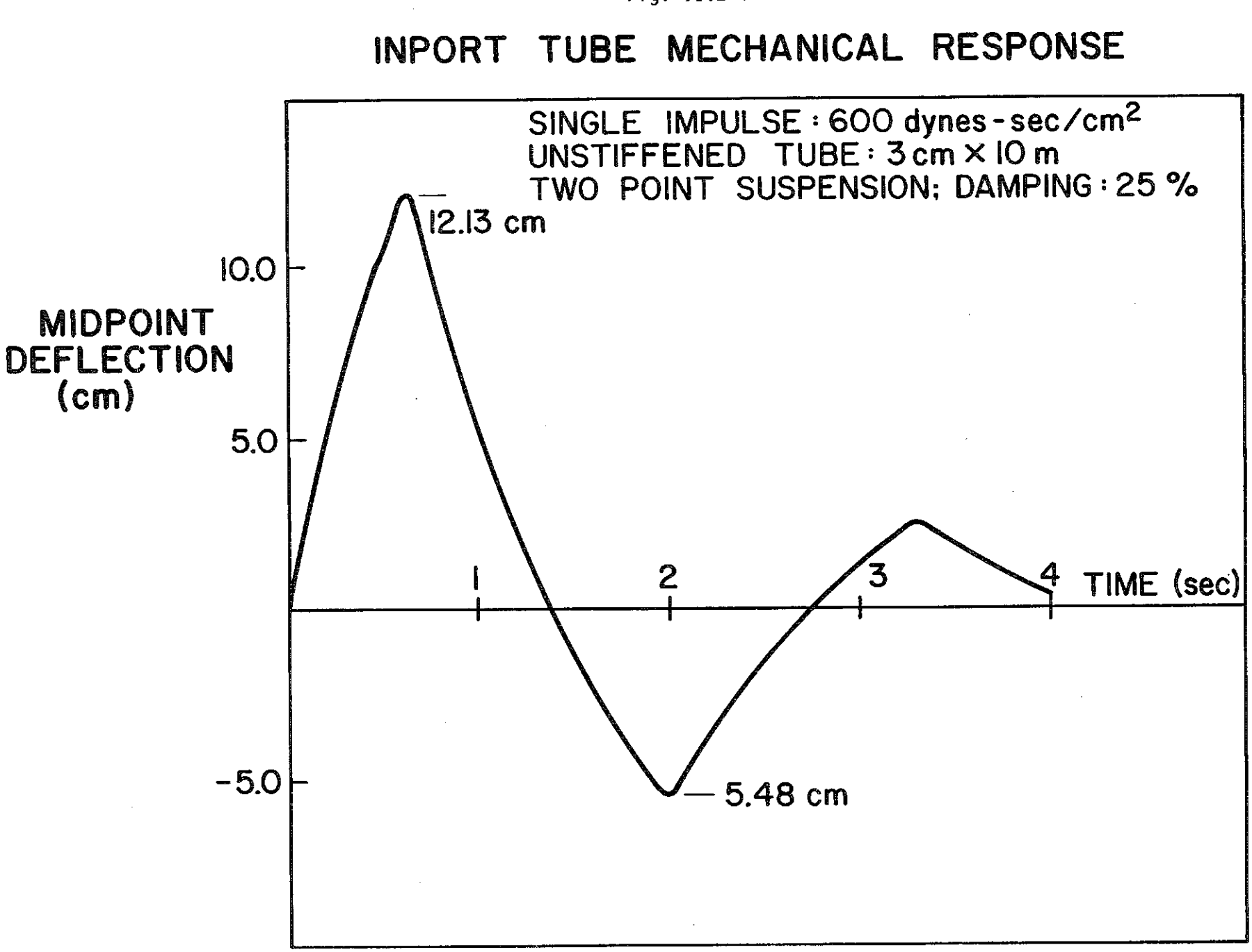
INPORT TUBE MECHANICAL RESPONSE
SINGLE IMPULSE : 600 dynes-sec/cm²
UNSTIFFENED TUBE : 3 cm × 10 m
TWO POINT SUSPENSION; DAMPING : 25 %
12.13 cm
10.0
MIDPOINT DEFLECTION (cm)
5.0
-5.0
1
2
3
4
TIME (sec)
5.48 cm

Fig. VI.2-16

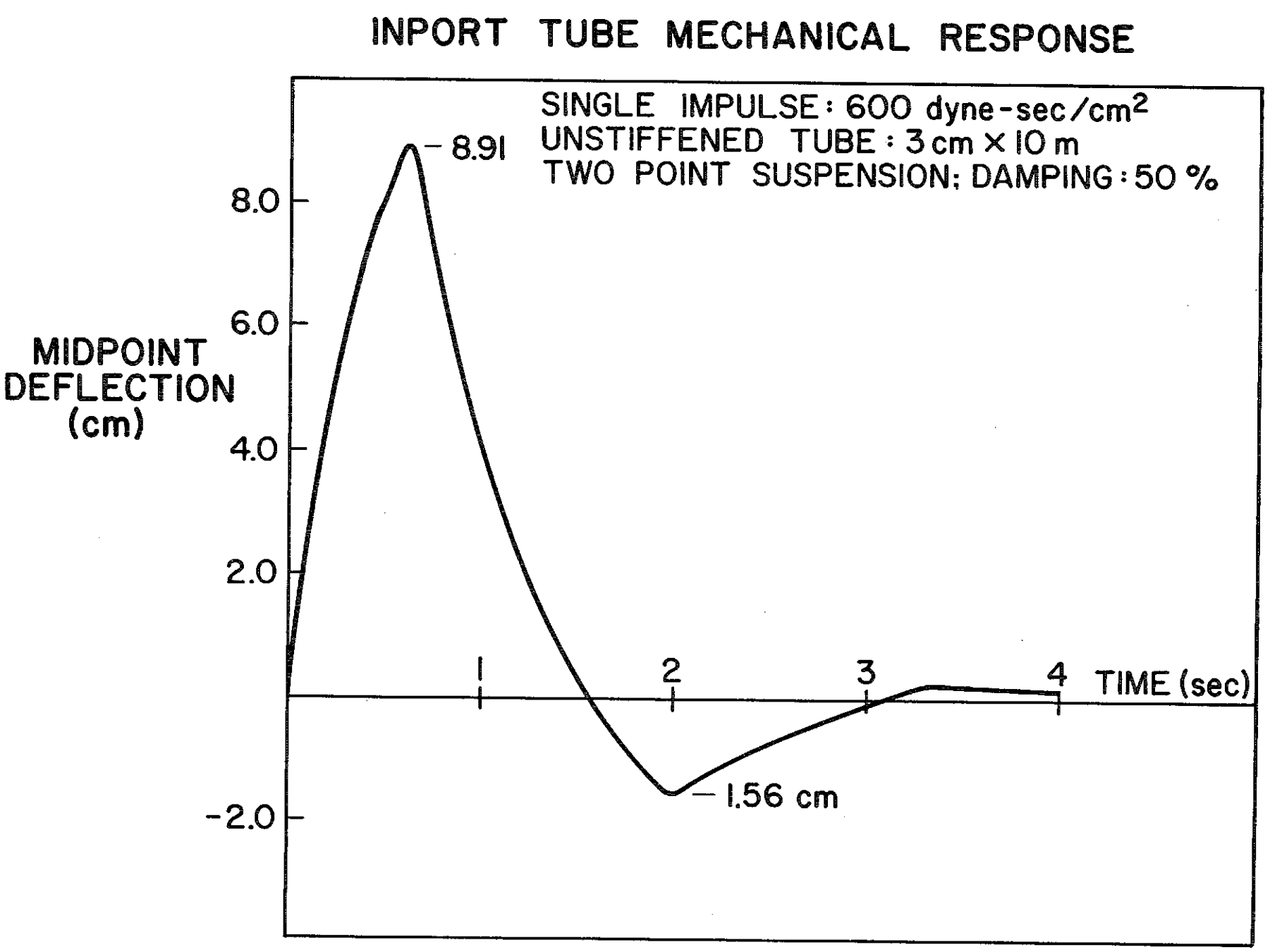
INPORT TUBE MECHANICAL RESPONSE
SINGLE IMPULSE: 600 dyne-sec/cm²
UNSTIFFENED TUBE: 3 cm × 10 m
TWO POINT SUSPENSION; DAMPING: 50 %
8.91
MIDPOINT DEFLECTION (cm)
8.0
6.0
4.0
2.0
-2.0
1
2
3
4
TIME (sec)
1.56 cm

Fig. VI.2-17

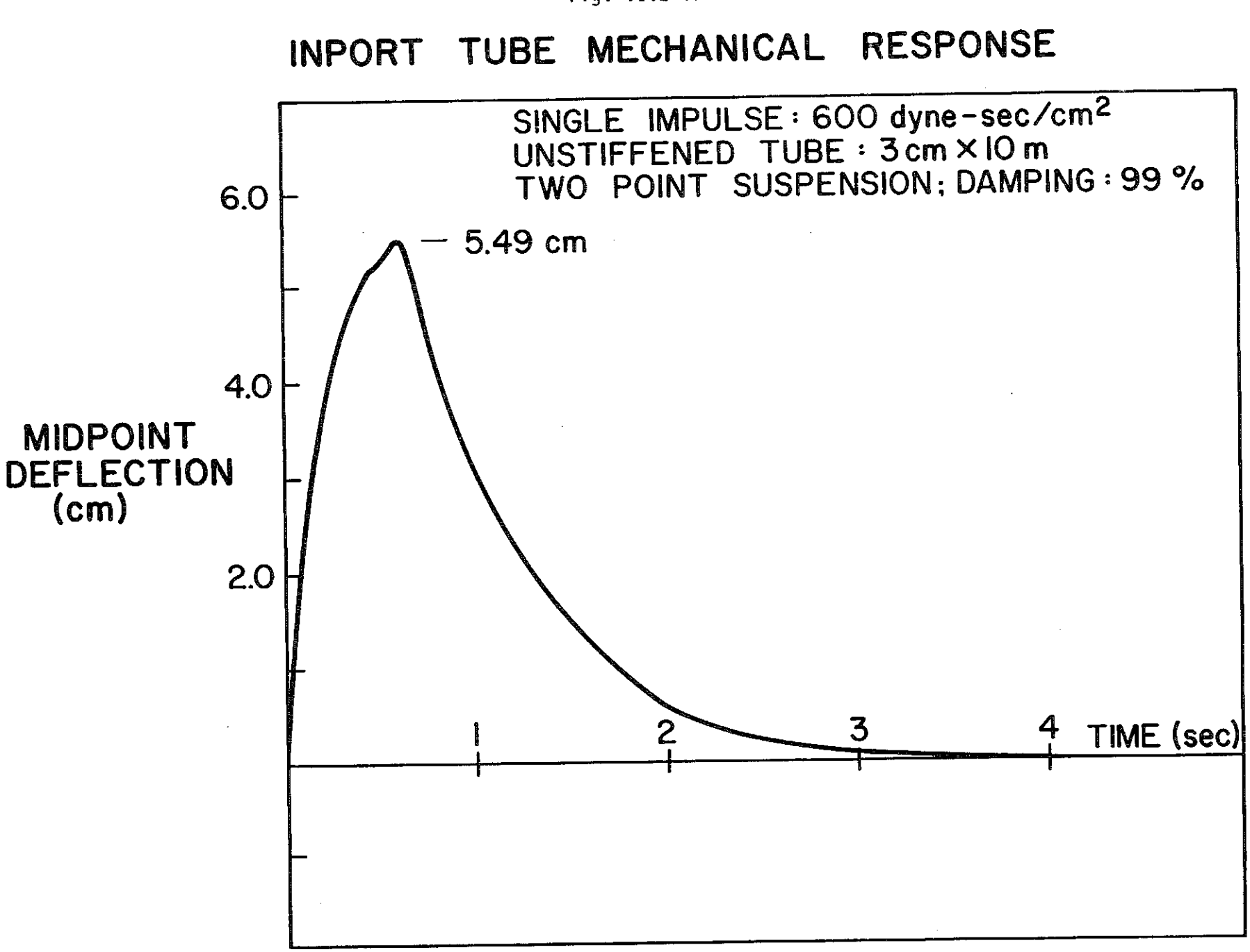
INPORT TUBE MECHANICAL RESPONSE
SINGLE IMPULSE : 600 dyne-sec/cm²
UNSTIFFENED TUBE : 3 cm × 10 m
TWO POINT SUSPENSION; DAMPING : 99 %
5.49 cm
MIDPOINT DEFLECTION (cm)
6.0
4.0
2.0
1
2
3
4
TIME (sec)

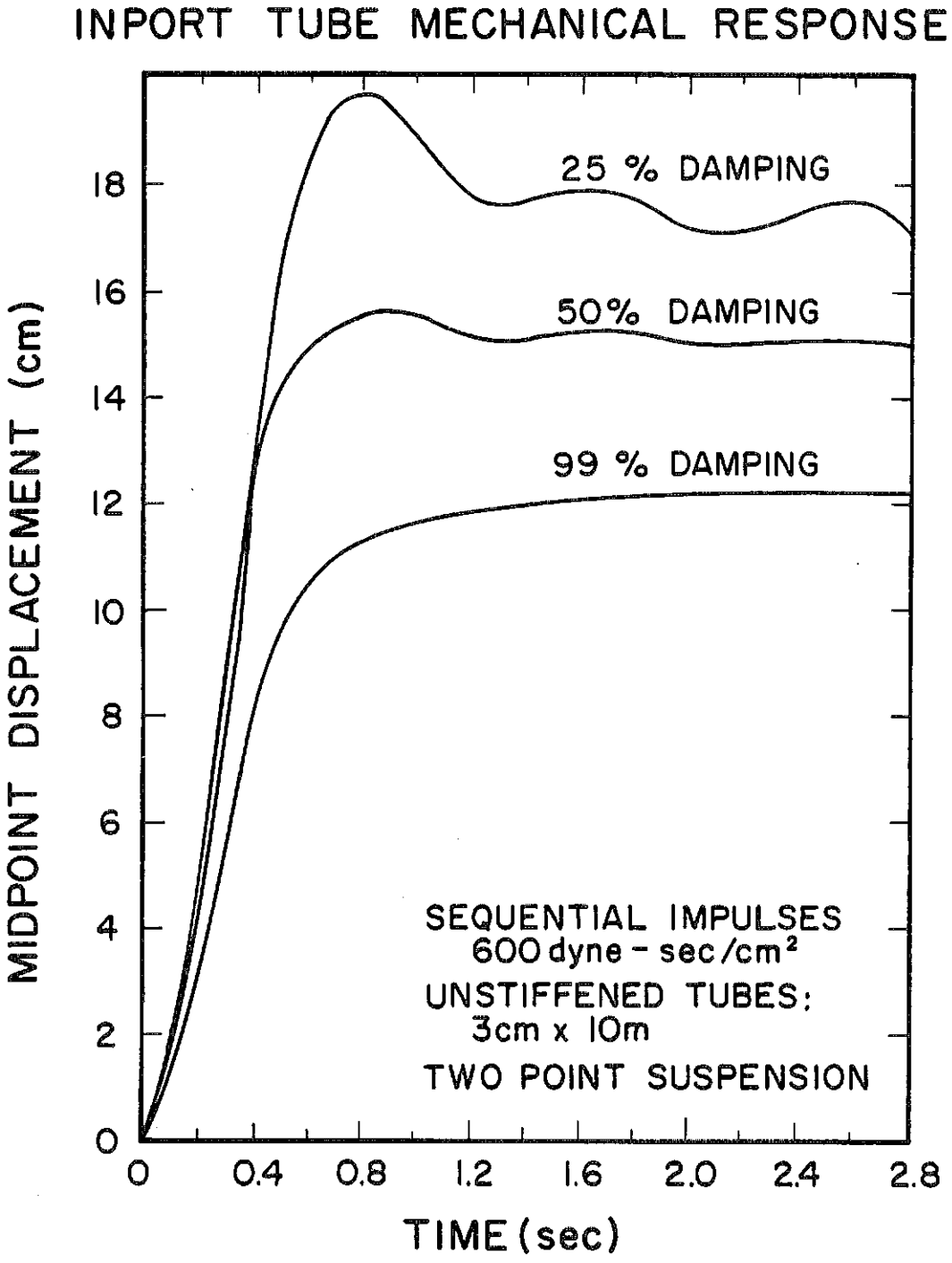
INPORT TUBE MECHANICAL RESPONSE
MIDPOINT DISPLACEMENT (cm)
0
2
4
6
8
10
12
14
16
18
0
0.4
0.8
1.2
1.6
2.0
2.4
2.8
TIME (sec)
25 % DAMPING
50% DAMPING
99 % DAMPING
SEQUENTIAL IMPULSES
600 dyne - sec/cm²
UNSTIFFENED TUBES:
3cm x 10m
TWO POINT SUSPENSION

Fig. VI.2-18

and displacement functions are evaluated and used as starting conditions with another uniform impulsive pressure. The process is repeated and carried out for fifty shots. These curves are for the first fifteen firings and show a small amount of overshoot with eventual stabilization about steady state mean values. On a relative basis the steady state mean amplitudes are moderate, e.g., less than 2% of the length. The limiting case of zero damping is shown for comparison in Fig. VI.2-19 along with the 20% value. The latter is recommended as a conservative estimate for such units. While theoretical and experimental values for metallic reactor components are much smaller single digit percentages, here the tube has a significant natural damping capacity from the woven soft construction and the ever present PbLi in liquid form. A level of 20% is a representative design figure for long span electrical conductors and transmission lines and is typical of experimental measurements (Ref 2).

Finally the response was determined following shutdown. Typical results are shown in Fig. VI.2-20 in which the load sequence was stopped after fifty shots. While the displacement history is very smooth, characteristic of a single mode, it should be noted that this result involves the contributions of the first eight modes in the series. Such results confirm expectations that no unusual characteristics develop for this scenario.

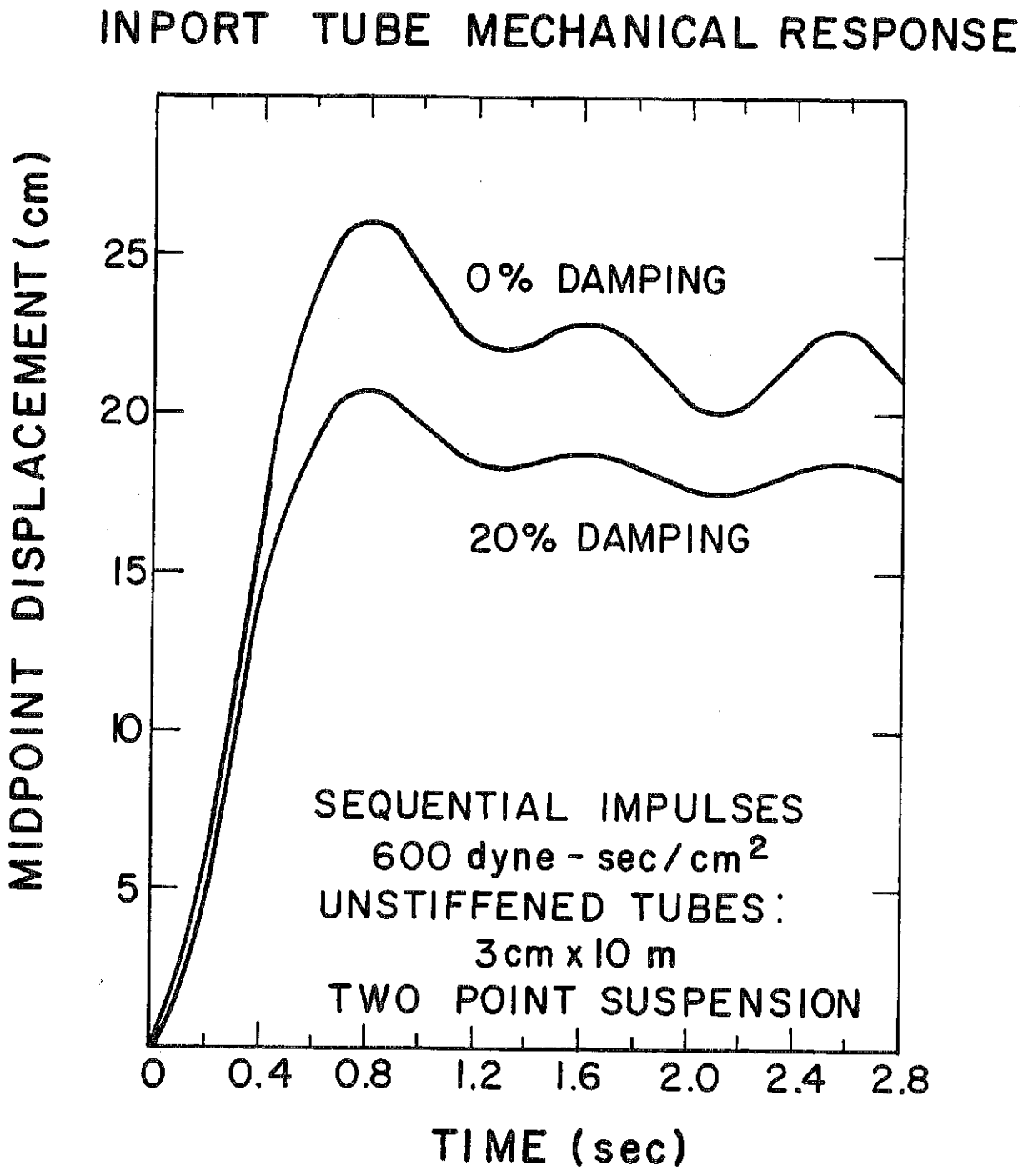
INPORT TUBE MECHANICAL RESPONSE
MIDPOINT DISPLACEMENT (cm)
25
20
15
10
5
0% DAMPING
20% DAMPING
SEQUENTIAL IMPULSES
600 dyne - sec/cm²
UNSTIFFENED TUBES:
3cm x 10 m
TWO POINT SUSPENSION
0
0.4
0.8
1.2
1.6
2.0
2.4
2.8
TIME (sec)

Fig. VI.2-19

Fig. VI.2-20

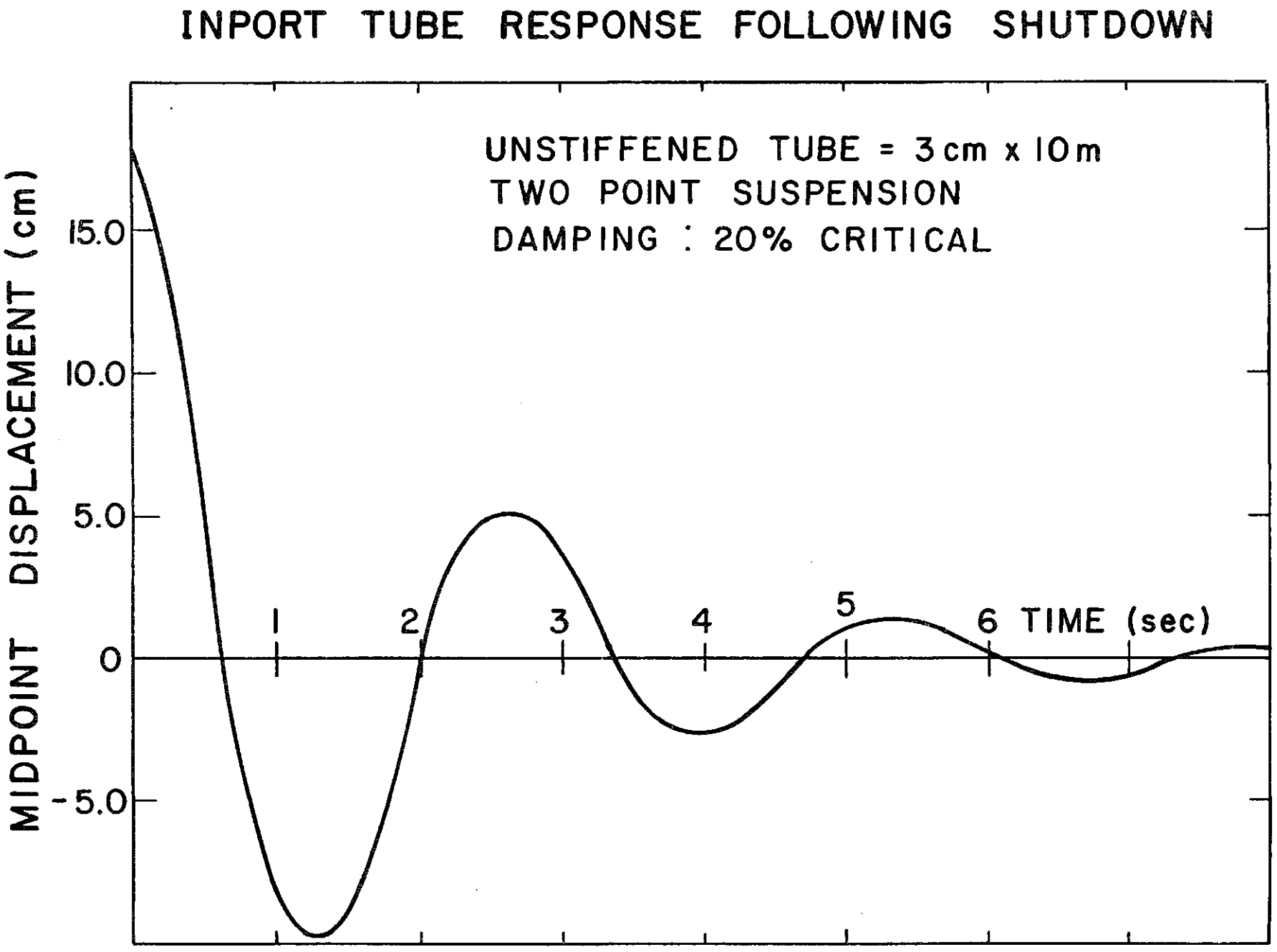
INPORT TUBE RESPONSE FOLLOWING SHUTDOWN
UNSTIFFENED TUBE = 3 cm x 10 m
TWO POINT SUSPENSION
DAMPING : 20% CRITICAL
MIDPOINT DISPLACEMENT (cm)
15.0
10.0
5.0
0
-5.0
1
2
3
4
5
6
TIME (sec)

References for Section VI.2

1. R.L. Engelstad and E.G. Lovel,"First Wall Mechanical Design for Light Ion Beam Fusion Reactors," University of Wisconsin Report UWFDM-322, Dec. 1979.

2. Y-K. Wen, "Dynamic Response of Transmission Line System to Wind Load," Engineering Science Research Report BLWT-9-68, University of Western Ontario, London, Ontario, April 1968.

VI.3 Neutronics and Photonics

VI.3.1 Introduction

The neutronics and photonics analysis for HIBALL is presented in this section. A one-dimensional spherical geometry analysis was performed to determine the optimum blanket design which gives the highest possible energy multiplication with adequate breeding ratio. The blanket consisting of the INPORT tubes is also required to protect the ferritic steel structure from radiation damage. The biological shield is also designed. The actual cylindrical cavity is modelled in a detailed three-dimensional neutronics and photonics analysis. All cavity geometrical details are included in this analysis. A time-dependent neutronics analysis is also presented to account properly for the pulsed nature of the neutron source. This analysis yields time-dependent radiation damage rates which form an important input to microstructure evolution calculations. Finally, the calculations of blanket and shield radioactivity and afterheat are given.

VI.3.2 One-Dimensional Time Integrated Studies

VI.3.2.1 Introduction

Neutronics and photonics calculations are required to determine important reactor parameters such as tritium breeding, nuclear heating, and radiation damage. In an inertial confinement fusion reactor, the DT fuel is heated and compressed to extremely high densities before it ignites. Neutron fuel interactions result in spectrum softening, neutron multiplication, and gamma production. In this section, a consistent coupled target-blanket neutronics and photonics study of HIBALL is given. The neutron and gamma source for blanket calculations was obtained from the target neutronics and photonics results given in section III.1.

The HIBALL blanket is required to breed tritium and convert the kinetic energy of the fusion reaction into heat. Furthermore, the INPORT tubes are required to protect the vacuum wall and HT-9 structure in the reflector from radiation damage. One-dimensional steady state calculations are performed to determine the optimum blanket thickness which yields the largest possible energy multiplication with adequate tritium breeding ratio and first wall protection. The thickness of biological shield required to reduce the biological dose to permissible levels is also determined.

VI.3.2.2 Blanket and Shield Model

The HIBALL fusion reactor power plant design incorporates four cylindrical cavities each having a radius of 7 m and a height of 10 m. The blanket region consists of an array of porous tubes (INPORT tubes) made of braided SiC through which the $Li_{17}Pb_{83}$ liquid metal eutectic flows. These tubes are placed inside the reactor cavity. Besides serving as the coolant and tritium breeder, the $Li_{17}Pb_{83}$ coolant is utilized for first wall protection. The tubes occupy 33% of the 2 m thick blanket region yielding an effective blanket thickness of 66 cm. The LiPb coolant occupies 98% of the tube volume with the SiC occupying the remaining 2%. SiC and $Li_{17}Pb_{83}$ have nominal densities of 3.17 and 9.4 g/cm^3, respectively. The first wall is made of ferritic steel (HT-9) which is an alloy composed of 85.25 wt% iron and 11.5 wt% chromium. The first wall has a thickness of 1 cm and a density of 7.8 g/cm^3. A 0.4 m thick reflector composed of 90 v/o ferritic steel structure and 10 v/o $Li_{17}Pb_{83}$ coolant is used. The reactor utilizes a 3.5 m thick concrete shield. The shield consists of 95% ordinary concrete and 5% H_2O coolant. A schematic of the blanket, first wall, reflector, and shield configuration for the HIBALL reactor is given in Fig. VI.3-1.

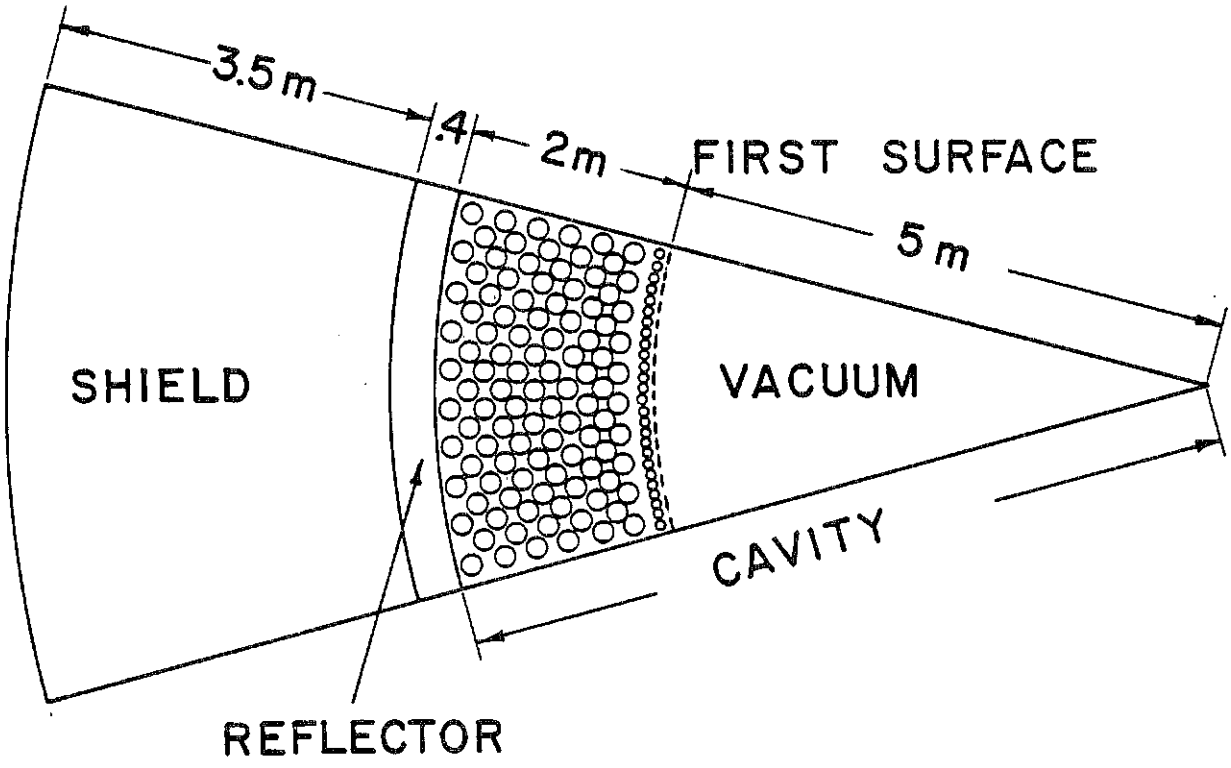

Fig. VI.3-1 HIBALL reactor cavity model.

VI.3.2.3 Calculational Method and Nuclear Data

The one-dimensional discrete ordinates code ANISN[1] was used to perform neutronics and photonics calculations yielding average time integrated results. A P3-S4 approximation was used. Spherical geometry was used in the calculations and hence the results represent the conditions at the central plane of the reactor. The results give conservatively high damage rates and low tritium breeding ratios. The neutron and gamma spectra obtained from the target calculations are used to represent the source for the blanket neutronics and photonics calculations. The source is considered to be an isotropic point source at the center of the cavity. The calculations account for neutron spectrum softening, neutron multiplication, and gamma production in the target. The one-dimensional finite element code ONETRAN[2] implemented at Karlsruhe Nuclear Laboratory was also used to perform the calculations for the final blanket design and the results are compared to the results from ANISN. A coupled 25 neutron-21 gamma group cross section library was used. The library consists of the RSIC DLC-41B/VITAMIN-C data library[3] and the DLC-60/MACKLIB-IV response data library.[4] This data library is based on ENDF/B-IV. The nuclide densities used in the calculations are given in Table VI.3-1. The results presented here are based on a DT yield of 400 MJ and a repetition rate of 5 Hz yielding 7.1×10^{20} fusion neutrons per second.

Neutron and gamma cross section requirements for the neutronic analysis of the HIBALL system are similar to those of fast fission reactor systems. Neutron data are required up to the fusion neutron energy of 14.1 MeV. Presently available neutron cross section libraries like ENDF/B[5] and KEDAK[6] cover this energy range. Although data in these libraries show a lower level of confidence above a few MeV than in the keV and thermal energy range, and some improvement in data, e.g., energy distribution of secondary neutrons is

Table VI.3-1

Nuclide Densities Used in Neutronics Analysis of HIBALL Fusion Reactor

Region	Constituent Elements	Nuclide Density (nuclei/b cm)
Blanket	^{6}Li	0.00040
[98 v/o $Li_{17}Pb_{83}$	^{7}Li	0.00505
+ 2 v/o SiC]	Si	0.00095
(.33 density factor)	C	0.00095
	Pb	0.02661
Ferritic Steel	Fe	0.07171
First Wall	Cr	0.01039
(1.0 density factor)	Ni	0.00040
	Mo	0.00049
	V	0.00028
	Si	0.00042
	Mn	0.00043
	C	0.00078
	W	0.00013
Reflector	Fe	0.06454
[90 v/o ferritic	Cr	0.00925
steel + 10 v/o $Li_{17}Pb_{83}$]	Ni	0.00036
(1.0 density factor)	Mo	0.00044
	V	0.00025
	Si	0.00038
	Mn	0.00038
	C	0.00070
	W	0.00011
	^{6}Li	0.00004
	^{7}Li	0.00051
	Pb	0.00272

conceivable, the quality of the data as stored in ENDF/B-IV is considered, with exceptions given below, to be adequate at this stage of the study.

One major parameter to be determined in the neutronic calculation is the tritium breeding ratio. Tritium is produced by the reactions

$$^{7}Li(n,n'\alpha)T \quad \text{and} \quad ^{6}Li(n,\alpha)T \ .$$

The division of the tritium breeding between these two processes is essentially design dependent. Strong doubts about the validity of the $^{7}Li(n,n'\alpha)T$ cross section in ENDF/B-IV have been expressed.[7-10] Lowering the cross section by 15-20% has been suggested.[8] Results of new differential measurements (Fig. VI.3-2) from different laboratories suggest reducing the ENDF/B-IV cross section by about 10%. Some of these results are still of a preliminary nature.

In the HIBALL blanket design, due to the presence of a large amount of lead, neutrons are rapidly slowed down below the threshold of the $^{7}Li(n,n'\alpha)T$ reaction. The contribution of this reaction to the tritium production is only about 2%. Thus ENDF/B-IV cross sections for this process can be used without introducing significant error in the tritium breeding ratio.

The other reaction responsible for tritium breeding; $^{6}Li(n,\alpha)T$ is used in neutron data measurements as a standard. Recently Hale[11] has re-evaluated this cross section below 1 MeV for the ENDF/B-V standard file. He made a thorough analysis of the ^{7}Li compound nucleus system including charged particle reactions. His result (Fig. II.3-3) gives a lower $^{6}Li(n,\alpha)T$ cross section for the 252 keV resonance and for lower energies. For ^{6}Li, group cross sections were generated using the ENDF/B-V Data and used to investigate the effect on HIBALL overall tritium breeding ratio.

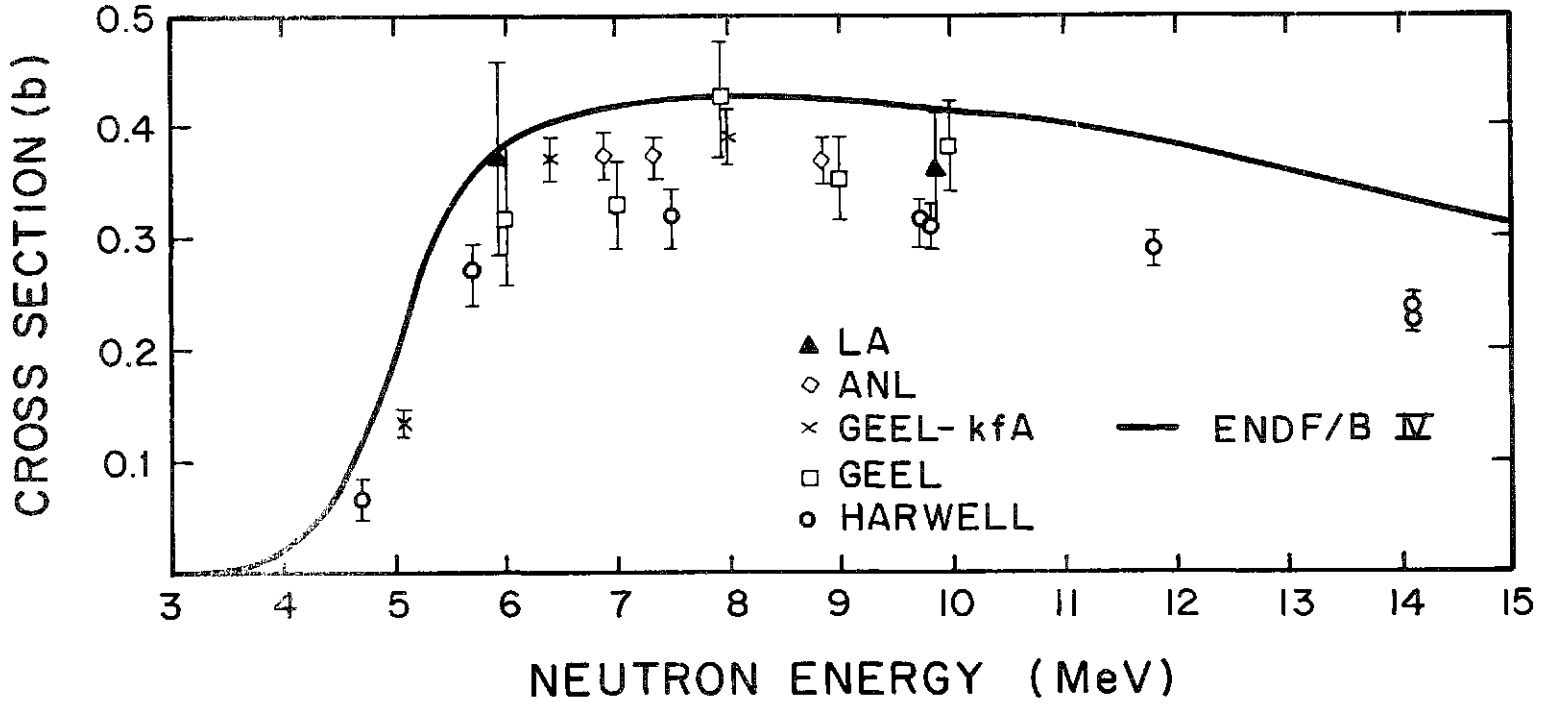

Fig. VI.3-2 Measurements of $^{7}Li(n,n'\alpha)T$ cross section.

VI.3-8

Figure VI.3-3

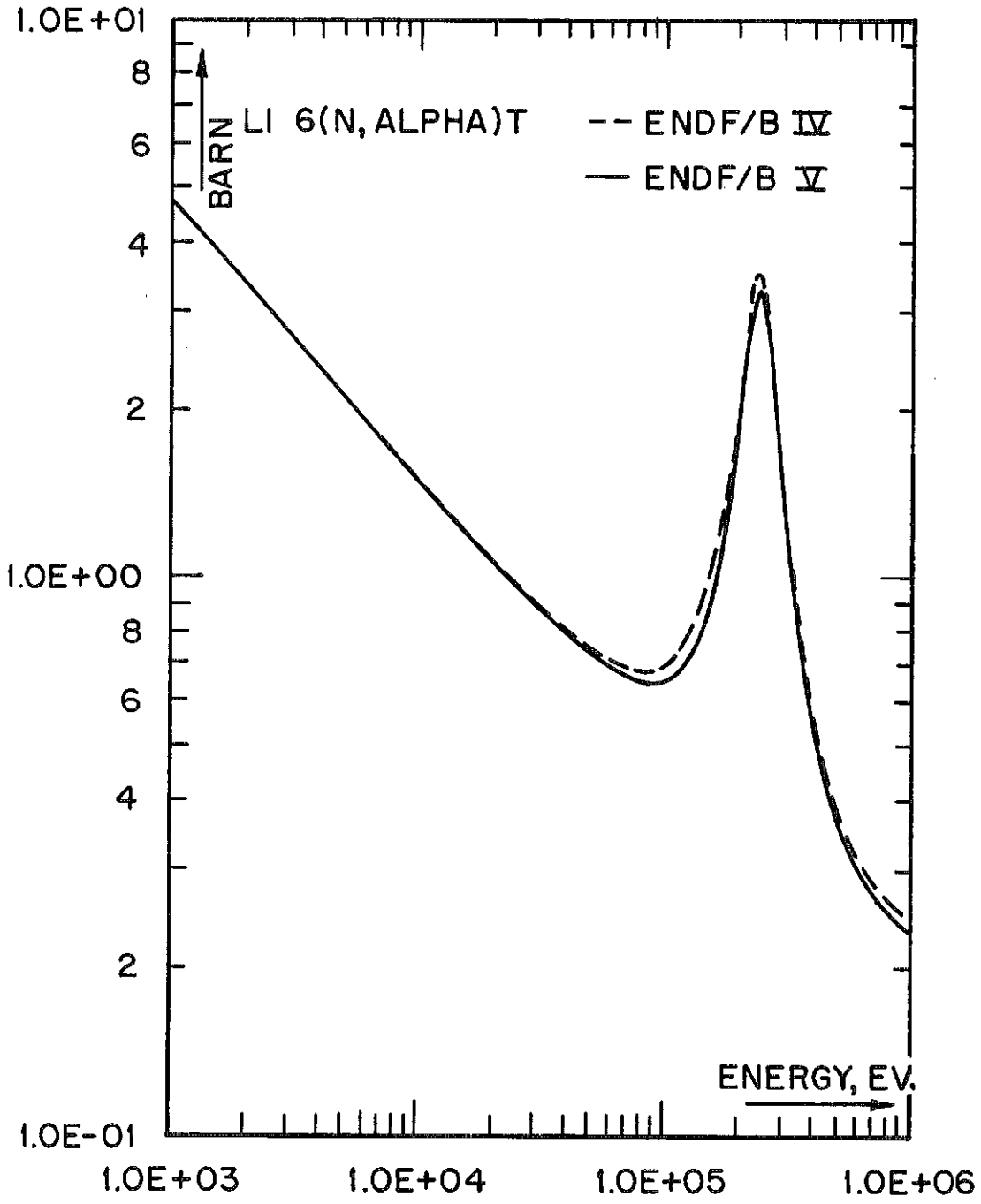

$^{6}Li(n,\alpha)T$ Cross Sections from ENDF/B IV and V

VI.3.2.4 Blanket Optimization

A series of one-dimensional neutronics and photonics calculations was made in which the packing fraction for the INPORT tubes was varied with the blanket region thickness fixed at 2 m. The effect of the tube packing fraction or the effective blanket thickness on radiation damage, tritium breeding and nuclear heating was investigated. The design criterion used in the optimization was that the energy deposition should be as high as possible with a tritium breeding ratio $\gtrsim$ 1.1 in the approximate one-dimensional calculation.

Table VI.3-2 gives the effect of packing fraction on tritium production. It is clear that tritium production in the blanket increases as the thickness increases. On the other hand, tritium production in the reflector region decreases as the effective blanket thickness increases. The net effect is that the overall breeding ratio increases nearly linearly with the effective blanket thickness.

Figure VI.3-4 gives the spatial distribution of tritium production in the blanket and reflector for a packing fraction of 0.33. The contributions to tritium production from $^{7}Li(n,n'\alpha)$ and $^{6}Li(n,\alpha)$ reactions are shown. The contribution from ^{7}Li, which is a high energy reaction (threshold energy = 2.86 MeV), decreases sharply as one moves into the blanket away from the source because of the increased softening of the spectrum. Table VI.3-3 gives a comparison between the results of ANISN and ONETRAN. The effect of using the ENDF/B-V data for the $^{6}Li(n,\alpha)T$ cross section is also given. Using the $^{6}Li(n,\alpha)T$ cross section from ENDF/B-V results in a 2% reduction in the calculated tritium breeding ratio.

Table VI.3-4 gives the neutron, gamma, and total energy deposition in the different regions for different values of the packing fraction. Notice that

Table VI.3-2 Effect of Tube Packing Fraction on Tritium Breeding

Packing Fraction	0	.30	.33	.35	.40
Blanket	0	1.094	1.177	1.226	1.331
Reflector	0.043	0.022	0.018	0.016	0.012
System Total	0.043	1.116	1.195	1.242	1.343

Table VI.3-3 Comparison Between Results for Tritium Production

Tritium Production (Tritons/Fusion)				
Region	Element	ANISN, S_4P_3, ENDF/B-IV $^6Li(n,\alpha)T$	ONETRAN, S_8P_3, ENDF/B-IV $^6Li(n,\alpha)T$	ONETRAN, S_8P_3, ENDF/B-V $^6Li(n,\alpha)T$
Blanket	^6Li	1.1500	1.1558	1.1327
	^7Li	0.0270	0.0271	0.0271
	Total	1.1770	1.1829	1.1598
First Wall	Total	0.0	0.0	0.0
Reflector	^6Li	0.0180	0.0180	0.0175
	^7Li	0.0	0.0	0.0
	Total	0.0180	0.0180	0.0175
Tritium Breeding Ratio		1.1950	1.2009	1.1773

Table VI.3-4 Effect of INPORT Tube Packing Fraction on Nuclear Energy Deposition (MeV/Fusion)

Packing Fraction		0	.30	.33	.35	.40
Blanket	Neutrons	---	7.026	7.467	7.729	8.278
	Gamma	---	6.663	6.687	6.697	6.705
	Total	---	13.689	14.154	14.426	14.983
First Wall	Neutrons	0.407	0.020	0.016	0.014	0.009
	Gamma	1.141	0.208	0.180	0.163	0.125
	Total	1.548	0.228	0.196	0.177	0.134
Reflector	Neutrons	2.626	0.287	0.232	0.202	0.142
	Gamma	14.402	4.013	3.367	2.985	2.185
	Total	17.028	4.300	3.599	3.187	2.327
System Total		18.576	18.217	17.949	17.790	17.444
Overall Energy Multiplication		1.326	1.300	1.281	1.269	1.245

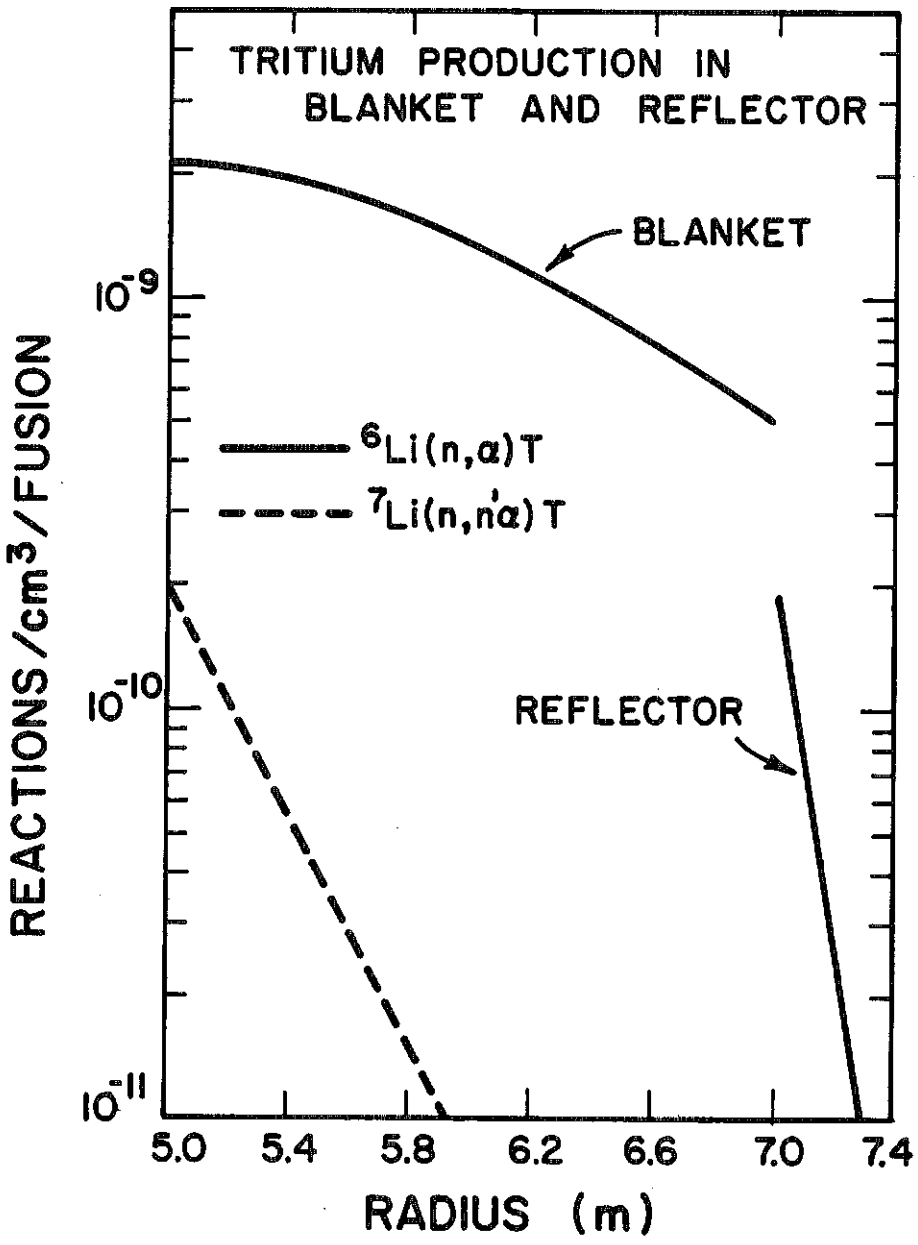

Figure VI.3-4 Tritium production in the blanket and reflector.

more than 50% of energy deposited comes from gamma-ray heating because of neutron reactions in the HT-9 structure. The contribution from gamma heating decreases as the INPORT tube region thickness increases. As the blanket thickness increases, the total energy deposited in it increases with a larger fraction of this energy being deposited by neutrons. The larger energy deposition results from the larger number of neutron and gamma interactions taking place in the thicker blanket. The relative gamma contribution to the heating decreases as the thickness increases because a smaller portion of the blanket will be adjacent to the first wall where large gamma production occurs. The neutron and gamma heating in the first wall and reflector decrease as the blanket thickness increases because of the increased neutron attenuation in the blanket. The total energy deposited in the system is found to decrease as the blanket thickness increases. This results because of the decreased gamma production in ferritic steel due to the lower neutron flux in the first wall and reflector. A neutron absorbed in ^{6}Li releases ~ 4.8 MeV while if it is absorbed in the structure ~ 7 MeV is released. The energy multiplication is also included in Table VI.3-4. This factor is defined as the total energy deposited in the system, including the energy deposited by X-rays and target debris at the first surface of the blanket, divided by the fusion reaction yield of 17.6 MeV.

The spatial variation of the total power density in the blanket for a packing fraction of 0.33 is given in Fig. VI.3-5. The power density decreases as one moves away from the source inside the blanket because of the increased neutron and gamma attenuation. The large gamma production in HT-9 causes the gamma heating to increase sharply as one approaches the first wall. This is the reason for the existance of a minimum in the power density at ~ 30 cm from the first wall.

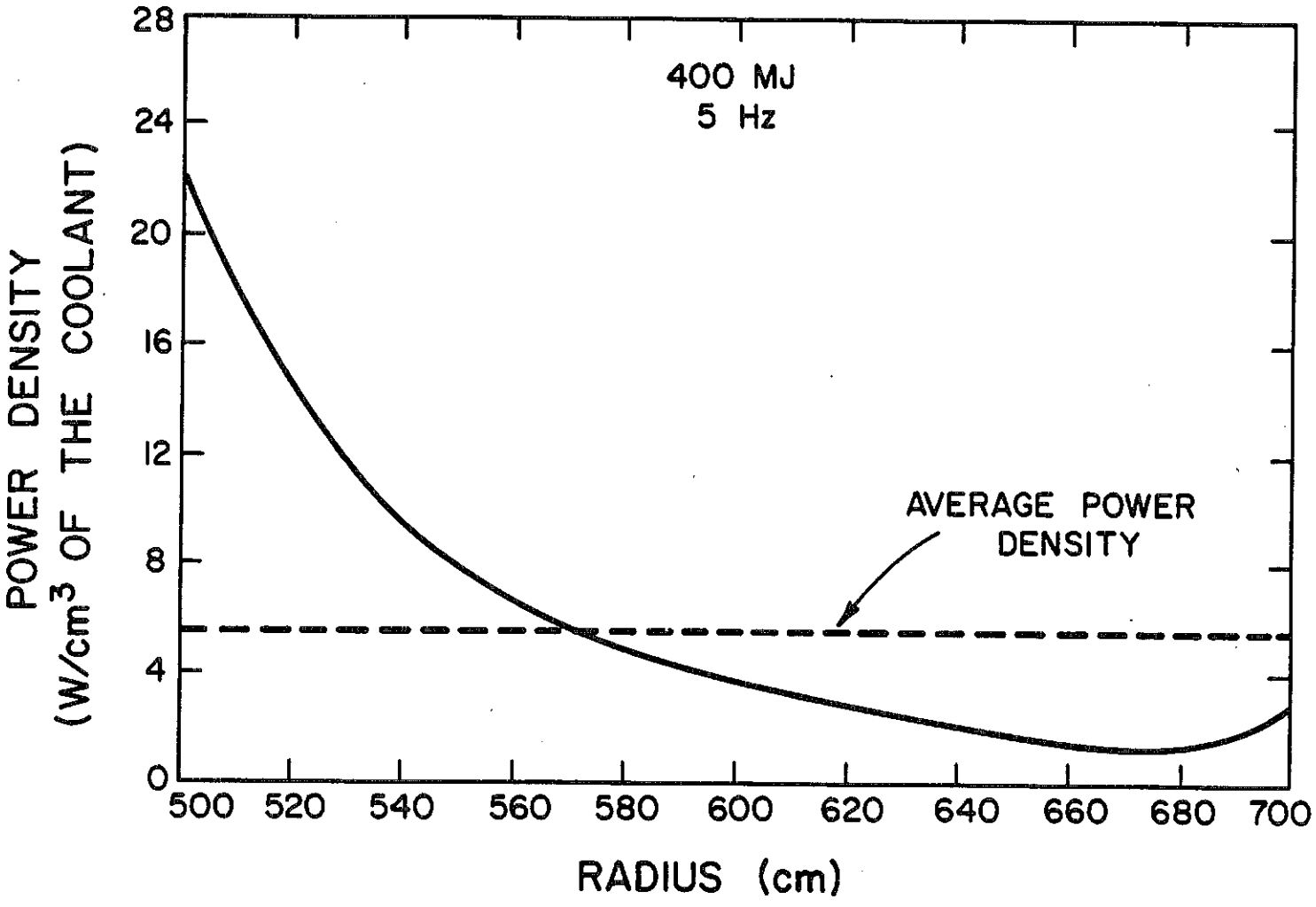

Figure VI.3-5 Spatial variation of power density in the blanket.

It is clear from the previous results that increasing the INPORT tube packing fraction results in increasing the tritium breeding ratio at the expense of power production. Since energy production is the primary goal of a fusion power reactor, a packing fraction of 0.33 is chosen. This yields an energy multiplication of 1.28 and a breeding ratio of 1.195. A relatively high breeding ratio is chosen here because of expected reduction in tritium production when one includes the penetrations and various structural support materials in the detailed three-dimensional cylindrical geometry. The breeding ratio should also be greater than one to account for uncertainties in data and calculational methods.

VI.3.2.5 Neutron and Gamma Spectra

Using the neutron and gamma spectra from the target calculations to represent the source for the blanket neutronics and photonics calculations, the neutron and gamma spectra were calculated at different positions in the blanket, first wall and reflector. The neutron spectra are given in Fig. VI.3-6. In the innermost part of the blanket the spectrum has a pronounced peak at 14.1 MeV with the lower energy part of the spectrum resulting from neutron target interactions and neutron slowing down in the blanket itself. In the first wall and reflector the spectrum is considerably softened primarily because of slowing down in the blanket - reflector system. In Fig. VI.3-7 the gamma spectra in the first wall and the center of the blanket are compared. The gamma photon density in the first wall is larger than that in the blanket because of the large gamma production in iron.

VI.3.2.6 Radiation Damage to Structural Materials

The effect of blanket thickness on the maximum number of atomic displacements (dpa) per full power year in the SiC INPORT tubes and the HT-9 first wall is given in Table VI.3-5. The average dpa rate in the SiC tubes

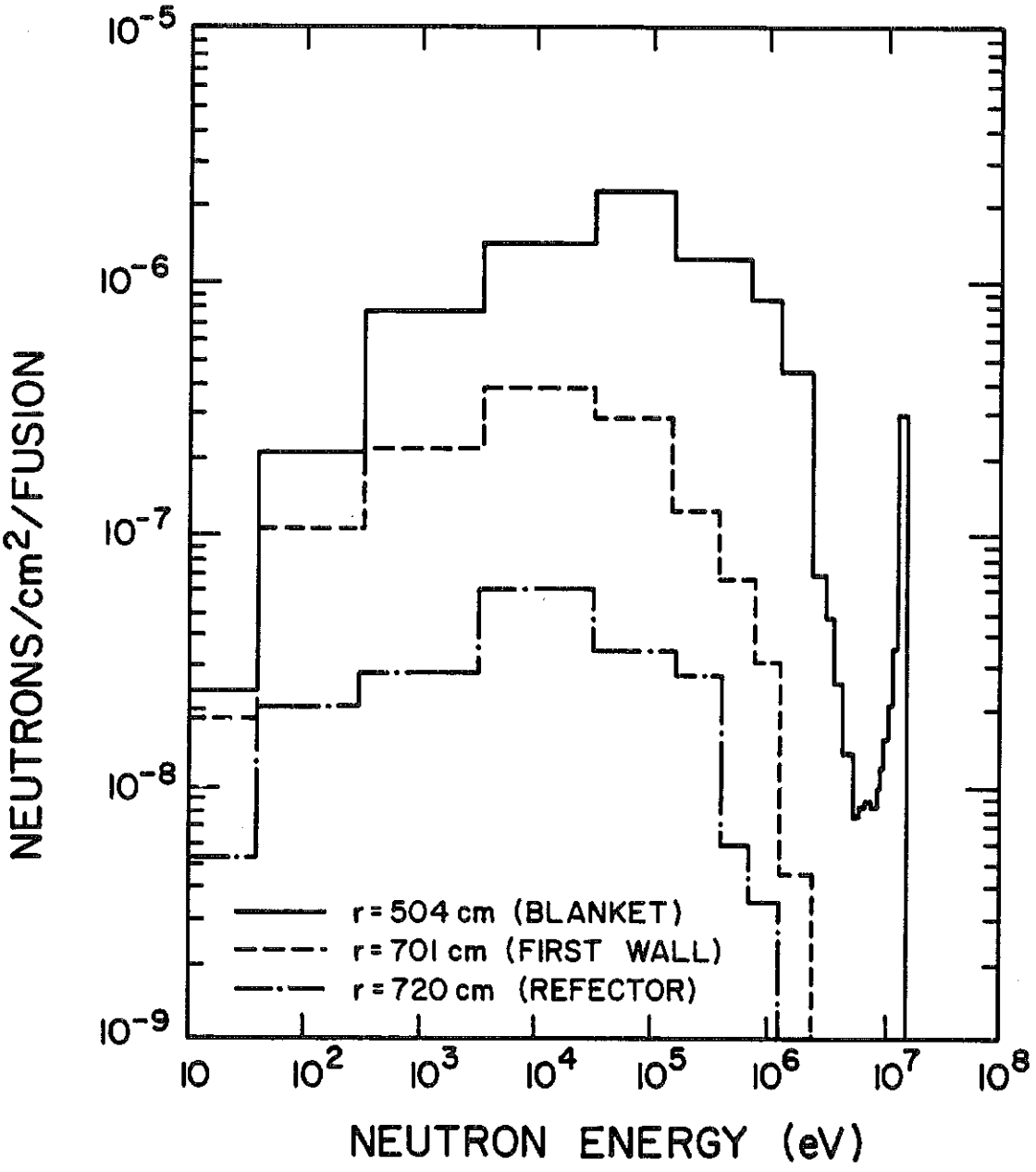

Figure VI.3-6 Neutron spectrum in the blanket, first wall, and reflector.

(The ordinate is the integral in each energy group.)

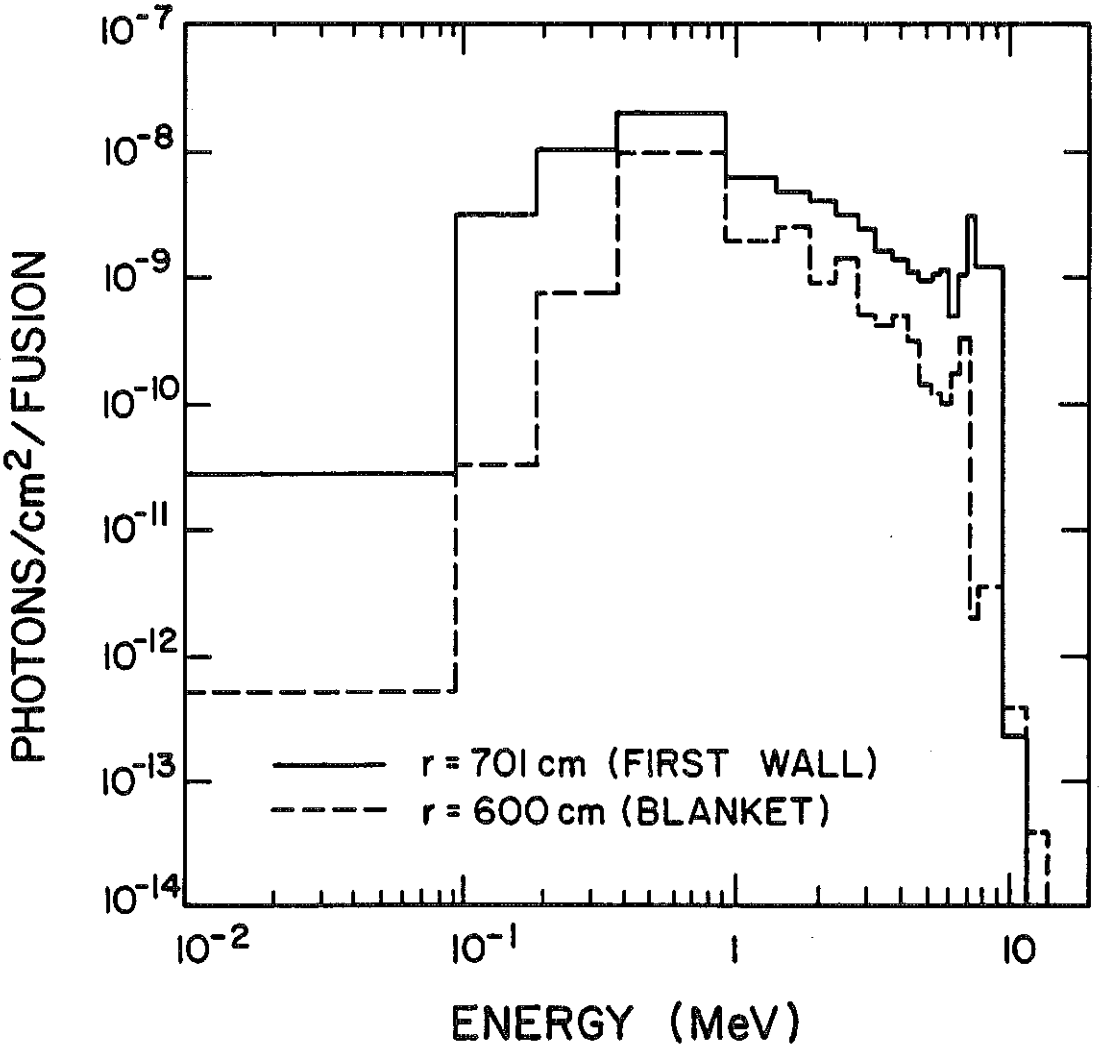

Figure VI.3-7 Gamma spectrum in the blanket and first wall.
(The ordinate is the integral in each energy group.)

Table VI.3-5 Effect of Blanket Thickness on Maximum DPA Rate (dpa/FPY)

Effective Blanket Thickness (cm)	0	60	66	70	80
SiC INPORT Tubes	---	116	118	119	121
HT-9 First Wall	25.360	3.411	2.688	2.289	1.525

increases slightly as the blanket thickness increases while the dpa rate in the ferritic steel first wall decreases as the blanket thickness increases. The reason is that the dpa cross section for iron peaks at 14.1 MeV and has a threshold energy of ~ 1 keV with the total dpa in iron decreasing as the spectrum becomes softer. On the other hand, the dpa cross section for ^{12}C peaks at ~ 3.5 MeV and has a lower threshold energy of ~ 0.2 keV resulting in an increase in the total dpa in C as the spectrum softens.

The helium and hydrogen gas production rates in the HT-9 first wall are given in Table VI.3-6 for different effective blanket thicknesses. The average gas production rate is found to decrease as the blanket thickness increases. The reason is that the hydrogen and helium production cross sections peak at 14.1 MeV. Furthermore, the reactions resulting in helium and hydrogen production are of a threshold nature with threshold energies in the low MeV energy range. The effect on gas production is more pronounced than the effect on dpa because of the lower dpa threshold energy. It is clear from the results that using INPORT tubes with an effective thickness of 66 cm reduces displacement damage and gas production in the HT-9 first wall considerably, allowing it to last for the whole reactor lifetime.

Table VI.3-6 Effect of Blanket Thickness on Gas Production Rate in First Wall (appm/FPY)

Effective Blanket Thickness (cm)	0	60	66	70	80
Helium	229.1	0.659	0.364	0.245	0.090
Hydrogen	736.9	2.451	1.380	0.942	0.362

Because of the large difference between the threshold energies for helium and dpa reactions, the helium to dpa ratio, which is an important parameter in microstructure calculations, decreases with spectrum softening. Figure VI.3-8 shows the effect of effective INPORT tube region thickness on dpa, helium production, and helium to dpa ratio in the HT-9 first wall. It is clear that the wall protection has a more pronounced effect on helium production. Consequently, the helium to dpa ratio decreases from a value of 9 for the unprotected wall to a value of 0.135 when an effective thickness of 66 cm is used. The helium to dpa ratio was also found to decrease as one moves inside the reflector. Figure VI.3-9 shows the spatial variation of dpa, helium production and helium to dpa ratio in the HIBALL reflector. The helium to dpa ratio decreases from 0.135 at the first wall to 0.019 at the back of the reflector.

A comparison between the results for the HT-9 first wall radiation damage obtained using the ANISN code and the results obtained using the ONETRAN code implemented at KfK, is given in Table VI.3-7. The differences obtained are attributed to the different methods used in the codes. ANISN treats the

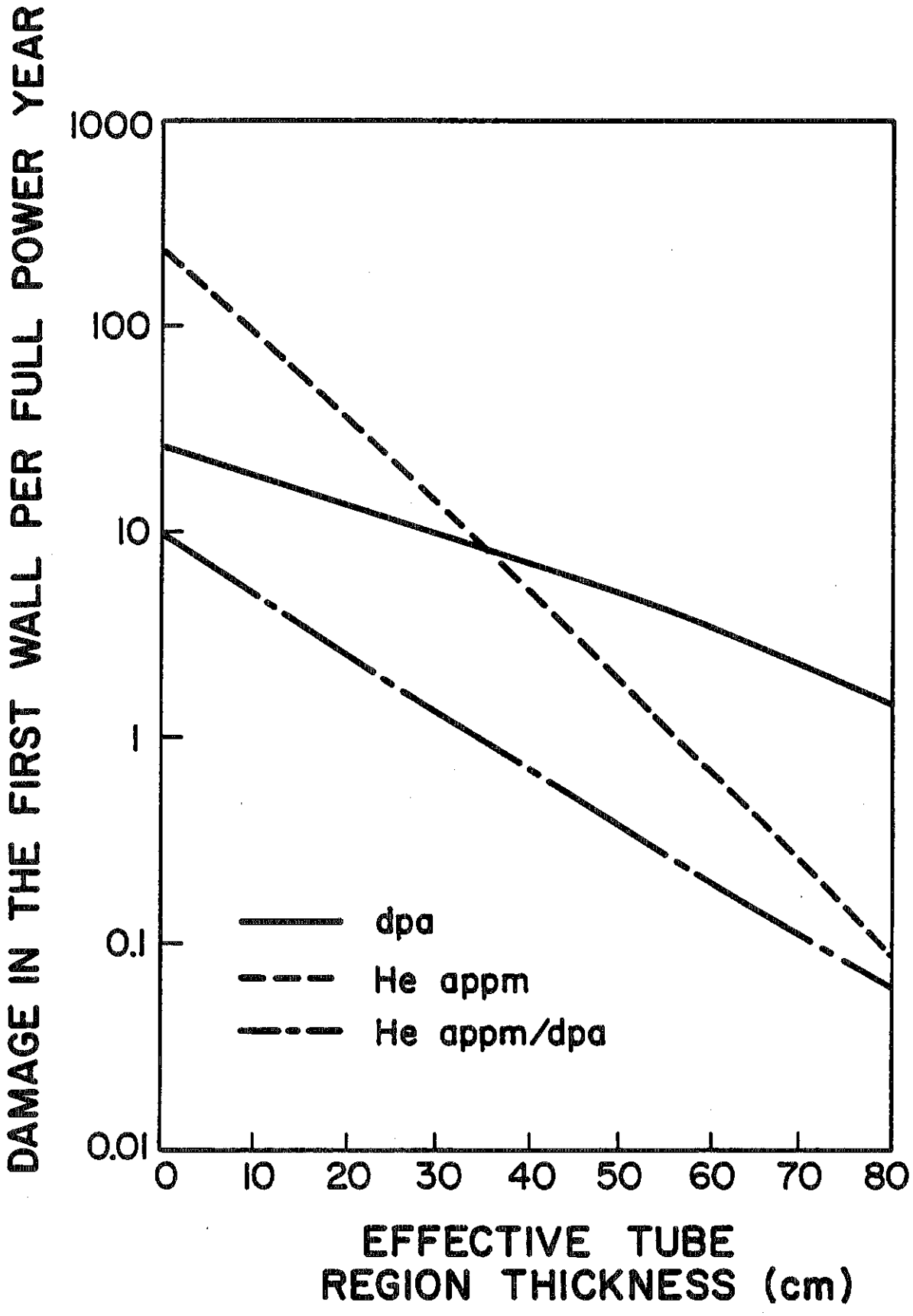

Figure VI.3-8 Effect of INPORT tubes on Damage in HT-9 first wall.

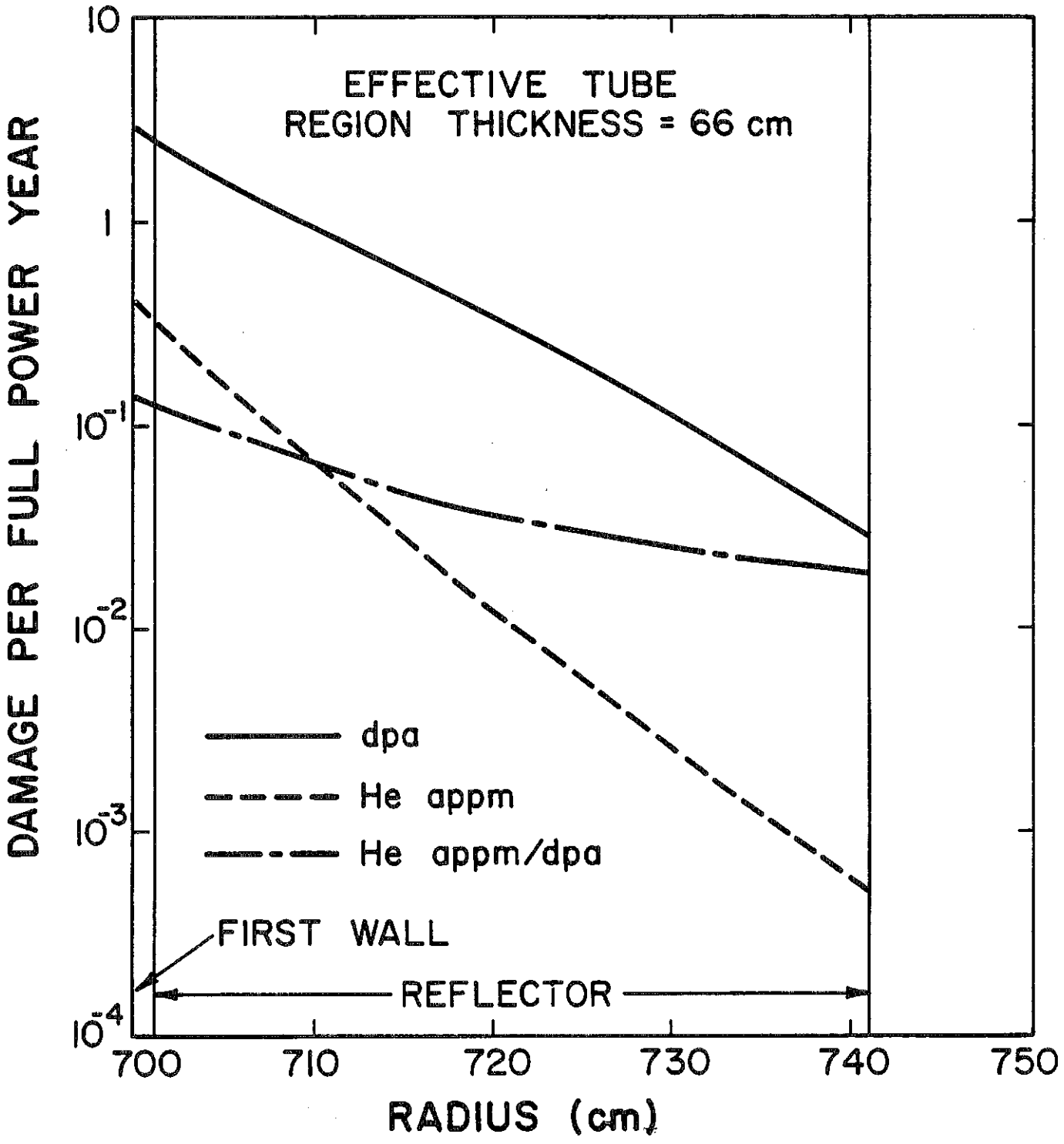

Figure VI.3-9 Spatial variation of damage in HT-9 structure in HIBALL reflector.

Table VI.3-7 Comparison Between First Wall Damage Results of ANISN and ONETRAN (S_4P_3)

	dpa/FPY	He appm/FPY	H appm/FPY
ANISN	2.688	0.364	1.380
ONETRAN	2.700	0.319	1.230

spatial variable in a finite difference form, while ONETRAN uses a finite element technique.

VI.3.2.7 Shield Design

Shielding of the reactor cavity does not pose special problems because of the simple geometrics involved as compared to shielding of the final focusing magnets discussed in section V.6. The reactor cavity shield is designed such that the biological dose rates outside the shield do not exceed ~ 5 mrem/hr during reactor operation. This design criterion has been set in order to allow hands-on maintenance of auxiliary components outside the reactor during operation. The shield for HIBALL consists of 95 v/o ordinary concrete (Type 3 concrete from reference 12) and 5 v/o water coolant. Ordinary concrete was considered because of its relatively low cost and the absence of materials which can cause high activation. The concrete used has a density of 2.3 g/cm^3 and the composition shown in Table VI.3-8.

A series of one-dimensional neutronics and photonics calculations was made to determine the flux attenuation as a function of shield thickness. Since a spherical geometry was used in the transport calculations, the results

Table VI.3-8 Concrete Composition

Element	Weight %
Calcium	24.33
Silicon	20.24
Oxygen	46.70
Carbon	4.92
Hydrogen	3.81

correspond to the conditions at the reactor midplane where the dose is expected to be greatest. Figure VI.3-10 shows the variation of neutron and gamma energy fluxes, at the shield outer surface, with shield thickness. It is clear that the neutron flux attenuates in the shield faster than does the gamma flux. This is due to the lack of high Z materials, which are more effective in attenuating gamma rays.

The neutron and gamma fluxes at the outer surface of the shield were used to determine the corresponding biological dose values for different shield thicknesses. The tissue composition used in these calculations is given in Table VI.3-9. The variation of the anticipated dose rate with shield thickness is shown in Fig. VI.3-11. A shield thickness of 3.5 m results in a dose rate of 2.64 mrem/hr which is less than the design limit of 5 mrem/hr set in this work. Almost all of the contribution to the dose comes from gamma radiation. The shielding effectiveness can be improved by using high Z materials such as lead to attenuate the gammas. Boron which has a high thermal neutron absorption cross section with only a soft 0.48 MeV gamma being produced can

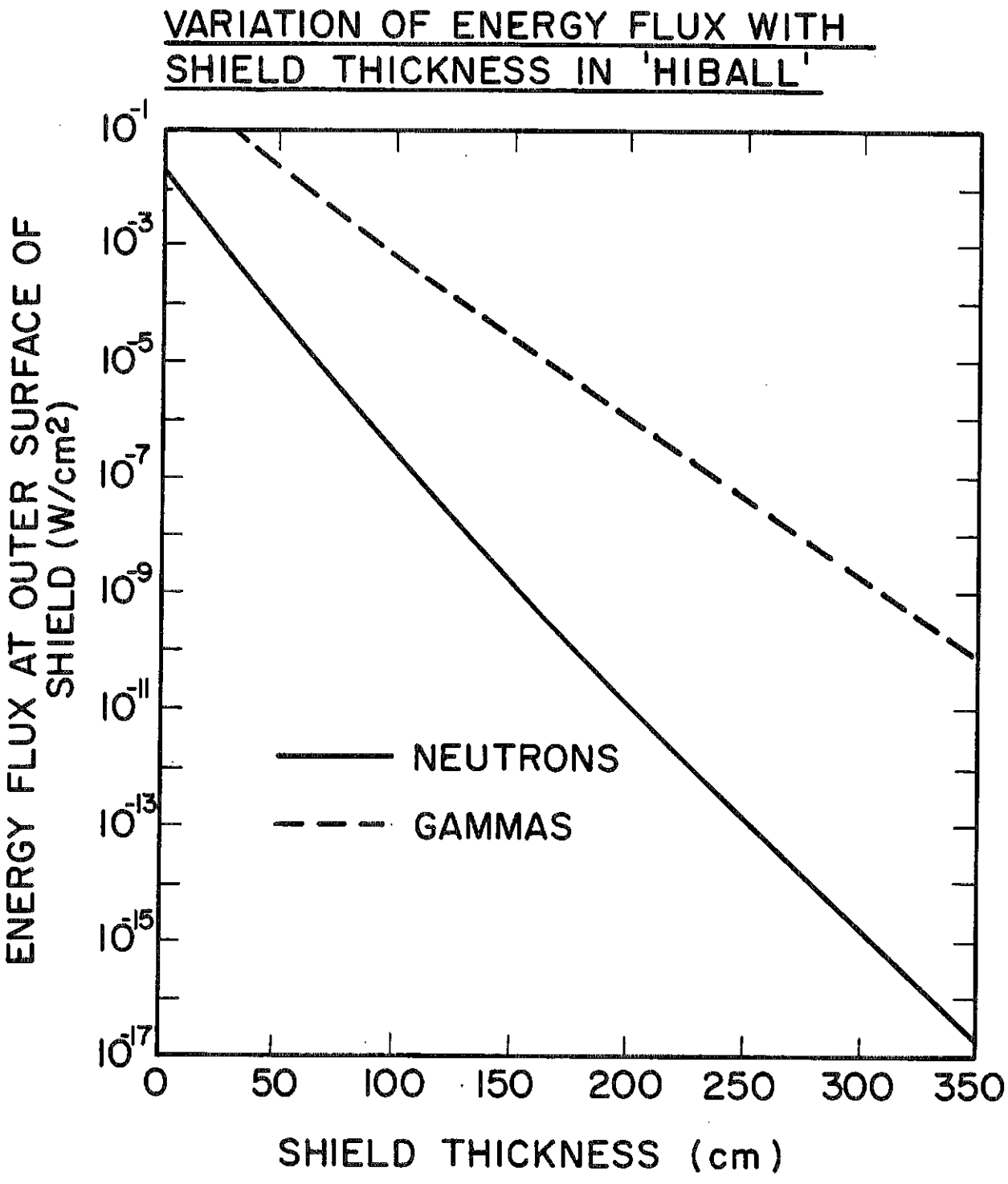

Figure VI.3-10 Variation of energy flux with shield thickness.

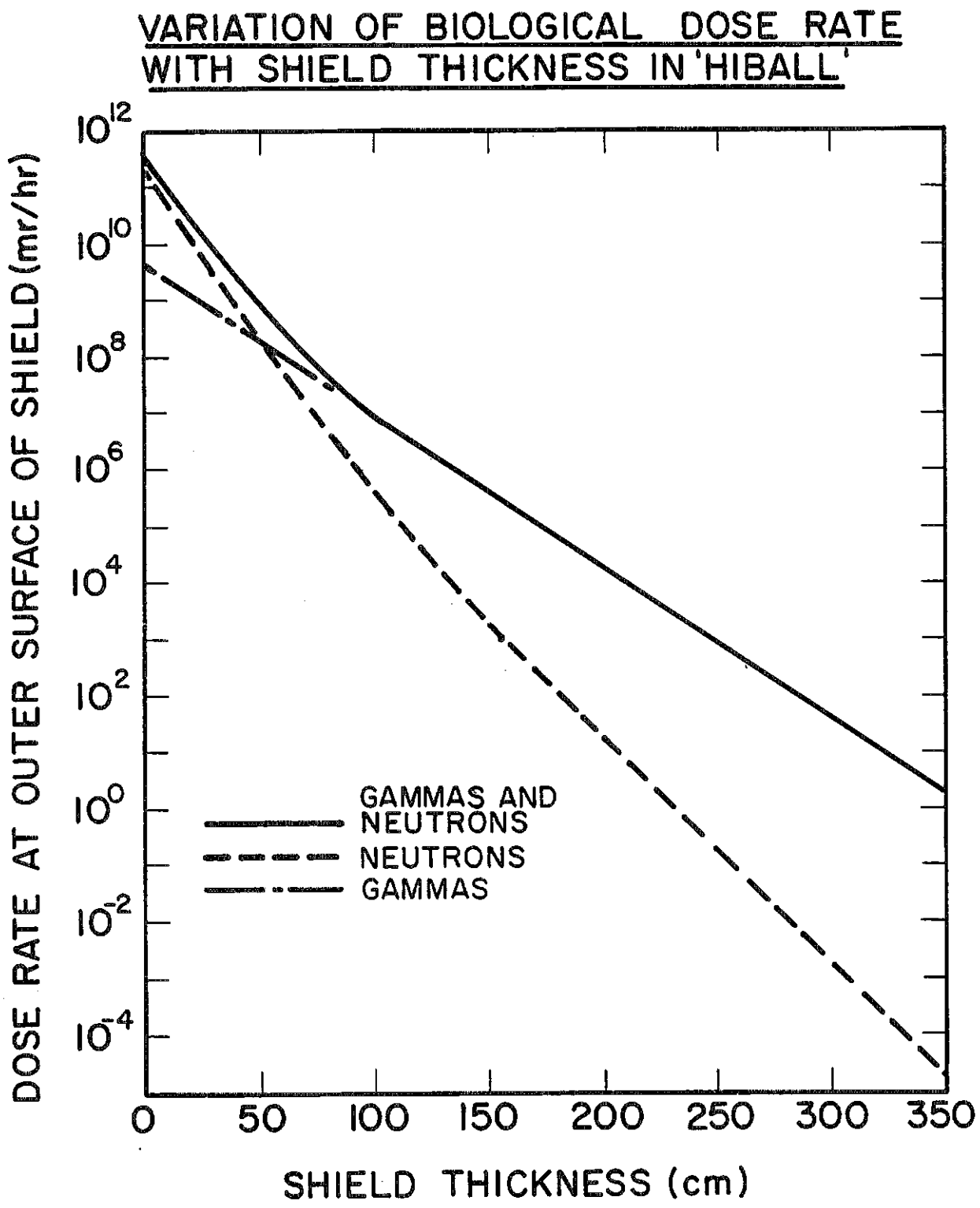

Figure VI.3-11 Variation of biological dose rate with shield thickness.

Table VI.3-9 Tissue Composition

Composition	Weight %
Oxygen	76.2
Carbon	11.1
Hydrogen	10.1
Nitrogen	2.6

also be used. However, cost considerations become an important factor if ordinary concrete is to be replaced by a more effective shield. A 3.5 m thick concrete shield is used in HIBALL, resulting in an extremely low dose rate of 2.64 mrem/hr outside the shield during reactor operation.

Figures VI.3-12 and VI.3-13 show the neutron and gamma spectra at different positions in the shield at the reactor midplane. It is clear that significant neutron and gamma spectrum softening occurs in the first 0.5 m of the shield. At this point most of the neutrons are in the thermal group. The neutron flux attenuates as one moves deep in the shield with the spectrum shape remaining nearly the same. The gamma spectrum assumes a nearly fixed shape peaking at ~ 0.2 MeV at 0.5 m inside the shield. No further significant spectrum softening occurs as one moves deep in the shield. Again, the gamma flux does not attenuate as fast as does the neutron flux because of the gamma production following neutron capture and the lack of high Z materials.

Figure VI.3-14 shows the spatial variation of power density in the reactor midplane. The contributions from neutron and gamma heating are also shown. The peak power density in the shield is 0.045 W/cm^3. The average

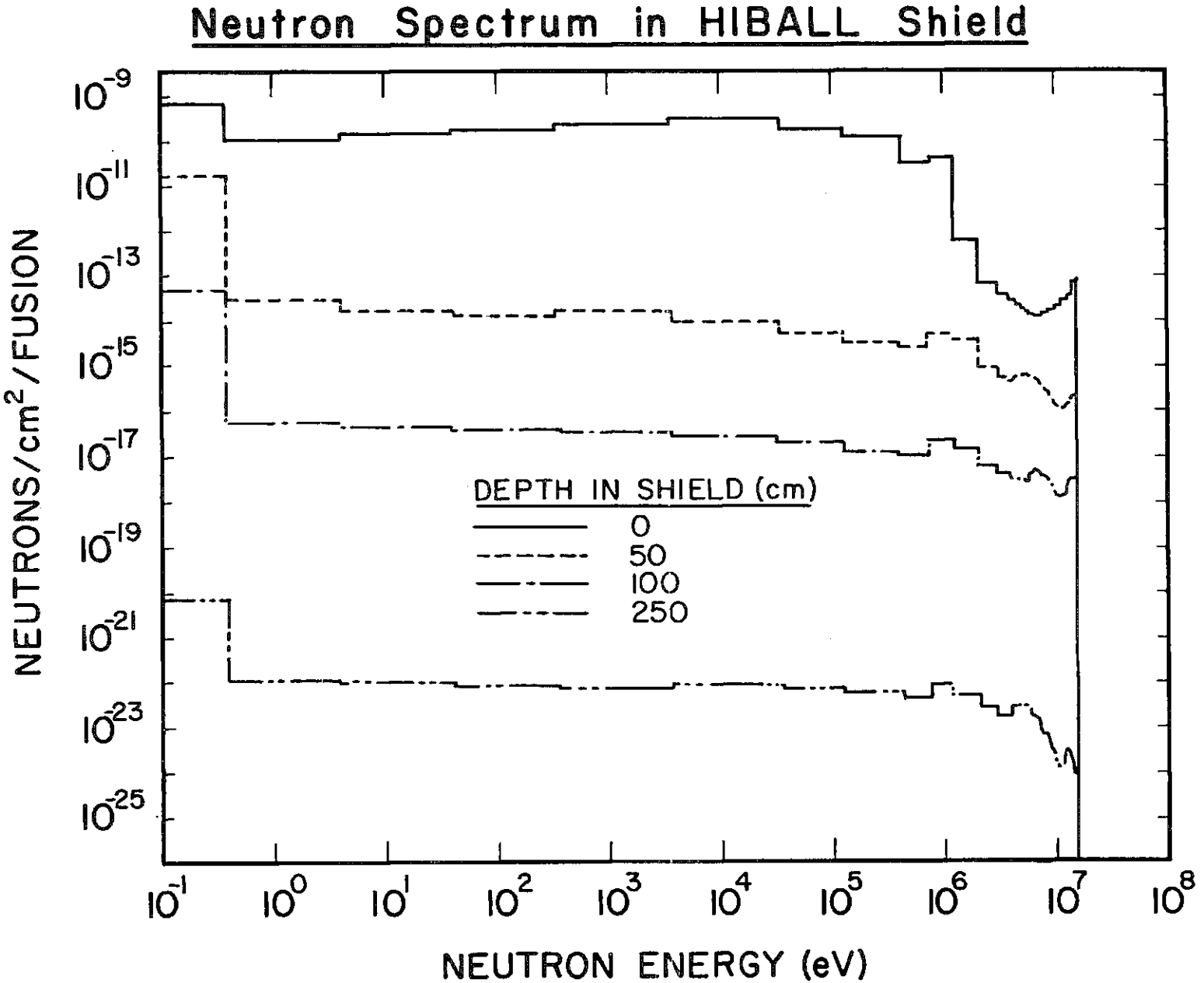

Figure VI.3-12 Neutron spectrum in HIBALL shield.
(The ordinate is the integral in each energy group.)

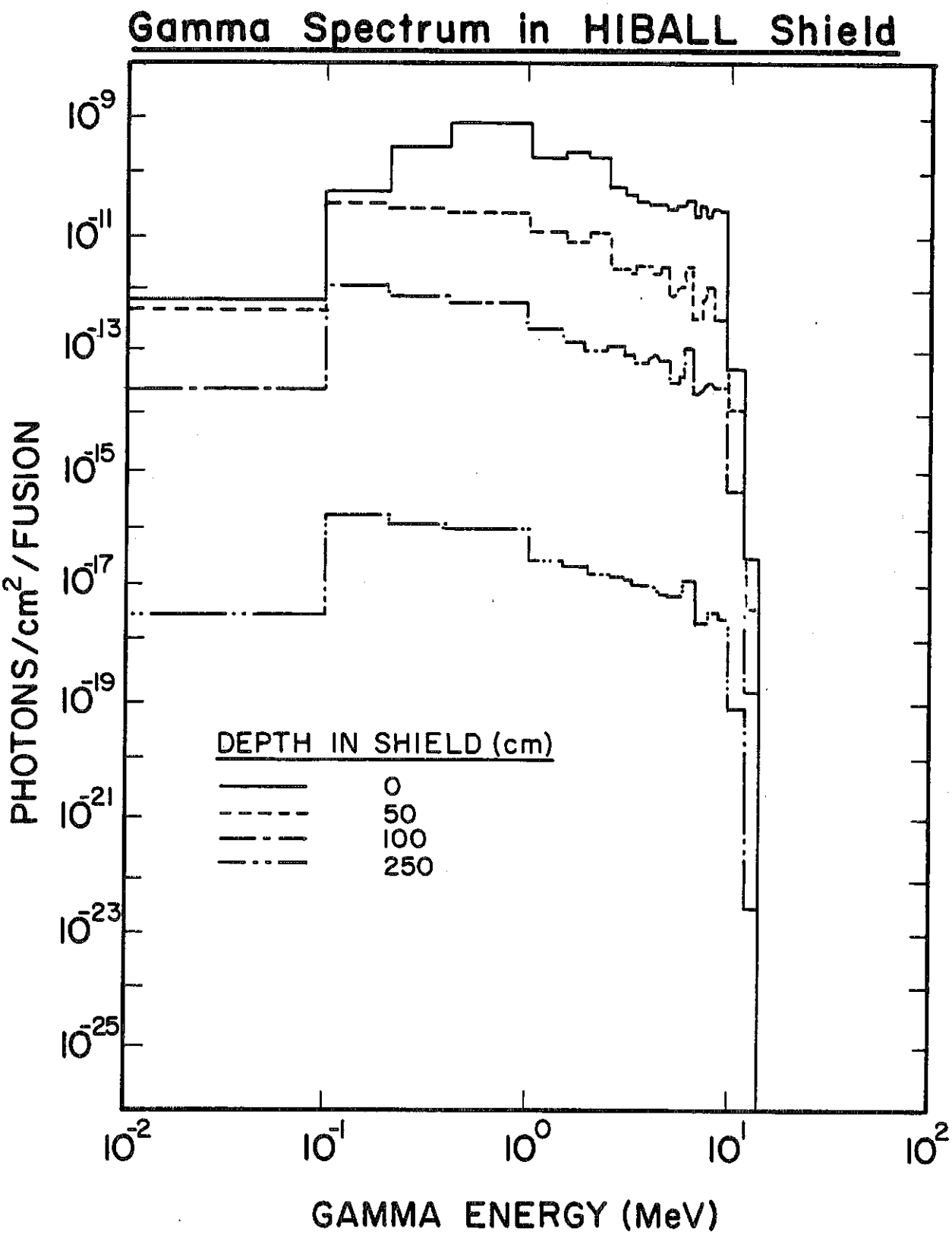

Figure VI.3-13 Gamma spectrum in HIBALL shield.
(The ordinate is the integral in each energy group.)

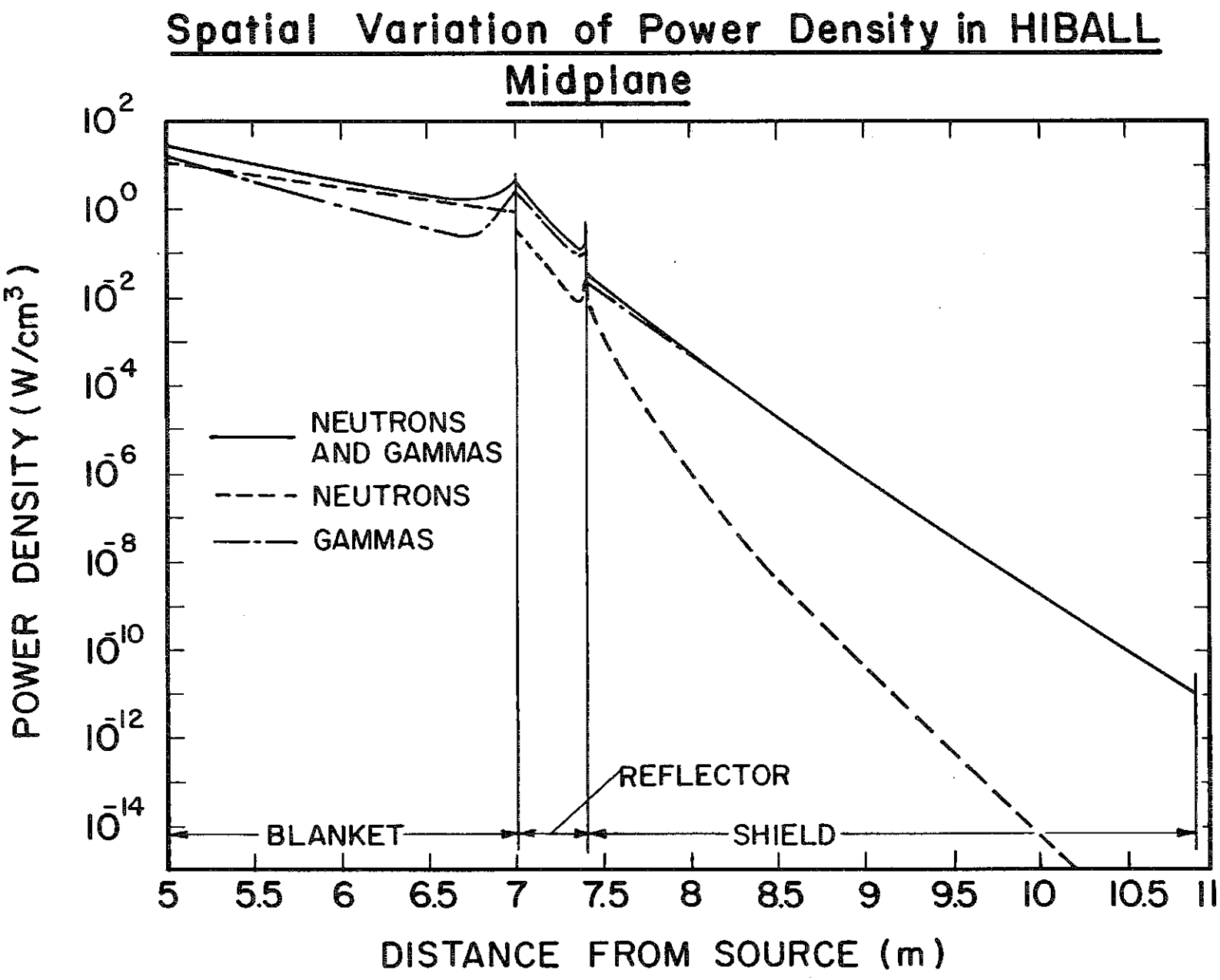

Figure VI.3-14 Spatial variation of power density at HIBALL midplane.

power density in the shield at the reactor midplane is found to be 1.83×10^{-3} W/cm^3.

VI.3.2.8 Summary

A one-dimensional spherical geometry neutronics and photonics analysis was performed to design the blanket and shield for HIBALL. The results show that by increasing the INPORT tube packing fraction, the tritium breeding ratio increases at the expense of energy multiplication. An effective tube region thickness of 66 cm was chosen resulting in an overall energy multiplication of 1.28 and a breeding ratio of 1.195. The INPORT tubes reduce radiation damage in the HT-9 first wall considerably allowing it to last for the whole reactor lifetime. A 3.5 m thick concrete shield was chosen resulting in an extremely low dose rate of 2.64 mrem/hr outside the shield during reactor operation.

VI.3.3 Three-Dimensional Time Integrated Studies

VI.3.3.1 Introduction

The one-dimensional spherical geometry calculations presented in section VI.3.2 are useful for survey studies and predicting conditions at the reactor midplane. However, the one-dimensional calculations are not capable of adequately modeling the HIBALL reactor in which a point source is at the the center of the reactor cavity which has a cylindrical shape with a conically shaped blanket at the top and a $Li_{17}Pb_{83}$ pool at the bottom. Furthermore, the HIBALL blanket/shield system is required to accommodate large penetrations for vacuum pumping which cannot be modeled in a one-dimensional analysis. These geometrical effects are expected to have an impact on the system's overall tritium breeding and energy multiplication. In this section, a three-dimensional neutronics and photonics analysis is presented which adequately models the HIBALL reactor cavity.

The neutronics and photonics problem for an inertial confinement fusion reactor is basically a time-dependent problem. However, the concern here is only with time-integrated quantities such as the tritium breeding ratio and the total nuclear heating which can be obtained using steady state transport calculations. In this work, neutron multiplication, spectrum softening, and gamma production in the target is accounted for by using the results of the target neutronics and photonics calculations presented in section III.1 as a source for the blanket and shield calculations.

VI.3.3.2 Reactor Geometrical Model and Method of Calculation

Figure VI.3-15 gives the blanket and shield configuration for HIBALL. The INPORT tube region has a thickness of 2 m and a height of 10 m. The INPORT tubes have a packing fraction of 0.33 with $Li_{17}Pb_{83}$ occupying 98 v/o of the tubes and the remaining 2 v/o occupied by SiC. The tube support structure is made of HT-9 and occupies 0.7 v/o of the tube region. A one meter deep $Li_{17}Pb_{83}$ pool exists at the bottom of the reactor cavity. The upper blanket consists of 30 segments. The design of an upper blanket segment is shown in Fig. VI.3-16. The upper blanket consists of 97 v/o $Li_{17}Pb_{83}$, 1 v/o HT-9, and 2 v/o SiC and is 50 cm thick. The $Li_{17}Pb_{83}$ in the region connecting the top blanket with the INPORT tubes helps protecting the HT-9 structure between the vacuum ducts. Thirty vacuum pumps are used to maintain the cavity pressure at 10^{-4} Torr. Each vacuum duct is 1 m wide and 0.6 m high. The first wall is 1 cm thick and is made of HT-9. The side wall is 12 m high. The top liner is 7 and 6 m above the midplane at reactor centerline and side wall, respectively. A 40 cm thick reflector consisting of 90 v/o HT-9 and 10 v/o $Li_{17}Pb_{83}$ is used. A 40 cm thick splash plate is used at the bottom of the reactor and is referred to as the bottom reflector in the following analysis. A 3.5 m thick biological shield made of 95 v/o ordinary concrete and 5 v/o H_2O coolant

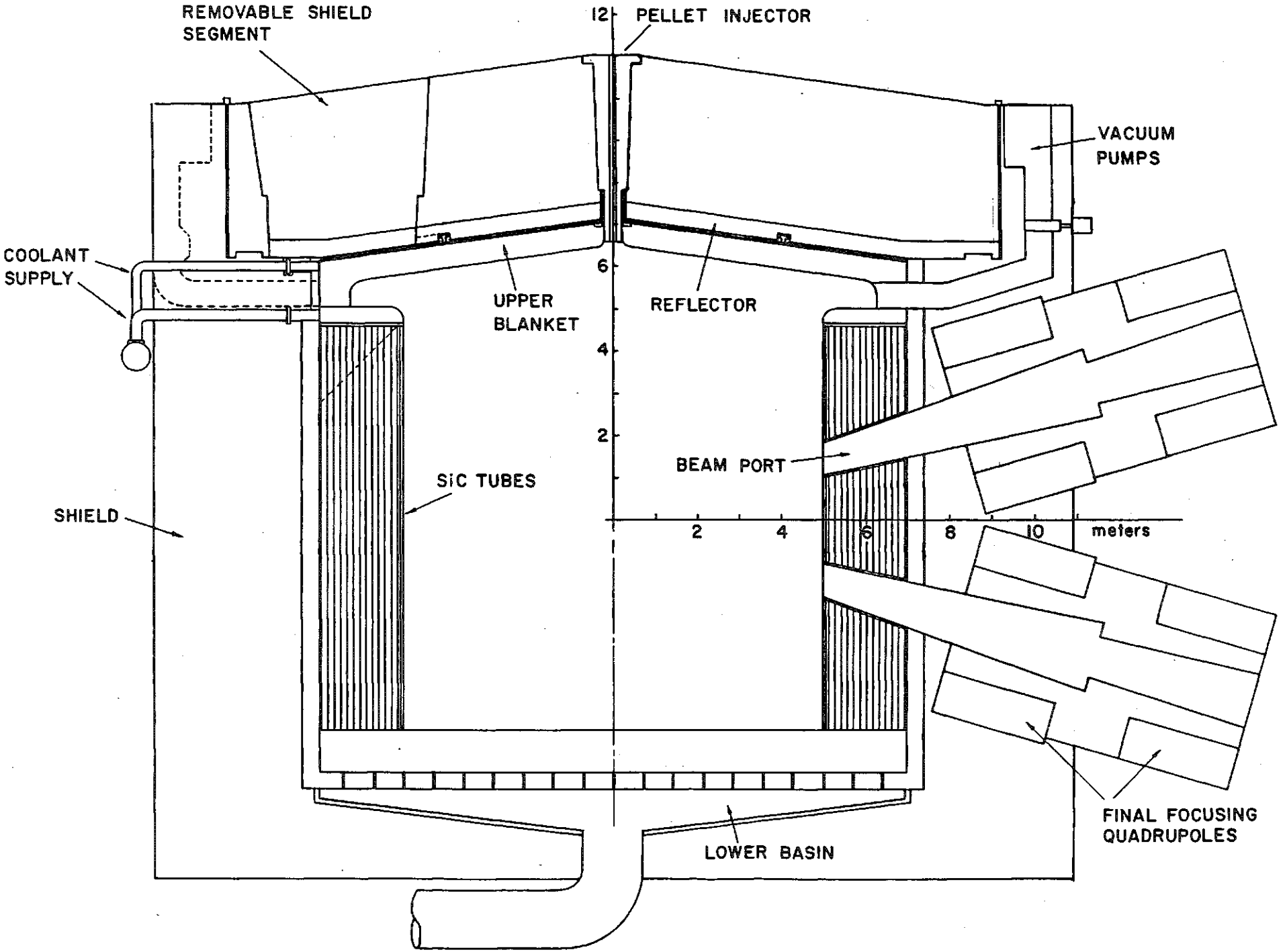

Figure VI.3-15 Blanket and shield configuration for HIBALL.

Figure VI.3-16 The design of an upper blanket segment.

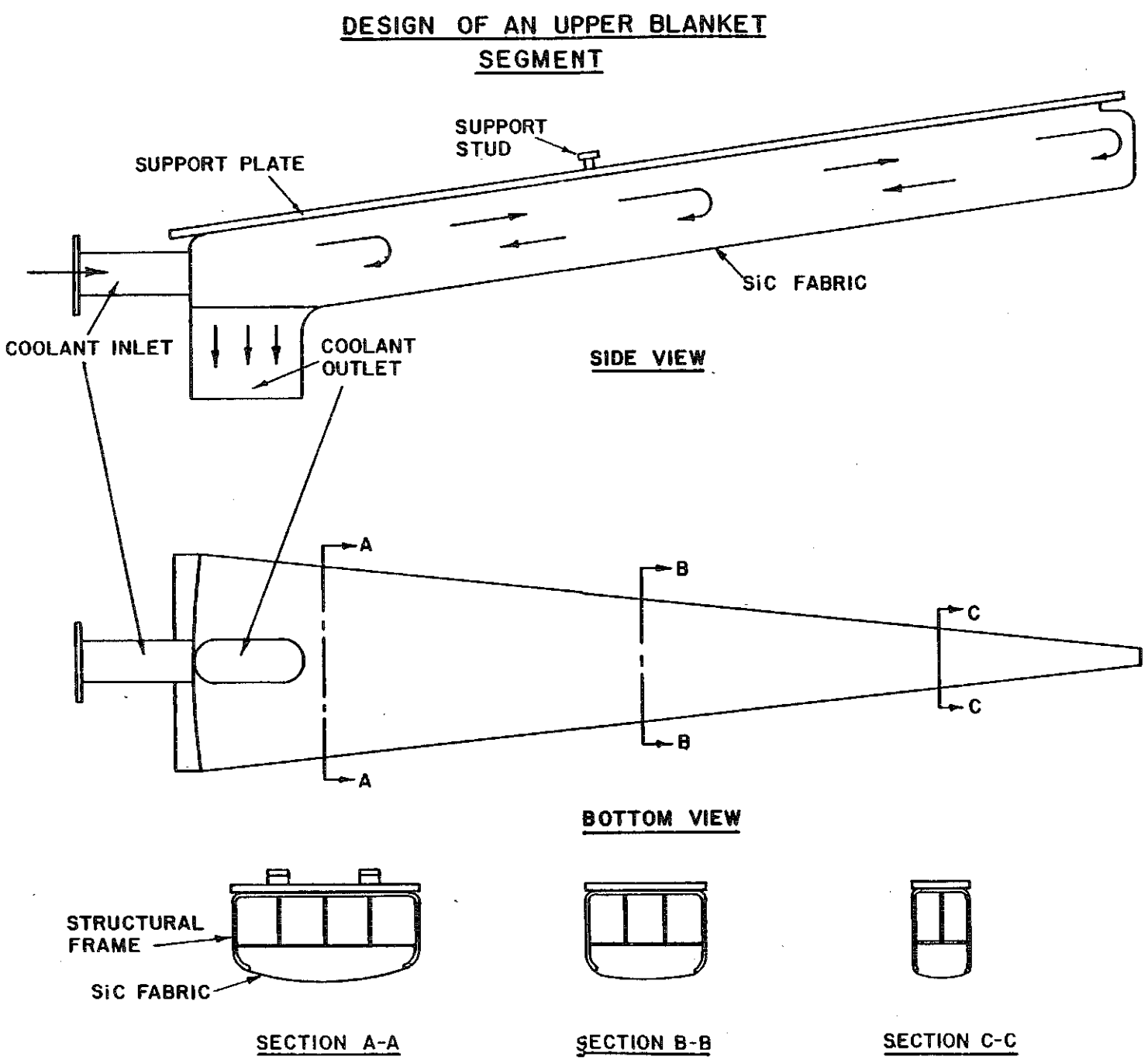

surrounds the reactor. The penetration for target injection in the chamber top is very small and is not considered in this analysis. The total area of the 20 beam line penetrations in the INPORT tube region is 3.6 m^2 implying that these penetrations occupy only ~ 1% of the blanket volume. This is smaller than the statistical uncertainty in the results obtained in the Monte Carlo calculations used in this analysis. Furthermore, the geometrical effects of these penetrations have negligible effects on the tritium breeding ratio and the energy multiplication. Hence, the beam line penetrations are not modelled in the present analysis. Detailed radiation shielding analysis for the final focusing magnets is given in section V.6.

The neutronics and photonics calculations were performed using the multigroup three-dimensional Monte Carlo code MORSE.[13] A coupled 25 neutron-21 gamma group cross section library was used. The library consists of the RSIC DLC-41B/VITAMIN-C data library[3] and the DLC-60/MACKLIB-IV response data library.[4] The combinatorial geometry capability of the MORSE code was used to model the problem geometry. Volume detectors were used to estimate the quantities of interest in the different reactor zones. The results presented here are based on a DT yield of 400 MJ and a repetition rate of 5 Hz yielding 7.1×10^{20} fusion neutrons per second. A point isotropic source was used at the center of the reactor cavity with neutron and gamma spectra obtained from the target neutronics and photonics calculations. 4000 histories were used in the Monte Carlo calculations yielding less than 2% statistical uncertainties in the estimates for the tritium breeding ratio and the energy multiplication.

Because of symmetry, only 1/60 of the reactor was modeled with reflecting albedo boundaries used at the planes of symmetry. This corresponds to a "pie slice" with an azimuthal angle of 6°. The geometry for the computational model used is given in Fig. VI.3-17. To quantify nuclear heating in the

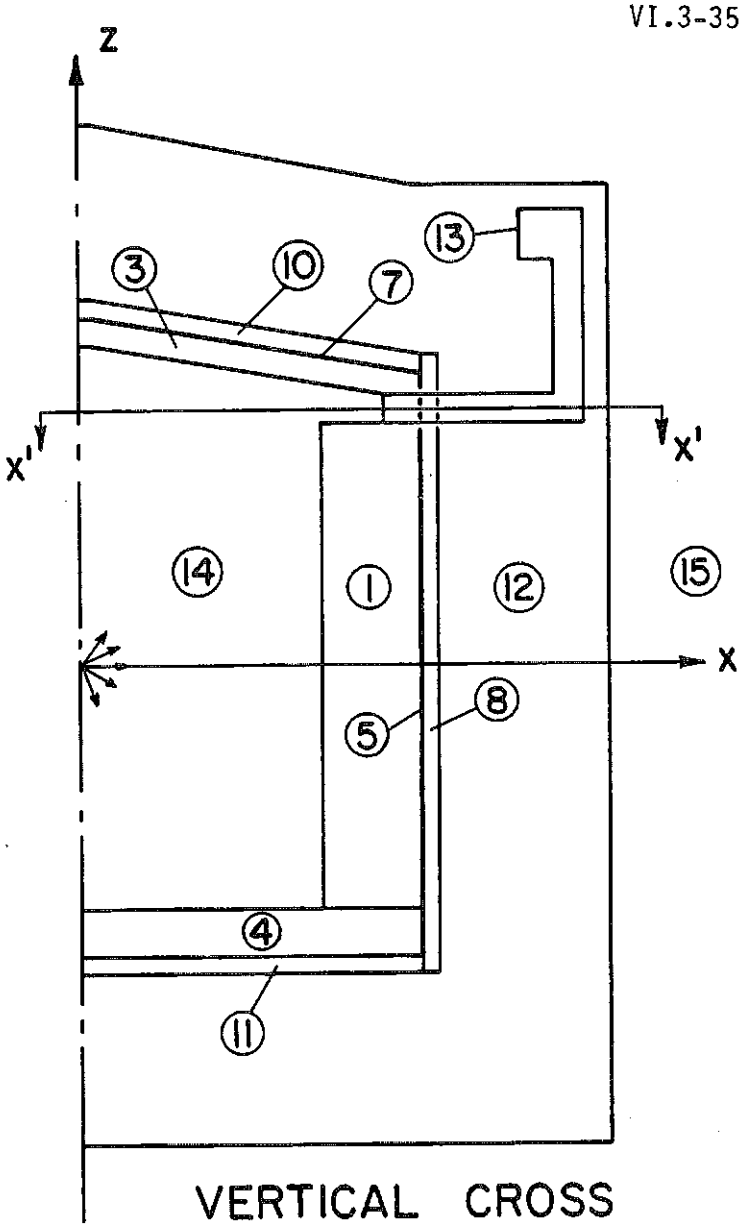

VERTICAL CROSS SECTION AT PLANE y=0

ZONE	DESCRIPTION
1	INPORT TUBES
2	BLANKET REGION AT VACUUM DUCT
3	TOP BLANKET
4	BOTTOM LiPb POOL
5	SIDE WALL
6	WALL AT DUCT
7	TOP LINER
8	SIDE REFLECTOR
9	REFLECTOR AT DUCT
10	TOP REFLECTOR
11	BOTTOM REFLECTOR
12	BIOLOGICAL SHIELD
13	VACUUM PUMP

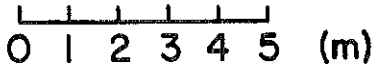

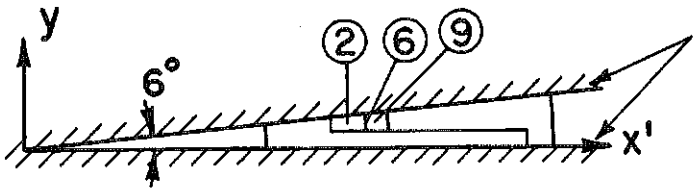

CROSS SECTION x'x'

Figure VI.3-17 HIBALL geometry for Monte Carlo calculations.

vacuum pump, a 2 cm thick region consisting of 50 v/o 316 SS and 50 v/o Cu is designated as zone 13 to simulate the cryo-panels. Zones 14 and 15 represent inner and outer vacuum regions, respectively.

VI.3.3.3 Scalar Flux

Table VI.3-10 gives the average neutron and gamma scalar fluxes in the different zones. The fractional standard deviation based on a 68% confidence interval is also included. It is clear from the results that the fractional standard deviation is very small in the breeding blanket zones and is relatively large in the optically thin regions such as the first wall. The results show that while the gamma flux is about two orders of magnitude less than the neutron flux in the breeding blanket zones, it is only one order of magnitude less than the neutron flux in the reflector zones. This results from the large gamma production following neutron capture in the HT-9 structure.

VI.3.3.4 Tritium Production

Table VI.3-11 shows the results for tritium production per DT fusion reaction in the different reactor zones. The contributions from $^{6}Li(n,\alpha)$ and $^{7}Li(n,n'\alpha)$ reactions are shown separately. It is clear that the contribution from ^{7}Li represents ~ 2% of the total tritium production in the breeding blanket region. The reason is that the number of Pb(n,2n) reactions occurring in the $Li_{17}Pb_{83}$ blanket is much larger than that of $^{7}Li(n,n'\alpha)$ reactions. The resulting (n,2n) neutrons are well below the threshold energy for $^{7}Li(n,n'\alpha)$ reaction and hence can produce tritium only through the $^{6}Li(n,\alpha)$ reaction. In the reflector region the ^{7}Li contribution to tritium production is very small because of the neutron spectrum softening in the breeding blanket.

We notice that as much tritium production occurs in the top blanket as in the bottom $Li_{17}Pb_{83}$ pool, even though the top blanket is only half as thick as

Table VI.3-10 Average Scalar Flux (Particles/cm^2/Fusion)

Region	Zone Number	Neutrons	Gammas
Breeding Blanket	1	3.191(-6) [.015]*	3.237(-8) [.026]
	2	1.691(-6) [.071]	4.453(-9) [.349]
	3	2.937(-6) [.023]	2.448(-8) [.056]
	4	1.708(-6) [.043]	1.108(-8) [.068]
First Wall	5	8.302(-7) [.041]	2.529(-8) [.118]
	6	9.282(-7) [.181]	1.124(-8) [.600]
	7	1.340(-6) [.047]	4.328(-8) [.164]
Reflector	8	2.384(-7) [.034]	1.274(-8) [.048]
	9	4.470(-7) [.153]	3.213(-8) [.245]
	10	3.789(-7) [.044]	2.230(-8) [.070]
	11	8.354(-8) [.126]	3.739(-9) [.132]

*Fractional Standard Deviation

Table VI.3-11 Tritium Production (Tritons/Fusion)

Region	Zone Number	$^{6}Li(n,\alpha)T$	$^{7}Li(n,n'\alpha)T$
Breeding Blanket	1	0.729	0.018
	2	0.014	0.00001
	3	0.212	0.004
	4	0.235	0.004
	Region Total	1.190	0.026
Reflector	8	0.022	0.000002
	9	0.001	0.0000001
	10	0.009	0.000002
	11	0.002	0.0000001
	Region Total	0.034	0.000004
System Total		1.224	0.026

the bottom pool and includes 1 v/o HT-9 structure. The reason in that the 2 v/o SiC present in the top blanket enhances neutron slowing down and hence increases the tritium breeding effectiveness. In fact, our results show that the breeding capability of $Li_{17}Pb_{83}$ can be improved considerably by enriching Li and/or using moderators in the blanket. The improvement in systems using $Li_{17}Pb_{83}$ is much more pronounced than that in systems using other breeding materials because most of the contribution to breeding in $Li_{17}Pb_{83}$ case comes from the $^{6}Li(n,\alpha)$ reaction which has a 1/v cross section in the low energy region.

The overall tritium breeding ratio is found to be 1.25. The confidence interval for the estimated breeding ratio is 0.025 which is 2% of the obtained estimate. The overall tritium breeding ratio obtained here with the actual reactor cavity cylindrical geometry is larger than that obtained from the one-dimensional spherical geometry calculations (1.195). The reason is that in the spherical geometry case, all source neutrons are incident on the blanket perpendicularly to its inner surface and hence will see the same blanket thickness. On the other hand, the source neutrons emitted isotropically at the center of the cylindrical cavity impinge on the inner surface of the blanket at different angles and hence will see larger blanket thicknesses. In other words, the neutron source is surrounded by a larger volume of breeding material in the actual cylindrical case as compared to the case of an equivalent spherical blanket.

VI.3.3.5 Nuclear Heating

Table VI.3-12 shows the nuclear energy deposition for neutrons and gammas in the different zones. The average power density is also included. It is clear that the contributions from neutron and gamma heating are nearly the same in the breeding blanket while the gamma contribution in the first wall and reflector is about an order of magnitude higher than the neutron contribution. This results from gamma generation in the HT-9 structure. About 60% of the total reactor thermal power comes from gamma heating. The energy deposited in the biological shield is 0.06 MeV/fusion which corresponds to a power of 6.82 MW. This represents only 0.27% of the total reactor thermal power. Only the energy deposited in the blanket, first wall, and reflector are considered as recoverable energy. The total recoverable neutron and gamma energy in the reactor per DT fusion is 17.553 ± .292 MeV which is slightly less than that obtained for an equivalent spherical reactor (17.95 MeV). The

Table VI.3-12 Nuclear Heating

Region	Zone Number	Energy Deposition (MeV/fusion)		Average Power Density (W/cm^3)
		Neutrons	Gammas	
Breeding Blanket	1	4.806	4.839	4.409
	2	0.074	0.017	3.911
	3	1.339	1.147	3.515
	4	1.430	1.007	1.800
	Region Total	7.649	7.010	4.409
First Wall	5	0.004	0.050	1.222
	6	0.0001	0.0004	2.010
	7	0.003	0.039	3.068
	Region Total	0.007	0.089	1.653
Reflector	8	0.155	1.628	0.939
	9	0.007	0.066	1.020
	10	0.070	0.733	1.465
	11	0.013	0.126	0.257
	Region Total	0.245	2.553	0.941
System Total		7.901	9.652	3.345

reason is that more tritium production is obtained in the cylindrical case with less neutrons being captured in the HT-9 structure. A neutron absorbed in ^{6}Li releases ~ 4.8 MeV while if it is captured in the HT-9 structure ~ 7 MeV is released.

In order to get a statistically adequate estimate of nuclear heating in the vacuum pump with a reasonable number of histories, a Monte Carlo calculation with an angular source biasing was performed. In this run, 4000 histories were used. A volumetric nuclear heating rate of 6×10^{-11} W/cm^3 was obtained in the vacuum pump (zone 13). The fractional standard deviation was 0.25. Because the vacuum ducts do not see direct line-of-sight source neutrons and they are bent twice, neutron streaming through the ducts was found to not cause any serious problem to the vacuum pump.

The energy flow for the HIBALL fusion reactor design is illustrated in Fig. VI.3-18. The values given for the power correspond to one reactor cavity. Therefore, these values need to be multiplied by 4 to calculate the power from the whole power plant. This corresponds to a total power plant thermal power of 10,193 MW(th). The overall energy multiplication defined as the total energy deposited in the system, including the energy deposited by X-rays and target debris at the first surface of the blanket, divided by the fusion reaction yield of 17.6 MeV, is found to be 1.274.

VI.3.3.6 Summary

A three-dimensional Monte Carlo neutronics and photonics analysis was performed for the HIBALL reactor cavity. An overall tritium breeding ratio of 1.25 and an overall energy multiplication of 1.274 were obtained. The tritium breeding ratio is higher than that for the equivalent spherical reactor cavity. Nuclear heating in the vacuum pump was found to be very small. The power

Figure VI.3-18

ENERGY FLOW IN HIBALL

HIB PULSE

(4.8 MJ)

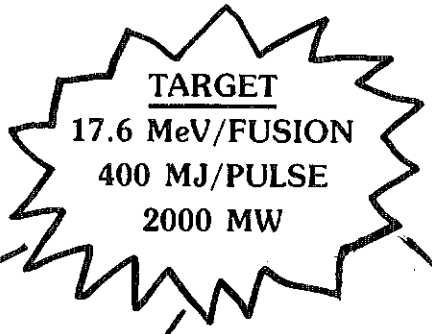

NEUTRON & GAMMA	X-RAY & DEBRIS	LOST IN ENDOERGIC REACTIONS
12.559 MeV	4.862 MeV	0.179 MeV
285.42 MJ	110.49 MJ	4.08 MJ
1427.1 MW	552 MW	20.35 MW

	NEUTRON & GAMMA	X-RAY & DEBRIS	TOTAL	
BREEDING BLANKET	14.659 MeV 333.16 MJ 1667.5 MW	4.862 MeV 110.49 MJ 552 MW	19.521 MeV 443.65 MJ 2219.5 MW (87.05%)	
WALL	0.096 MeV 2.24 MJ 10.8 MW		0.096 MeV 2.24 MJ 10.8 MW (0.42%)	22.415 MeV 509.39 MJ 2548.3 MW
REFLECTOR	2.798 MeV 63.5 MJ 318.0 MW		2.798 MeV 63.5 MJ 318.0 MW (12.53%)	

OVERALL ENERGY MULTIPLICATION = 1.274

in the biological concrete shield represents only 0.27% of the total reactor thermal power. The thermal power for the HIBALL power plant is 10,193 MW(th).

VI.3.4 Time-Dependent Neutronics and Photonics

VI.3.4.1 Introduction

In an inertial confinement fusion reactor the neutron source has a pulsed nature because of the very short burn time over which the fusion reactions occur (10-100 ps). Furthermore, the neutron pulse does not reach the first surface of the blanket until ~ 100 ns after the burn and the neutron slowing down time in the blanket is much greater than the duration of the neutron source. Significant softening of the energy spectrum of neutrons escaping from the target results from neutron interaction with the dense ($\sim 10^{25}/cm^3$) fuel and surrounding tamper material. This leads to a considerable time of flight spread as neutrons reach the first surface. Therefore, time dependent neutronics studies are essential for the proper analysis of inertial confinement fusion reactors.

As a result of the pulsed nature of the neutron source, high instantaneous damage rates are present in an inertial confinement fusion reactor wall and structure. This can lead to significant changes in the microstructure[14] of the first wall material. It has also been found that high instantaneous dpa rates result in higher recombination rates with the void growth being inhibited and swelling decreased.[15] Accurate instantaneous damage rates can be calculated by performing time-dependent neutronics studies. Previous time dependent neutronics studies have been used to calculate the instantaneous dpa rate in the first wall of a laser fusion reactor[16] and an electron beam fusion reactor.[17] No correction for the time of flight spread of neutrons within each energy group was made in these studies.

A modified version of the time dependent discrete ordinates code TDA[18] has been used to perform time-dependent neutronics analysis for HIBALL. The effects of the INPORT first wall protection concept on the peak instantaneous and average dpa and gas production rates in the ferritic steel first wall have been investigated. The steady state discrete ordinates ANISN[1] code was used to determine the average time integrated radiation damage rates.

Energy deposition in the porous tubes and first wall of the HIBALL fusion reactor is important in the determination of their structural integrity. The temporal and spatial dependence of energy deposition is also required for stress analysis studies. The energy deposition rate integrated over the volume of the blanket of a laser fusion reactor was calculated in a previous study.[19] However, no detailed time dependent fluxes or energy deposition rates at different points were given. In this work, the instantaneous energy deposition rates at different positions in the blanket and first wall are calculated.

VI.3.4.2 Heavy Ion Beam Reactor Computational Model

A schematic of the blanket, first wall, reflector, and shield configuration for the HIBALL fusion reactor is given in Fig. VI.3-1. The nuclide densities used in the calculations are given in Table VI.3-1 The results presented here for the damage and energy deposition rates are based on a DT yield of 400 MJ which corresponds to 1.42×10^{20} source neutrons per pulse. A repetition rate of 5 Hz is used to determine the total dpa and helium production in the first wall per full power year (FPY).

The steady state discrete ordinates code ANISN was used to perform detailed neutronics and photonics calculations within the target, giving the time integrated energy spectrum of neutrons escaping from the target as explained in section III.1. This spectrum was used as a source for the time

dependent blanket neutronics analysis performed using the time dependent multi-group discrete ordinates code TDA. ANISN was used to calculate the time integrated reaction rates. Since the particle transport codes used are one-dimensional, spherical geometry was used in the blanket calculations and hence the results represent the worst conditions at the central plane of the cylindrical reactor. A P3-S8 approximation was used in the transport calculations. A coupled 25 neutron-21 gamma group cross section library has been used. This library consists of the RSIC DLC-41B/VITAMIN-C data library[3] and the DLC-60/MACKLIB-IV response data library.[4]

VI.3.4.3 Neutron Source

The target, though absolutely very small, is an extremely dense medium composed primarily of light elements. This results in a substantial collision probability for fusion neutrons created within it. The 14.1 MeV fusion neutrons are degraded in energy as a result of elastic collisions with the fuel (DT) and inelastic collisions with the high Z materials (Pb). Neutron multiplication also results from (n,2n) and (n,3n) reactions with the constituent elements of the target. Since the neutrons escaping from the target represent the neutron source for the blanket neutronics calculations, it is essential to perform detailed neutronics calculations for the target to account accurately for spectrum softening and neutron multiplication.

Since the burn time of the target (10-100 ps) is much greater than the slowing down time of fusion neutrons in the extremely dense target ($\sim$ 0.1 ps), steady state calculations yield useful information. Furthermore, since the burn time is much smaller than the time neutrons take to reach the first surface of the blanket including the time of flight spread, neutrons are assumed to be emitted in a pulse with zero time duration ($\delta(t)$). This implies that the time integrated spectrum of the neutrons leaking from the target as calcu-

lated by the steady state code ANISN gives the correct neutron source spectrum. In other words, if $n_L(E,t)$ is the exact spectrum of neutrons leaking from the target at time t within the burn, the time integrated spectrum calculated by ANISN is given by

$$n_L(E) = \int_{t_B} n_L(E,t)dt \ , \qquad \text{(VI.3-1)}$$

where t_B is the burn time. Since the burn time is very small, all neutrons leaking at different times during the burn are assumed to be emitted at t=0 and the source for the blanket calculations is given by

$$S(E,t) = n_L(E)\ \delta(t) \ . \qquad \text{(VI.3-2)}$$

Since the target has a very small radius compared to the radius of the reactor cavity, the neutron source is represented by a point source at the center of the reactor. Furthermore, neutrons are emitted isotropically from the target and the complete representation of the neutron source is given by

$$S(\mu,r,E,t) = n_L(E)\ \delta(r)\ \delta(t)\ \delta(\mu-1) \ . \qquad \text{(VI.3-3)}$$

Detailed neutronics and photonics calculations have been performed for the HIBALL target as discussed in Section III.1. The results show that a target neutron multiplication of 1.046 is obtained. This results mainly from (n,2n) reactions in the dense DT fuel core and LiPb pusher. The average energy of neutrons leaking from the target is 11.98 MeV implying that 71.2% of the fusion energy is carried by the emerging neutrons. The spectrum of neutrons leaking from the target, $n_L(E)$, is given in Fig. VI.3-19.

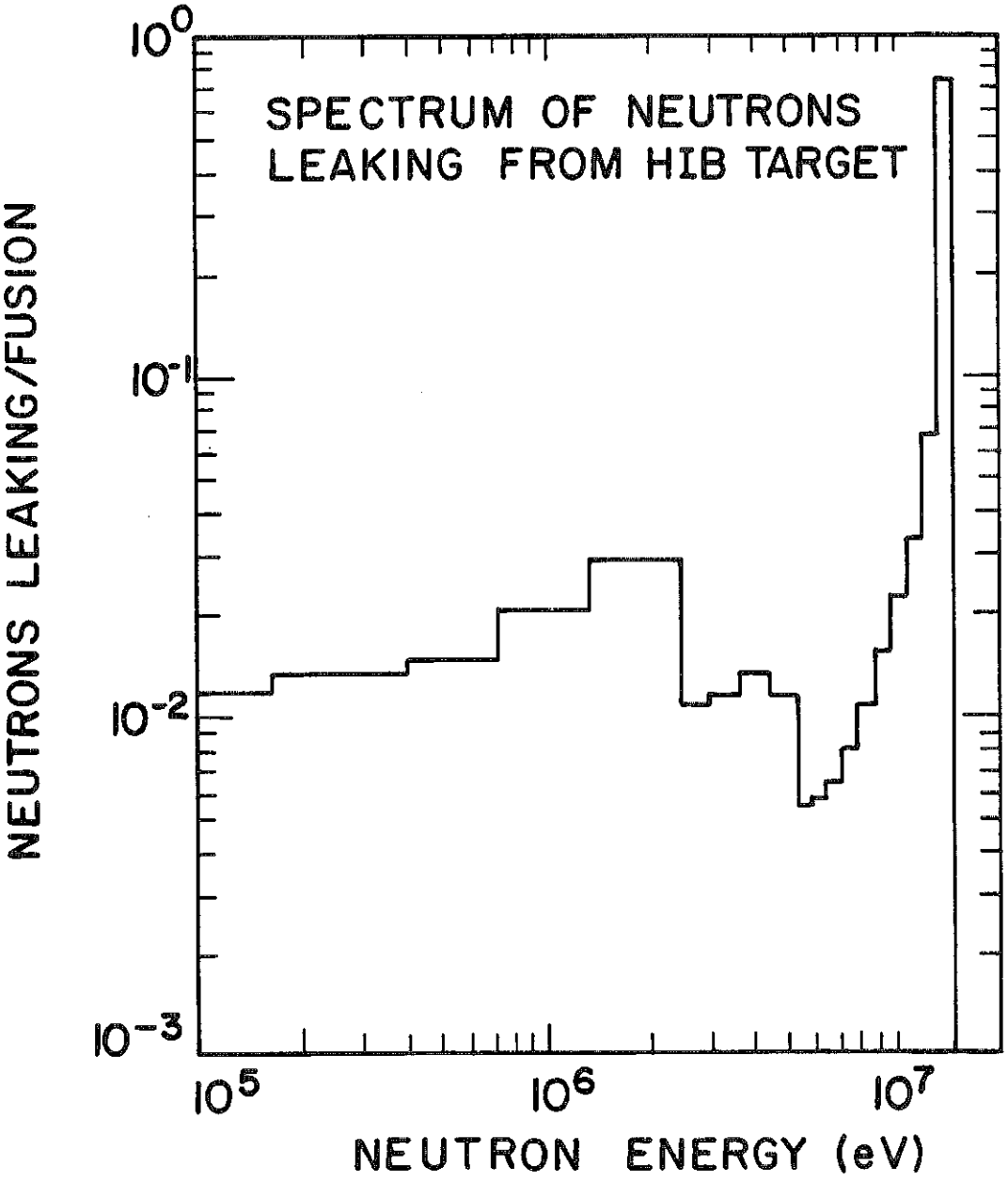

Fig. VI.3-19 Spectrum of neutrons leaking from the pellet. (The ordinate is the integral in each energy group.)

As neutrons travel from the target to the first surface of the blanket considerable time of flight spreading occurs because of the broad energy distribution of these neutrons. The arrival time spectrum at the first surface located 5 m from the neutron source is shown in Fig. VI.3-20. The numbers at the bottom of the graph indicate the energy groups associated with the various times. Since all neutrons in a specified energy group are forced by the multigroup treatment of the neutronics code to travel at the same velocity corresponding to the average group energy, these neutrons will arrive at the first surface simultaneously and no time of flight spread corresponding to the energy group width will be observed. In order to preserve the correct arrival time spectrum at the first surface, source neutrons are given artificial birth times associated with their energies within the group. If the time of flight spread corresponding to the gth energy group width is Δ_g, the modified neutron source for group g is represented by a rectangular pulse with a time duration of Δ_g. This necessary correction for time of flight spread of neutrons within each energy group was not made in the previous time dependent neutronics analysis of inertial confinement fusion reactors.

VI.3.4.4 Time Dependent Neutron Spectrum in the HT-9 First Wall

A version of the time dependent multigroup discrete ordinates code TDA, modified to facilitate its use for the analysis of inertial confinement fusion reactors[20], has been used to perform time dependent neutronics and photonics calculations for the HIBALL blanket and reflector model illustrated in Fig. VI.3-1. For comparison, calculations have been also made for the case of an unprotected wall.

The source for the problem involves Dirac delta functions which are quite difficult to represent with standard finite difference methods. To circumvent this difficulty the uncollided flux is determined analytically and an analytic

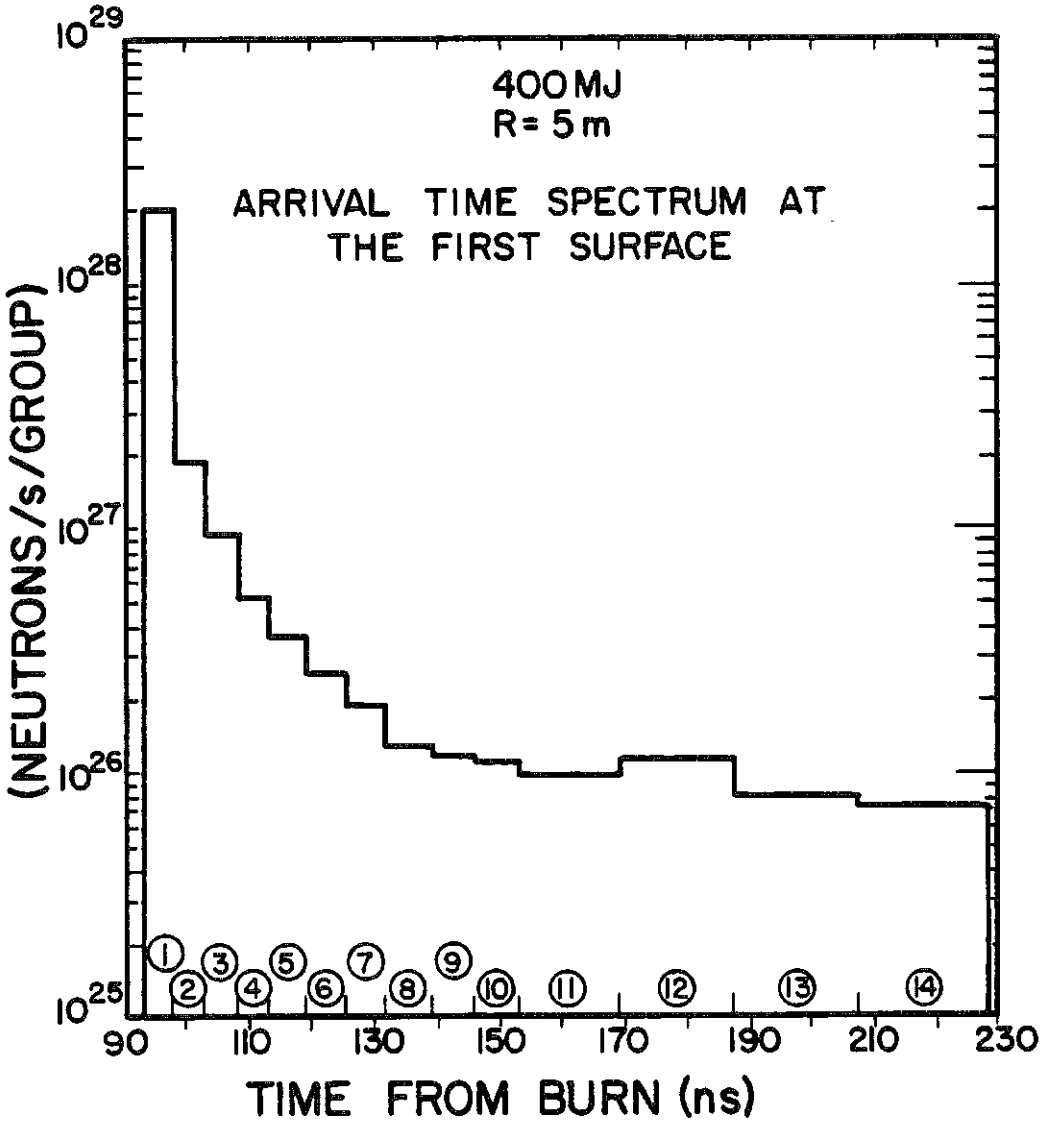

Figure VI.3-20 Arrival time spectrum at the first surface of the blanket.

first collision source is used by the code to determine the collided part of the flux.

The neutron spectrum in the protected ferritic steel first wall is illustrated in Fig. VI.3-21. The results are shown at 10 ns and 70 ns after the uncollided neutrons of the highest energy strike the wall. The neutron spectra in the unprotected wall at different times following the arrival of the leading edge of the pulse at the wall are given in Fig. VI.3-22. Comparing the results in Figs. VI.3-21 and VI.3-22, we notice that significant neutron attenuation occurs in the INPORT tubes.

Neutrons slowed down in the inner blanket region take a relatively long time to reach the first wall. This time depends on the slowing down time of neutrons in the blanket, the speed of slowed down neutrons, and the position within the blanket at which the slowing down interaction occurs. At early times, following the arrival of the fastest uncollided neutrons at the first wall, most of the neutrons in the first wall are in the high energy groups. Only neutrons which have been slowed down in the porous tubes close to the first wall are able to arrive at the wall by this time. Neutrons slowed down in the wall itself result in the relatively low peak at ~ 1 MeV in Fig. VI.3-21. At 60 ns later, most of the high energy neutrons have already passed the first wall while neutrons slowed down in the blanket are still arriving at the first wall primarily because of the relatively long slowing down time of neutrons in the blanket. Therefore, the time dependent spectrum and consequently the instantaneous damage rates in the first wall are governed by two factors; the time of flight spread and the slowing down time spread in the blanket. In lead, which is the main constituent of the blanket, the slowing down time from 14.1 MeV to the inelastic threshold energy of 0.57 MeV is about 1 μs. At energies below 0.57 MeV, slowing down is due to elastic scattering

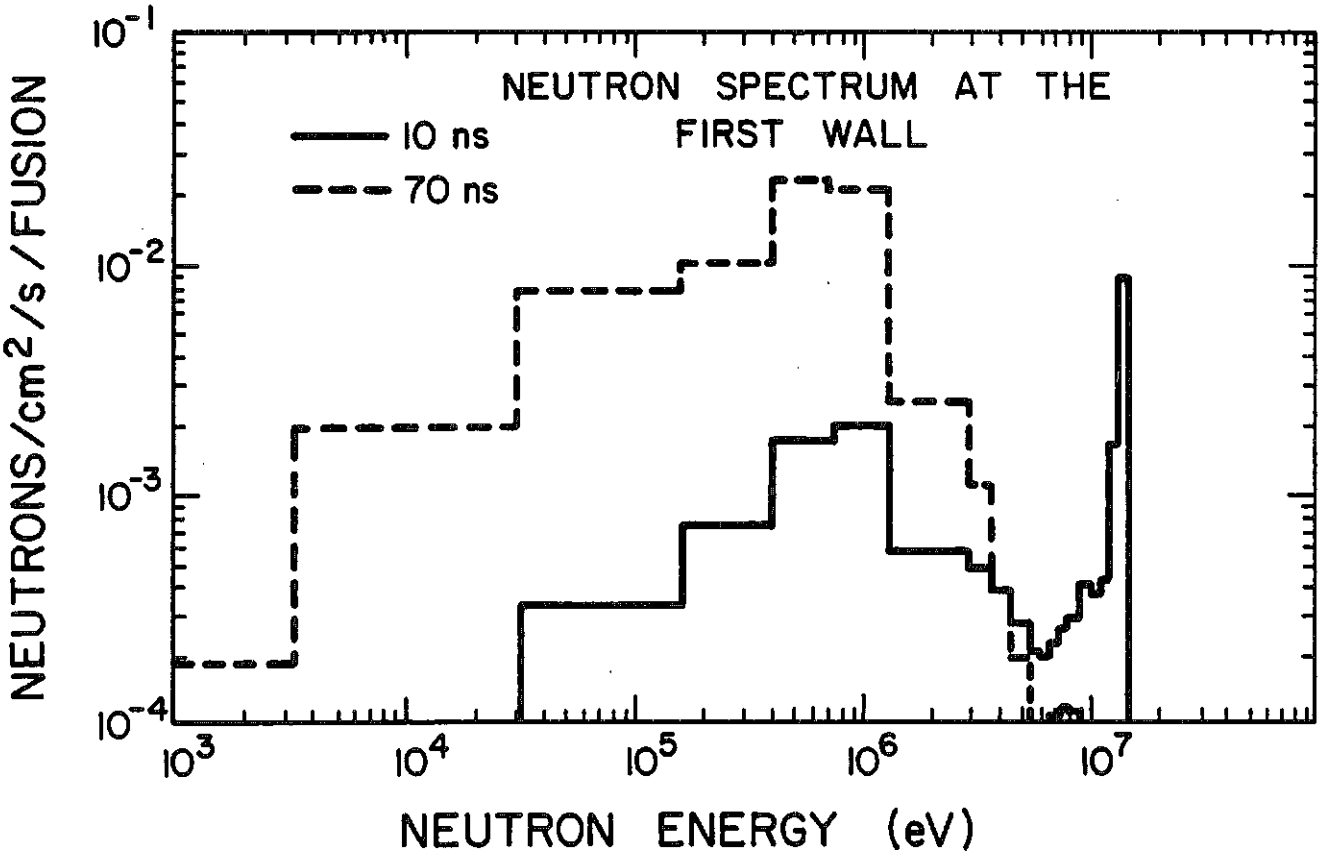

Figure VI.3-21 Neutron spectrum in HIBALL first wall. (The ordinate is the integral in each energy group.)

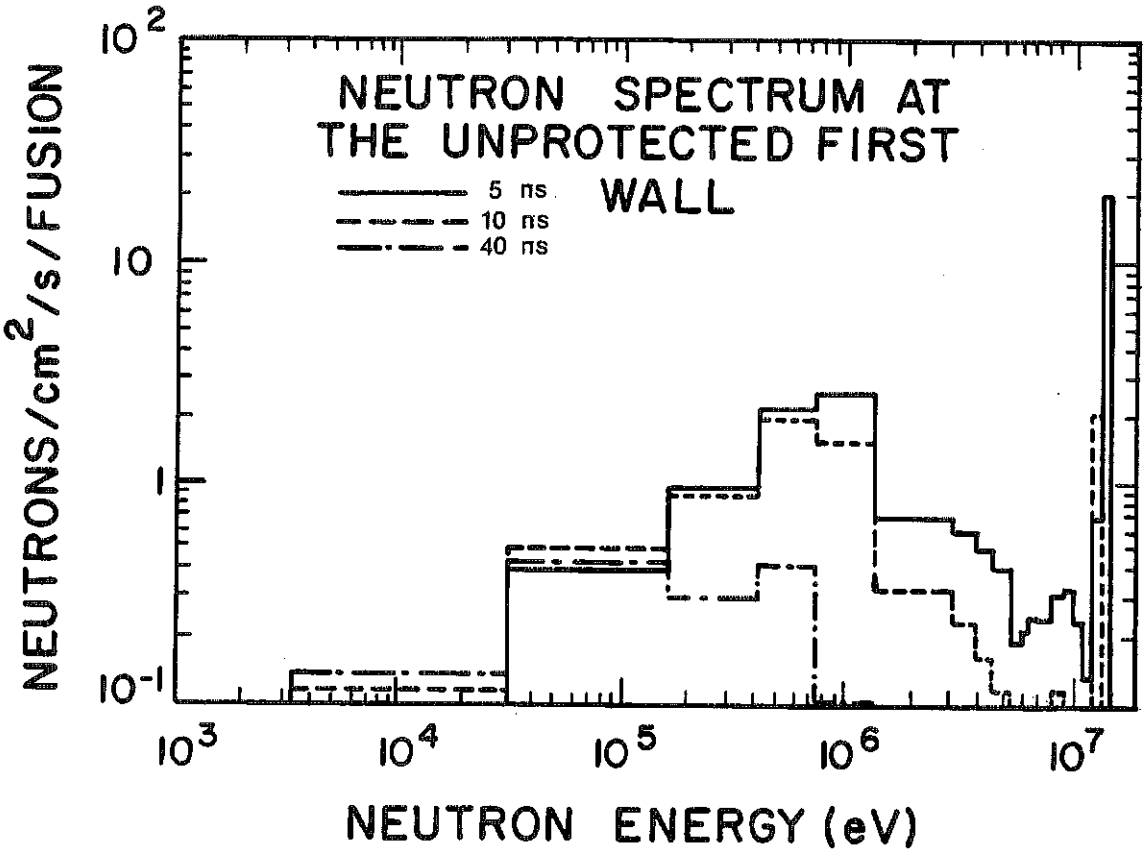

Figure VI.3-22 Neutron spectrum in the unprotected first wall. (The ordinate is the integral in each energy group.)

with a very small energy loss per collision resulting in much longer slowing down times. Therefore, the time spread of the spectrum in the first wall of our system is determined primarily by the slowing down time in the blanket.

On the other hand, the time of flight spread is the dominant factor in the case of the unprotected wall because of the absence of the "inner" slowing down region. The spectrum at 5 ns after the arrival of the leading edge of the neutron pulse consists mainly of first group neutrons coming directly from the source. The soft part of the spectrum shown in Fig. VI.3-22 is due to backward scattering of 14.1 MeV neutrons in the reflector region and neutron slowing down in the wall itself. As time elapses, lower energy source neutrons arrive at the first wall. The effect of neutron slowing down in the reflector is not as pronounced here as compared to the effect of neutron slowing down in the inner blanket for the case of protected wall. The reason is that the probability of backscattering of high energy neutrons is small compared to the probability of forward scattering. Therefore, the time-dependent damage rate in the unprotected wall is affected primarily by the time of flight spread.

VI.3.4.5 Atomic Displacement Rate

The instantaneous damage rates in the first wall have been calculated using the time dependent neutron spectrum in the wall and the appropriate reaction cross sections. The instantaneous dpa rate in the protected ferritic steel first wall is given in Fig. VI.3-23. The results correspond to a 400 MJ fusion yield. The cumulative dpa is illustrated in Fig. VI.3-24. It is clear that the damage occurs over a relatively long time resulting in a peak instantaneous dpa rate of 0.009 dpa/s at 140 ns after burn. This peak corresponds to the 14 MeV source neutrons arriving without collision. A broad peak at $\sim$ 270 ns corresponds to neutrons emitted in (n,2n) reactions with lead in the

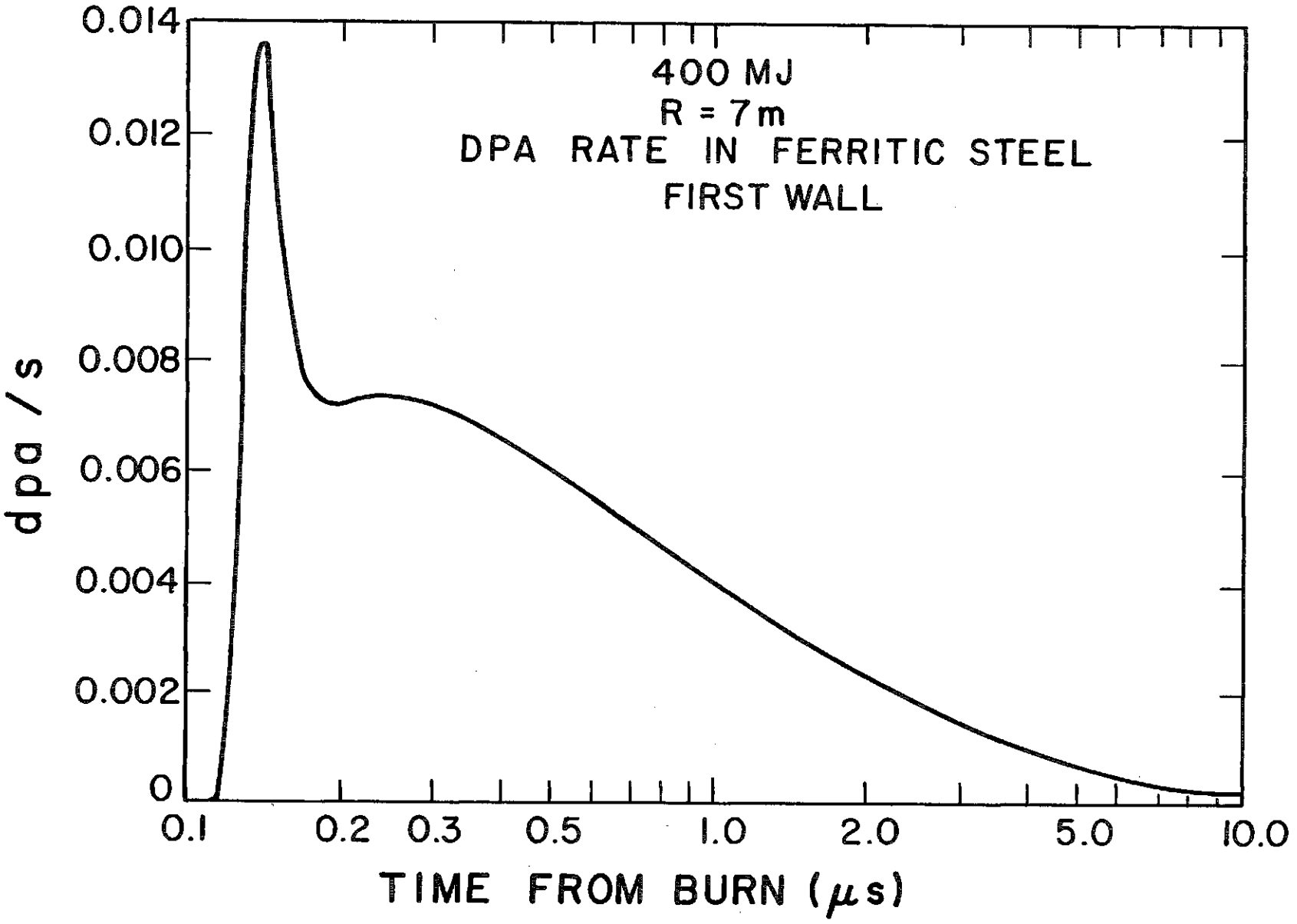

Figure VI.3-23 DPA rate in the protected first wall.

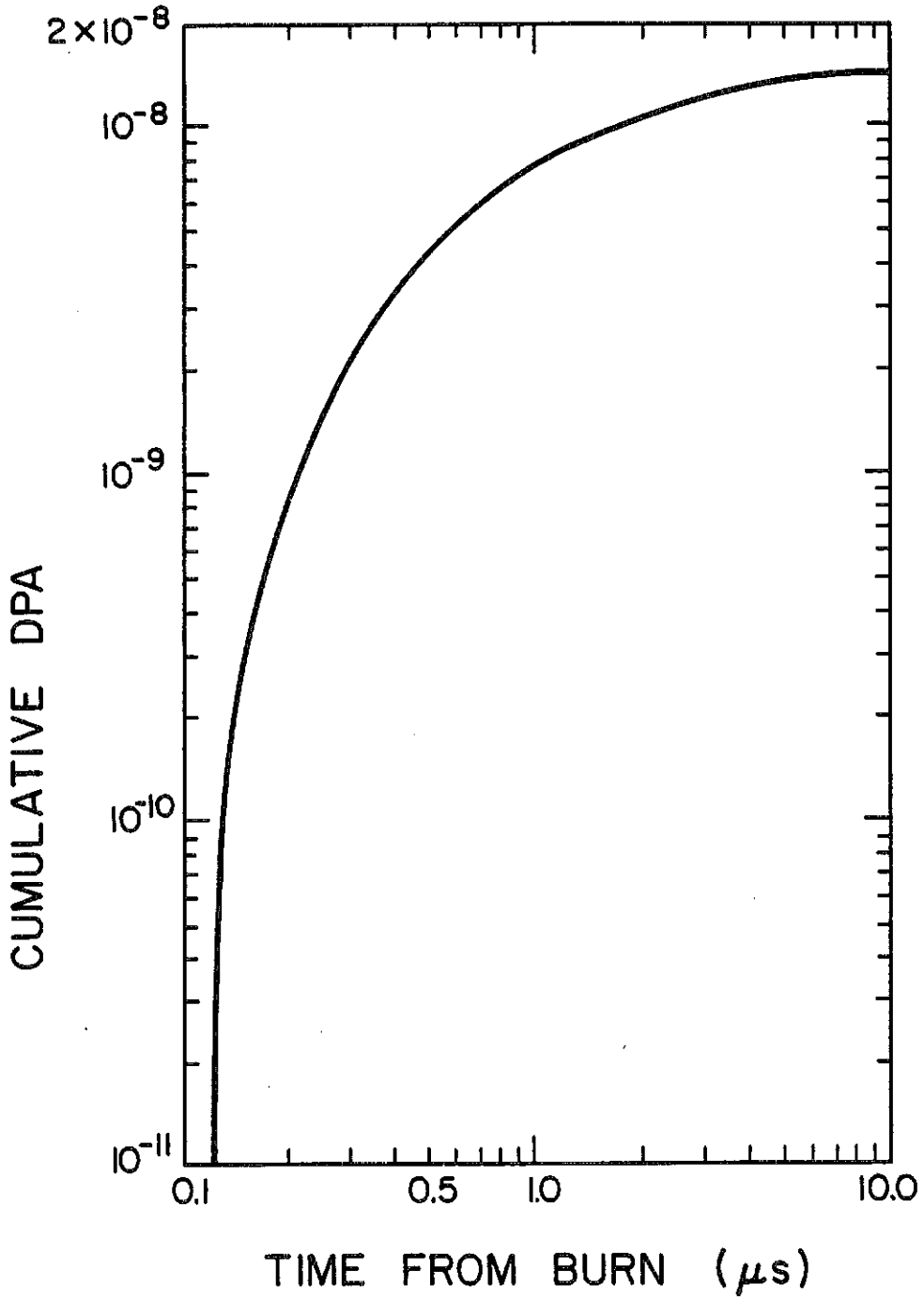

Figure VI.3-24 Cumulative DPA in the protected first wall.

INPORT tubes. This considerable time spread results from the relatively long slowing down time in the blanket allowing neutrons of energies greater than the dpa threshold energy of iron (~ 1 keV) to exist in the first wall over a long period of time.

The instantaneous dpa rate in an unprotected wall is shown in Fig. VI.3-25. The time spread is very small compared to the case of the protected wall. The time spread is determined here by the time of flight spread of neutrons as they travel from the source to the wall. The effect of the INPORT tube protection, used in HIBALL, on the atomic displacement in the first wall is given in Table VI.3-13. The total dpa per full power year (FPY) was determined using the steady state code ANISN with a repetition rate of 5 Hz.

The wall protection is found to decrease the total cumulative dpa and the peak instantaneous dpa rate by factors of 9.4 and 1190, respectively. The larger reduction in the peak instantaneous dpa rate results from time spread FWHM increasing from 5 to 980 ns. The reduction in dpa achieved here is much larger than that achieved in a 316 SS first wall protected by 0.5 m of liquid Li,[17] typical of the HYLIFE concept.[21] In this case the average rate was found to decrease by a factor of 3.6 and the peak instantaneous rate to decrease by a factor of 13. Larger reduction is obtained in our case because Pb is more effective than Li in slowing down high energy neutrons and C is more effective than Li in slowing down low energy neutrons. If we assume that the life of the wall will approach 10 Mw-y/m^2 (the target for the U.S. fusion materials program), and 1 MW-y/m^2 = 11 dpa, then only 4.9 MW-y/m^2 will be accumulated with the INPORT units and 46 MW-y/m^2 without them. This implies that the wall protection concept used in HIBALL will be very effective in reducing damage to the first wall, allowing it to last for the lifetime of the reactor (20 full power years).

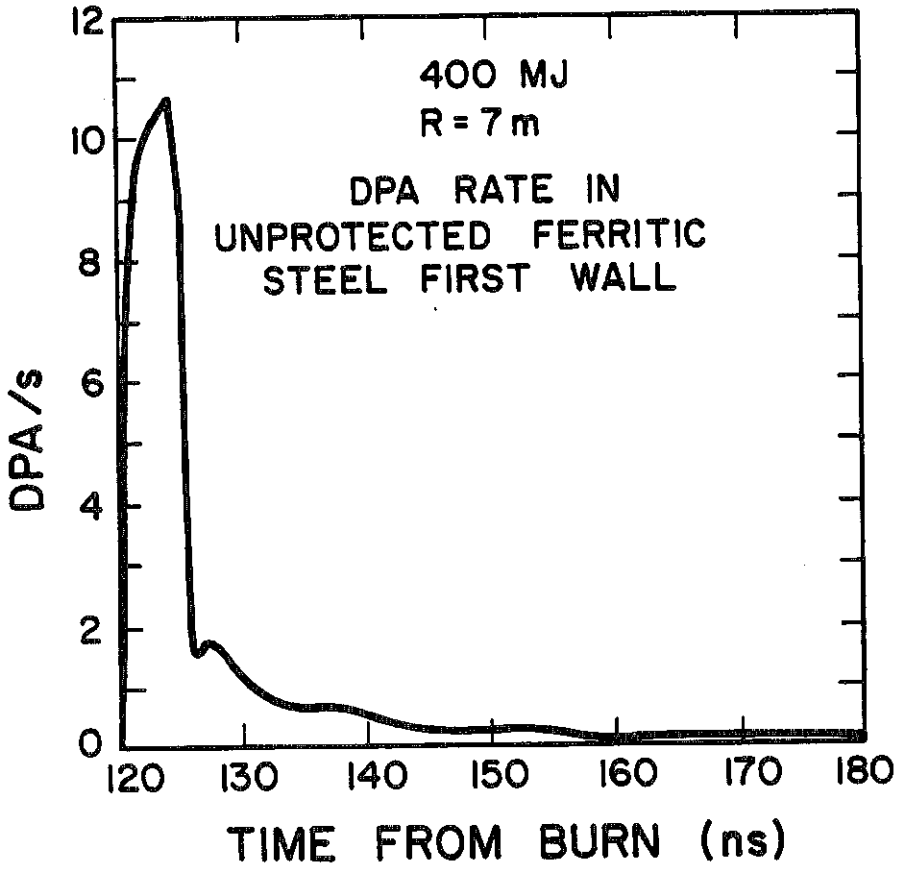

Figure VI.3-25 DPA rate in the unprotected first wall.

Table VI.3-13

Effect of First Wall Protection on Atomic Displacement

	Peak Instantaneous dpa rate (dpa/s)	Time Spread fwhm (ns)	Total dpa (dpa/FPY)
Protected Wall	0.009	980	2.7
Unprotected Wall	10.7	5	25.4

VI.3.4.6 Helium Production Rate

The instantaneous helium production rate in the protected ferritic steel first wall is given in Fig. VI.3-26. A peak instantaneous helium production rate of 0.11 appm/s occurs about 15 ns after the leading edge of the pulse arrives at the wall. The cumulative helium production is given in Fig. VI.3-27. It is clear that the time spread here is much smaller than that for the dpa. The reason is that the (n,α) reaction in iron has a threshold energy of $\sim$ 2.7 MeV and neutrons at energies greater than this energy exist in the first wall over a relatively short period. Only one peak occurs because the (n,2n) neutrons do not contribute to helium production. The instantaneous helium production rate in an unprotected wall is given in Fig. VI.3-28. Again the time spread in this case is determined primarily by the time of flight spread of source neutrons.

The effect of the INPORT first wall protection on the helium production is given in Table VI.3-14. The total helium production in a full power year is found to decrease by a factor of 630 while the peak instantaneous helium production rate is found to decrease by a larger factor of 1627. Since the helium production reaction is a high energy reaction, neutron slowing down in

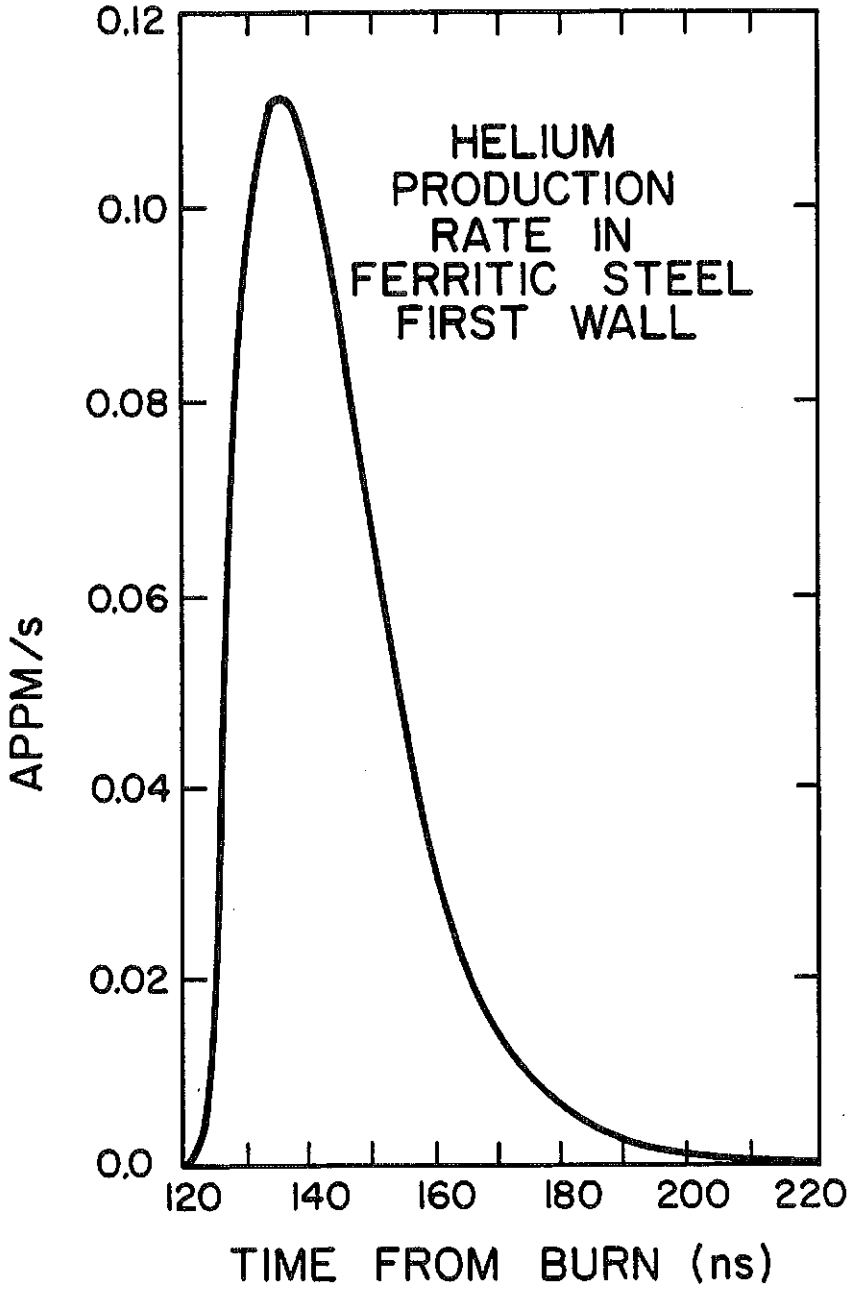

Figure VI.3-26 Helium production rate in the protected first wall.

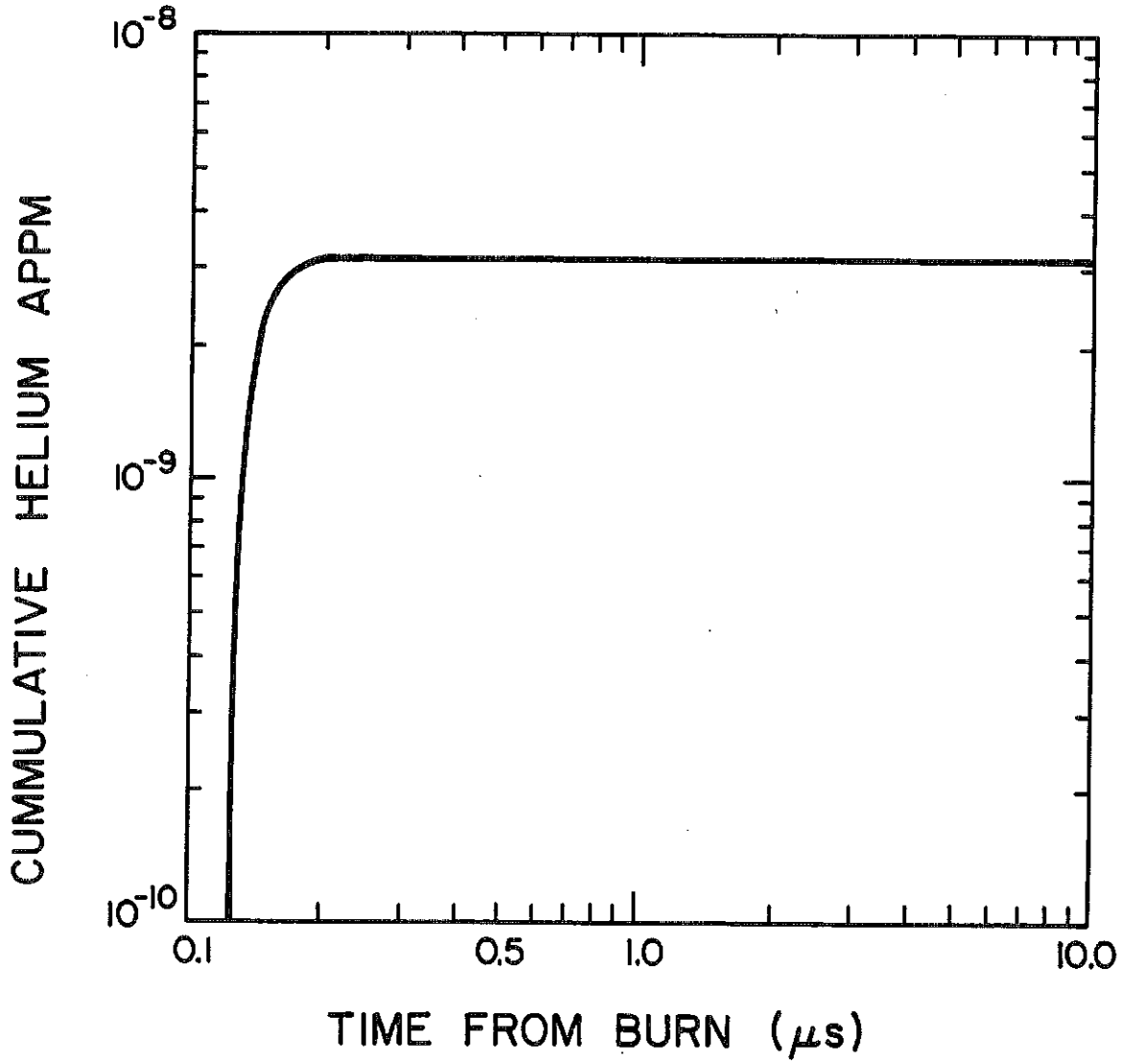

Figure VI.3-27 Cumulative helium production in the protected first wall.

VI.3-61

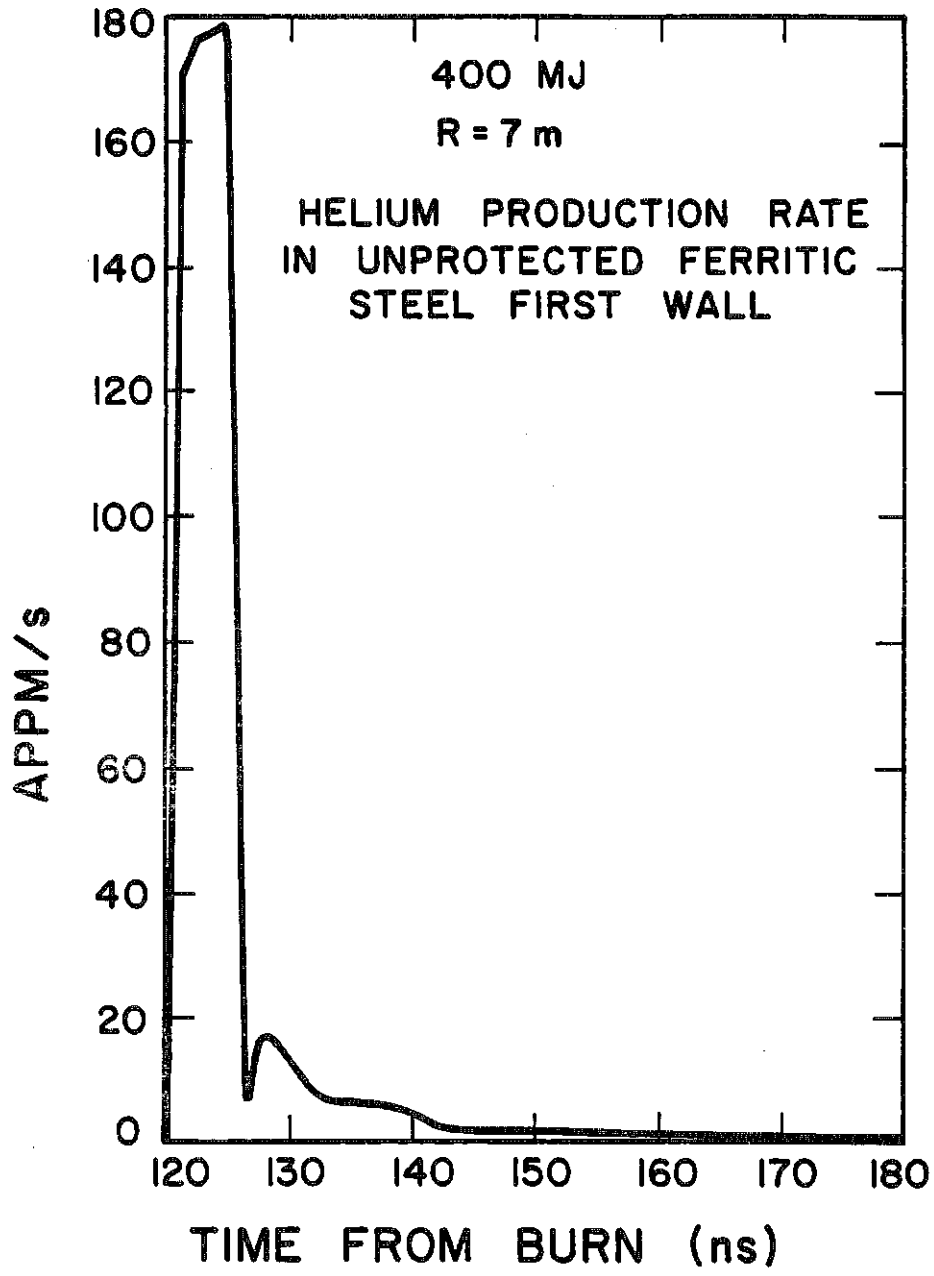

Figure VI.3-28 Helium production rate in the unprotected first wall.

Table VI.3-14

Effect of First Wall Protection on Helium Production

	Peak Instantaneous Helium Production Rate (appm/s)	Time Spread FWHM (ns)	Total Helium Production (appm/FPY)
Protected Wall	0.11	26	0.364
Unprotected Wall	179	5	737

the blanket is found to have a pronounced effect on helium production in the wall.

VI.3.4.7 Energy Deposition Rate

The time-dependent neutron and gamma fluxes are used together with the appropriate kerma factors for neutron and gamma energy deposition to calculate the energy deposition rate in the blanket and first wall. The results are given in Fig. VI.3-29 at the blanket first surface, the center of the blanket, and the first wall. The time distribution is very narrow at the first surface and broadens as one moves towards the first wall. While the time spread at the first surface is determined by the time of flight spread, the spread at the first wall is determined by the slowing down time in the inner blanket. For a 400 MJ fusion yield the peak instantaneous power densities in the blanket and the first wall are found to be 1.82×10^8 and 2.73×10^5 W/cm^3, respectively. This corresponds to peak to average temporal power density ratios of 8.48×10^6 and 1.65×10^5, respectively. The results in Fig. VI.3-30 give the instantaneous energy deposition rate in the unprotected first wall. The distribution is very narrow with a peak power density of 3.3×10^8

VI.3-63

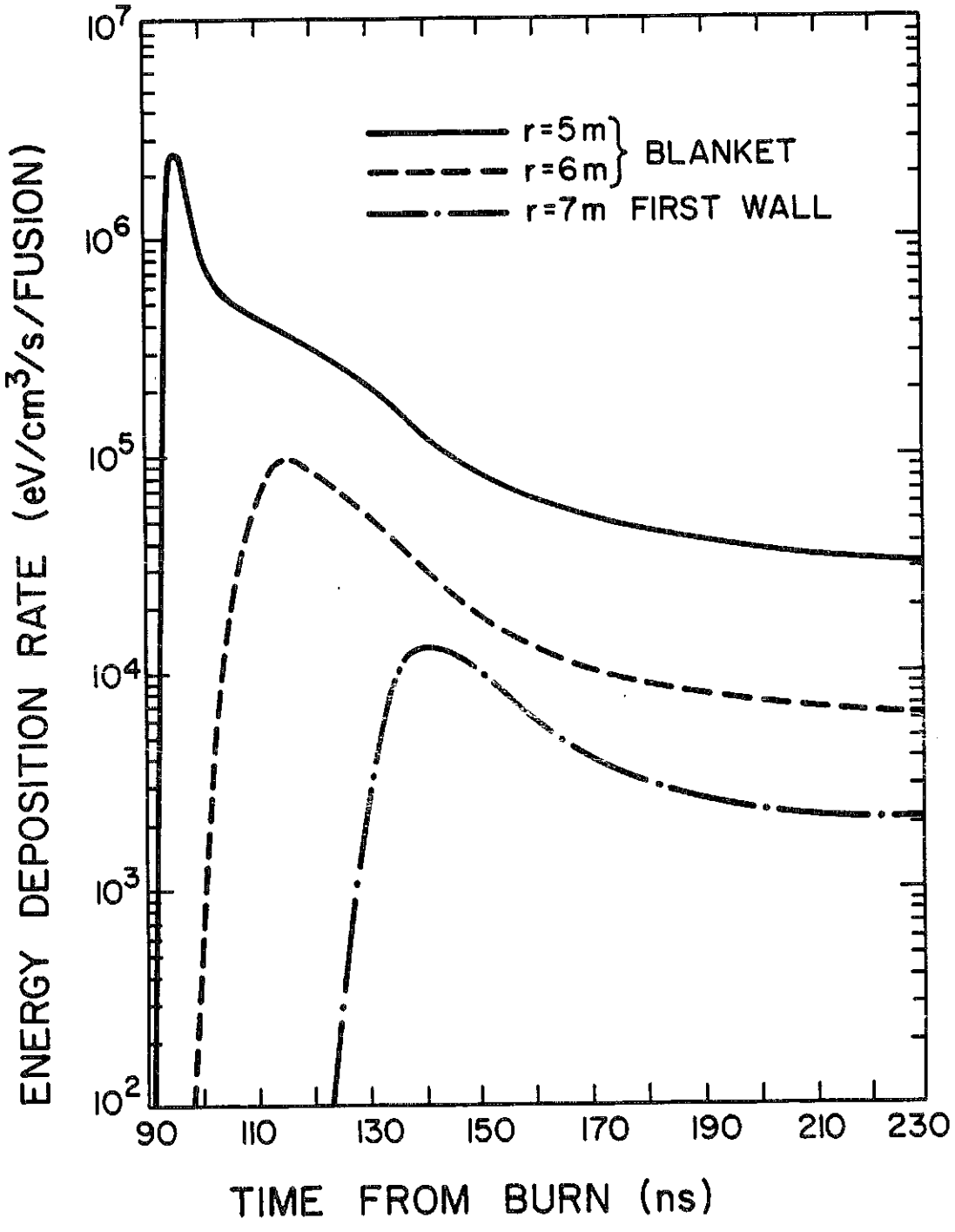

Figure VI.3-29 Energy deposition rate in HIBALL blanket and first wall.

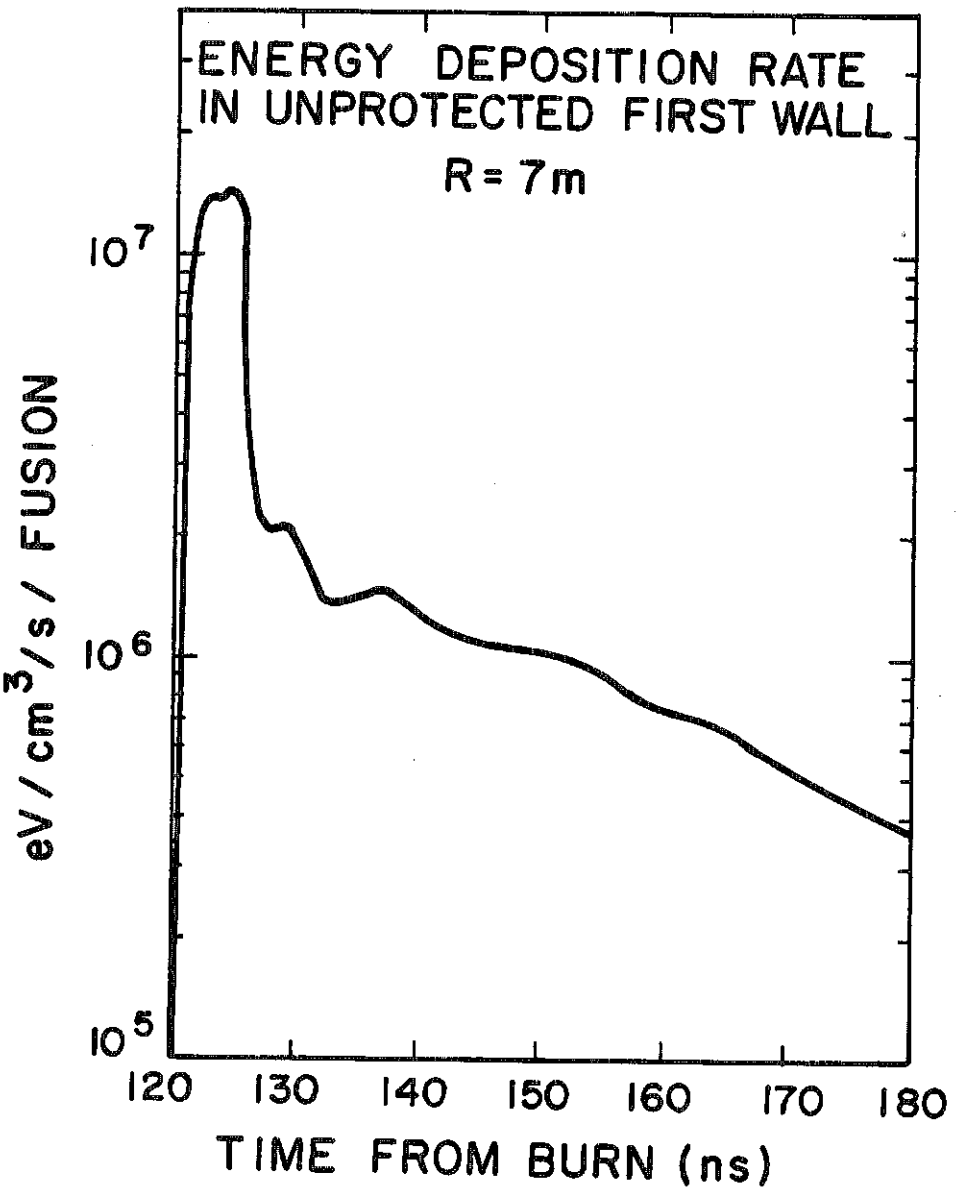

Figure VI.3-30 Energy deposition rate in the unprotected first wall.

W/cm^3 for a 400 MJ fusion yield. The peak to average temporal power density ratio in the wall is found to be 1.1×10^7. The INPORT concept is found to decrease the peak instantaneous power density in the wall by a factor of ~ 1210 and the total nuclear heating in the wall by a factor of ~ 18. These results are useful for stress analysis studies.

VI.3.4.8 Summary and Concluding Remarks

Time dependent neutronics analysis for the ferritic steel first wall of the HIBALL fusion reactor design has been performed. The analysis accounts for neutron interactions in the target resulting in neutron multiplication and significant spectrum softening. The time dependence of the neutron source is modified in such a way that the multigroup treatment adopted in the time dependent transport code predicts the correct time of flight spread of neutrons in each group as they travel from the source to the first surface of the blanket. A modified version of the time dependent discrete ordinates code TDA has been used.

Neutron slowing down in the INPORT first wall protection system is found to have a significant effect on the time dependent spectrum and damage in the first wall. The time over which the damage occurs is found to be determined primarily by the slowing down time in the blanket. In the case of an unprotected wall, where no slowing down occurs in front of the wall, the spread is determined primarily by the time of flight spread.

Using the INPORT first wall protection concept results in significant reductions in peak instantaneous and total dpa and helium production rates allowing the first wall to last for the reactor lifetime (~ 20 FPY). Our results also show that the peak power density in the first wall resulting from nuclear heating decreases considerably when the porous tube concept is used to protect the wall.

VI.3.5 Radioactivity and Afterheat

Radioactivity will be induced in the coolant and structure of the HIBALL reactor through activation by the fusion neutrons. To treat the problem exactly energy dependent neutron fluxes must be calculated for each point in the cavity. Since the ability to perform these calculations with reasonable cost and effort does not exist at this time a simplified approach was taken. Specifically the reactor was modeled in spherical geometry with materials and dimension consistent with a cut through the midplane of the reactor. The multigroup neutron flux used in the activation calculations was taken from the one-dimensional ANISN calculations described in section VI.3.1. For the purpose of the calculation the reactor was broken up into 37 intervals and the average flux in each interval was used. The size and compositions of the various regions is shown in Fig. VI.3-31. The DKR code[22] was used to calculate the radioactivity parameters -- activity, afterheat, and biological hazard potential (BHP).

The activities were calculated for an operating time of two years. Previous calculations on other fusion reactor designs show that the buildup of radioactivity is quite rapid, becoming significant after only a few hours of operation. By the end of two years all short-lived isotopes saturate and the buildup continues at a slower rate. Thus the activity at times after shutdown of much less than two years is relatively independent of operating time while the activity at times very much longer than two years after shutdown is approximately proportional to operating time.

The total activity per unit of thermal power for the cavity region, first material wall and reflector is shown in Fig. VI.3-32. The level at shutdown is 0.62 Ci/watt. this value is somewhat larger than might be expected considering that the bulk of the activity is due to the steel which is shielded

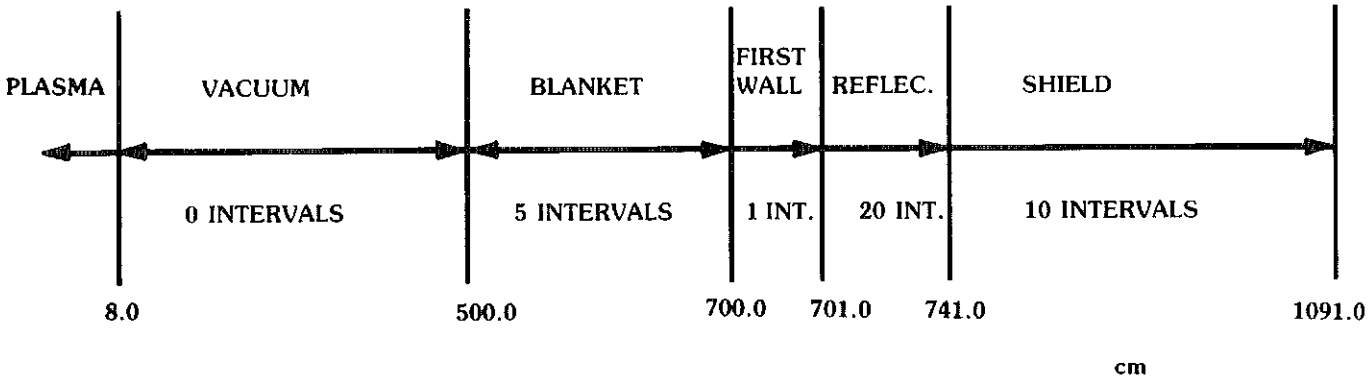

COMPOSITIONS

BLANKET	FIRST WALL	REFLECTOR	SHIELD
99.3 w/o $Li_{17}Pb_{83}$	100% HT-9	88 w/o HT-9	13 w/o Fe
0.7 w/o SiC		12 w/o $Li_{17}Pb_{83}$	28 w/o Si
			.5 w/o H
			44 w/o O
			7 w/o Ca
			4 w/o Al
			3.5 w/o Others

DENSITIES

LiPb: 9.4 g/cm^3
SiC: 3.17 g/cm^3
HT-9: 7.8 g/cm^3

Figure VI.3-31

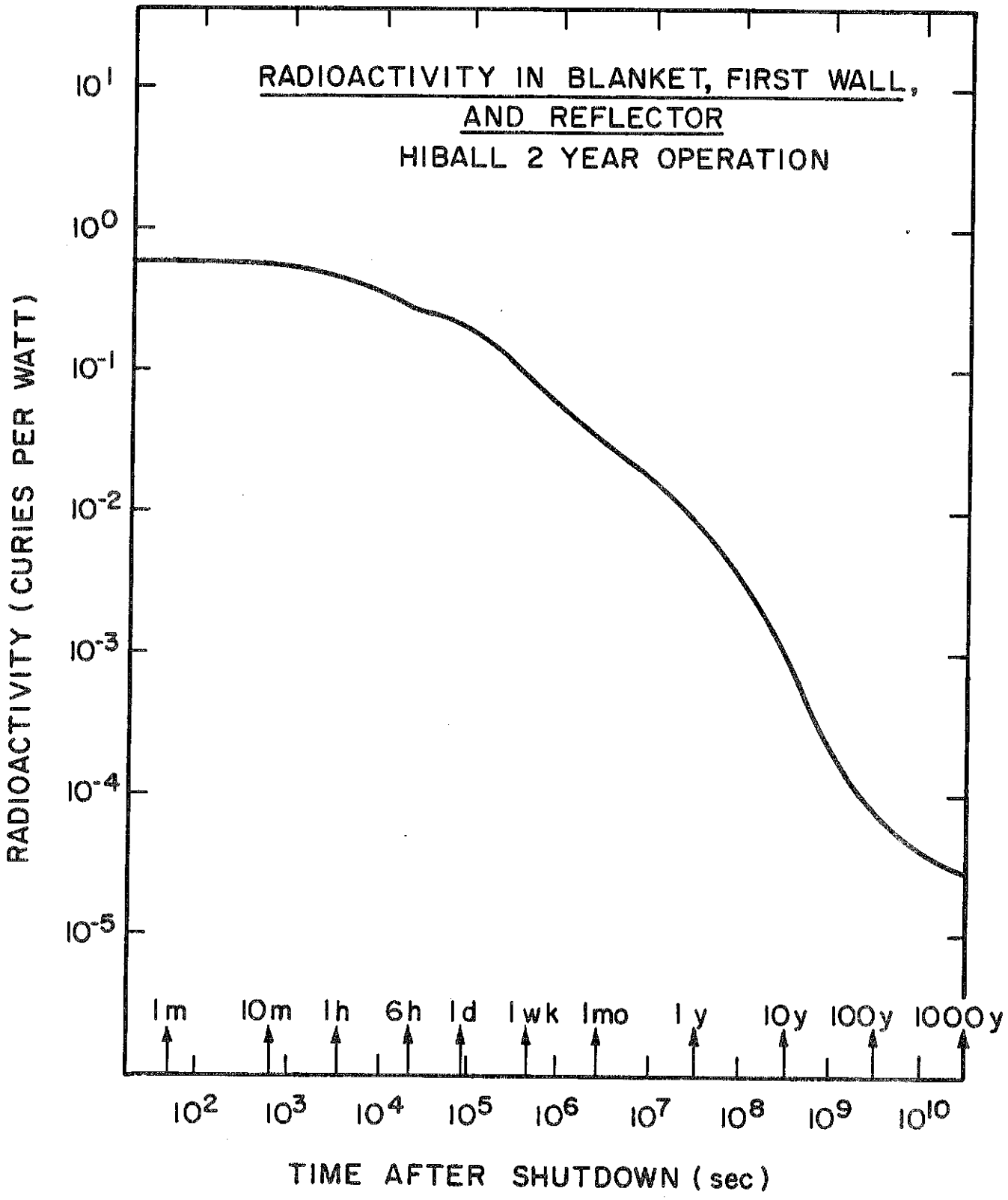

Figure VI.3-32

from the neutron source by the Pb-Li INPORT region. However, the neutron multiplying effects of the Pb in the INPORT region results in the flux in the reflector region remaining relatively high and this feature combined with the large amount of steel in the reflector produces the high activity level. As is typical with steel systems the activity falls off rather slowly with time after shutdown requiring approximately three weeks to be reduced by a factor of 10 and two years to be reduced by a factor of 100. The relative contributions of individual isotopes is shown in Fig. VI.3-33. The initial activity is dominated by the contributions of ^{56}Mn and ^{203}Pb. ^{56}Mn ($T_{1/2}$ = 2.58 hr) decays away first followed by ^{203}Pb ($T_{1/2}$ = 52 hr). Note that unless flow were maintained, the ^{203} Pb activity would not be present in the reactor itself but would be associated with the coolant storage facility. The next major decrease in activity is due to the decay of ^{51}Cr ($T_{1/2}$ = 27.7 days). It is followed by the decay of ^{55}Fe ($T_{1/2}$ = 2.7 yr) which produces the large activity drop between 1 and 100 years. The long term activity is due to ^{93}Mo and ^{93}Nb originating in the small amount of Mo in the steel (HT-9).

The afterheat is shown in Fig. VI.3-34. The value at shutdown is 0.66% of the operating power. For the same reasons as the radioactivity this value is somewhat higher than expected, but is consistent with the activity level. Since the decay energies of the various isotopes are different the afterheat curve has a shape which differs from that of the activity. It falls off much more rapidly, by a factor of 10 in about two days and a factor of 100 in two weeks. The relative contributions of the various isotopes are shown in Fig. VI.3-35. At shutdown ^{56}Mn is the dominating isotope. The decay of this isotope plus the relatively rapid decay of ^{203}Pb account for the order of magnitude drop in two days. ^{51}Cr, which contributes significantly to the activity in the one week to one month period, contributes very little to the afterheat,

FRACTION OF TOTAL RADIOACTIVITY FOR
THE MAJOR CONTRIBUTING ISOTOPES
HIBALL 2 YEAR OPERATION

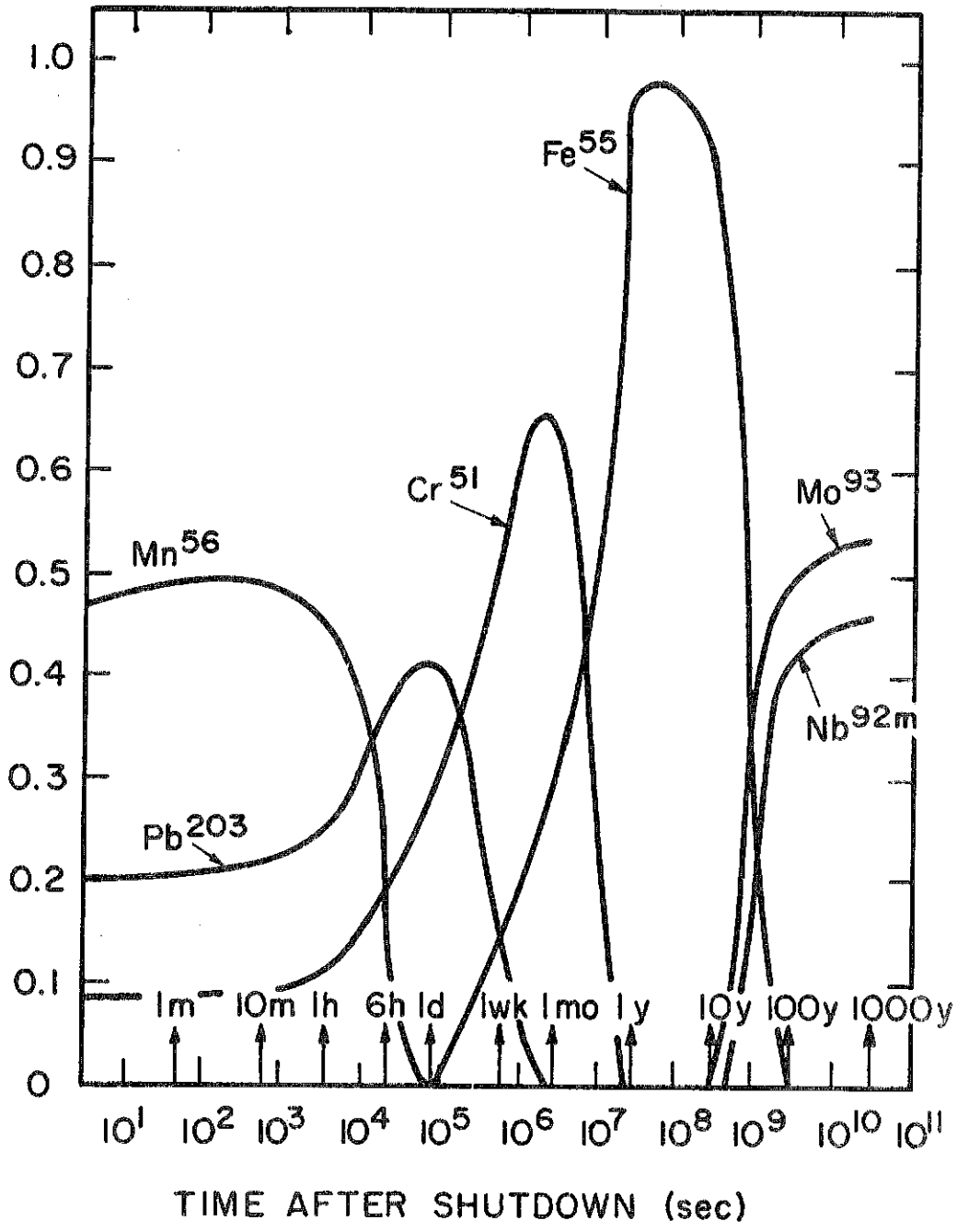

Figure VI.3-33

VI.3-71

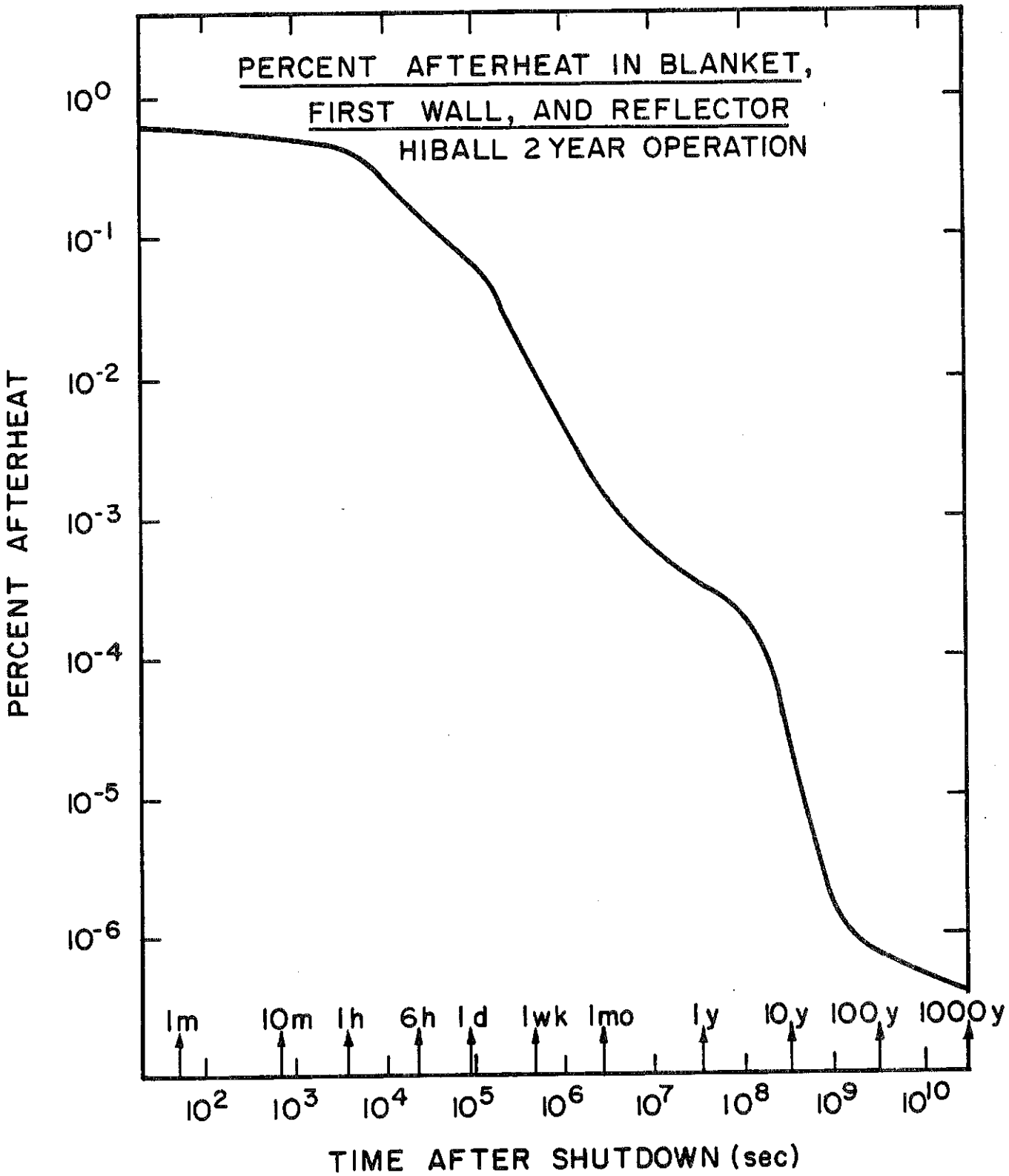

Figure VI.3-34

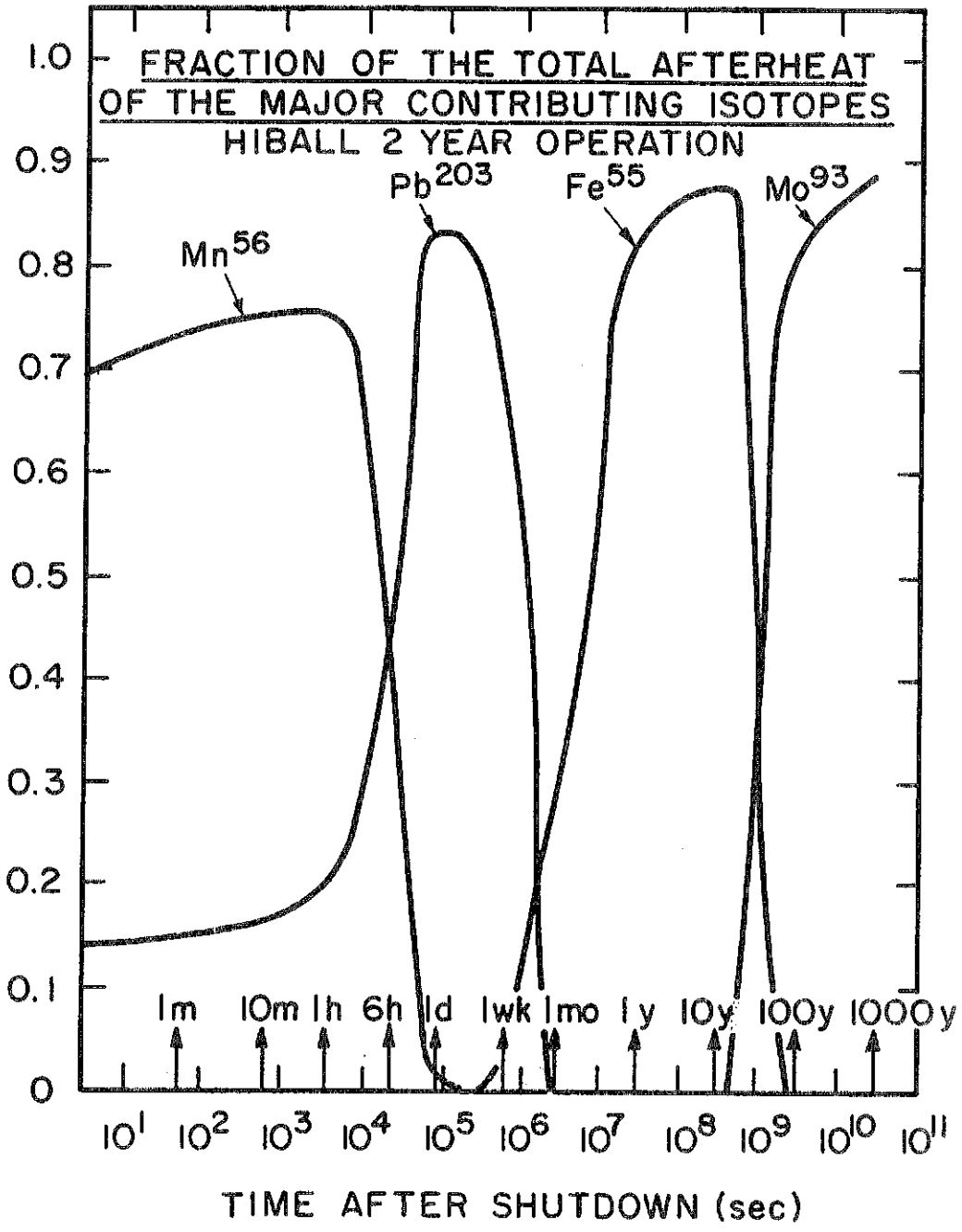

Figure VI.3-35

thus the afterheat in this period is governed primarily by the decay of ^{203}Pb. The decay energy of ^{55}Fe is also low as is the decay energy of the remaining isotopes which leads to the rather low residual afterheat subsequent to about 100 years.

The Biological Hazard Potential (BHP) is shown in Fig. VI.3-36. BHP is defined as the ratio of the activity present in the system per unit of power to the level of activity allowed per unit volume of air in the U.S. Nuclear Regulatory Commission Regulations (10 CFR 20). Thus it is a measure of the potential hazard of a radioactive material. The BHP of the coolant first wall and reflector is shown in Fig. VI.3-36. The units are cubic kilometers of air per kilowatt of thermal power. The shape of the curve is similar to the shape of the activity curve being 26.0 at shutdown and requiring almost one month to be down by a factor of ten and with a long term reduction of only three orders of magnitude.

The activity, afterheat and BHP of the shield are shown in Figs. VI.3-37, VI.3-38, and VI.3-39. The neutronics calculations for the shield were performed for a concrete with no reinforcing material. For the purpose of obtaining a better estimate of the radioactivity related parameters of the shield the fluxes from the above calculations were used with a concrete having reinforcing material and with composition typical of the sacrificial shield of a BWR.[23] It is this composition which was shown in Fig. VI.3-31. The activity in the shield is significantly lower than the activity in the reflector, but the value of 6.3×10^{-3} Ci/watt is still significant. The time behavior of the activity is dominated after the first day by the activity of ^{55}Fe which continues to be the major contributor until times greater than 100 years. The afterheat at shutdown is 7.7×10^{-2}% of the operating power which while relatively small, will still require some residual heat removal capacity.

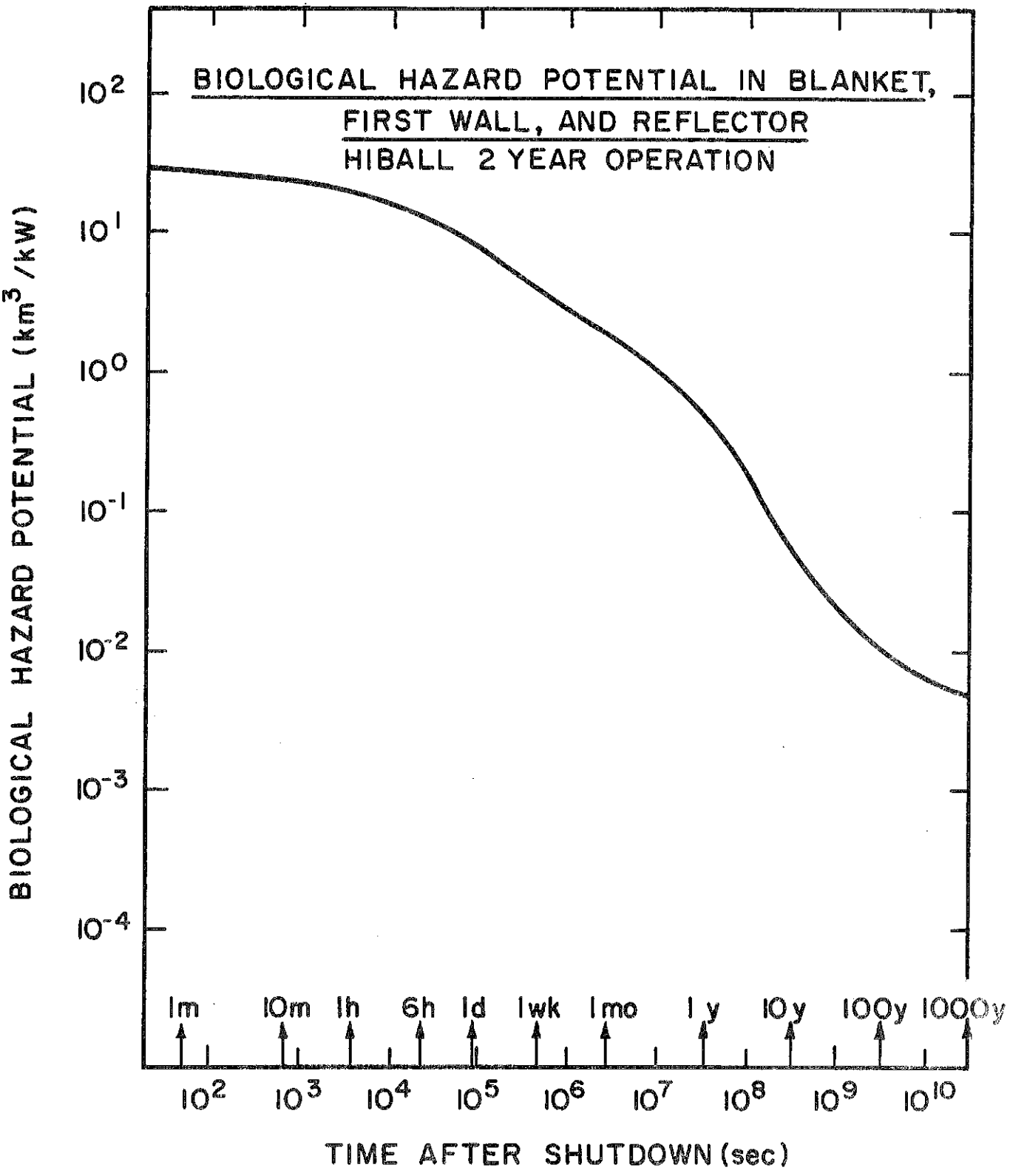

Figure VI.3-36

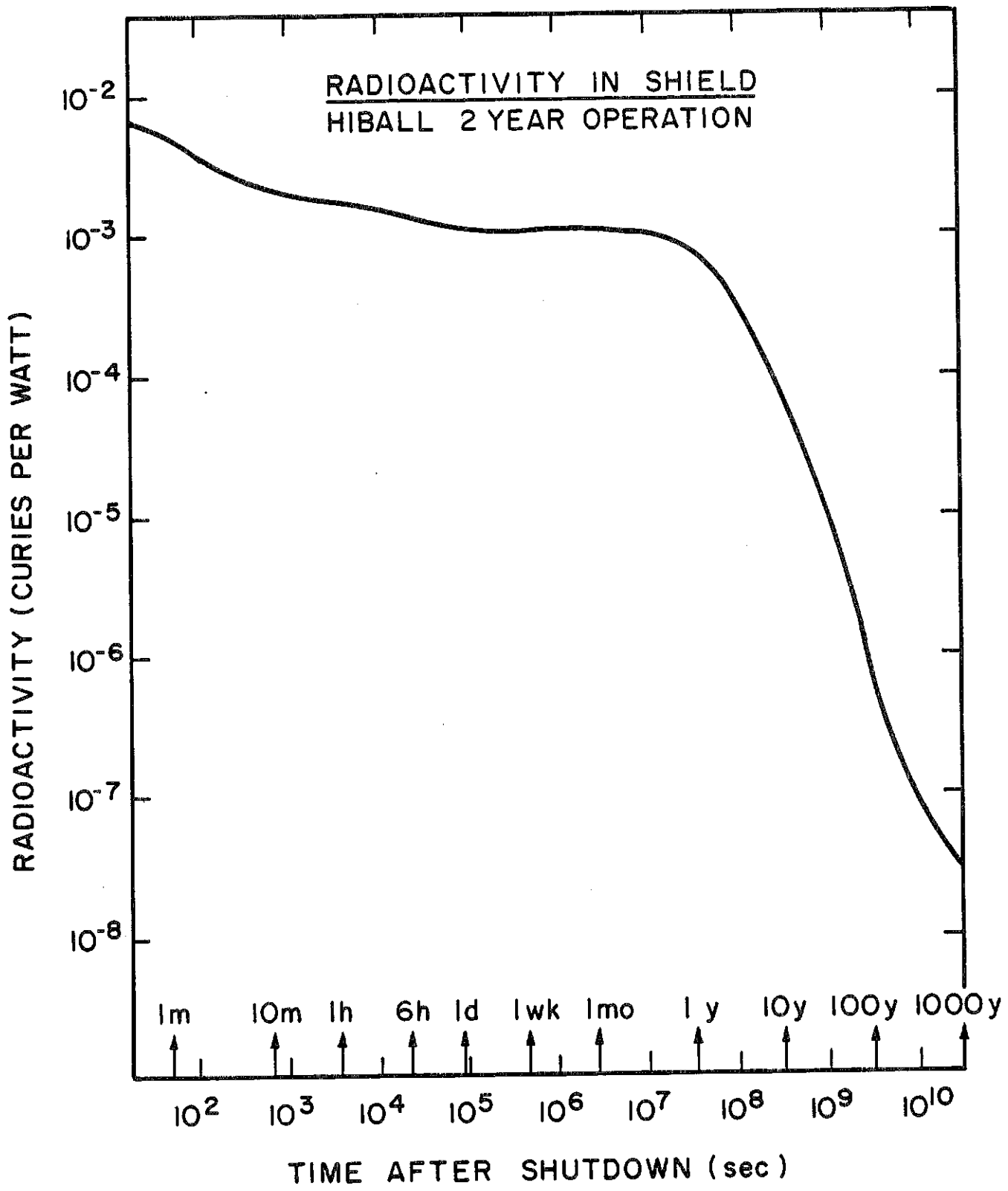

Figure VI.3-37

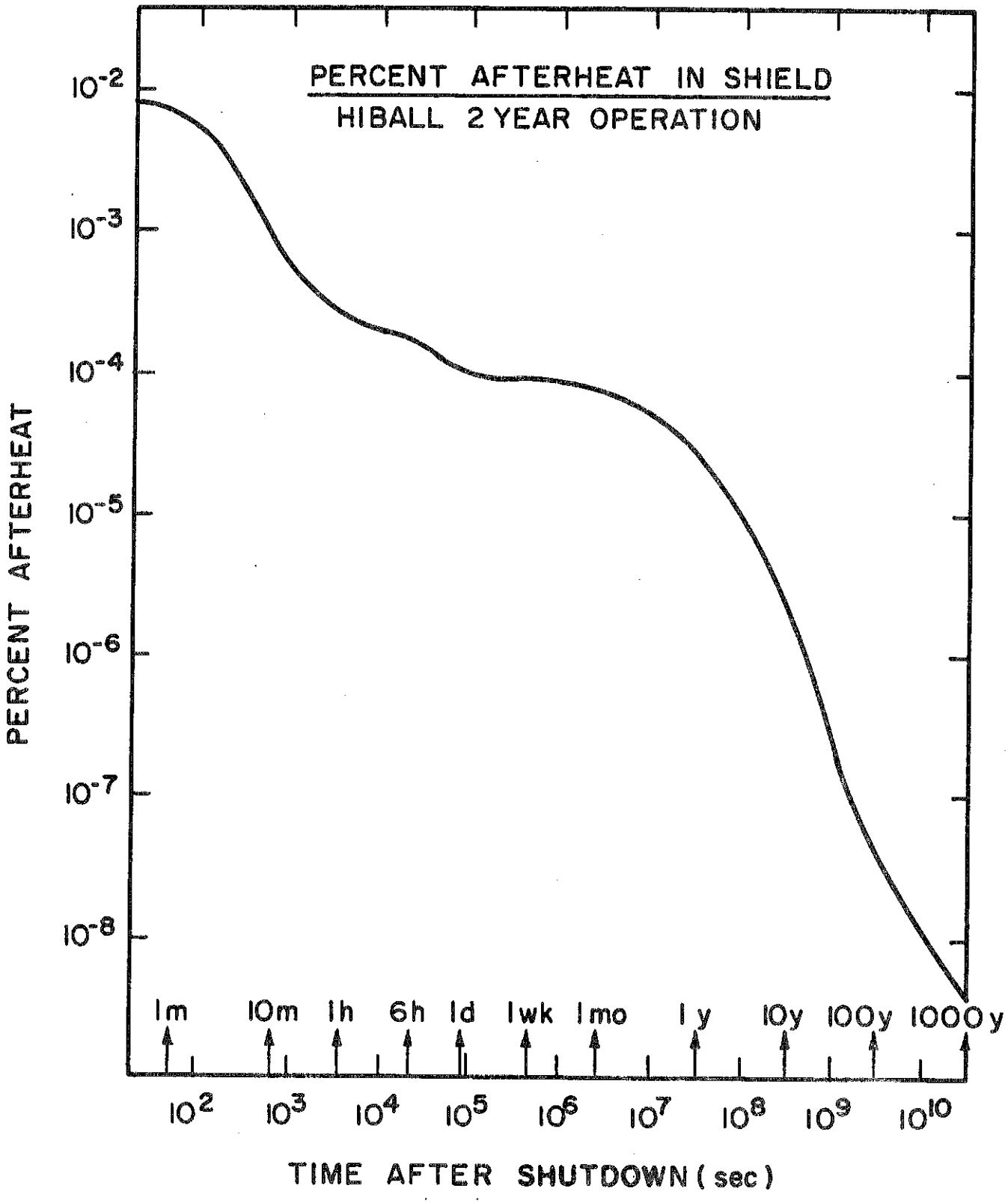

Figure VI.3-38

VI.3-77

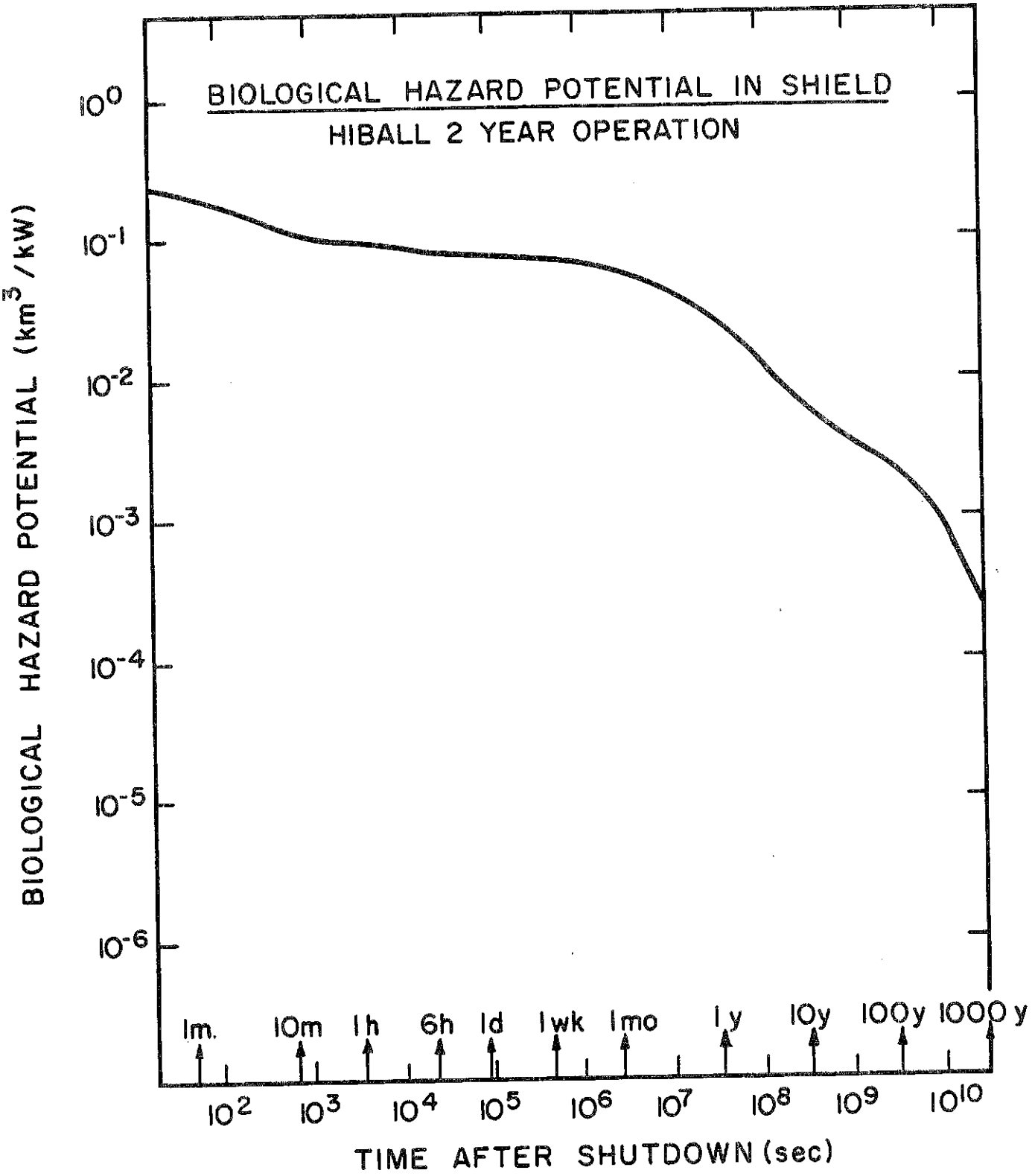

Figure VI.3-39

The afterheat drops off faster with time than does the activity primarily because of the low decay energy of ^{55}Fe. The BHP is also relatively low and falls off slowly, again because of the hazard characteristics of nuclei involved. To get a somewhat different appreciation of the magnitude of the activities in the shield the above values at shutdown correspond to an average activity of 3.4×10^{-3} Ci/cm^3, an afterheat of 4.1×10^{-5} W/cm^3, and a BHP of 6.7×10^{-11} km^3/cm^3.

The calculated neutron and gamma doses outside the shield have been presented in section VI.3.2. An additional component is the dose due to activation products. This component is present during operation and shutdown periods. To calculate this dose the activities calculated above have been used along with a one-dimensional gamma transport program. The results of this calculation indicated that the dose outside the shield from activation of the reflector and materials in the shield is quite low, 4.7×10^{-5} mrem/hr at shutdown.

These low values plus the consideration that the neutronics and prompt gamma calculations were done with no high Z materials in the shield, reinforce the idea that the shield is somewhat overdesigned and that a more realistic choice of shield composition would lead to a thinner shield using less materials while still showing acceptable dose levels outside the chamber.

These calculations must be used with a certain amount of care. First the geometric modeling of the system is very simple. It would have been much more satisfactory to have three-dimensional fluxes for the actual geometry. Furthermore no account has been taken of some of the special features of the system. For example, activation and shielding of the vacuum system has been ignored. The activation of the tube support structure in the INPORT region has been omitted. Also no calculations have been performed to get activities in the

beam transport system. The omission of these details do not invalidate the calculations presented but do require that they be used with care.

The calculations are also only as good as the cross section data used in them. While the data set used in DKR[24] was compiled with care using the best available data either experimental or calculational, it is likely that some reactions have been omitted. For example it is known that if lead is exposed to a neutron flux, an isomeric state at 0.91 MeV in ^{204}Pb is excited ($T_{1/2}$ = 66.9 min). However, the cross section for this reaction is not known and therefore has not been included.

As a final point the effect of impurities has not been accounted for in the LiPb. Bismuth, for example, is a common impurity in commercial lead. The reaction $^{209}Bi + n \rightarrow {}^{210}Bi \xrightarrow{\beta^-} {}^{210}Po$ is then possible and of concern because ^{210}Po is alpha emitting and volatile. This problem was considered in the NUWMAK[25] study. A Bismuth concentration of 42 appm was used as a basis for the calculation. This value was taken from the assay of a relatively high purity lead purchased for a slowing down time spectrometer. Assuming Bismuth has an 1/v absorption cross section the ^{210}Po content was calculated to be 0.26 Ci/tonne of Pb. There is approximately 2300 tonnes of Pb/cavity in HIBALL. If the previous ratios were correct the corresponding amount of ^{210}Po would be ~ 600 Ci. This amount of activity, while significant, is very much less than the activity of the rest of the material in the system (and) should present no special problem. Also, since the half-life of ^{210}Po is short (138.4 days) it presents no long term storage problem.

References for Section VI.3

1. RSIC Code Package CCC-254, "ANISN-ORNL," Radiation Shielding Information Center, ORNL.

2. T.R. Hill, "ONETRAN: A Discrete Ordinates Finite Element Code for the Solution of the One-Dimensional Multigroup Transport Equation," LA-5990-MS, Los Alamos Scientific Laboratory (1975).

3. RSIC Data Library Collection, "VITAMIN-C, 171 Neutron, 36 Gamma-Ray Group Cross Sections Library in AMPX Interface Format for Fusion Neutronics Studies," DLC-41, ORNL.

4. RSIC Data Library Collection, "MACKLIB-IV, 171 Neutron, 36 Gamma-Ray Group Kerma Factor Library," DLC-60, ORNL.

5. D. Garber (Comp.), ENDF/B Summary Documentation BNL 17541 (ENDF 201) Brookhaven National Laboratory, Upton, NY (Oct. 1975).

6. B. Goel, B. Krieg, "Status of the Nuclear Data Library KEDAK-3," KfK 2386/I, Kernforschungszentrum Karlsruhe, July 1979.

7. R. Herzing, L. Kuijpers, P. Cloth, D. Filges, R. Hecker, and N. Kirch, Nucl. Science and Eng., 60, 169 (1976).

8. H. Bachmann, U. Fritscher, F.W. Kappler, D. Rusch, H. Werle, and H.W. Wiese, Nucl. Science and Eng., 67, 74 (1978).

9. A. Hemmendinger, E.E. Ragan, E.R. Shunk, A.N. Ellis, J.M. Anaya, and J.M. Wallace, Nucl. Science and Eng., 70, 274 (1979).

10. W.A. Reupke and D.W. Muir, Trans. Am. Nucl. Soc., 23, 21 (1976).

11. G.M. Hale, Proc. Internat. Specialists Symposium on Neutron Standard and Applications, Gaithersburg (1977).

12. D.K. Trubey and M.B. Emmett, "Some Calculations of the Fast-Neutron Distribution in Ordinary Concrete from Point and Plane Isotropic Fission Sources," ORNL-RSIC-4, Oak Ridge National Laboratory (1965).

13. RSIC Code Package CCC-203, "MORSE-CG," Radiation Shielding Information Center, ORNL.

14. N. Packen et al., J. Nucl. Mater., 78, 143 (1978).

15. N.M. Ghoniem and G.L. Kulcinski, Nucl. Engr. Design, 52, 111 (1979).

16. F. Beranek and R.W. Conn, "Neutron Moderation in ICF Pellets and Effects on Damage and Radioactive Inventory," University of Wisconsin Fusion Design Memo UWFDM-310, (May 1979).

17. M.M. Ragheb and G.L. Kulcinski, Trans. Am. Nucl. Soc., 34, 644 (1980).

18. RSIC Code Package CCC-180, "TDA," Radiation Shielding Information Center, ORNL.

19. G.E. Bosler and T.G. Frank, Trans. Am. Nucl. Soc., 21, 16 (1975).

20. M. Sawan and G. Moses, "The TDA and TIMEX Codes for Time-Dependent Neutronics and Photonics Analysis of ICF Reactors," University of Wisconsin Fusion Design Memo UWFDM-399, (January 1981).

21. M. Monsler et al., "Electric Power from Laser Fusion: The HYLIFE Concept," proc. IECEC Conf., San Diego, CA, August 1978.

22. T.Y. Sung and W.F. Vogelsang, "DKR: A Radioactivity Calculation Code for Fusion Reactors," University of Wisconsin Fusion Design Memo UWFDM-170, (Sept. 1976).

23. H.D. Oak, G.M. Holter, W.G. Kennedy, Jr., and G.J. Konzek, Technology, Safety and Costs of Decommissioning a Reference Boiling Water Reactor Power Station, NUREG/CR-0672, Appendix E. Prepared by Pacific Northwest Laboratories for the U.S. Nuclear Regulatory Commission, June 1980.

24. T.Y. Sung and W.F. Vogelsang, "Decay Chain Data Library for Radioactivity Calculations," UWFDM-171 (September 1976).

25. B. Badger et al., "NUWMAK, A Tokamak Reactor Design Study," University of Wisconsin Fusion Design Memo UWFDM-330, (March 1979).

VI.4 Behavior of Pb-Li Vapor

A unique engineering problem for ICF reactors is the design of a first surface which can carry away the steady-state average surface heat and at the same time survive the transient temperature increase generated by X-ray and ion debris from the target explosion. In HIBALL, the INPORT tubes serve this purpose. The INPORT tubes, filled with flowing $Pb_{83}Li_{17}$ coolant, protect the first structural wall from excessive neutron damage. The SiC tubes themselves are protected from the short range X-ray and ion debris by a thin layer of PbLi that flows down the outside of the porous tube.

After a target explosion, the X-ray energy is deposited within 10^{-3} cm of the first surface. The temperature of a thin layer of $Li_{17}Pb_{83}$ exceeds its boiling temperature, and is vaporized. This ablated material flows toward the center of the cavity and intercepts the ions generated by the explosion. The energy associated with the ions is absorbed by the $Li_{17}Pb_{83}$ gas and does not directly impinge on the first surface. The gas heats up to a very high temperature and starts to release its energy by thermal radiation toward the cool first surface. The liquid surface temperature increases upon receiving energy from this thermal radiation and condensation of the vapor. The higher surface temperature increases the vapor pressure and consequently increases the vaporization rate. The cavity pressure is very high after the initial X-ray deposition, and varies by the combined effects of evaporation and condensation. It is of critical importance to beam transport and, to a lesser degree, vacuum pumping to calculate the pressure history after an explosion. One important factor determining repetition rate is that the vacuum condition in the cavity be low enough to allow beam transport.

In this section, the behavior of the Pb-Li vapor is discussed. In section VI.4.1 the deposition of target generated X-rays and the subsequent

vaporization of the Pb-Li is described. Section VI.4.2 deals with the stopping of target generated ions in the vapor, the flow of Pb-Li into the reactor chamber and the radiation of photon energy from the vapor back onto the tubes. Section VI.4.3 contains a description of the vaporization and condensation of the Pb-Li vapor. The pressure history of the cavity is thus established. Different X-ray spectrums result in different masses of evaporated material and this is also investigated.

VI.4.1 X-ray Energy Deposition and the Resulting Evaporation

Target generated X-rays will deposit their energy over a short range in Pb-Li and will heat this thin layer to high temperatures. The X-ray deposition and the energy densities of the Pb-Li after deposition are computed. This leads to a simple heat balance method of calculating the mass of vaporized Pb-Li.

The energy deposition from X-rays can be described by exponential attenuation inside the material. The photo-electric cross sections are those given by Biggs.(1) Determination of the energy deposited from a given spectrum must also account for transport of any scattered photons. If, however, the primary interaction is the photo-electric effect, the scattering can be ignored and an exponential deposition profile can be assumed. The photo-electric effect comprises 90% of the interactions for photon energies up to 10 keV, 30 keV and 70 keV for carbon, iron and molybdenum, respectively.(2) Since lead is of yet higher Z, the photo-electric effect is dominant to even higher photon energy.

The volumetric energy deposition for a monoenergetic spectrum can be represented by

$$q_\nu = \mu_\nu F_{o\nu} e^{-\mu_\nu x}$$

where q_ν = energy/unit volume/unit frequency

$F_{o\nu}$ = incident intensity, energy/unit area/unit frequency

μ_ν = absorption cross section at energy $h\nu$.

The total energy deposited per unit volume is obtained by integration over the X-ray spectrum.

Figure VI.4-1 shows the X-ray energy spectrum obtained from the target calculations[3] discussed in section III.1. The spectrum is peaked around 3 keV and extends up to 300 keV. Since most of the photons have energies well below 100 keV, we have used the Biggs data.

Figure VI.4-2 shows the volumetric energy deposition in Pb using the spectrum given in Fig. VI.4-1. The A*THERMAL[4] code was used in this calculation. Note that 88 MJ or 22% of the target yield is in the form of X-rays.

The amount of mass vaporized due to the X-ray energy deposition is computed using a simple model. We calculate the total energy per unit volume required to vaporize the lead, 8.7×10^3 J/cm^3. From the X-ray energy deposition calculation the depth of the material that will be vaporized can be determined. This adiabatic model becomes more accurate for very short X-ray deposition times, i.e. instantaneous.

We simply balance heat in the following manner.

$$\text{Heat of vaporization of lead} = 8.7 \times 10^5 \text{ J/kg} \simeq 8.7 \times 10^3 \text{ J/cm}^3$$

$$C_p(T_b - T_o) = C_p\ (1750°C - 400°C) \simeq 1944 \text{ J/cm}^3$$

$$\text{Total (J/cm}^3\text{) for vaporization} = 1.06 \times 10^4 \text{ J/cm}^3.$$

From the X-ray energy deposition curve (Fig. VI.4-2) this corresponds to a thickness of approximately 2.5 microns. To account for energy deposition above $C_p(T_b - T_o)$ in the region between the saturated liquid and the sensible

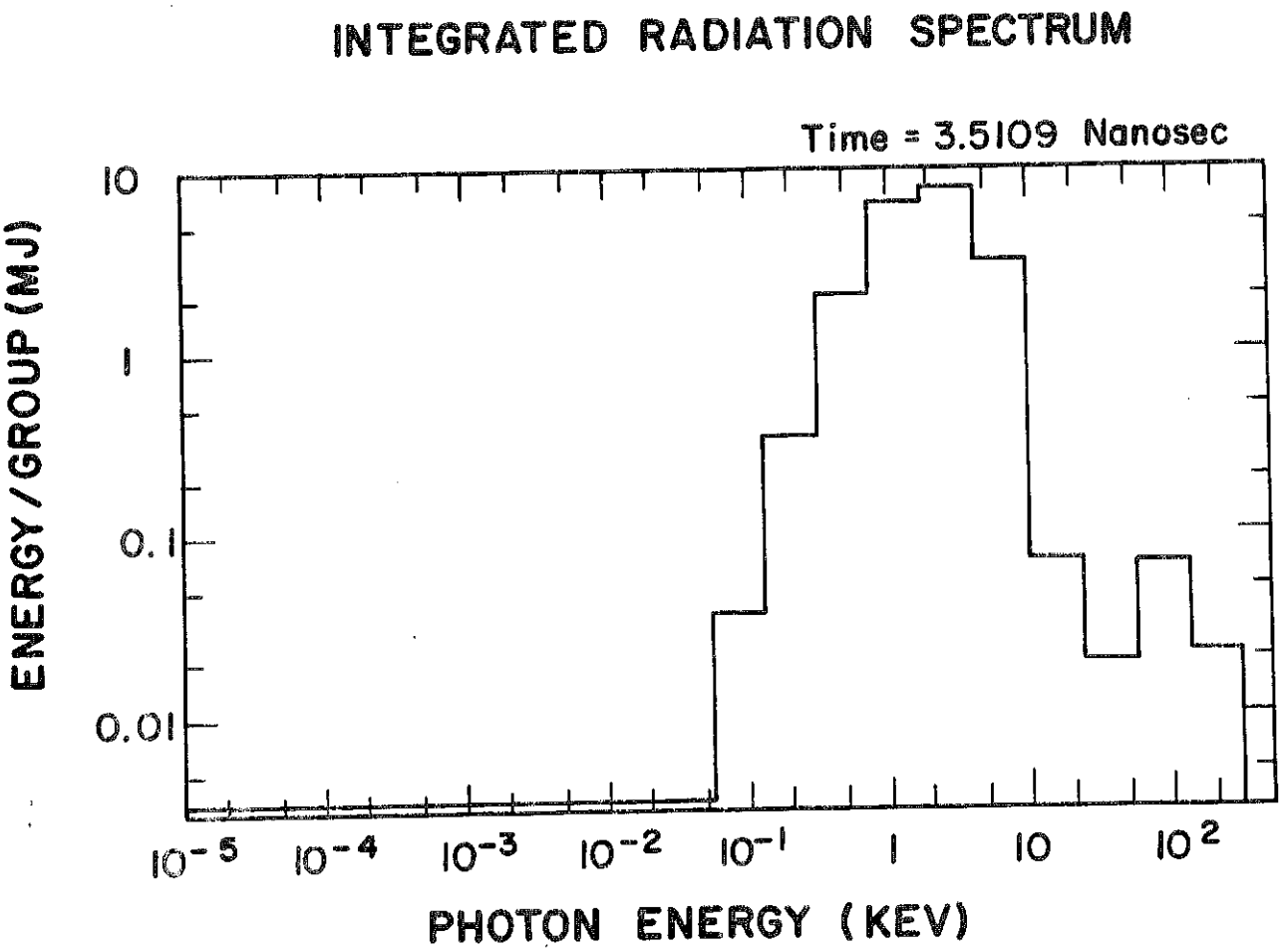

Fig. VI.4-1 X-Ray energy spectrum resulting from pellet burn.

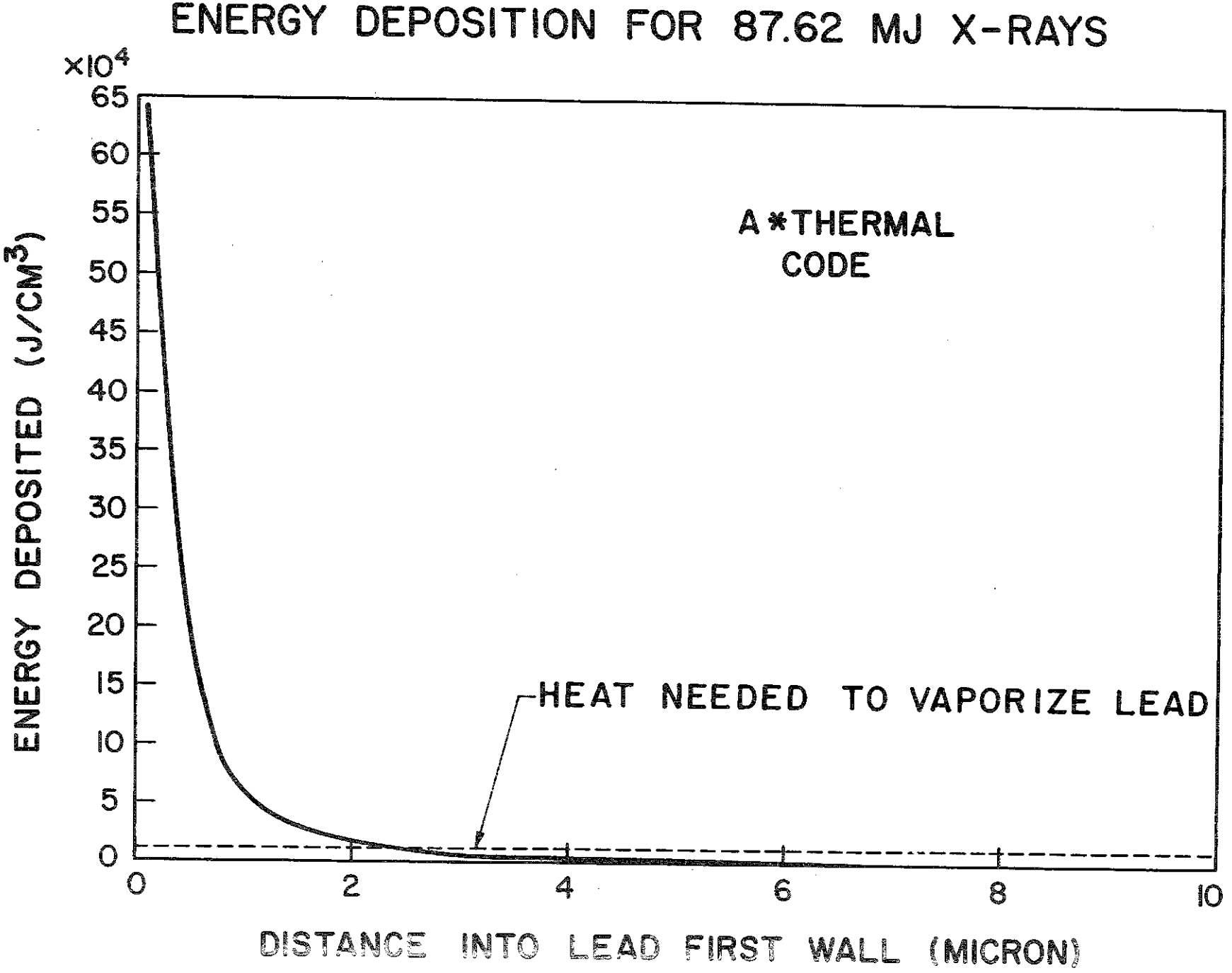

Fig. VI.4-2. X-Ray volumetric energy deposition in liquid lead.

heat, we have assumed that there is some additional vaporization. This additional vaporization accounts for the additional energy deposition above $C_p(T_b - T_o)$ as is shown schematically in Fig. VI.4-3. This gives an additional thickness of the vaporized layer of about 1.8 microns. Therefore the total thickness of material vaporized ≃ 4.3 microns.

We now can calculate the mass of vaporized Pb-Li,

$$M_o \cong \rho 4\pi R^2 \delta$$

where ρ = density of lead

R = radius of the cavity

δ = thickness of material vaporized

Substituting, we get $M_o \simeq 13$ kg/shot.

These calculations were repeated using cylindrical geometry and the results did not differ by very much. This is because the geometry is almost a square cylinder.

An example of how the X-ray spectrum affects the mass of material vaporized is shown in Fig. VI.4-4. Three different blackbody spectrums were used. In this example, the total energy contained in X-rays is 33.6 MJ. The softer spectrum of 0.5 keV has a very short range. The harder the spectrum, the more it penetrates through the material. We conclude that the mass of material vaporized will be determined by the X-ray spectrum and X-ray yield. This is determined by the specific target design.

VI.4.2 Pb-Li Gas Dynamics and Radiation

As discussed in the preceding section, target generated X-rays vaporize several kilograms of Pb-Li off of the INPORT tubes. The resulting gas absorbs the target generated ions, reaches a temperature of about 1 eV and becomes

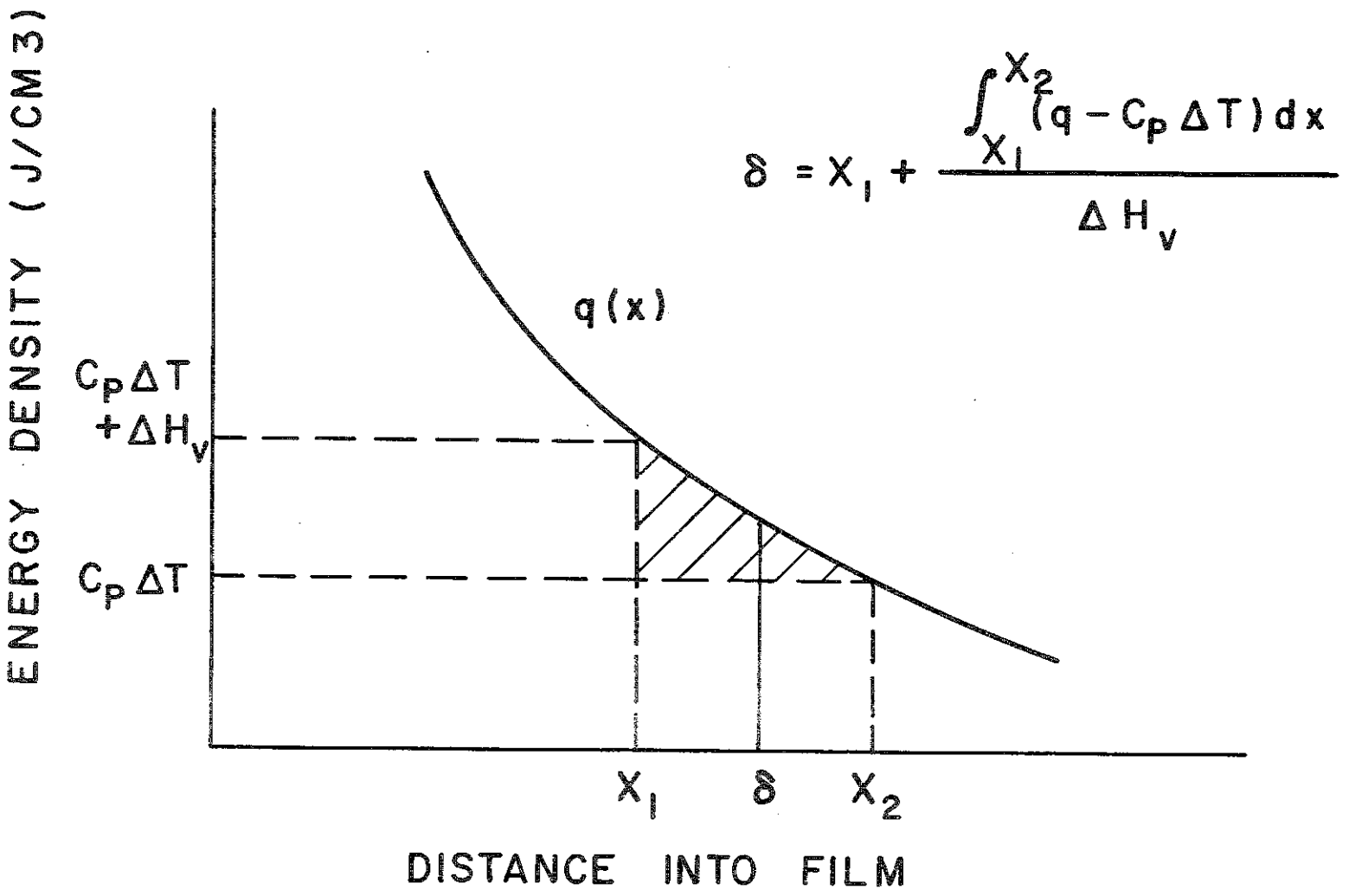

Fig. VI.4-3 Conceptual representation of Pb-Li vaporization.

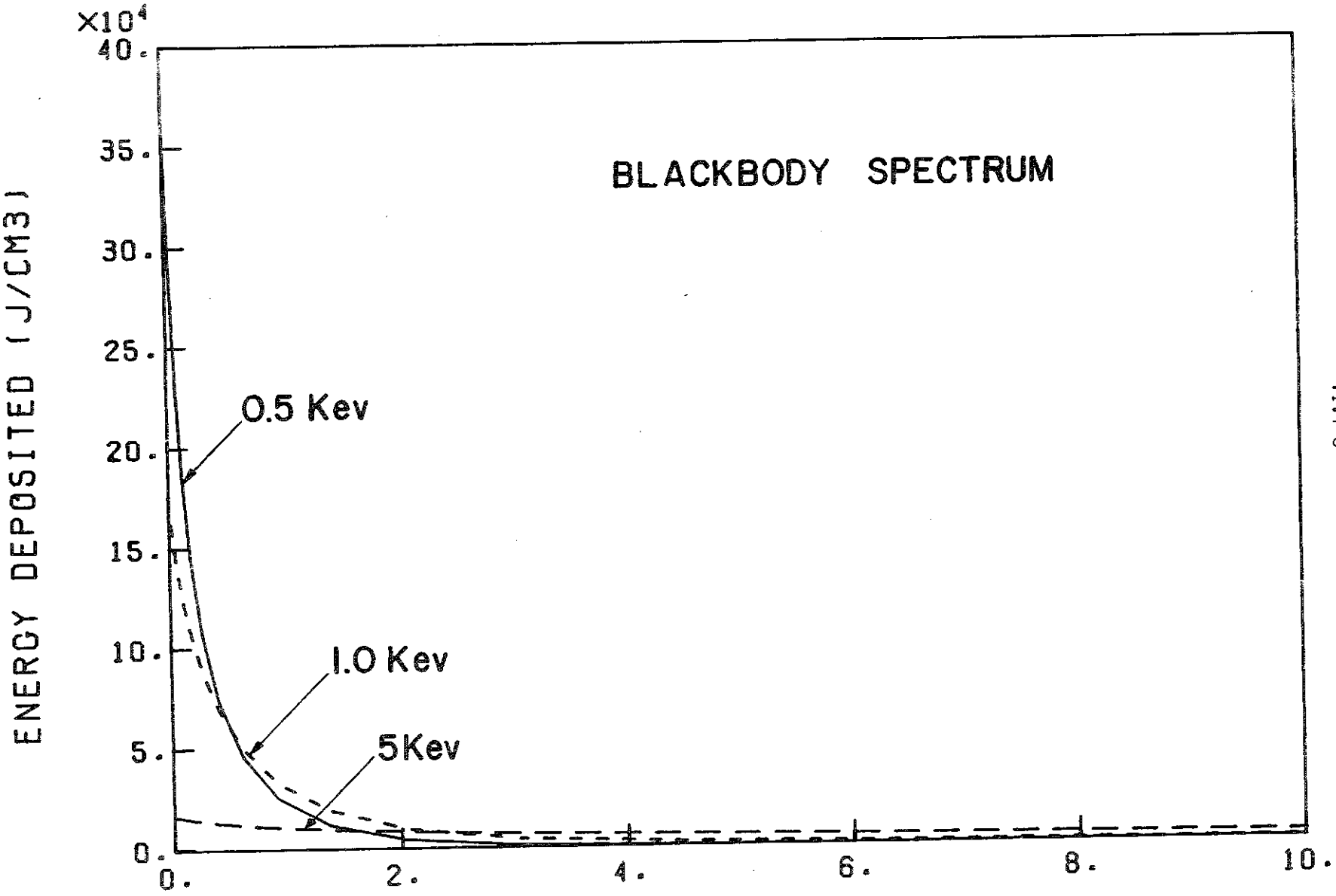

Fig. VI.4-4 X-Ray energy deposition for different blackbody spectra.

partially ionized. As this gas spreads from the tubes into the center of the reactor cavities, it radiates photons which put a heat flux back onto the tubes. Eventually, the gas uniformly fills the cavity and cools enough that the heat flux on the tubes is insignificant. Before this happens, though, there may be some additional vaporization of Pb-Li due to the heat flux. As the gas radiates, it also cools, affecting the rate of recondensation. For these reasons, it is important to consider the behavior of this gas between the time of vaporization and recondensation.

To study this problem, it is necessary to know the equation-of-state and optical data for gaseous Pb-Li. We describe an atomic physics calculation providing this information in section VI.4.2.1.

Once the atomic physics of the gas is understood, the motion and radiation of the gas can be studied. In section VI.4.2.2 we discuss a computer simulation of the gas behavior which uses the results of the atomic physics calculations in section VI.4.2.1.

With this computer model, we can predict what heat fluxes the INPORT tubes might experience from gas radiation and we investigate the sensitivity of such radiation to the total mass of the Pb-Li vaporized. In section VI.4.2.2 we present heat fluxes and average gas temperatures versus time for various Pb-Li masses.

Finally, in section VI.4.2.3 we state our conclusion that the gas behavior is fairly sensitive to the mass of the gas and comment on the significance of these results.

VI.4.2.1 Equation of State and Opacity of Gaseous Pb-Li

The atomic physics of gaseous Pb-Li is studied with the MIXER[5,6] computer code. This code has been developed at the University of Wisconsin to

provide data tables of internal energy density, ionization state, heat capacity and radiation opacities of gas mixtures. This is done as functions of gas temperature, gas density and radiation temperature. Ionization is assumed to occur in either the Saha[7] or the Coronal[8] model and radiative processes to follow a semi-classical formalism.[9] In a mixture of gases the electron density is calculated self-consistently and the interaction of radiation is considered with the 20 lowest excited states of the six most common ionization states for each gas species.

Some results of calculations with this code for $Pb_{83}Li_{17}$ are shown in Figs. VI.4-5 and VI.4-6. Figure VI.4-5 is a plot of the ionization state of $Pb_{83}Li_{17}$ over the plane of gas temperature and density. One can see on this plot where the Saha model is used by remembering the fact that Saha ionization can be a function of density while Coronal ionization cannot. The boundary between the two regions follows the criterion

$$n_e = 10^{16} \, (k_B \, T_{gas})^{7/2} \, cm^{-3}$$

where $k_B \, T_{gas}$ is in eV.[8] Saha ionization is used at high density and low gas temperature. It is also important to note that the dependence of the ionization on the gas temperature makes the equation-of-state rather non-ideal.

Figure VI.4-6 shows the Planck averaged mean free path plotted over the gas temperature - radiation temperature plane for a given density. Notable features of this are the transparency of cool gas to low temperature radiation and the extreme variability of this parameter. This variability can make radiation transport very sensitive to the changes in the conditions in a gas.

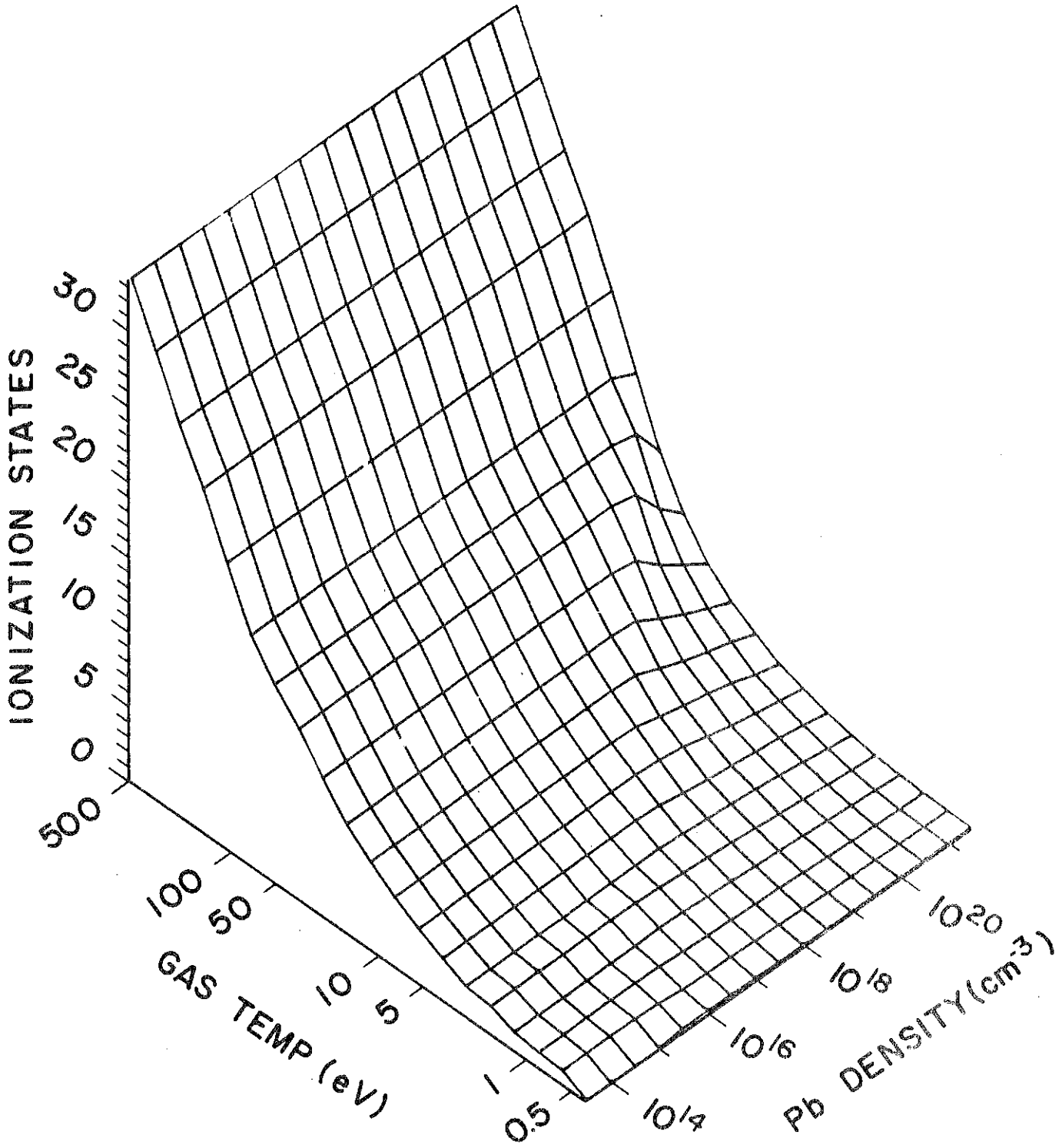

$Pb_{83}Li_{17}$
CHARGE STATE

Fig. VI.4-5

VI.4-12

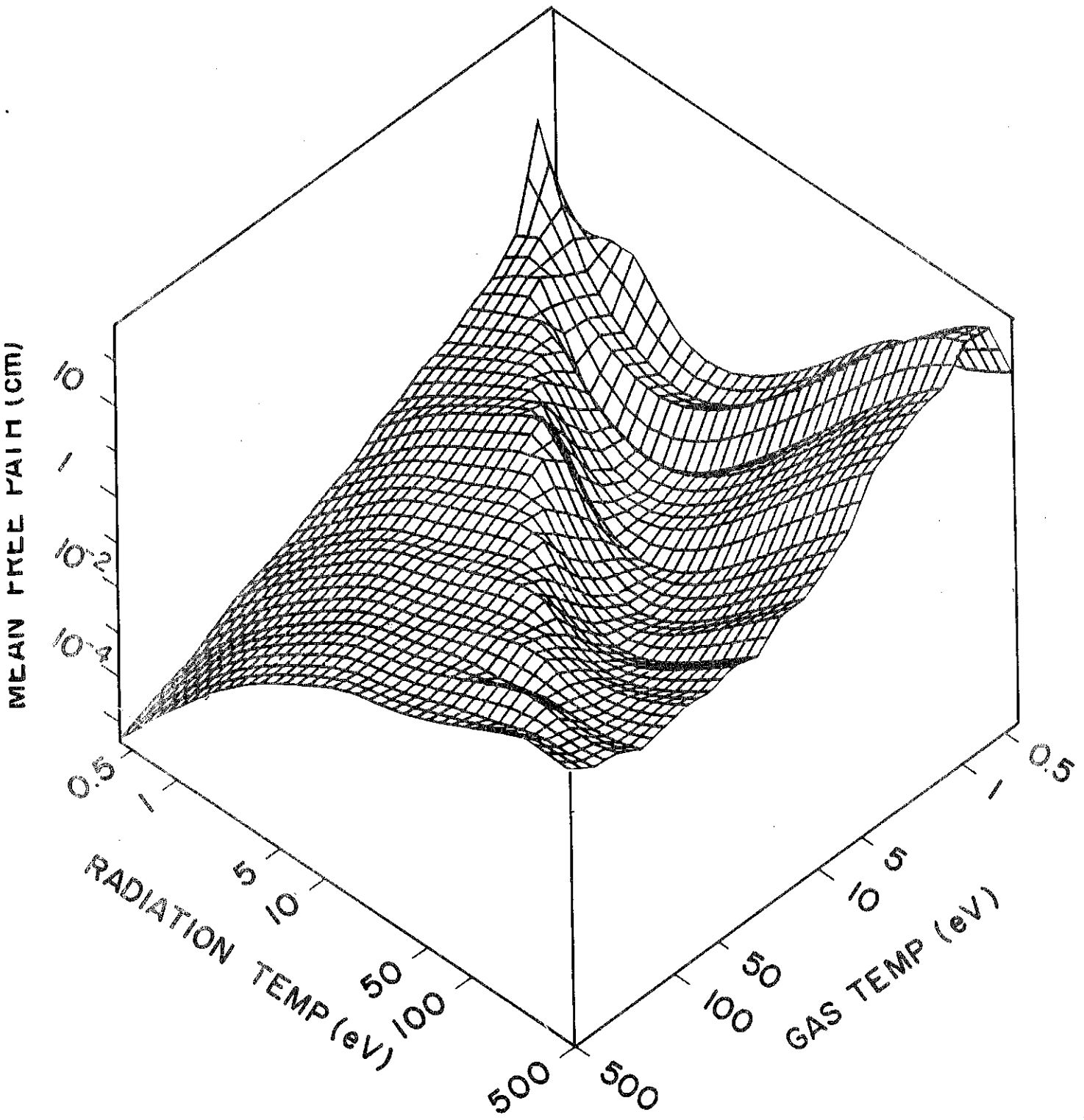

$Pb_{83}Li_{17}$

PLANCK MEAN FREE PATH

Pb DENSITY = $2.7 \times 10^{18}\ cm^{-3}$

Fig. VI.4-6

VI.4.2.2 Radiation - Hydrodynamics in Pb-Li

We have modeled the behavior of the Pb-Li gas with the 1-D Lagrangian radiation-hydrodynamics computer code, FIRE.[10] This code has explicit hydrodynamics and implicit energy transport where heat is conducted through two fluids - the gas at a local temperature of T_{gas} and the radiation fluid at a temperature of $T_{radiation}$. In these calculations, conduction through the radiation field dominates the thermal transport. Transport coefficients and equation-of-state information is obtained from a table of data provided by a calculation with MIXER.

FIRE cannot accurately model the behavior of fluid which is as dense as a liquid. Thus, we must analytically calculate the dynamics from the time when the Pb-Li is at liquid density until the time that the density is low enough for FIRE calculations to be appropriate. We assume that the gas obeys an isothermal blow-off formalism where the temperature of the gas is that due to the deposited target generated X-ray energy minus the energy of vaporization and the energy of ionization. We arbitrarily assume that the energy from target generated ions is uniformly deposited in the gas at 1.5×10^{-4} seconds after vaporization and that FIRE can be used any time after this. Thus, at this time we start the computer calculations with the gas density profile being the Gaussian shape predicted by the blow-off model and the total energy in the gas being the target generated X-ray and ion energy minus the vaporization and ionization energy.

The FIRE calculation simulates the gas dynamics until the time the gas reaches the center of the cavities. Figure VI.4-7 shows the positions of the Lagrangian zone boundaries for a typical calculation during this period. Upon reaching the center, the gas begins to convert its bulk kinetic energy into heat, but FIRE, being a one-dimensional code, predicts that the gas will

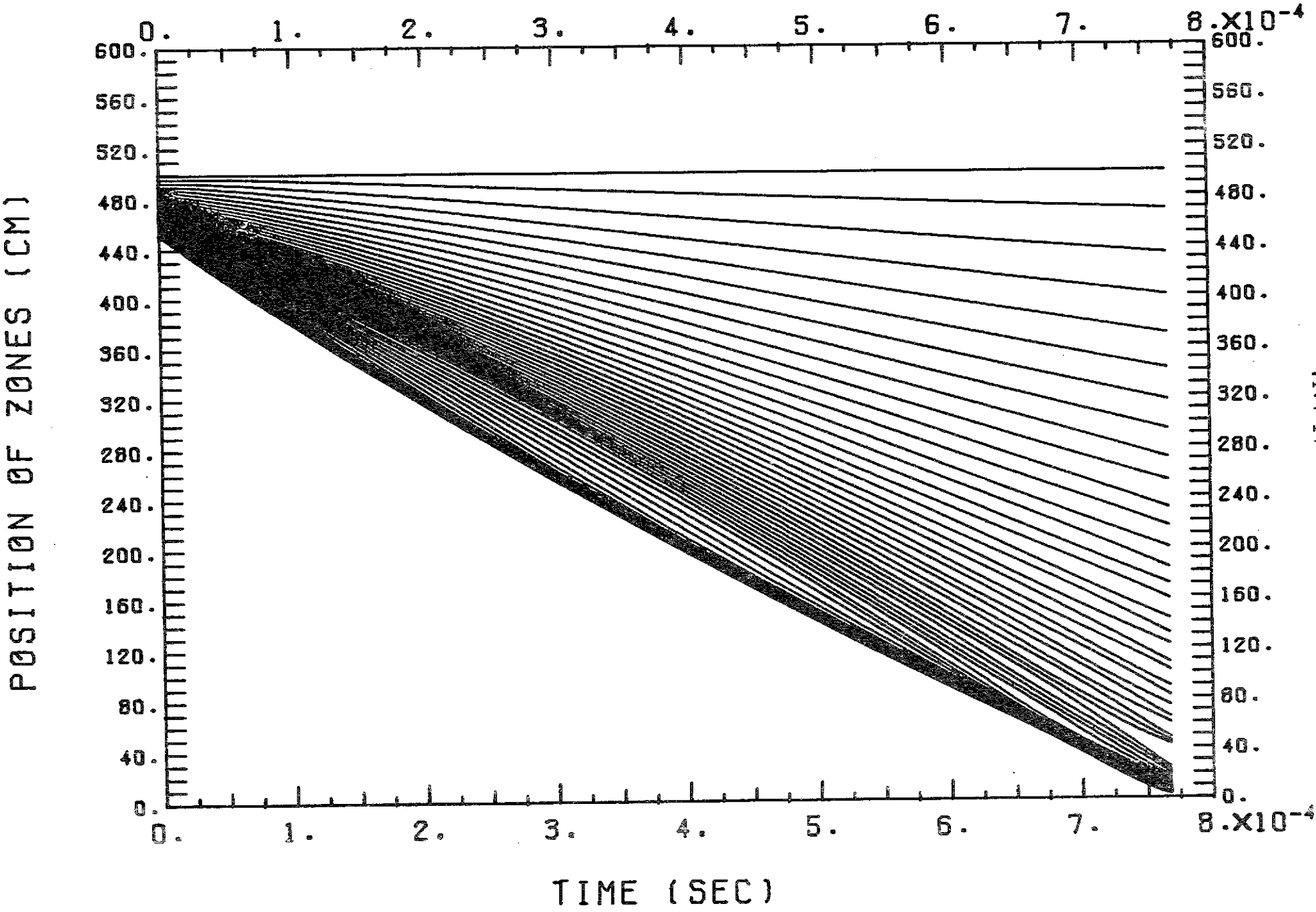
POSITION OF ZONES (CM)
TIME (SEC)
0.
1.
2.
3.
4.
5.
6.
7.
8.X10-4
600.
560.
520.
480.
440.
400.
360.
320.
280.
240.
200.
160.
120.
80.
40.
0.

Fig. VI.4-7

reflect off the center and propagate back towards the tubes. This is not physical because the system does not have the symmetry needed for such reflections. For this reason we stop this first simulation calculation at the time when the gas reaches the center, typically about 1 millisecond after vaporization.

To simulate the behavior past this time we assume that the gas has a uniform temperature and density and has no bulk kinetic energy immediately after the gas collapses in the center. We find the temperature that will give the proper amount of energy,

$$E_{gas} = E_{x\text{-}ray} + E_{ion} - E_{vaporization} - E_{ionization} - E_{radiation} ,$$

where $E_{radiation}$ is the energy radiated back into the tubes by this time. We then use FIRE again with this new initial condition and with the gas constrained not to move. By combining both uses of FIRE, we calculate the heat flux on the tubes due to radiation and the average temperature of the gas versus time.

To test the sensitivity of the gas behavior to the total mass of Pb-Li vaporized, we have completed calculations for three different total masses; 6.7 kg, 13.3 kg and 26.6 kg. In Figs. VI.4-8 through VI.4-10 the heat fluxes on the surfaces of the tubes are shown for total masses of 6.7 kg, 13.3 kg and 26.6 kg, respectively.

The average temperatures are shown in Figs. VI.4-11 through VI.4-13. Notice that there is in each case a large pulse of heat reaching the surface immediately after the gas collapses in the center. This is an effect of the conversion of bulk kinetic energy into heat. As is seen in Figs. VI.4-11 through VI.4-13, there is also a pulse in the average temperature of the gas

VI.4-16

Fig. VI.4-8

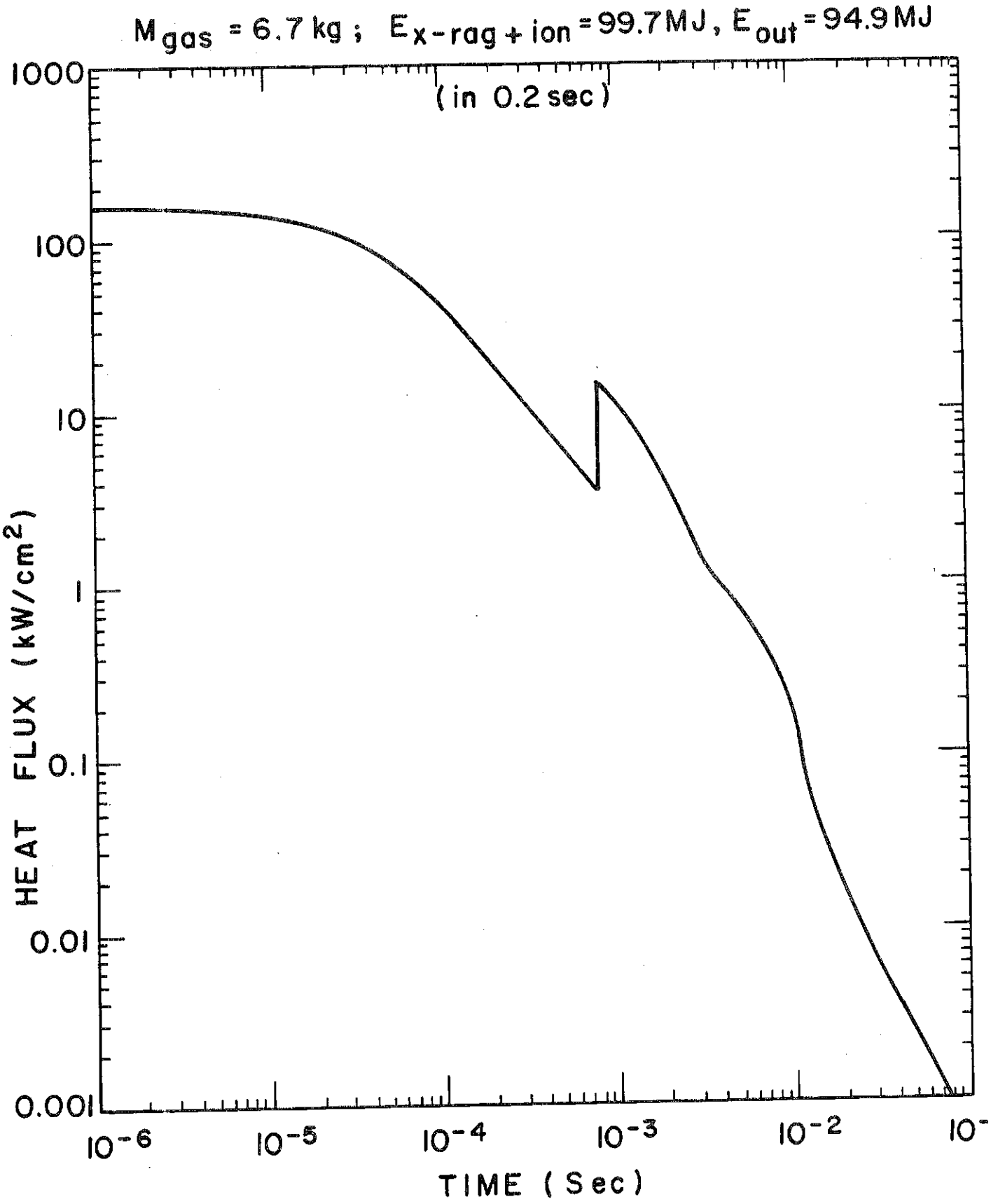

Fig. VI.4-9

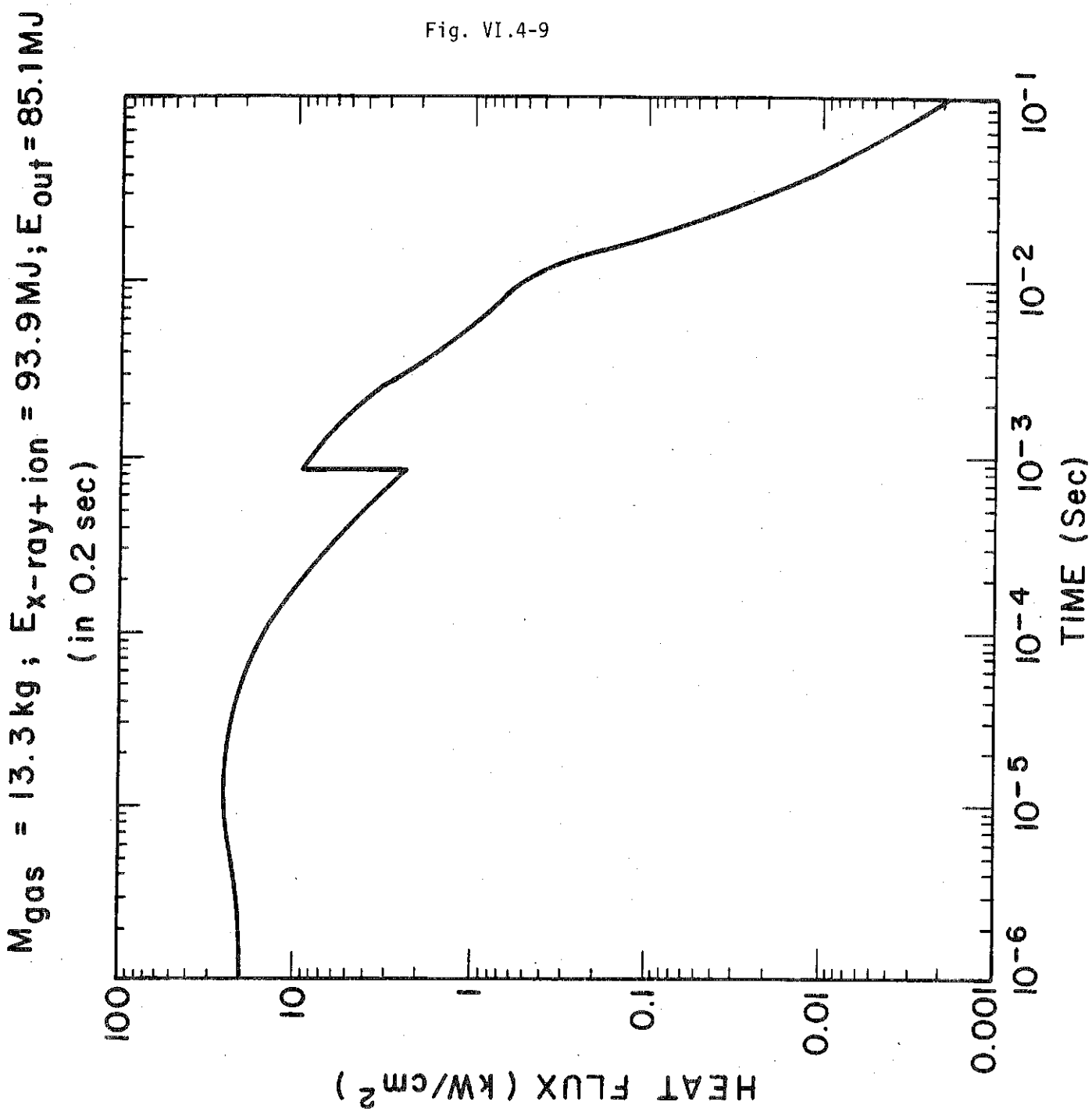
M_{gas} = 13.3kg ; $E_{x-ray+ion}$ = 93.9MJ; E_{out} = 85.1MJ
(in 0.2 sec)
HEAT FLUX (kW/cm²)
100
10
1
0.1
0.01
0.001
TIME (Sec)
10⁻¹
10⁻²
10⁻³
10⁻⁴
10⁻⁵
10⁻⁶

Fig. VI.4-10

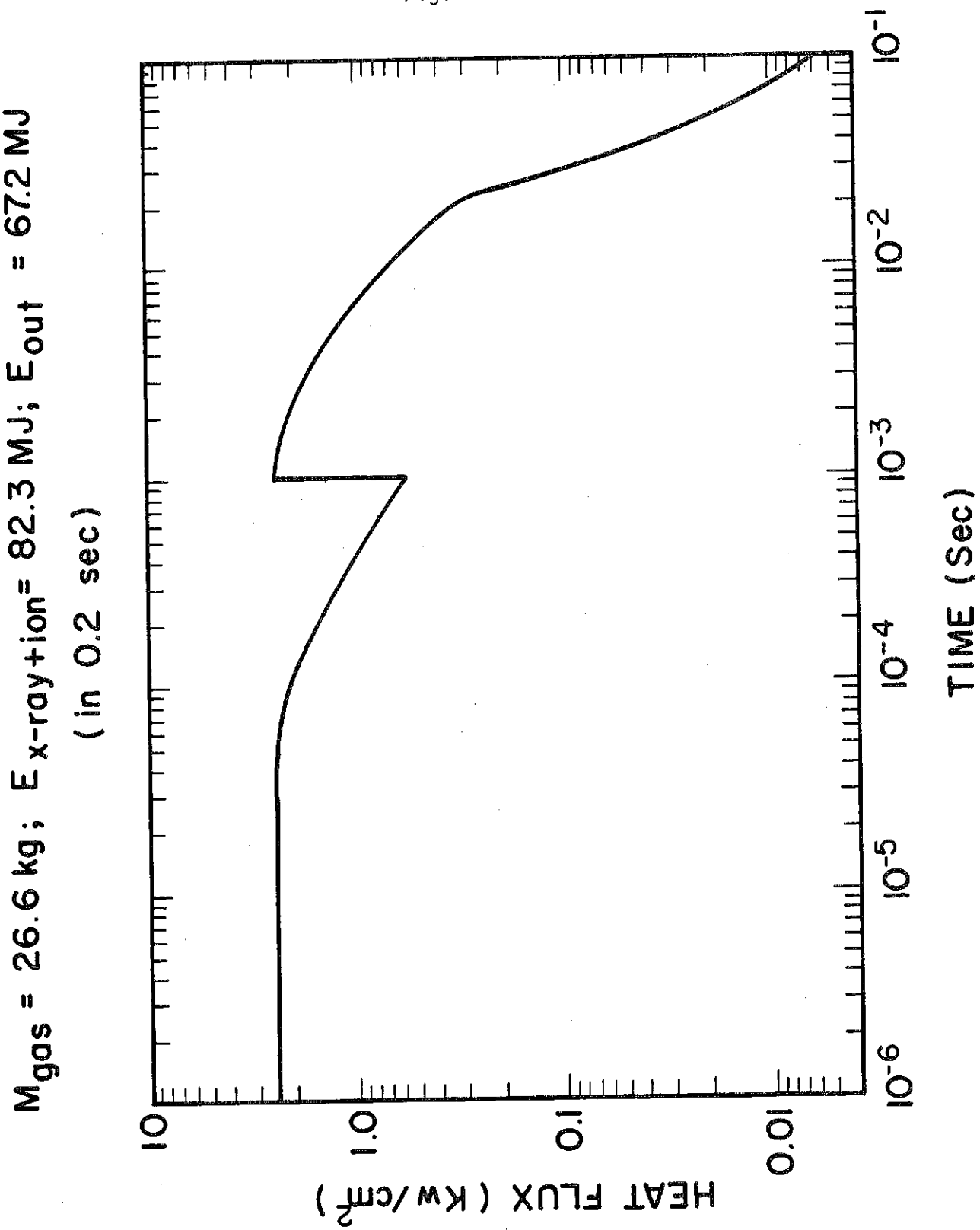
M_{gas} = 26.6 kg; $E_{x\text{-}ray+ion}$ = 82.3 MJ; E_{out} = 67.2 MJ
(in 0.2 sec)
HEAT FLUX (Kw/cm²)
10
1.0
0.1
0.01
TIME (Sec)
10^{-1}
10^{-2}
10^{-3}
10^{-4}
10^{-5}
10^{-6}

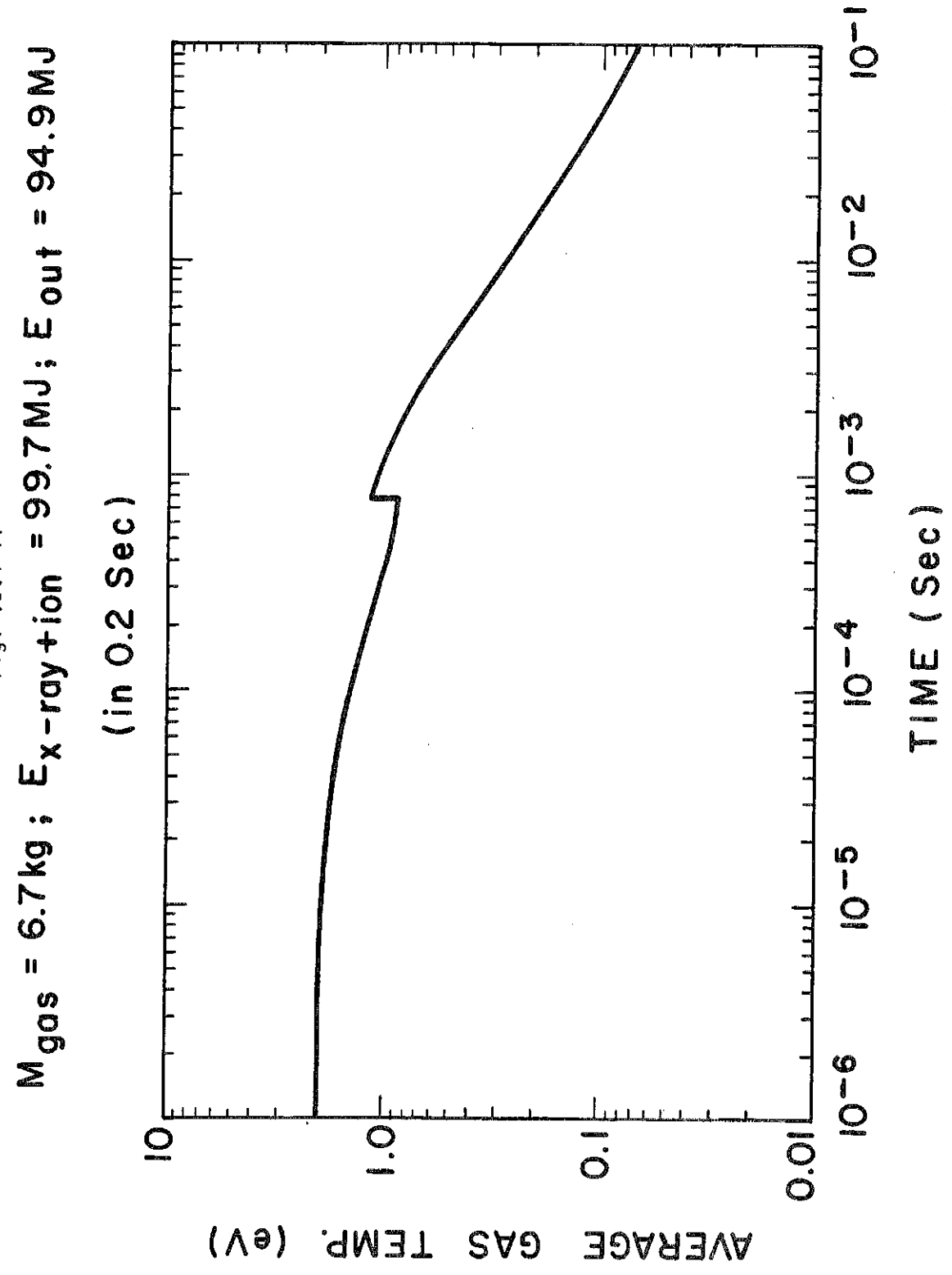
M_{gas} = 6.7kg ; $E_{x-ray+ion}$ = 99.7MJ ; E_{out} = 94.9MJ
(in 0.2 Sec)
AVERAGE GAS TEMP. (eV)
10
1.0
0.1
0.01
TIME (Sec)
10^{-6}
10^{-5}
10^{-4}
10^{-3}
10^{-2}
10^{-1}

Fig. VI.4-11

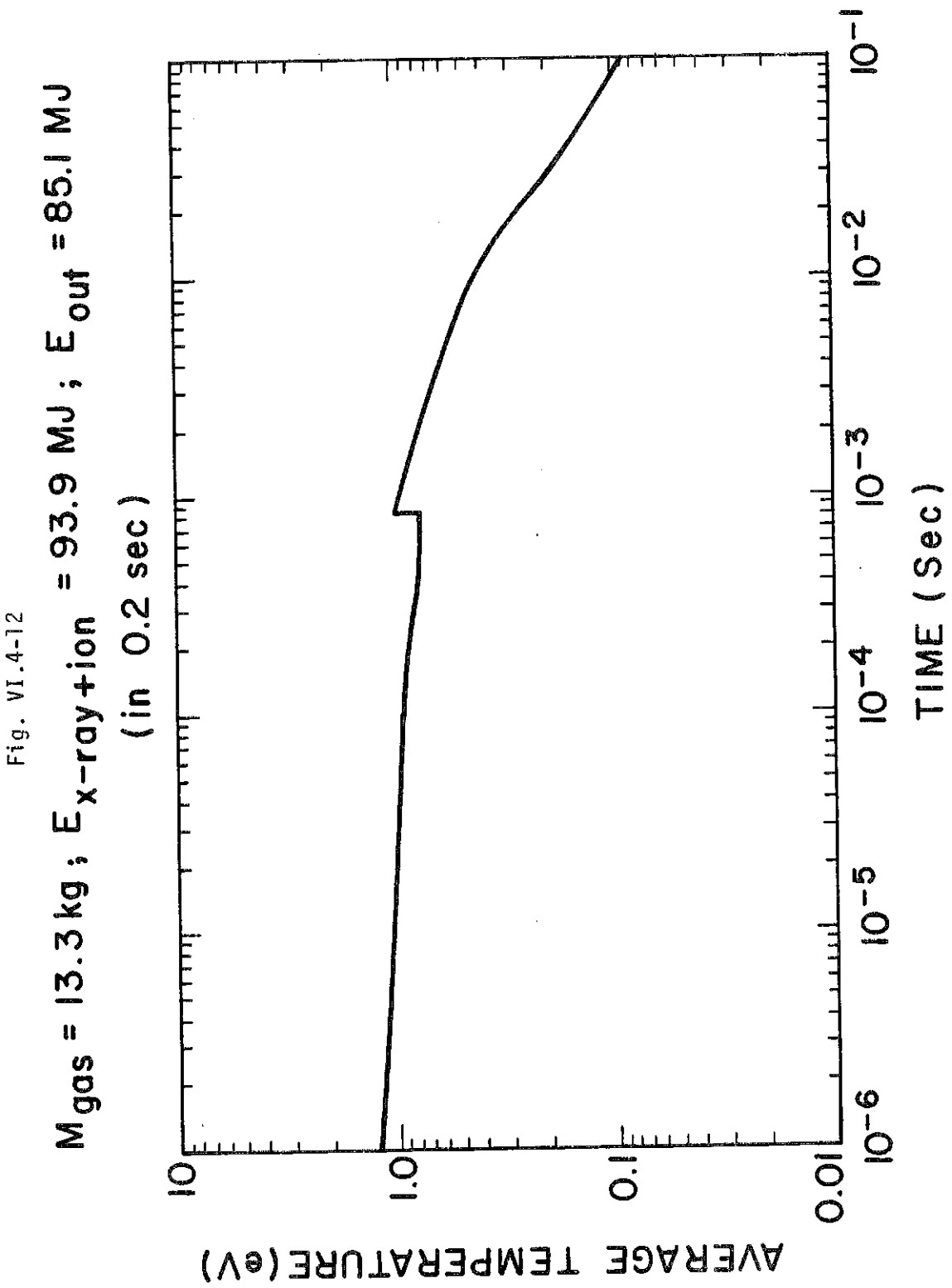
M_{gas} = 13.3 kg ; $E_{x\text{-}ray+ion}$ = 93.9 MJ ; E_{out} = 85.1 MJ
(in 0.2 sec)
AVERAGE TEMPERATURE (eV)
10
1.0
0.1
0.01
TIME (Sec)
10^{-6}
10^{-5}
10^{-4}
10^{-3}
10^{-2}
10^{-1}

Fig. VI.4-12

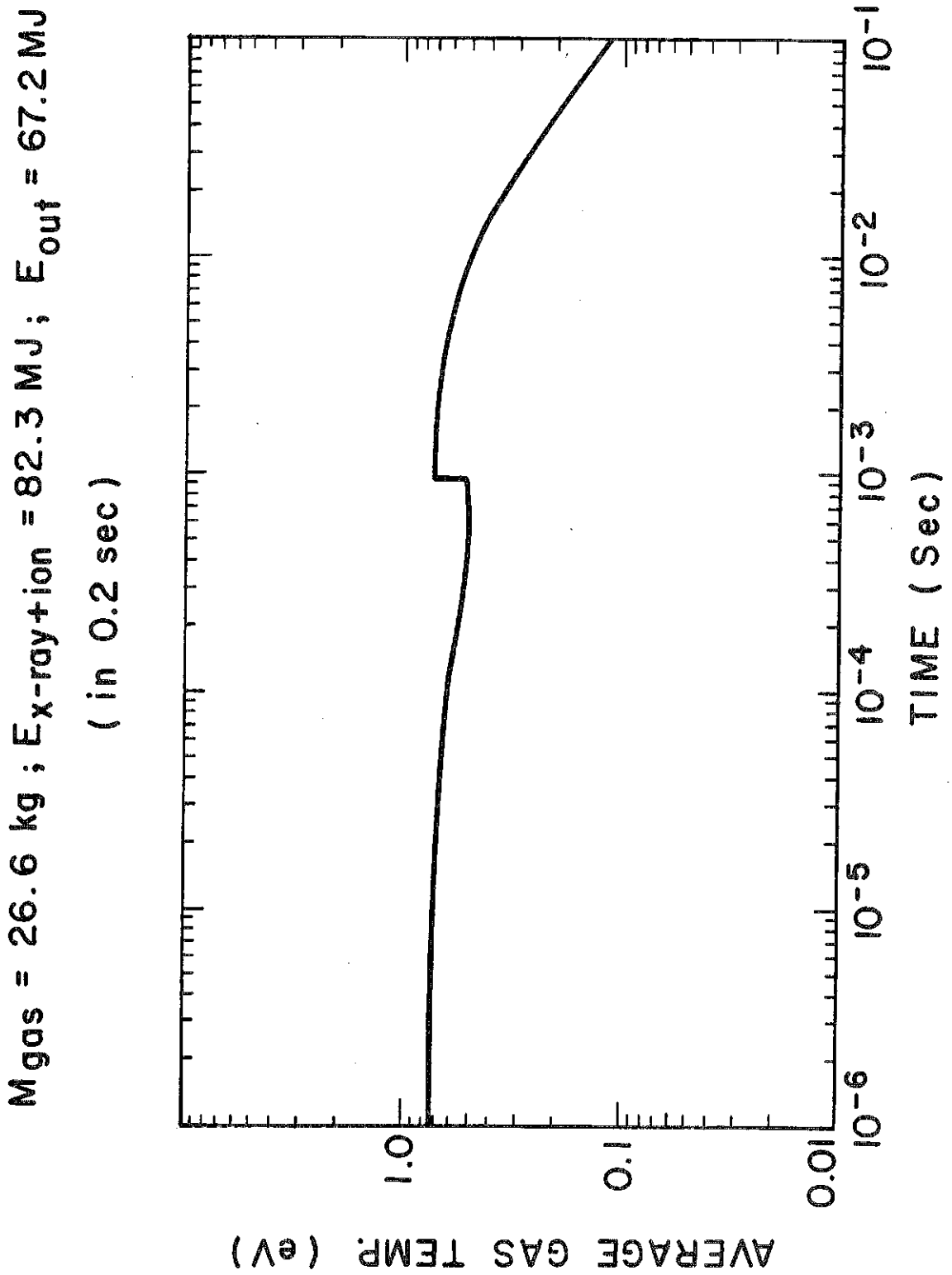
M_{gas} = 26.6 kg ; $E_{x\text{-}ray+ion}$ = 82.3 MJ ; E_{out} = 67.2 MJ
(in 0.2 sec)
AVERAGE GAS TEMP. (eV)
1.0
0.1
0.01
10^{-6}
10^{-5}
10^{-4}
10^{-3}
10^{-2}
10^{-1}
TIME (Sec)

Fig. VI.4-13

which is due to this conversion of kinetic energy into heat and which causes the increase in heat flux. The same process has been seen in imploding wire experiments.

VI.4.2.3 Conclusions

Comparison of Figs. VI.4-8 through VI.4-10 shows that the heat flux can vary by two orders of magnitude when the total mass is changed by a factor of four. At low gas mass the temperature must be high because the internal energy density is high. Also, the radiation passes through less dense gas more easily. Thus, the heat fluxes are higher for low total gas mass. As the mass of the gas is increased, both of these trends are reversed and the gas radiates energy more slowly back to the tubes.

VI.4.3 Evaporation/Condensation Calculations

Once the radiation heat flux and the temperature of the gas is known, the behavior of the gas density in the cavity over time can be investigated. The rate that gas leaves the cavities is governed by geometry of the cavities and the gas temperature. The rate that gas is added to the cavity through evaporation off of the tubes is determined by the temperature of the Pb-Li film on the tubes. This temperature can be found through a temperature diffusion calculation in this film for the surface heat fluxes calculated in section VI.4.2.

In section VI.4.3.1 we describe the methods used in the temperature diffusion calculation, in the condensation and in the evaporation. In section VI.4.3.2 we present and discuss results. Conclusions of a general nature are made in section VI.4.3.2.

VI.4.3.1 Calculation Procedure

The governing equations for heat transfer, condensation and evaporation are:

$$K \frac{\partial^2 T}{\partial x^2} = \rho c_p \frac{\partial T}{\partial t} \qquad \text{(VI.4-1)}$$

$$m_{cond.} = 3.64\ P_g\ (M/RT_g)^{1/2} \qquad \text{(VI.4-2)}$$

$$m_{vap.} = P_s\ \left(\frac{M}{RT_s}\right)^{1/2} \qquad \text{(VI.4-3)}$$

in which:

K	is thermal conductivity of $Li_{17}Pb_{83}$
ρ	is density, g/cm^3
C_p	is specific heat, J/g K
T	is temperature, K
x	is distance from first surface, cm
t	is time, sec
$m_{cond.}$	is condensation rate, g/sec - cm^2
P_g	is pressure of the gas, Torr
M	is molecular weight
T_g	is temperature of the gas, K
$m_{evp.}$	is evaporation rate, g/sec - cm^2
P_s	is saturation vapor pressure of first surface
T_s	is the temperature of the first surface, K.

The initial conditions are:

$$T = 1150\ K \quad 0 < x < 10^{-4}\ cm$$

$$T = T(x) \quad x > 10^{-4}\ cm$$

$$P_g = 108\ Torr$$

$$T_g = 14500\ K$$

The boundary conditions for Eq. VI.4-1 are:

$$- K \frac{dT}{d\chi} = q_{tot} \text{ at } \chi = 0$$

$$K \frac{dT}{d\chi} = h\ (T - T_c) \text{ at } \chi = \chi_o$$

in which $q_{tot} = q_r + q_c - q_v$. We have used the following definitions:

q_r is energy deposited due to radiation

q_c is energy deposited due to condensation

q_v is energy loss due to evaporation

h is heat transfer coefficient

T_c is temperature of the coolant.

$T(\chi)$ is the temperature profile in the coolant tube wall. This temperature is unknown at the beginning of the calculation and has to be estimated. However, after a few cycles, a quasi-steady-state will be established and $T(\chi)$ can be calculated.

Equation VI.4-1 cannot be solved exactly due to the complicated initial and boundary conditions. Therefore, the following finite difference form is used:

$$T_i' = T_i + \sum_j \frac{cond_{ji}}{[v\rho c_p]_i} (T_j - T_i)\ \Delta\theta \qquad \text{(VI.4-4)}$$

in which $\Delta\theta$ is time step and is $< \frac{[v\rho c_p]_i}{\sum_j cond_{ji}}$, T_i is temperature of zone i

before time step $\Delta\theta$, $cond_{ji}$ is the conductance $(\frac{KA}{X})$ between zones j and i, $[v\rho c_p]_i$ is the thermal inertia of zone i and T_i' is new temperature of zone i after $\Delta\theta$.

By using Eqs. VI.4-2, VI.4-3, and VI.4-4, and starting from the initial condition, all the information in the cavity can be calculated step by step.

VI.4.3.2 Results and Conclusions

We have calculated heat transfer in the Pb-Li film, evaporation and condensation with the following assumptions:

a. The cavity is spherical with R = 5 m.

b. The gas zone has a uniform temperature and pressure.

c. The condensation and evaporation are by Pb only.

d. The material properties are independent of temperature.

e. The first surface forms a spherical enclosure over the cavity.

f. The thickness of the tube wall is 1.5 mm.

g. The coolant temperature is 324°C and has a heat transfer coefficient of 12 W/cm^2-°C.

The results of a series of calculations for 13 kg of vaporized Pb-Li are summarized from Fig. VI.4-14 to Fig. VI.4-20. Figure VI.4-14 shows the temperature of the first surface as a function of time. An examination of this curve shows that the temperature history is not the same for the first two shots. Figure VI.4-15 shows the temperature of the wall as a function of distance from first surface just before the first three explosions. It can be seen that temperature has almost converged to a quasi-steady-state after 3 shots. Figure VI.4-16 shows the condensation and evaporation rates. Note that for a vaporized mass of 13 kg, evaporation is not important. Figure VI.4-17 shows the total condensation and evaporation and the mass in the cavity as a function of time. At times after 0.1 sec, the mass of gas in the

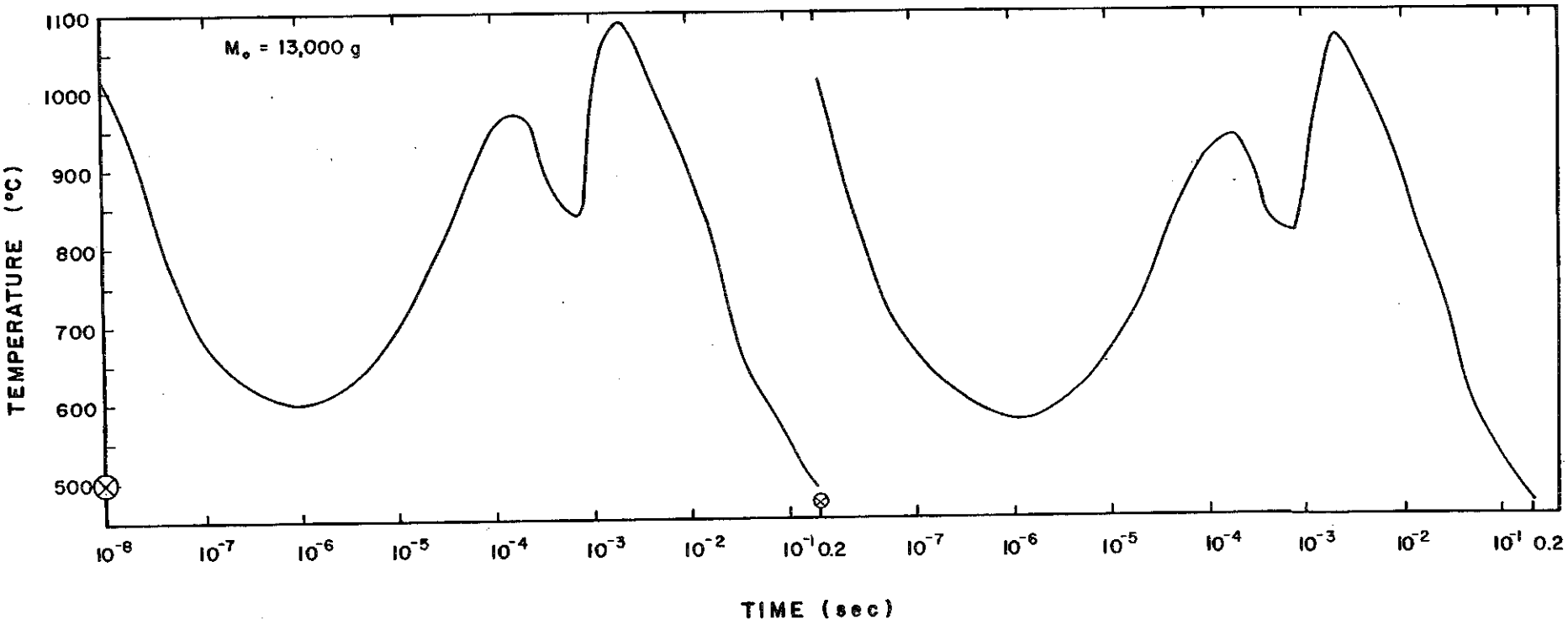

Fig. VI.4-14 Temperature of the first surface during the first two shots. Mass of vaporized gas = 13000 g.

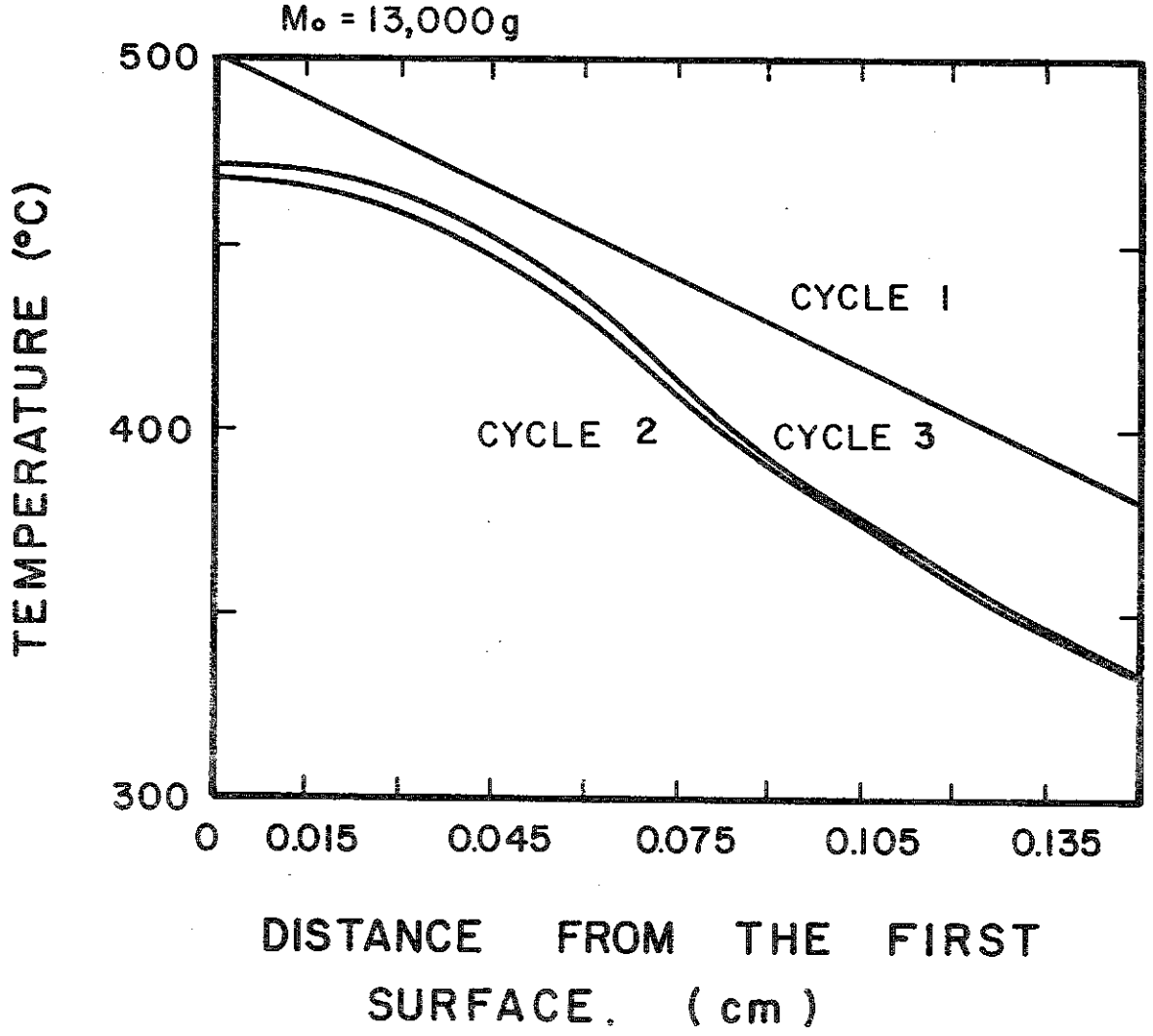

Fig. VI.4-15 Temperature of the PbLi at the start of the first three cycles. Mass of vaporized gas = 13000 g.

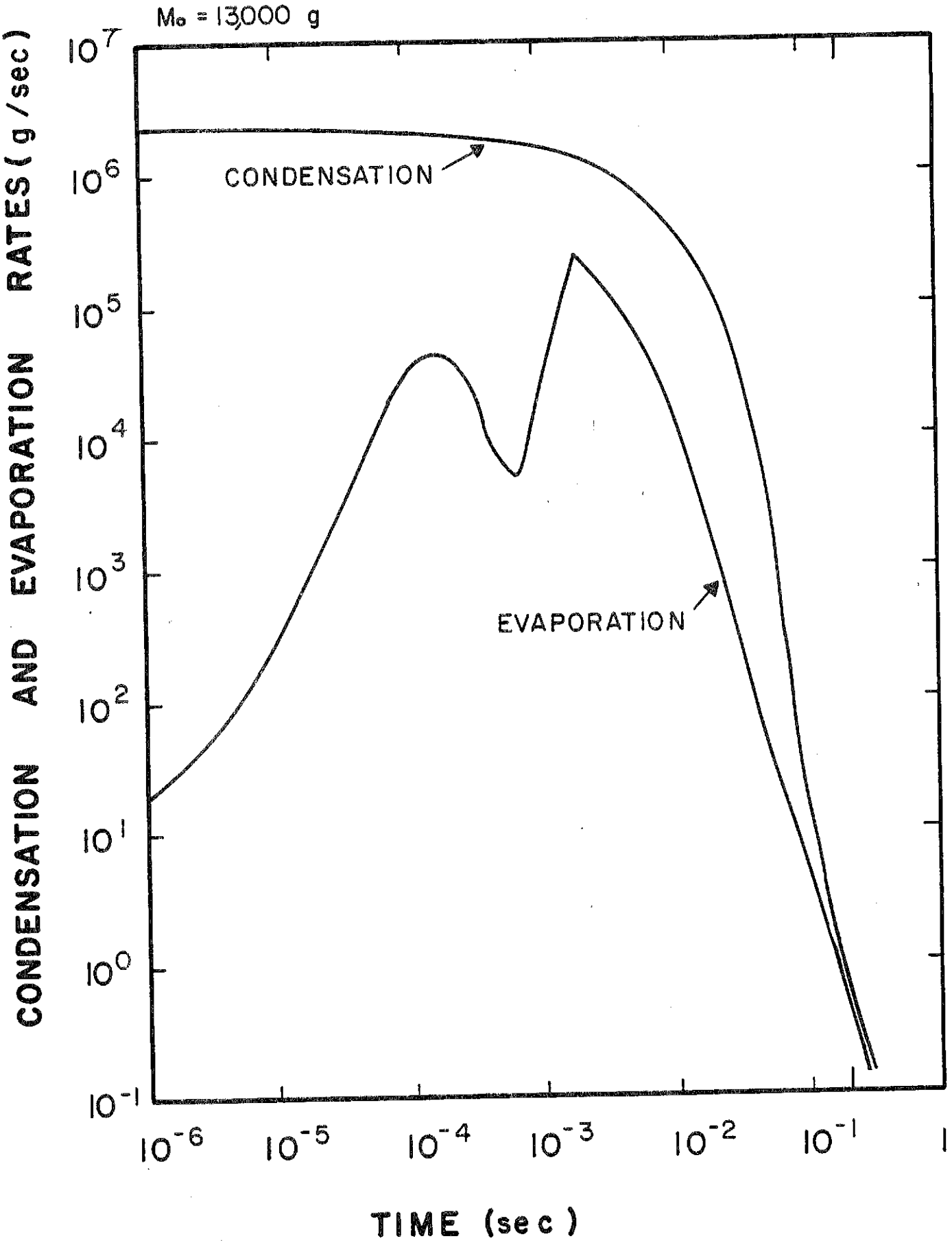

Fig. VI.4-16 Condensation and evaporation rates on first surface for mass of vaporized gas = 13000 g.

VI.4-29

Fig. VI.4-17 Total condensation, evaporation and mass in cavity for mass vaporized = 13000 g.

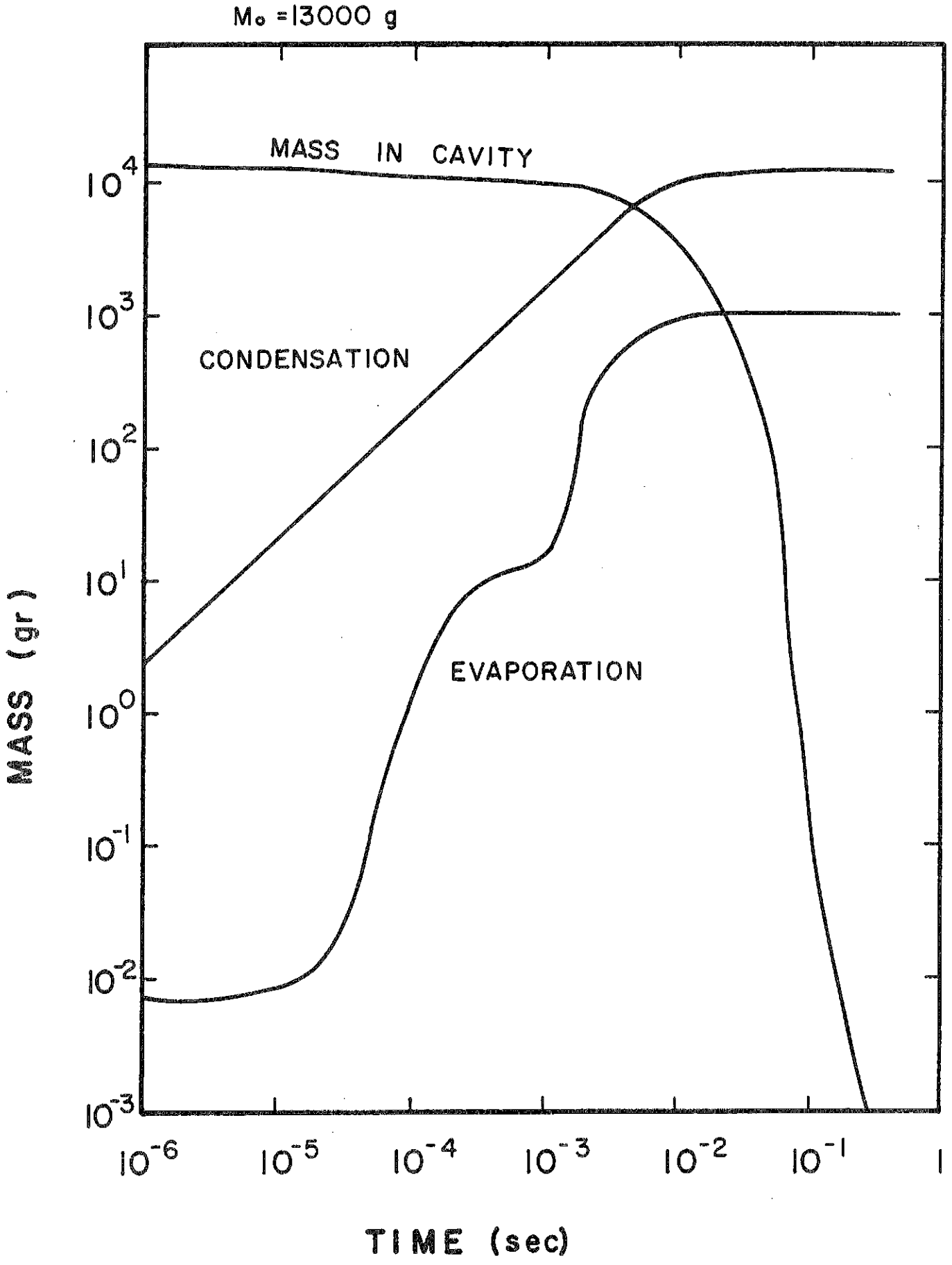

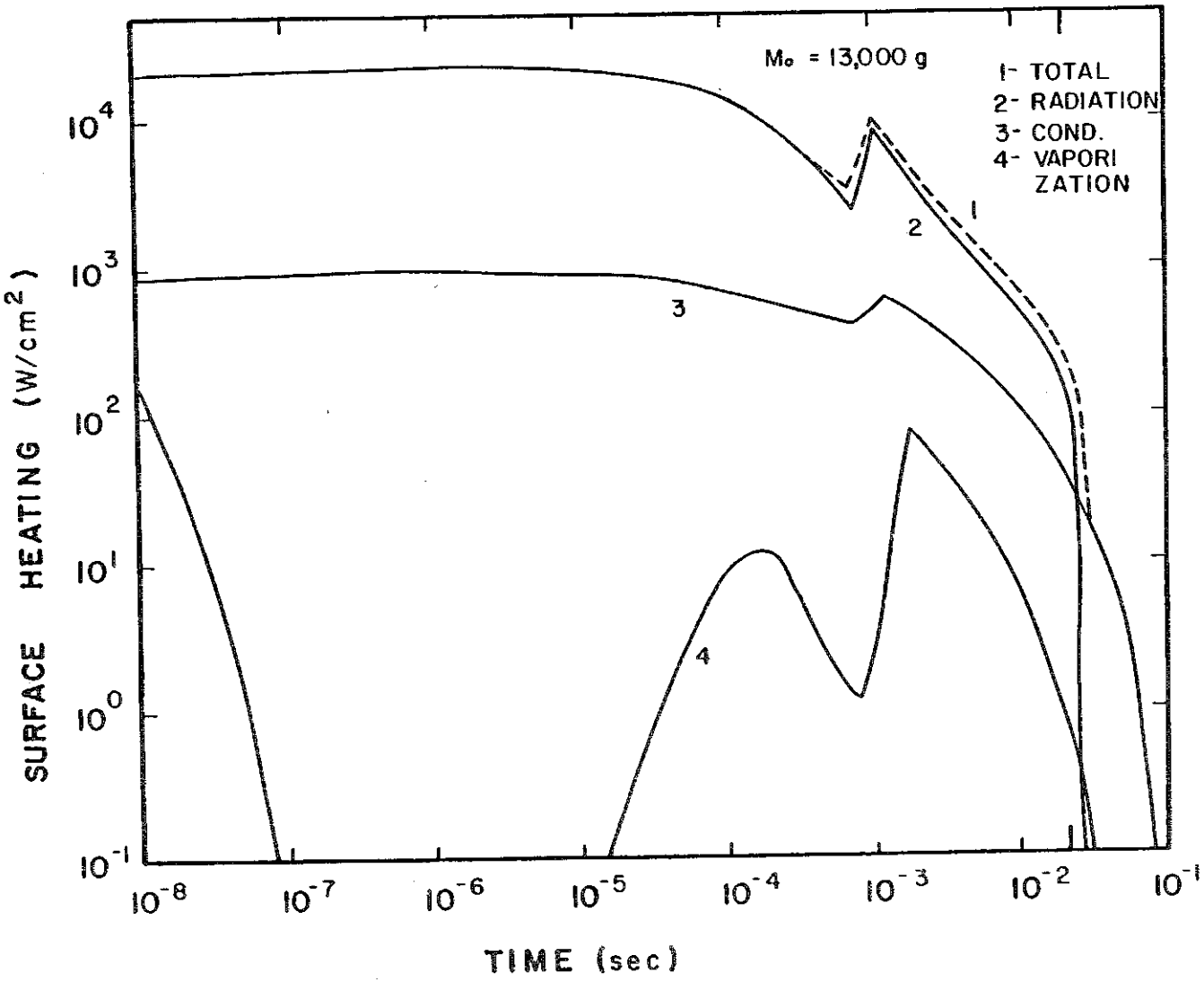

Fig. VI.4-18 First surface heat flux. Mass of vaporized gas = 13000 g.

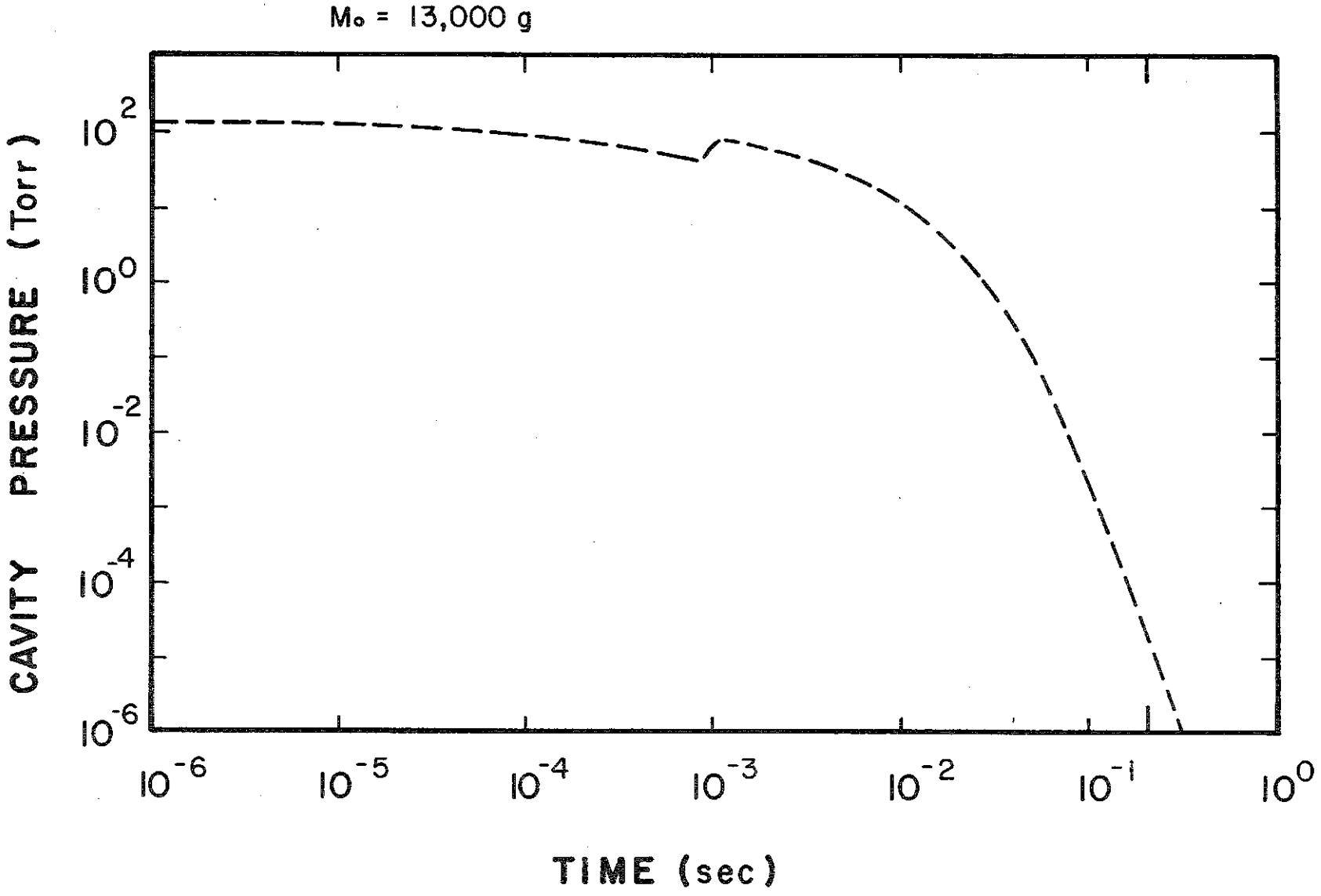

Fig. VI.4-19 Cavity pressure versus time. Mass of vaporized gas =13000 g.

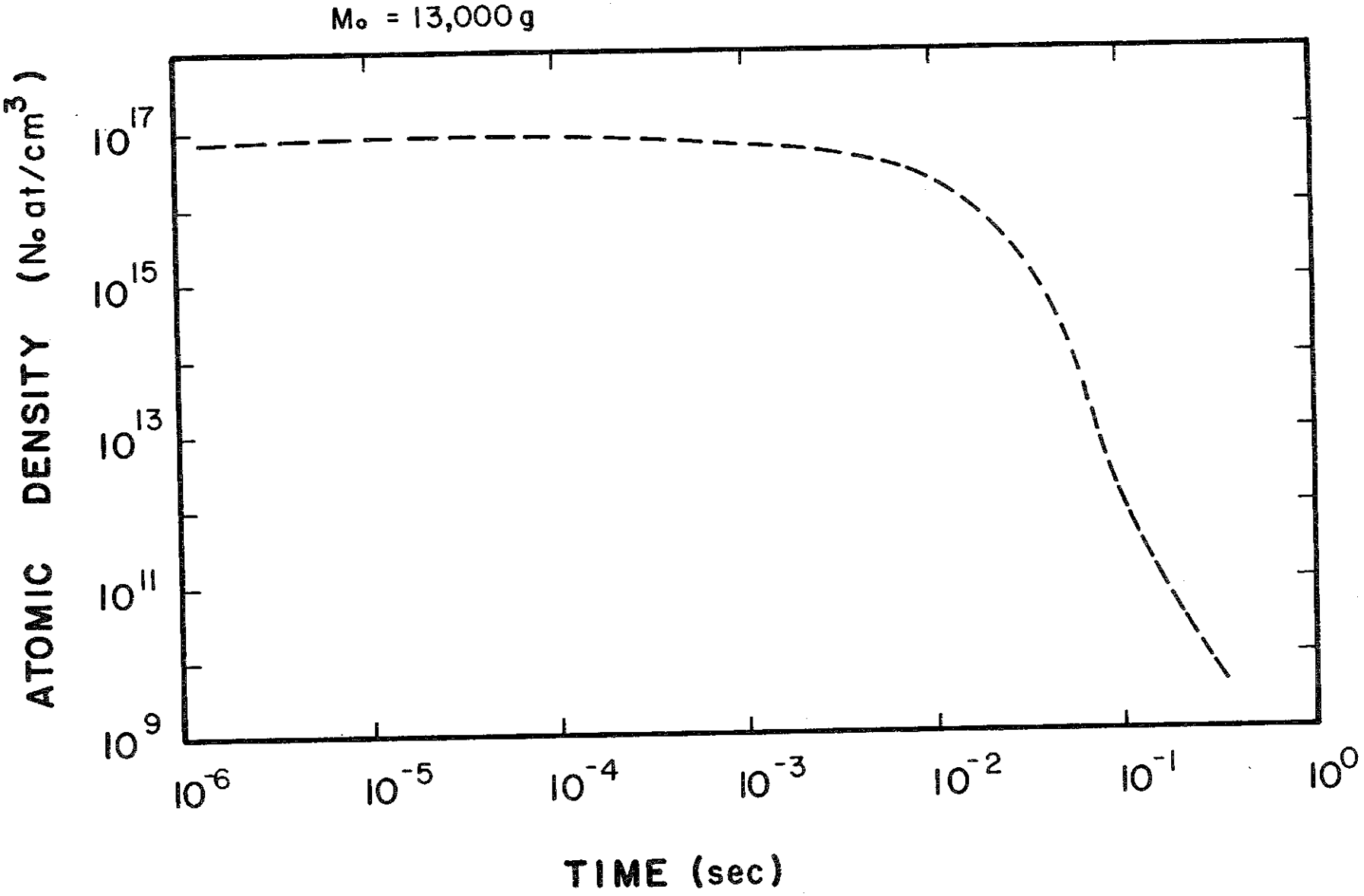

Fig. VI.4-20 Atomic density in cavity versus time. Mass of vaporized gas = 13000 g.

cavities is a small number which is the difference of two larger numbers, M_o and the condensed mass. Figure VI.4-18 shows the surface heating rate due to radiation, condensation and evaporation, the summation of which is the heating on the first surface. Notice that the heat from radiation is dominant for much of the time. Figure VI.4-19 shows the pressure and Fig. VI.4-20 shows particle density in the cavity as a function of time.

The vacuum pressure at time = 0.2 second should be low enough to allow beam propagation. The particle density at this time is 4×10^{10} cm^{-3}. The calculation of the beam stripping cross section will show that this pressure is acceptable. It must be noted, however, that the total mass in the cavity is only 7×10^{-3} g. This is obtained by subtracting the condensation mass from the sum of initial mass and evaporation mass, both of which are large and very close. The total condensation mass is 1.5×10^{4} gm. Therefore, the uncertainty of the total mass in the cavity at t = 0.2 second is very large. A change of assumptions may lead to a significant variation on the final particle density.

A change of the target design may change the energy associated with the X-rays and/or the spectrum of the X-rays. This will change the initial mass evaporated by the X-ray deposition. To study the effect of different X-ray energy or spectra, a different initial mass is assumed. Two additional computer calculations are performed with M_o = 26 kg and 6.5 kg. The larger mass reduces the initial gas temperature and also the radiation heat flux to the first surface. Consequently, the thermal energy deposited on the first surface is spread over a longer period of time, as can be seen on Fig. VI.4-21. The lower gas temperature also reduces the condensation rate, as can be seen in Eq. VI.4-2. Smaller initial mass, on the other hand, increases the initial gas temperature. The high gas temperature results in a large heat flux to the

first surface and, consequently, causes a large evaporation rate. Thus, the effect of evaporation dominates cavity mass transfer. Figure VI.4-22 shows the surface temperature of the three cases. As expected, the surface temperature increases drastically if the mass of vaporized gas is reduced. This occurs because the heat flux shown in Fig. VI.4-21 is so much higher at low mass. This leads to a higher evaporation rate in the low mass (6.7 kg) case shown in Fig. VI.4-23. Here the evaporation rate is shown to be, at times, much larger than the condensation rate. This leads to the increases in cavity pressure, mass and atomic density with time at low mass shown in Figs. VI.4-24, VI.4-25, and VI.4-26, respectively. Fig. VI.4-27 shows the atomic density at 0.2 second for the three cases of initial mass. There is a sharp minimum at M_o = 13 kg which is due to the gas temperature being high enough for quick condensation and the heat flux being low enough for insignificant evaporation. When M_o = 26.6 kg the gas temperature is too low and recondensation is slow. When M_o = 6.7 kg, the radiation heat flux is high enough that evaporation is a problem.

In summary, we have considered the vaporization, gas dynamics and condensation of Pb-Li from the film on the INPORT tubes. The mass of the gas vaporized by the target generated X-rays is 13.3 kg and the gas density in the cavity 0.2 seconds after the target explosion is low enough for ion beam propagation. The gas density at 0.2 seconds has been found to be sensitive to the mass of vaporized Pb-Li and thus, sensitive to changes in the target X-ray spectrum.

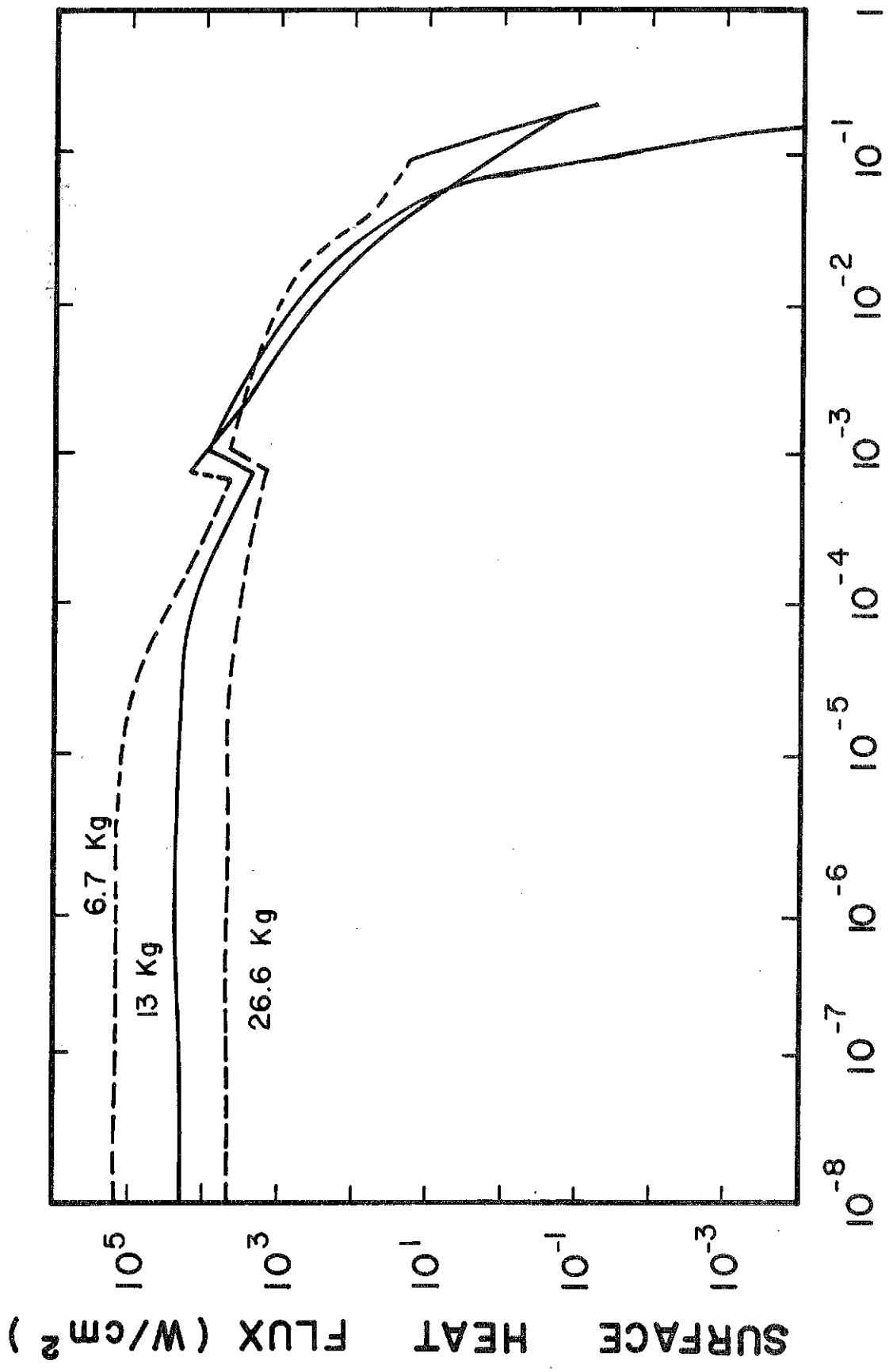

Fig. VI.4-21 Total surface heat flux for different vaporized masses.

Fig. VI.4-22 Temperature of the first surface versus time for different initial cavity gas masses.

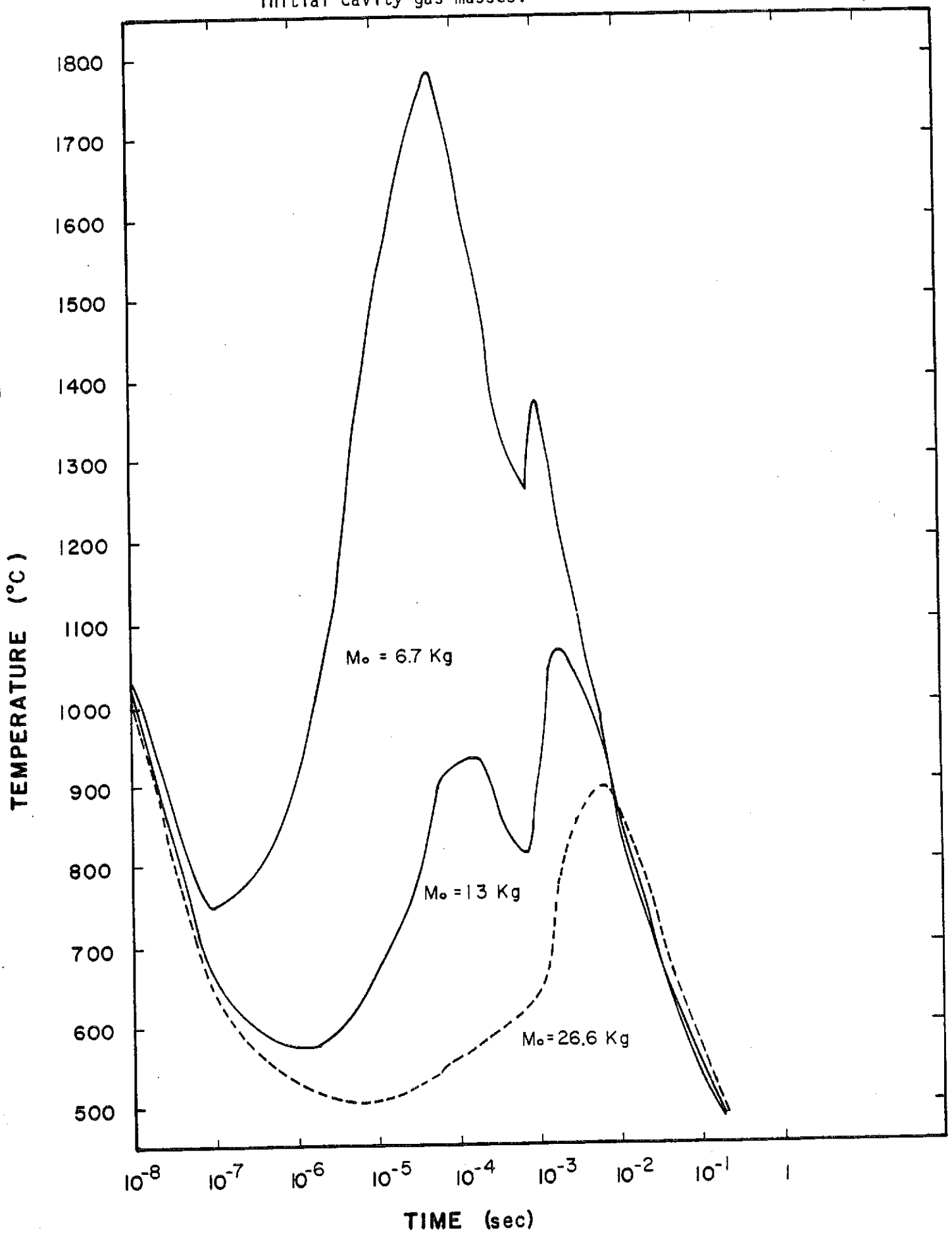

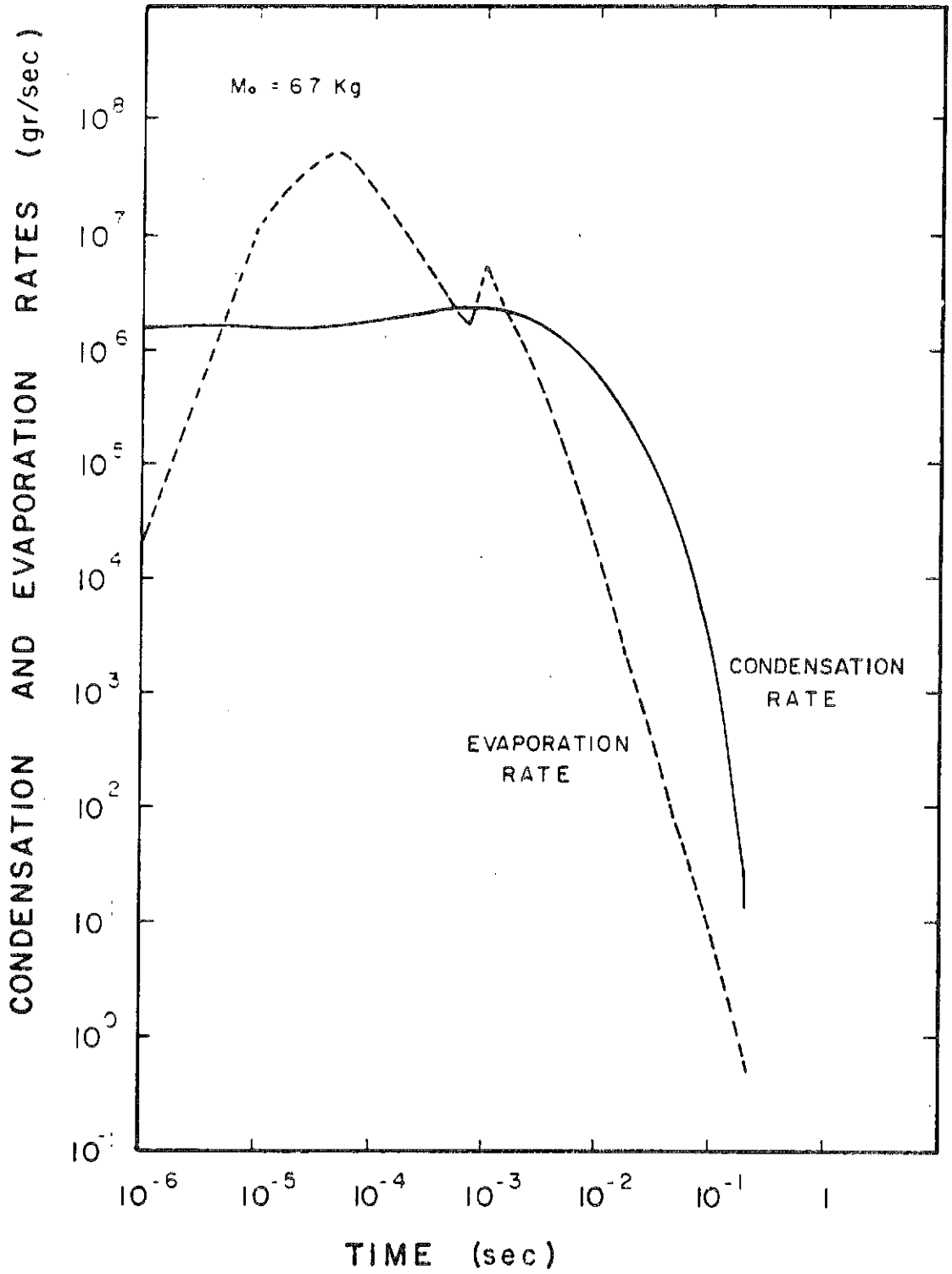

Fig. VI.4-23 Condensation and evaporization rates for mass of vaporized gas = 6700 g.

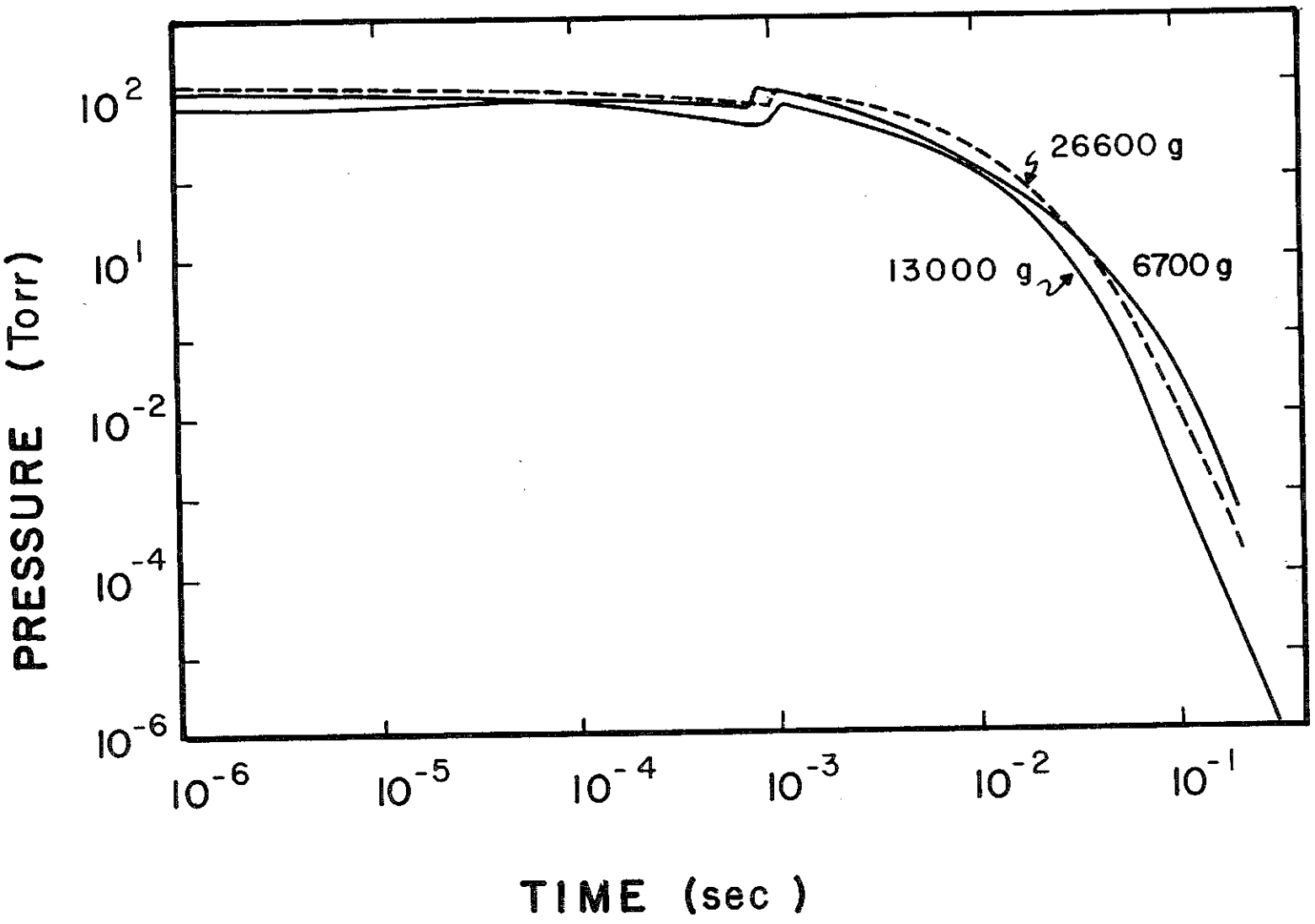

Fig. VI.4-24 Cavity pressure versus time for different masses of vaporized gas.

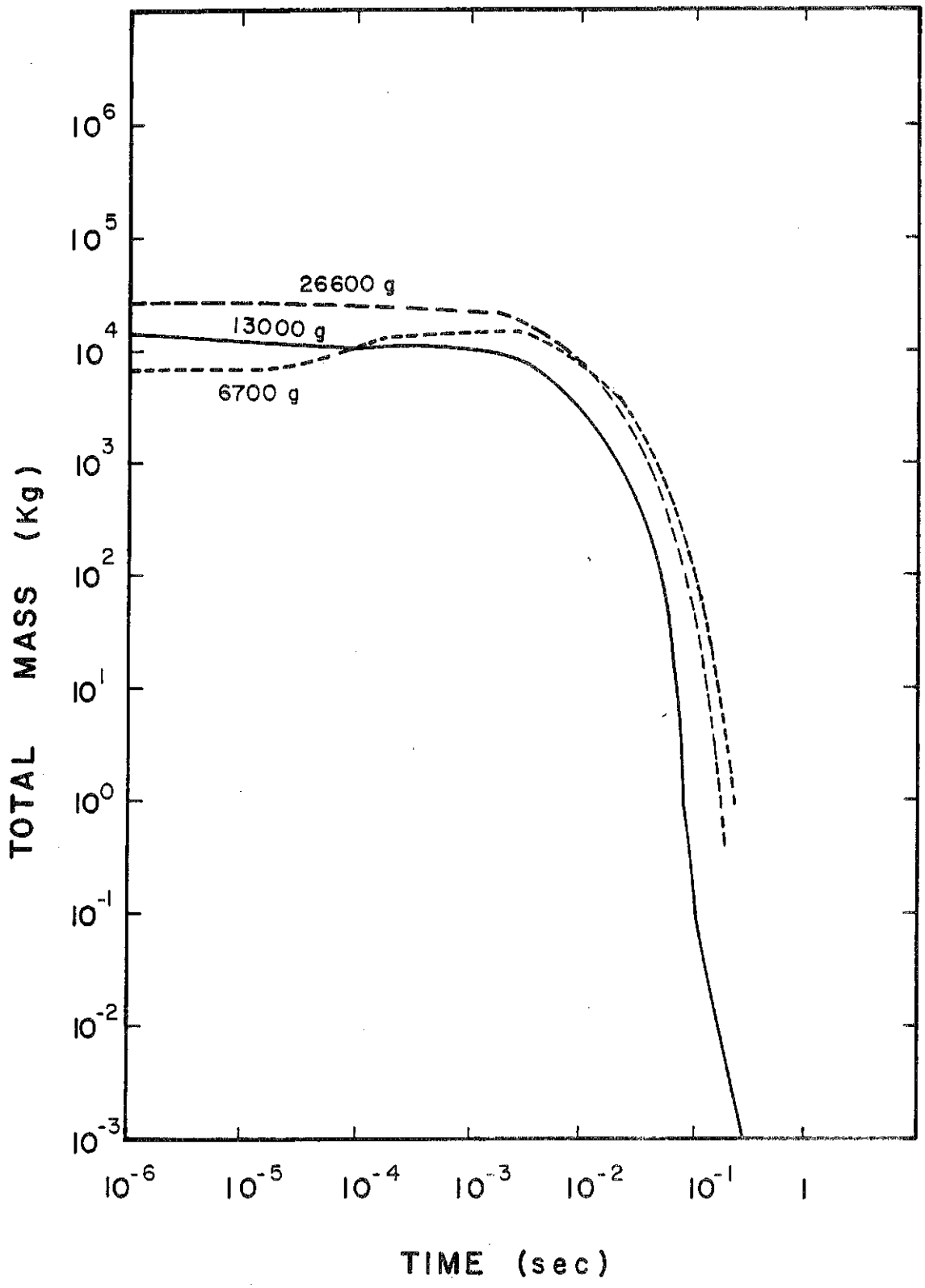

Fig. VI.4-25 Total mass in cavity versus time for diffent masses of vaporized gas.

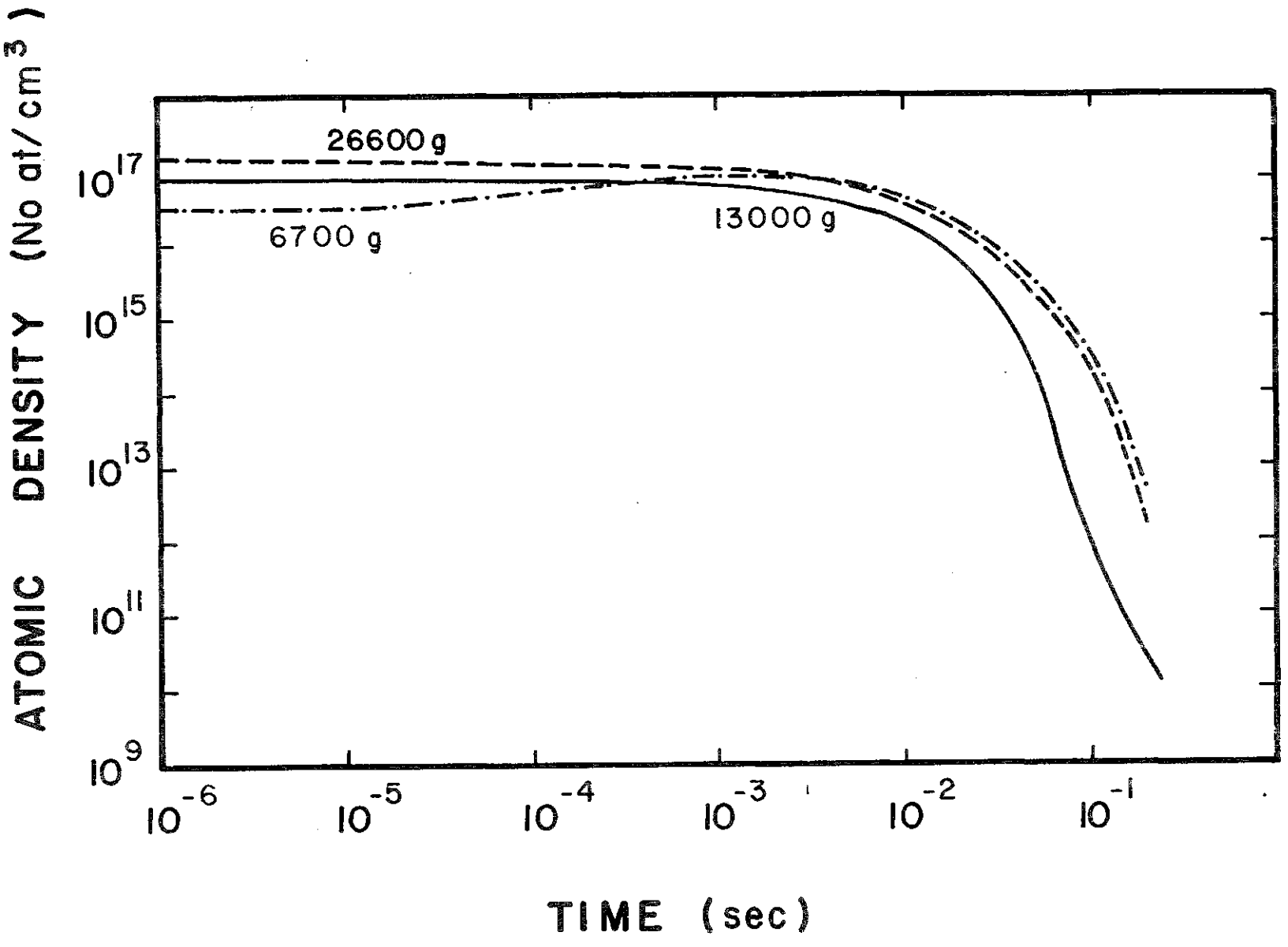

Fig. VI.4-26 Atomic density versus time for different masses of vaporized gas.

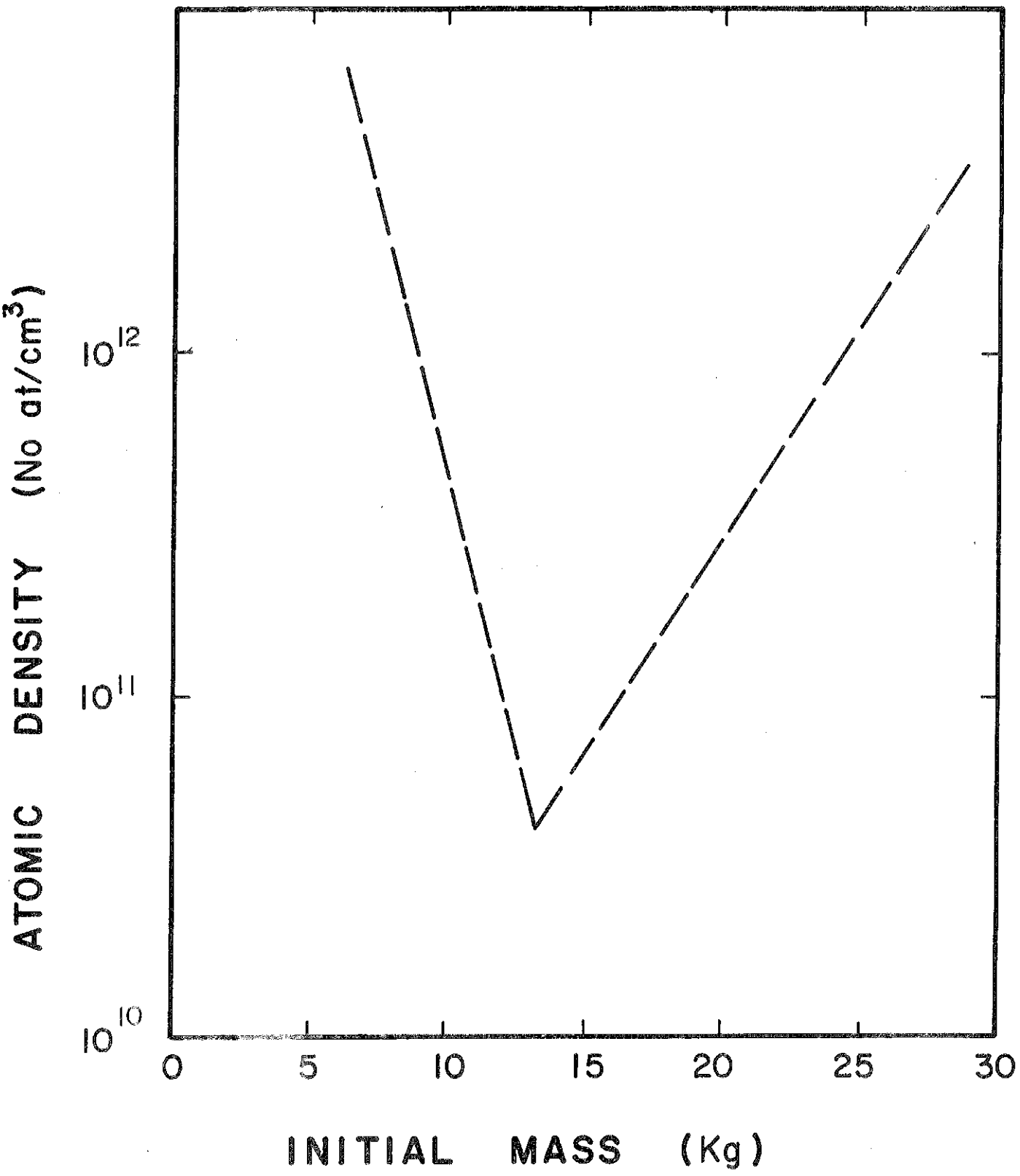

Fig. VI.4-27 Final atomic density in the cavity versus mass of PbLi vaporized.

References for Section VI.4

1. F. Biggs and R. Lighthill, Analytical Approximation for X-ray Cross Sections II, SC-RR-710507, Sandia Laboratory, Albuquerque, NM, December 1971.

2. T.O. Hunter and G.L. Kulcinski, "Description of the Response of Reactor First Walls to Pulsed Thermonuclear Radiation (Part I)," University of Wisconsin Fusion Engineering Program Report UWFDM-196, (March 1977).

3. G. Moses, et al., "High Gain Target Spectra and Energy Partitioning for Ion Beam Fusion Reactor Design Studies", University of Wisconsin Fusion Engineering Program Report UWFDM-396, (November 1980).

4. A.M. Hassanein and G.L. Kulcinski, to be published.

5. R.R. Peterson and G.A. Moses, "MFP - A Code for Calculating Equation-of-State and Optical Data for Noble Gases", Computer Physics Communications 20, 353 (1980).

6. R.R. Peterson and G.A. Moses, "MIXER - A Multi-Species Optical Data and Equation-of-State Computer Code", University of Wisconsin Fusion Engineering Program Report UWFDM-372, (Sept. 1980).

7. D. Mihalas, Stellar Atmospheres (W.H. Freeman and Co., San Francisco, 1978).

8. D. Mosher, NRL Memorandum Report 2563 (March 1973).

9. Ya. B. Zel'dovich and Yu. P. Raizer, Physics of Shock Waves and High Temperature Hydrodynamic Phenomena (Academic Press, New York, 1967), Chapter III.

10. G.A. Moses and R.R. Peterson, "FIRE - A Computer Code to Simulate Cavity Gas Response to Inertial Confinement Target Explosions", University of Wisconsin Fusion Engineering Program Report UWFDM-336 (January 1980).

VI.5 Vacuum System

VI.5.1 General Description

The previous section described the behaviour of the PbLi vapor in the cavity after each shot. It was found that the vapor pressure of PbLi falls below 10^{-4} torr in the order of 200 ms after the shot. In the present section we will deal with the non-condensable fraction of the gas load within the cavity, namely D_2, T_2 and He. We will attempt to access the effect of the PbLi vapor on the vacuum systems for the cavity and the beam lines.

The cavity atmosphere is primarily dictated by the requirements needed to propagate the beams to the target with minimal losses due to stripping and charge exchange. These issues have been addressed in Chapter V. Similarly, the equilibrium pressure of the non-condensable fraction has to be maintained reasonably low, although their effect on beam propagation is not as great as PbLi at the same number density, simply because of the difference in mass. Furthermore, the noncondensable partial pressure has to be kept low because it constitutes a continuous source of molecules migrating into the beam lines where the pressure must be kept at $\sim 10^{-7}$ torr.

The source of hydrogen in the cavity is from the unburned fuel in the target, the newly bred T released within the cavity and the deuterium gas load from the target injector. Helium comes primarily from the DT reaction and T_2 breeding, with a minor contribution from T_2 decay. At pressures on the order of 10^{-4} torr, outgassing does not dominate and will be neglected. Outgassing is a serious problem in the beam lines where the pressure must be three orders of magnitude lower.

Immediately after a shot, the walls of the INPORT tubes as well as other cavity surfaces act as condensers for the PbLi vapors. Although the pressure reaches $\sim$ 100 torr, because of the sticking coefficient of unity for PbLi, no

boundary layer develops on the cavity surfaces. For this reason the gas behaves more as in molecular flow rather than viscous flow. The behaviour of the non-condensable species within the vacuum ducts will thus be treated with molecular flow theory rather than viscous flow.

Most of the recent fusion reactor design studies have utilized compound cryopumps for pumping hydrogen and helium. In these pumps, hydrogen species are condensed on chevrons cooled to ~ 15 K while the helium is cryotrapped on molecular sieves applied to panels which are at 4.2 K. Typically these pumps have speeds of ~ 5 ℓ/s cm^2 for D_2, T_2 and ~ 2 ℓ/s cm^2 for He. A major disadvantage of any cryopump is the need for periodic regeneration. This is done by valving the pump off and warming up the cryosurfaces. Although regeneration may only take ~ 20-30 min., during this time the pump is not available for operation. Some designs have resorted to providing twice as many pumps as needed, such that only half are on line at any one time. This is not space efficient, particularly where there are space limitations. In several past designs[1,2] the UW group has proposed the use of back to back cryopumps such as that shown in Fig. VI.5-1. Two sets of cryopanels, with integral baffles and chevron shields, are provided back to back. While the front panel is in use, the rear panel is being regenerated and the pump body itself constitutes the shut-off valve. Although some development work will be needed to perfect the seals for such a pump, we feel that it holds the promise for substantially increasing the pumping capacity in systems which are space limited. We are proposing such pumps for the present study.

In the HIBALL design, vacuum ports have been provided at the junction between the upper blanket modules and the top of the INPORT tubes. The spaces between the headers which connect the two blanket systems together are devoted to vacuum ports. There are 30 ports 65 cm high and 120 cm wide, connected to

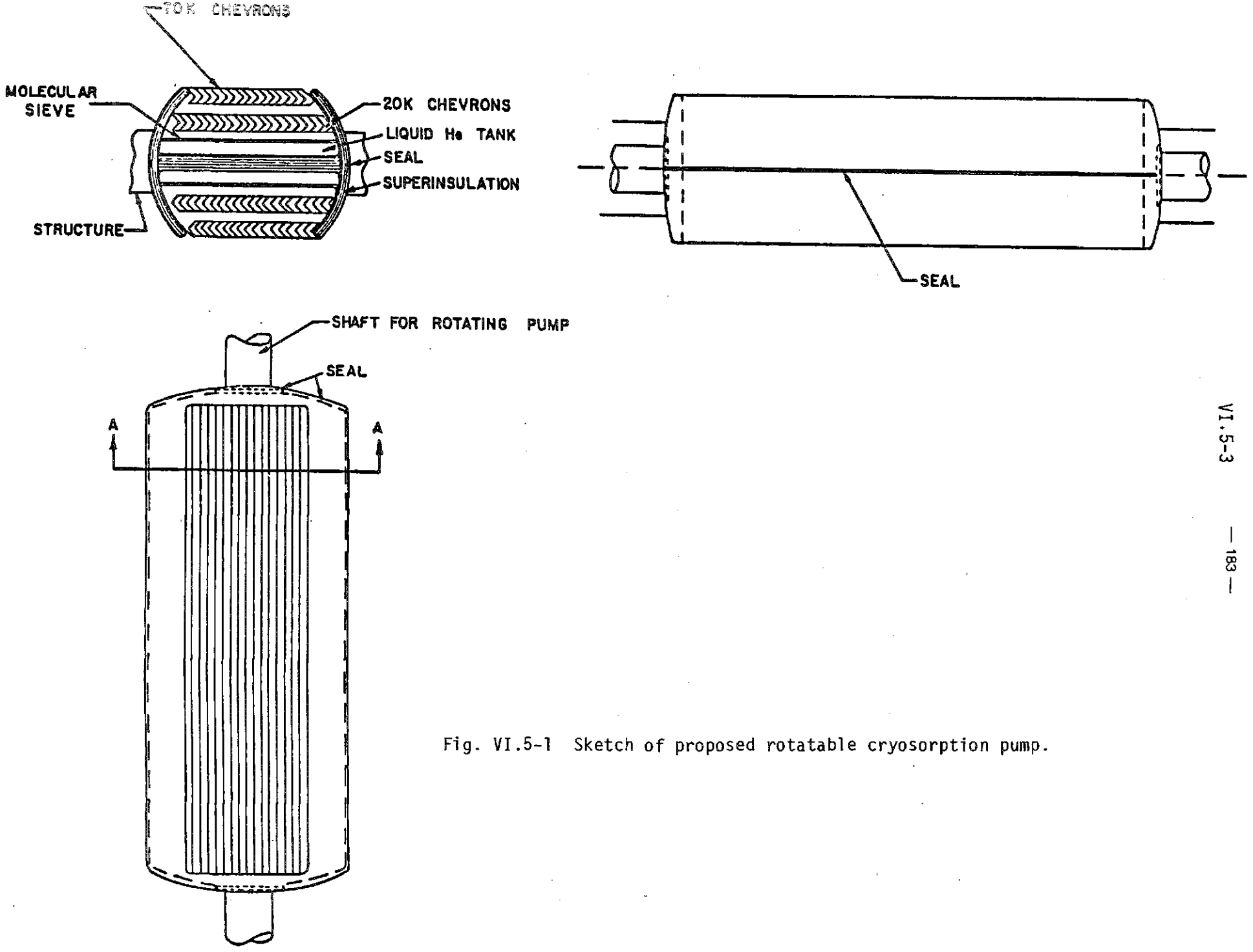

Fig. VI.5-1 Sketch of proposed rotatable cryosorption pump.

rectangular ducts of the same dimensions, leading to cryopumps located in the upper corners of the cavity as shown in Fig. VI.5-2. These pumps are well out of the radiation field and Monte Carlo analysis has shown that the effect of neutron streaming on them is negligible.

VI.5.2 Pumping of Non-Condensable Species

Table VI.5-1 gives the source and species of the non-condensable gas load.

At the initial gas temperature in the cavity (1 eV) of ~ 10,000 K, the non-condensables constitute a gas load of:

D_2 = 320 torr. ℓ/shot

T_2 = 265 torr. ℓ/shot

He = 326 torr. ℓ/shot

The vacuum ducts are assumed to be about 400°C in order to condense any PbLi vapor that they admit. At this temperature the throughput becomes:

D_2 = 108 torr. ℓ/sec.

T_2 = 89 torr. ℓ/sec.

He = 110 torr. ℓ/sec.

The conductance of a short duct (L < 25 r) for molecular flow is given by the relationship:[3]

$$\frac{1}{C_{duct}} = \left(\frac{3}{16}\frac{LU}{A^2} + \frac{1}{A}\right)\sqrt{\frac{2\pi M}{RT}}\,\frac{sec}{cm^3}$$

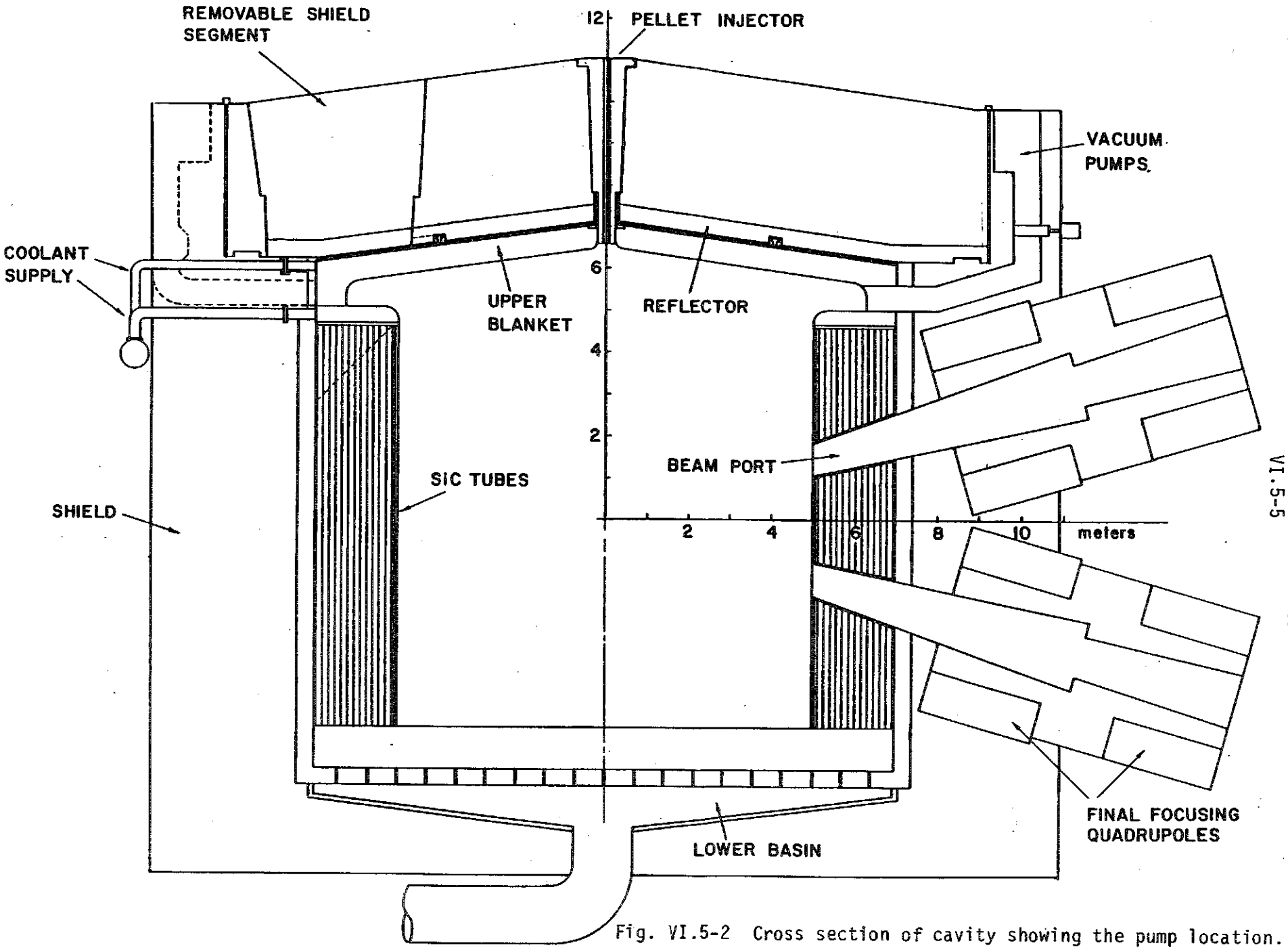

Fig. VI.5-2 Cross section of cavity showing the pump location.

Table VI.5-1

Source	Species	Atoms/Shot	Total (atoms/shot)
Target Injector	D	2.83×10^{20}	
Unburned Fuel	D	3.4×10^{20}	6.23×10^{20}
Unburned Fuel	T	3.4×10^{20}	
Newly Bred	T	1.76×10^{20}	5.16×10^{20}
DT Reaction	He	1.4×10^{20}	
T_2 Breeding	He	1.76×10^{20}	
T_2 Decay	He	1.9×10^{11}	3.16×10^{20}

where C_{duct} is the conductance of the duct in cm^3/sec, L the length in cm, A the cross-sectional area in cm^2, U the perimeter in cm, M the molecular weight in gms., R the gas constant (8.3×10^7 ergs/mole) and T the temperature in degrees Kelvin.

For the given duct area of 65×120 cm^2, L = 450 cm, M = 5 for D_2T_2 and taking T = 673 K we get:

$$C_{duct} = 6.6 \times 10^7 \text{ cm}^3/\text{sec} = 6.6 \times 10^4 \text{ ℓ/s} .$$

For 30 ducts the conductance is:

$$C_{D_2T_2} = 2 \times 10^6 \text{ ℓ/s}$$

$$C_{He} = 2.2 \times 10^6 \text{ ℓ/s} .$$

The area available for locating the cryopumps is ~ 85 m^2 and the utilization factor for back to back pumps is ~ 85%. The total pumping speeds (using 5 ℓ/s cm^2 for D_2, T_2 and 2 ℓ/s cm^2 for He) are then:

$$S_{D_2T_2} = 3.6 \times 10^6 \text{ ℓ/s}$$

$$S_{He} = 1.44 \times 10^6 \text{ ℓ/s} .$$

The effective pumping speed is obtained from:

$$\frac{1}{S_{eff.}} = \frac{1}{S_p} + \frac{1}{C_{duct}}$$

where S_p is the pump speed and C_{duct} the conductance of the ducts. The effective pumping speed is then:

$$S_{eff.\ D_2\ T_2} = 1.3 \times 10^6 \text{ ℓ/s}$$

$$S_{eff.\ He} = 8.7 \times 10^5 \text{ ℓ/s} .$$

Using the throughputs obtained earlier, the equilibrium pressures of the non-condensable species in the cavity at 400°C are:

$$P_{D_2T_2} = \frac{(108+89) \text{ torr ℓ/s}}{1.3 \times 10^6 \text{ ℓ/s}} = 1.5 \times 10^{-4} \text{ torr}$$

$$P_{He} = \frac{110 \text{ torr ℓ/s}}{8.7 \times 10^5 \text{ ℓ/s}} = 1.3 \times 10^{-4} \text{ torr} .$$

The equivalent pressure rise/shot at 400°C consistent with a cavity volume of 900 m^3 is 4.4×10^{-5} torr for D_2T_2 and 2.5×10^{-5} torr for He. The time needed to evacuate the chamber to the equilibrium pressure is given by:

$$t = \frac{V}{S_{eff.}} \text{Ln} \frac{P_1}{P_2}$$

where t is the time, V the cavity volume, $S_{eff.}$ the effective pumping speed, P_1 the pressure in the cavity after a shot and P_2 the equilibrium pressure. For both D_2, T_2 and He, it is found that the time needed to reach equilibrium pressure is less than 200 msec. Thus, from the standpoint of reconditioning the chamber with respect to the non-condensable species, a repetition rate of 5 Hz is reasonable.

VI.5.3 Effect of PbLi Vapor on the Vacuum Ducts

It was mentioned earlier that the walls of the vacuum ducts will be maintained at 400°C. At this temperature, the surfaces are essentially black to PbLi vapor, and will condense it immediately upon contact. There will not be a boundary layer developed and the vapor will obey molecular flow conditions. For this reason we feel that all the PbLi vapor which enters the vacuum ducts will be condensed before it reaches the cryopumps. Since it will be maintained molten, the PbLi will be returned to the cavity and will rejoin the bulk of the breeding material. The surfaces in the vicinity of the cryopumps will be cooled to ~ 70 K with liquid N_2 and they will certainly cryotrap any itinerant PbLi molecules before they can contaminate the hydrogen and helium pumping surfaces. Since we feel this quantity of frozen PbLi will be very small, a periodic regeneration, perhaps every 6 months, will be adequate to prevent excessive buildup.

VI.5.4 Effect of Cavity Atmosphere on the Beam Lines

The beam lines' interface with the reactor cavity presents some unique problems to the beam line vacuum system. Because the pressure in the cavity during operation never gets below 10^{-4} torr, it represents a continuous gas load which is admitted into the beam lines. Beam stripping and charge exchange problems require that the beam line pressure be on the order of 10^{-7} torr. The storage rings themselves operate at vacuum on the order of 10^{-10} torr.

In the early stages of the study we had proposed rotating shutters in the beam ports in order to minimize the influx of PbLi vapor into the beam lines. The chief concerns were the accumulation of PbLi on the beam ducts amounting to ~ 30 tonnes/day for the 20 beams, and the migration of the vapor deep into the beam line system due to viscous effects. We have been reassessing this problem all along and have concluded that shutters may not be needed. There are two complimentary developments which have led to this conclusion; they are:

1. If the beam duct wall temperature can be carefully controlled such that the condensed vapor runs off in liquid form and is returned to the cavity, then accumulation ceases to be a problem.
2. With a sticking coefficient of unity on the beam duct walls, the vapor does not develop a boundary layer and there are no viscous effects from the walls. By using molecular flow theory, it is evident that the expanding vapor which enters the beam port is immediately condensed on the walls. It can be shown that the pressure can fall two orders of magnitude per meter of beam line if the narrow dimension of the line is < 40 cm.

Although the problem of PbLi vapor in the beam line needs a more rigorous analysis before it can be put to rest, for the present we will assume that the rotating shutters will not be needed.

The non-condensable species, however, will not condense on the beam line walls but will proceed further into the beam lines. The conductance of a beam line for D_2, T_2 and He at 673 K is estimated at $\sim 2.8 \times 10^3$ ℓ/s which gives rise to a throughput of $\sim 2.8 \times 10^{-1}$ torr ℓ/s. For this gas load to be pumped at 10^{-6} torr requires a cryopump system with a capacity of 2.8×10^5 ℓ/s, namely ~ 5.6 m^2 of cryosurface for each beam line. Differential pumping downstream from the main beam line pumping station will quickly reduce the pressure to the prescribed value of 10^{-7} torr and lower.

The main beam line pumping station will be located between the second and third focusing quadrupoles, where a distance of 2 m was allowed for this purpose. We envisage the same kind of back to back cryopumps proposed for the cavity vacuum system to be used in the beam lines as well.

References for Section VI.5

1. B. Badger et al., "NUWMAK - A Tokamak Reactor Design Study," UWFDM-330, Fusion Engineering Program, Nuclear Engineering Dept., University of Wisconsin, Madison, March 1979.

2. B. Badger et al., "WITAMIR-I, A University of Wisconsin Tandem Mirror Reactor Design," UWFDM-400, Fusion Engineering Program, Nuclear Engineering Dept., University of Wisconsin, Madison, Sept. 1980.

3. H.A. Steinherz, "Handbook of High Vacuum Engineering," Reinhold Publishing Corporation, New York, 1963.

VI.6 Flow Characteristics

The coolant and breeding material in HIBALL is $Li_{17}Pb_{83}$. This material is chosen for its high breeding potential, low tritium inventory and inertness with water.(1) The coolant in HIBALL also serves a unique function, that of protection of the first structural surface from X-ray bombardment. It is critical, therefore, that $Li_{17}Pb_{83}$ will form a continuous layer of film outside the coolant tubes. One of the reasons for using braided SiC coolant tubes is that there is enough open space in between the SiC fibers so that $Li_{17}Pb_{83}$ can weep out to form this protection layer. This protection layer has to be regenerated after each shot. Since this layer is directly exposed to the cavity, the maximum allowable temperature is determined by the allowable vapor pressure in the cavity.

The heat transfer problem for the coolant tubes directly exposed to the plasma is completely different from those in the back. The front tubes are subjected to a large surface heat load and, therefore, require a large heat transfer coefficient. Therefore, a high velocity is required. The back tubes are only subjected to energy deposited by neutrons and, therefore, the heat is deposited in the coolant. A low velocity is preferred here to increase the coolant temperature rise and thus reduce the coolant mass flow rate. One of the major objectives of the INPORT tubes is to reduce the flow rate so that the coolant pumping power can be reduced.

The coolant flow pattern, the heat transfer considerations and the stress effect due to the sudden neutron deposition is discussed in this section. The first wall protection from the X-ray deposition, the condensation, and re-evaporation of the protection layer is discussed in section VI.4. The important thermal-hydraulic parameters for HIBALL are summarized in Table VI.6-1.

Table VI.6-1 Thermal Hydraulic Parameters for HIBALL

(For One Cavity)

Structural Material	HT-9, SiC
Coolant and Breeding Material	$Li_{17}Pb_{83}$
Total Thermal Power	2538 MW
Coolant Inlet Temperature	338°C
Coolant Exit Temperature	500°C
Maximum First Surface Temperature	500°C
Maximum First Surface Coolant Temperature	400°C
Maximum Structural Temperature	530°C
Maximum Coolant Velocity	7.5 m/sec
Coolant Flow Rate	3.38×10^8 kg/hr
Total Coolant Pressure Drop	2.0 MPa
Coolant Pumping Dower Required	19 MW
Maximum Blanket Coolant Pressure	.07 MPa
Shield Coolant	Water
Coolant Temperature	45 ~ 60°C
Coolant Flow Rate	3.6×10^5 kg/hr
Maximum Shield Temperature	60°C
Estimated Steam Generator Surface Area	1.3×10^4 m^2
Estimated Steam Condition	
Temperature	482°C
Pressure	15.5 MPa
Flow Rate	4.5×10^6 kg/hr
Gross Thermal Efficiency	.42

VI.6.1 Coolant Flow Pattern

The coolant flow pattern is shown in Fig. VI.6-1 with the upper blanket design shown in Fig. VI.6-2. The coolant enters the reactor at 330°C. A fraction of the coolant will cool the top blanket and exit from the top blanket at 400°C. This coolant will enter the back section of the tube region

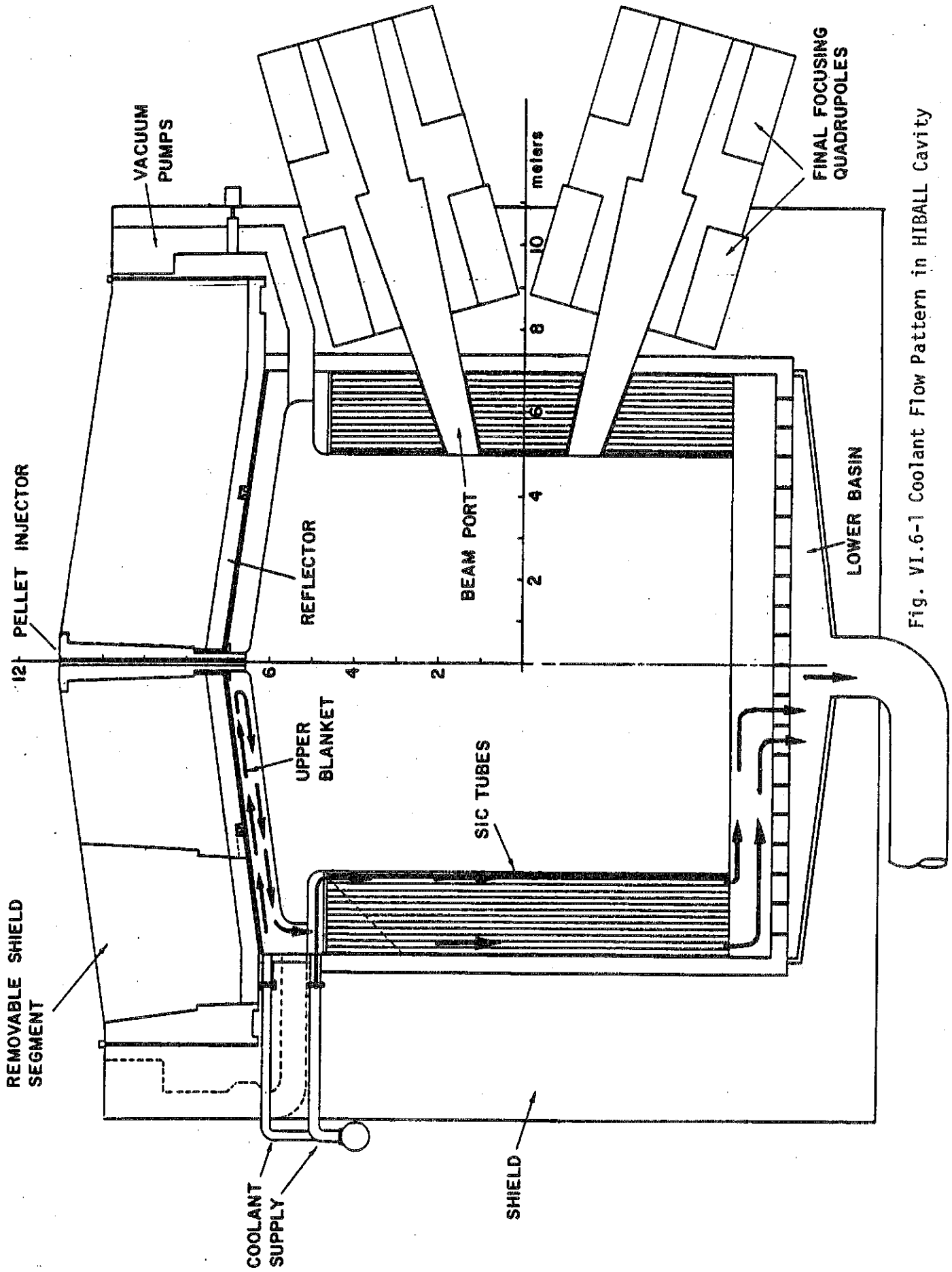

Fig. VI.6-1 Coolant Flow Pattern in HIBALL Cavity

DESIGN OF AN UPPER BLANKET SEGMENT

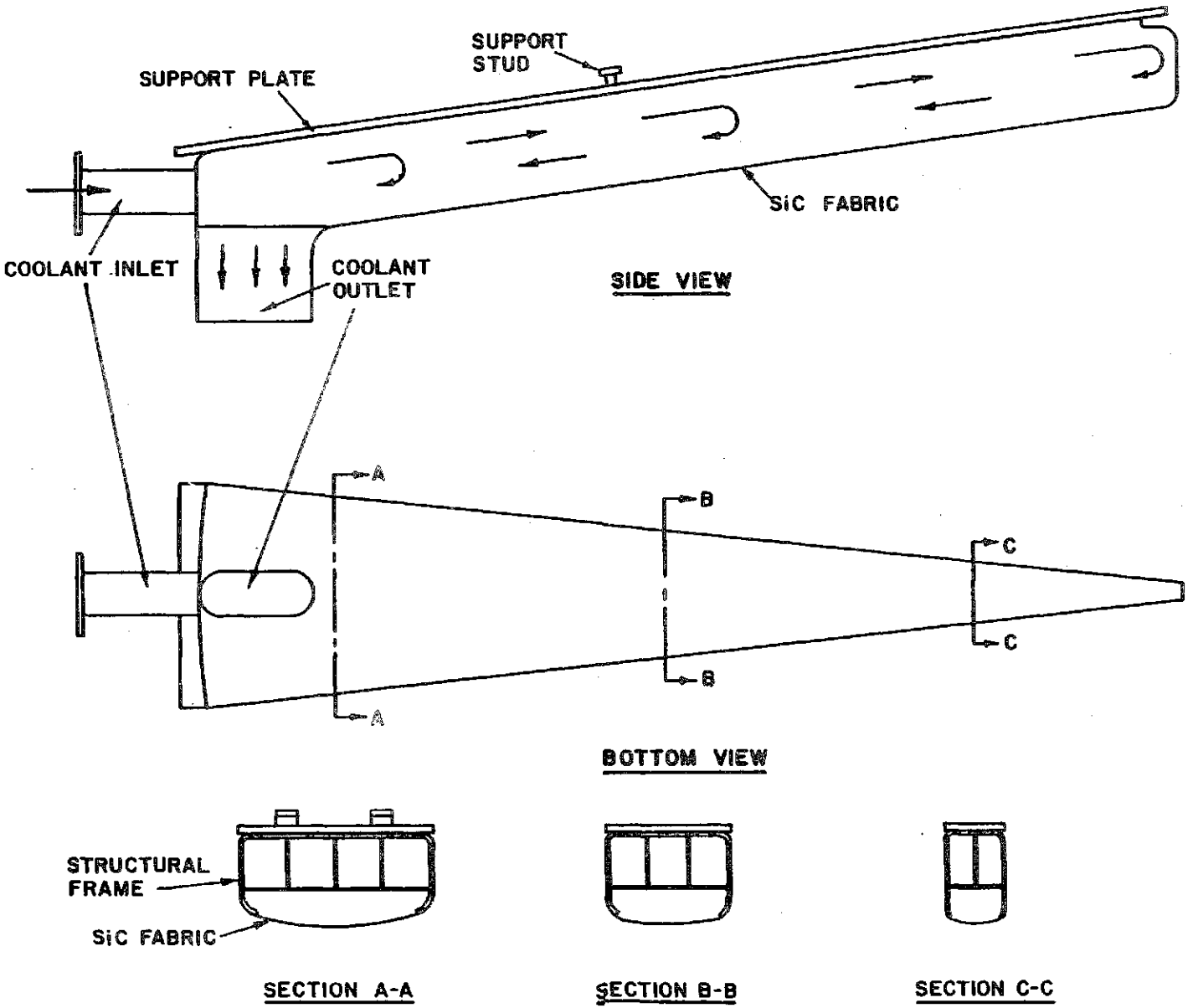

Fig. VI.6-2

and exit from the tube region with a temperature of 500°C. Another fraction of the coolant will cool the row of tubes facing the plasma, then exit from the tube region with a temperature of 400°C. This coolant will be heating the bottom part of the cavity and exit from the reactor also at 500°C. The maximum coolant temperature at the first surface is 400°C.

The basic design philosophy in the coolant flow pattern is to insure a uniform coolant exit temperature. The maximum allowable structural temperature is estimated to be 530°C, and the coolant exit temperature should be as close to this temperature as possible so that a high thermal conversion efficiency can be insured. The coolant entrance temperature is a compromise between the power cycle requirement and the coolant freezing temperature consideration. The 170°C coolant temperature rise is large enough to insure a reasonable coolant flow rate.

VI.6.2 First Surface Heat Transfer Considerations

The first surface of a D-T fusion reactor receives ~ 20% of the total energy in various forms. This heat is deposited in the form of surface energy. A severe heat transfer problem exists in this area. In an inertially confined system, the surface energy will be deposited in a pulsed form and may cause excessive ablation problems. The non-uniform heat deposition on the first surface and its associated problems are discussed in section VI.4. In this section, the heat transfer problem on a time average basis is discussed.

The restrictions and conditions of the first surface of HIBALL are:

1. The maximum time average surface heating load is 172 W/cm^2.
2. Maximum temperature on the surface of the coolant tubes is 500°C due to vapor pressure considerations.
3. Maximum coolant velocity is 7.5 m/sec due to erosion considerations.

The exit coolant temperature has to be maximized under these limitations.

The energy deposited on the first coolant tubes can be divided into two categories, that of volumetric heating and surface heating. The volumetric energy deposition is caused by neutrons, while the surface energy deposition is caused by X-rays, debris and alpha particles. Because of the cylindrical geometry, the energy deposition is a function of distance from the center and is shown in Fig. VI.6-3. The maximum surface heating is 172 W/cm^2, which is very large. This surface heating rate will cause temperature drops across the protection layer, the tube wall and coolant boundary layer. The sum of these temperature drops has to be small enough to keep $T_{max} \leq 500^0C$.

The velocity required in the first tubes can be calculatd by an energy balance as shown in Fig. VI.6-4. To ensure good heat transfer and a minimum degradation of coolant temperature, it is necessary to keep the diameter of the first tubes as small as possible. The required coolant velocity, however, increases with decreasing coolant tube size and coolant temperature rise. To keep a velocity $\leq$ 7.5 m/sec, a coolant tube ID of 3 cm and a coolant temperature rise of 70°C are required.

The surface temperature of the first coolant tube can be calculated as a function of combined thickness of $Li_{17}Pb_{83}$ film and coolant tube wall. The maximum allowable temperature on the surface is 500°C. The calculated results are shown in Fig. VI.6-5. The maximum temperature occurs at the middle point of the cylinder due to the maximum surface heat deposition, as shown in Fig. VI.6-5. It is clear that the total wall thickness has to be $\leq$ 1.5 mm without exceeding the maximum allowable surface temperature. This calculation defines the first tube coolant parameters, as listed in Table VI.6-2.

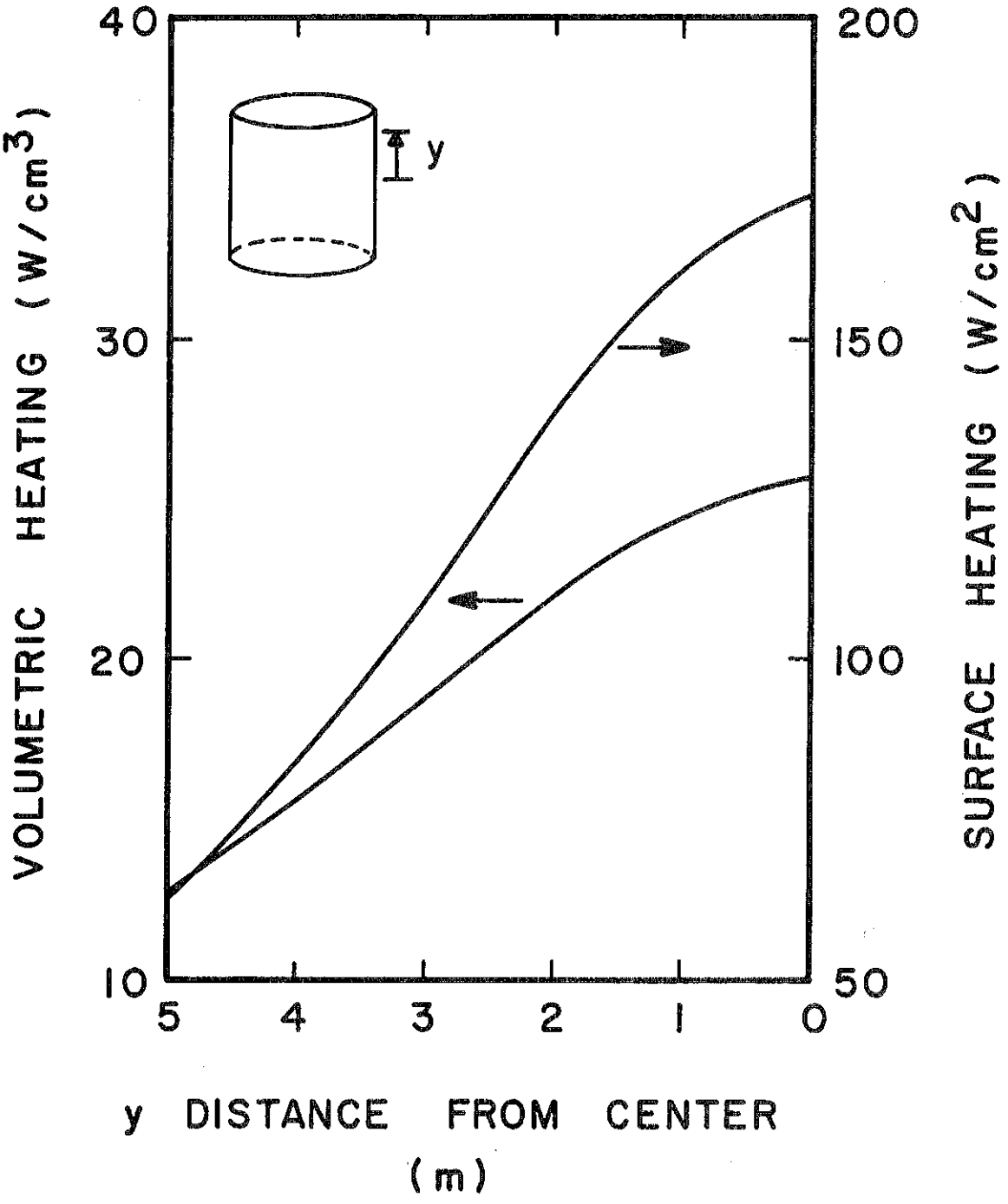

Fig. VI.6-3 Energy Deposition Along the First Coolant Tube

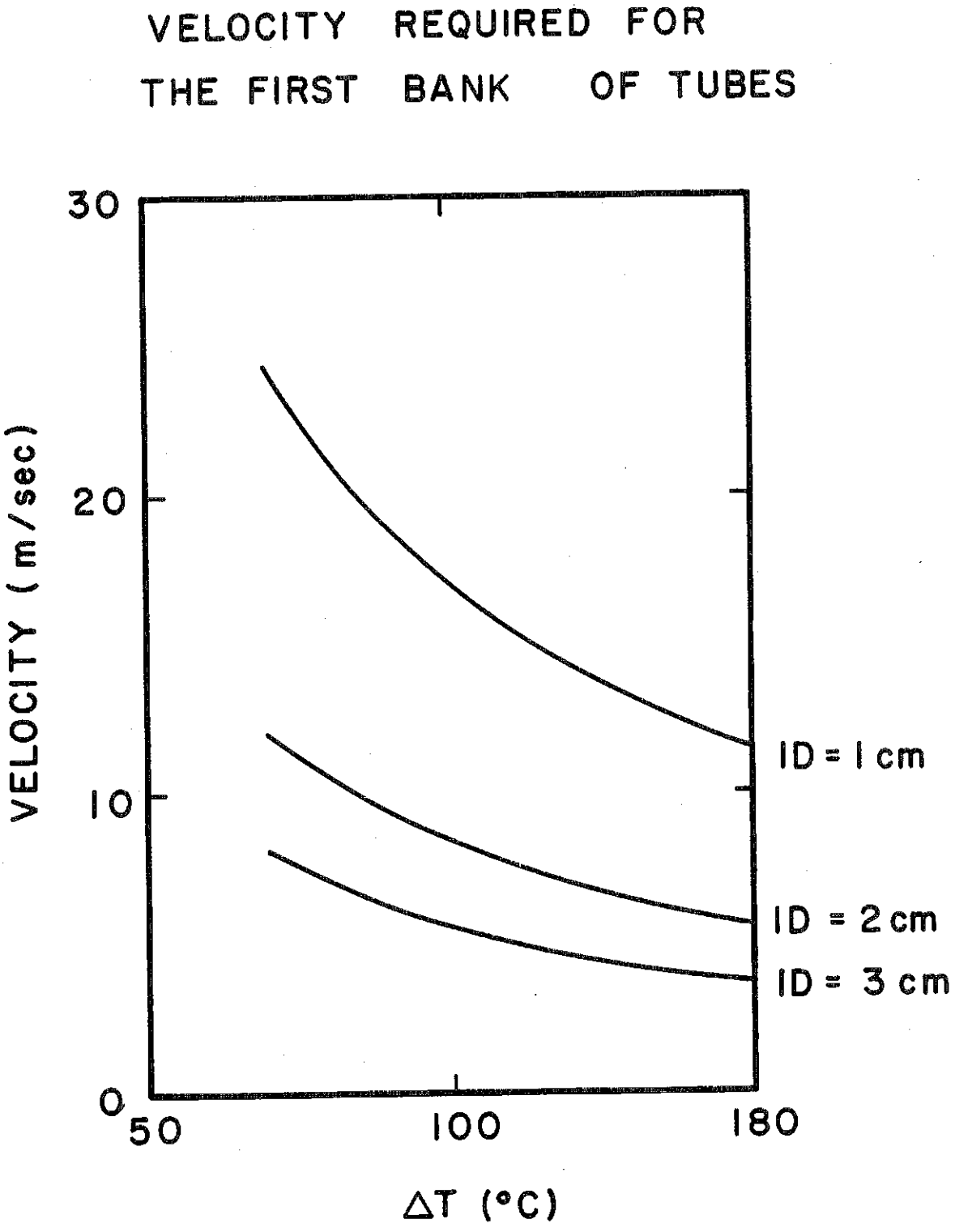
VELOCITY REQUIRED FOR
THE FIRST BANK OF TUBES
VELOCITY (m/sec)
30
20
10
0
50
100
180
ΔT (°C)
ID = 1 cm
ID = 2 cm
ID = 3 cm

Fig. VI.6-4

Fig. VI.6-5 First Surface Temperature as a Function of First Surface Thickness and Coolant Temperature Rise

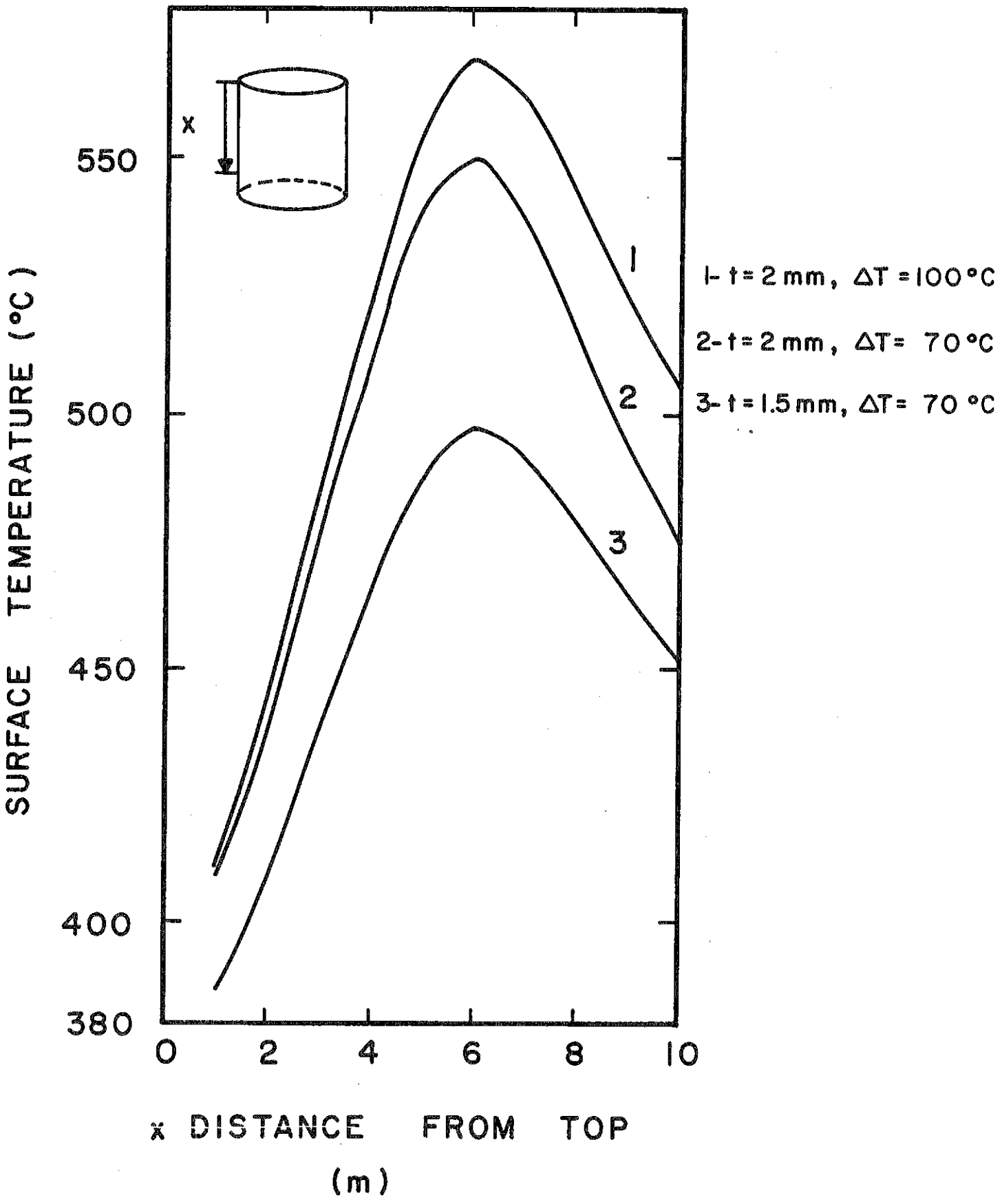

Table VI.2-2

System Parameters for First Flow of Coolant Tubes

Tube I.D.	3 cm
Total Tube Wall Thickness (including $Li_{17}Pb_{83}$ layer)	1.5 mm
Maximum Surface Heat Flux	17.2 W/cm^2
Maximum Volumetric Heat Deposition	25 W/cm^3
Coolant Tube I.D.	3 cm
Coolant Tube Thickness (including $Li_{17}Pb_{83}$ layer)	1.5 mm
Coolant Velocity	7.5 m/sec
Maximum Surface Temperature	500°C
Minimum Surface Temperature	380°C
Maximum Vapor Pressure of $Li_{17}Pb_{83}$	10^{-5} Torr

VI.6.3 Effect of Expansion Due to Sudden Nuclear Energy Deposition

A unique phenomena in an inertially confined system is caused by the sudden deposition of energy. The rapid thermal expansion caused by the temperature rise will send a shock wave outward. If a tube with a radius of r is subjected to a temperature rise of ΔT, the radius change can be written as

$$dr = r\beta\Delta T/2$$

in which β is the linear thermal expansion coefficient or

$$v = \frac{dr}{dt} = r\beta\Delta T/(2\ dt)$$

in which dt is the time for energy deposition.

For the first tubes in HIBALL

$$\Delta T = q_{max}/5\rho c_p$$
$$= 3.4^0 C/\text{shot}$$
$$dt = 10^{-6} \text{ sec}$$
$$\beta = 7.4 \times 10^{-5}/^0C$$
$$r = 1.5 \text{ cm} .$$

Therefore,

$$dr = 2 \times 10^{-4} \text{ cm}$$
$$v = 200 \text{ cm/sec} .$$

The pressure on the coolant tube caused by this sudden outward expansion can be calculated by

$$p = \frac{\rho}{2g} v^2$$

in which ρ is the density of the material.

The pressure calculated for the INPORT tubes is only 3 psi and is readily acceptable. However, similar calculations show that under different conditions, such as those in HYLIFE,[2] the sudden deposition of neutron energy can have a large impact on the reactor design. This is caused by a large coefficient of expansion for lithium and a larger ΔT/shot due to the lower repetition rate.

References for Section VI.6

1. D.K. Sze, R.G. Clemmer and E.T. Cheng, "LiPb, A Novel Material for Fusion Applications", the Fourth Topical Meeting on the Technology of Controlled Nuclear Fusion, King of Prussia, PA, Oct. 1980

2. J. Maniscalco, et al., "A Laser Fusion Power Plant Based on a Fluid Wall Reactor Concept", The Third Topical Meeting on the Technology of Controlled Nuclear Fusion, May 1978, Santa Fe, NM.

VI.7 Support Mechanism and Stress Considerations

VI.7.1 General Description

The SiC tubes are designed to be suspended from the top such that they hang freely. They are attached to an upper support plate which also is the coolant distribution manifold. Restraint against lateral motion is provided by a support plate on the bottom which also contains the flow control nozzles.

The cylindrical blanket zone is divided into 30 modules, each subtended by 12° of cavity circumference. Each module consists of the upper distribution manifold and tube support plate, the tubes themselves and the bottom support plate. Ten of the 30 modules fall in line with the cavity beam ports. These modules will have beam tubes built in as part of the units.

The first two rows which are 4 cm apart consist of tubes which are 3 cm in diameter spaced at ~ 5.1 cm center to center. There are 41 such tubes in each module. The remaining tubes which are 10 cm in diameter follow behind. These tubes are arranged on a 12.5 cm triangular pitch in between support struts as shown in Fig. VI.7-1. There are 102 such tubes in each module.

Several schemes for attaching the tubes to the upper support plate were considered, two of which are shown in Fig. VI.7-2(a) and Fig. VI.7-2(b). In Fig. VI.7-2(a) a bead is woven into the tube at the end. This bead is then captured between a threaded conical flange and the upper plate. Figure VI.7-2(b) shows several plies of the braided fabric encircling a conical restraining ring. The tube is simply inserted from the top through the hole and is held in place by the conical ring.

The upper tube support plate is welded to struts which anchor into the 40 cm thick reflector wall. The sections at the end of each strut slide into milled slots in the reflector. Pulling up on the upper manifold which is part of the tube support plate disengages the module from the reflector. This

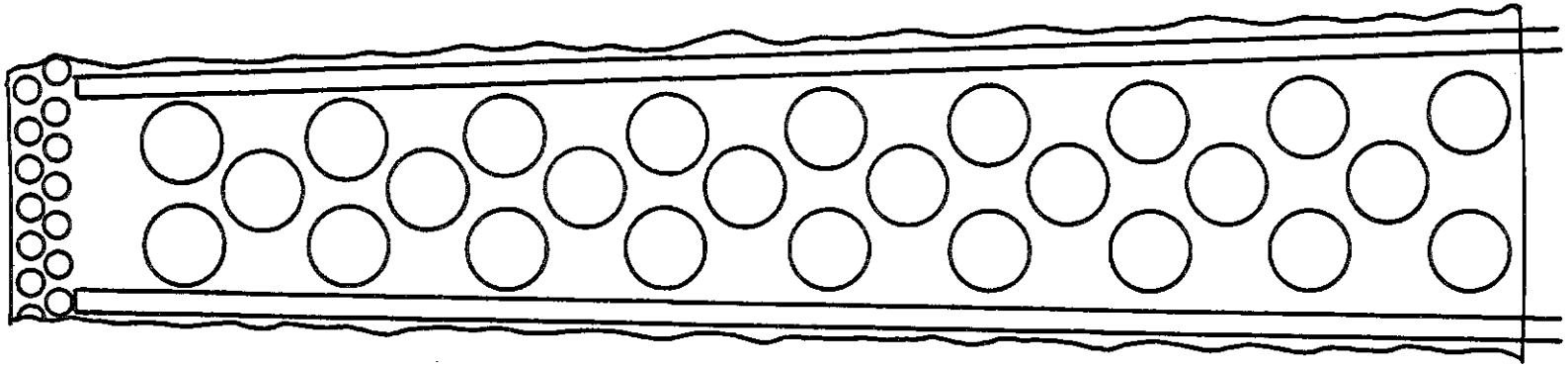

Fig. VI.2-1 Distribution of INPORT tubes between support struts.

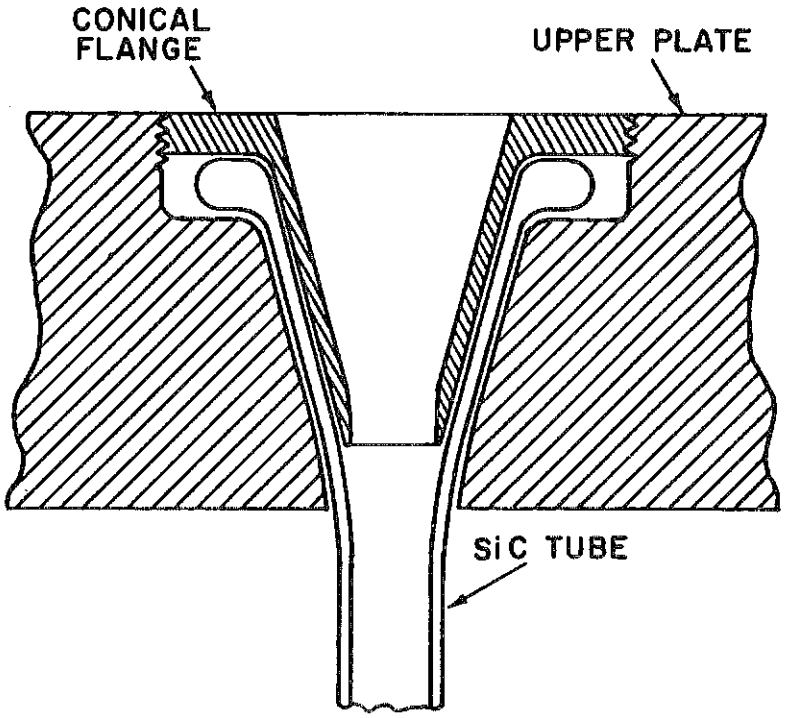

Fig. VI.2-2a

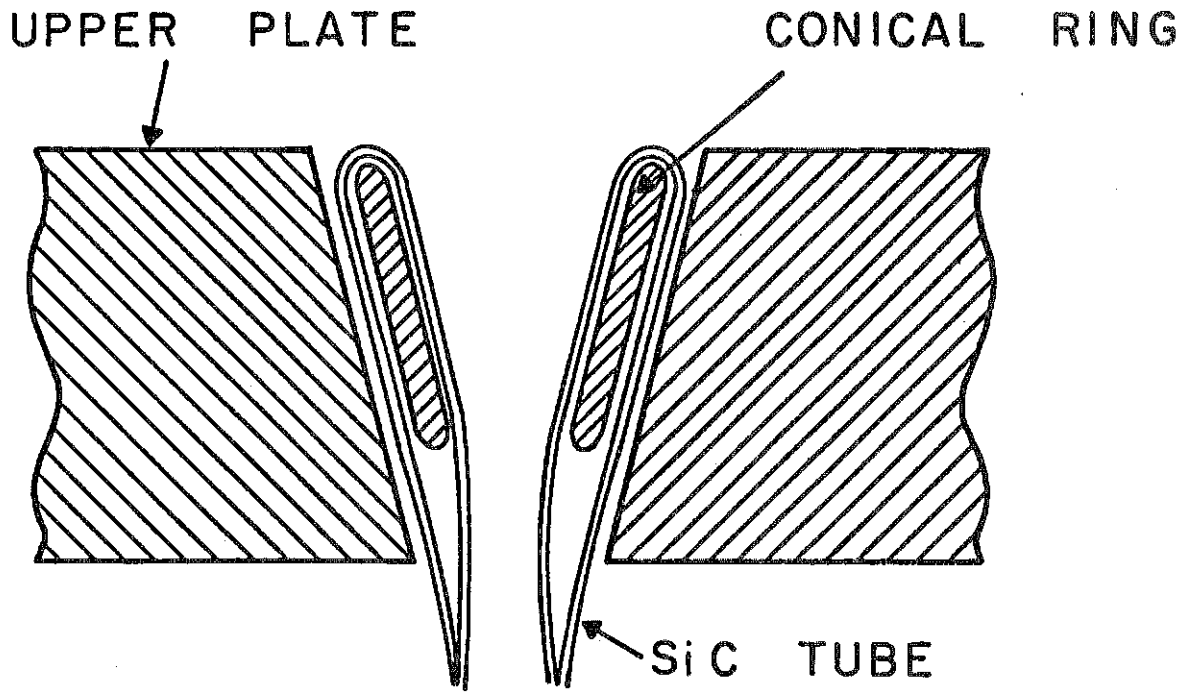

Fig. VI.2-2b

Two methods for attaching INPORT tubes.

attachment scheme is needed for maintaining the blanket modules and will be discussed in a later section.

VI.7.2 INPORT Tube Stresses

The stresses in the SiC tubes can be divided into two parts, the longitudinal and the circumferential stresses. Circumferential stresses are from the pressure of the coolant and vary linearly from the top to the bottom as a function of the supported head. The longitudinal stresses consist of two components, the pressure component and the dead weight (weight of the coolant) component. The former component is small at the top and builds up linearly to the bottom while the latter component is maximum at the top and falls off linearly to zero at the bottom.

A reliable value for allowable stress is not known for braided SiC tube construction. However, estimates can be made based on experience with other composite materials. Various sources give SiC fiber strength of 2450-3720 MPa (355-540 ksi). Strength depends on fiber diameter and when braided into a tube, the fiber strength is reduced substantially. Experience with graphite material systems indicates that the strength for orthogonal layup could be ~ 276 MPa (40 ksi) considering each principal stress individually. Ceramic materials typically have a wide variation in strength due to their extreme sensitivity to minute flaws. Because of this sensitivity a safety factor of two was taken and thus the maximum allowable stress is 139 MPa (20 ksi).

In this design the wall thickness for the 10 cm diameter tubes is 2.25 mm and in the 3 cm diameter tubes it is 0.9 mm. This means that there will be 5 plies and 2 plies in the 10 cm and 3 cm diameter tubes respectively (the thickness per ply is 0.45 mm). The fibers in the orthogonal layup are oriented at 45° and cover 50% of the available surface area. The fibers themselves are made up of filaments with a density factor of 75%.

In calculating the stresses, it was assumed that the incoming coolant had an initial presure of 0.1 MPa (~ 15 psi). At the bottom of the tubes the added head produces a pressure of 1.04 MPa (150 psi). The masses supported by the tubes are 700 kg and 61.3 kg for the 10 cm and 3 cm diameter tubes, respectively. Stress distribution as a function of tube distance from the top is given in Fig. VI.7-3 and Fig. VI.7-4 and numerically in Table VI.7-1. The principal circumferential and longitudinal stresses are amplified by a factor of 1.4 because of the 45° orientation of the fibers in the orthogonal layup.

The total stress represents the sum of all the stress components. It can be seen that the maximum stress occurs at the bottom of the tubes and is 130 MPa (18.9 ksi) for the 10 cm tubes and 97 MPa (14 ksi) for the 3 cm tubes. The thickness of the wall in the front (3 cm) tubes is dictated by thermal hydraulic considerations. The 25% lower stress in these tubes is desirable because they will be subjected to impact loading from their reaction to the target implosion, as discussed in section VI.2.

Table VI.7-1

Stresses in INPORT (SiC) Tubes

Stress	TOP (MPa)		BOTTOM (MPa)	
	10 cm	3 cm	10 cm	3 cm
Longitudinal (Dead Weight)	36.2	26.2	0	0
Longitudinal (Pressure)	4.17	3.1	43.4	32.3
Circumferential (Pressure)	8.34	6.22	86.8	64.7
TOTAL (MPa)	48.71	35.52	130.2	97.0
(psi)	(7,060)	(5,147)	(18,870)	(14,060)

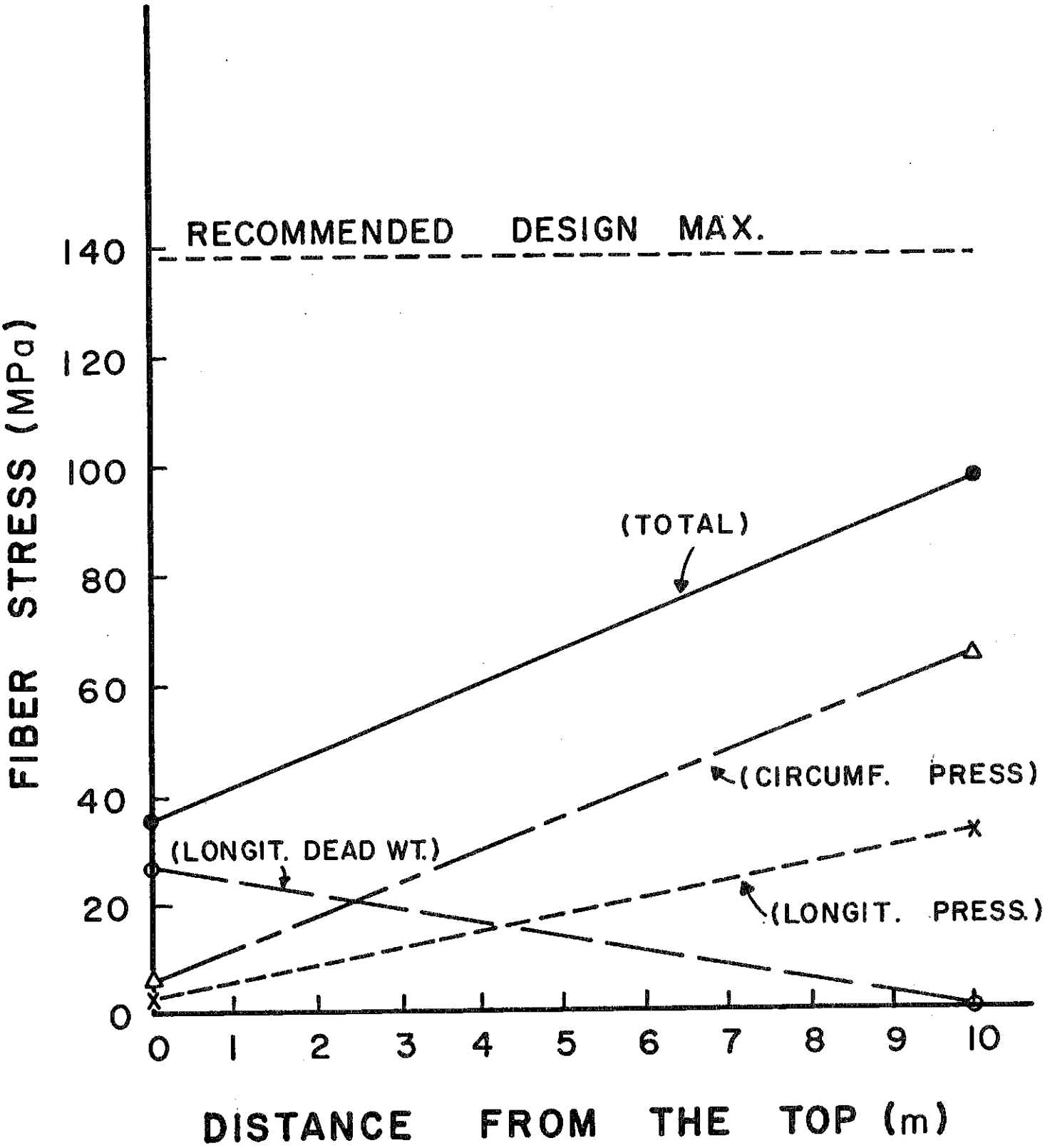

Fig. VI.2-3 Stresses in 10 cm diameter INPORT tubes.

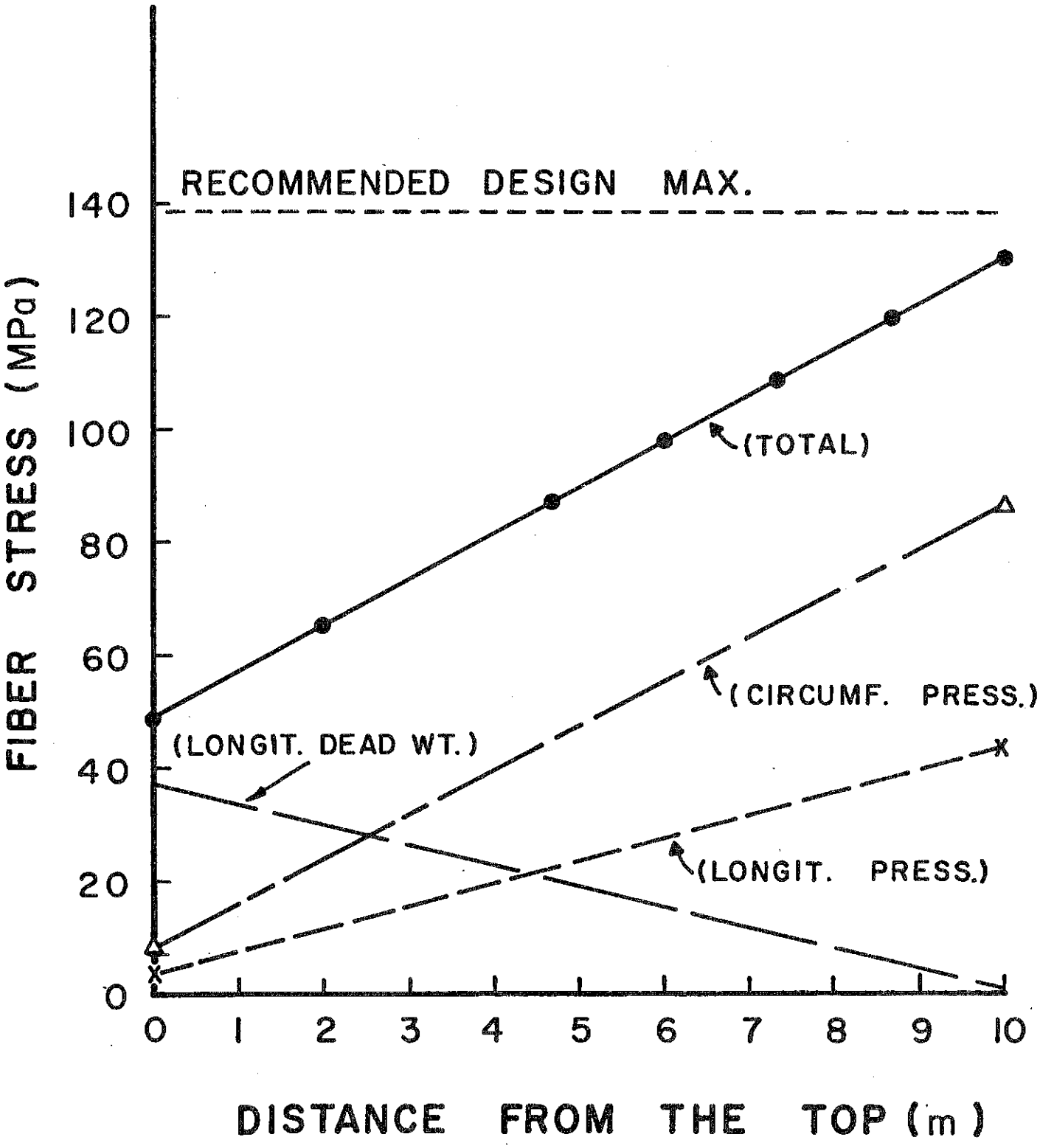

Fig. VI.2-4 Stresses in 3 cm diameter INPORT tubes.

VI.7.3 Tube Support

The tube support scheme has to be analyzed in two parts:

a) Analysis of the upper support plate

b) Analysis of the support struts

Figure VI.7-5 shows a top view and a side view of a single module support structure. It consists of an upper plate (the holes have been omited for simplicity) and struts which terminate in a tee section. These tee sections fit into slots milled in the cavity reflector. Thus, a module with integral tubes and bottom plate can be taken out by simply lifting on the assembly to disengage the tee sections from the reflector. The struts will have cooling passages such that $Li_{17}Pb_{83}$ will flow through them. After traversing the struts, the coolant then flows down the reflector side to the bottom pool.

It was decided to use four struts to support each module. The tube distribution between two struts is shown in Fig. V.7-6(a) and the loading on the plate in Fig. V.7-6(b). The upper support plate was modelled as a statistically indeterminate beam of varying cross sections and concentrated loads. The stress in the plate is then:

$$\sigma(x) = K \frac{M(x)C}{I(x)}$$

where K is a stress concentration factor taken as 2, M(x) the local moment, C is one-half of the plate thickness and I(x) the local moment of inertia. Using a maximum design stress of 70 MPa (10 ksi) for HT-9, we calculate a plate thickness of 3 cm.

Similarly, the struts were analyzed as cantilevered beams of varying cross section and a variable loading as shown in Fig. VI.7-7. The weight of the tubes is reacted by a moment on the tee sections and an upward force

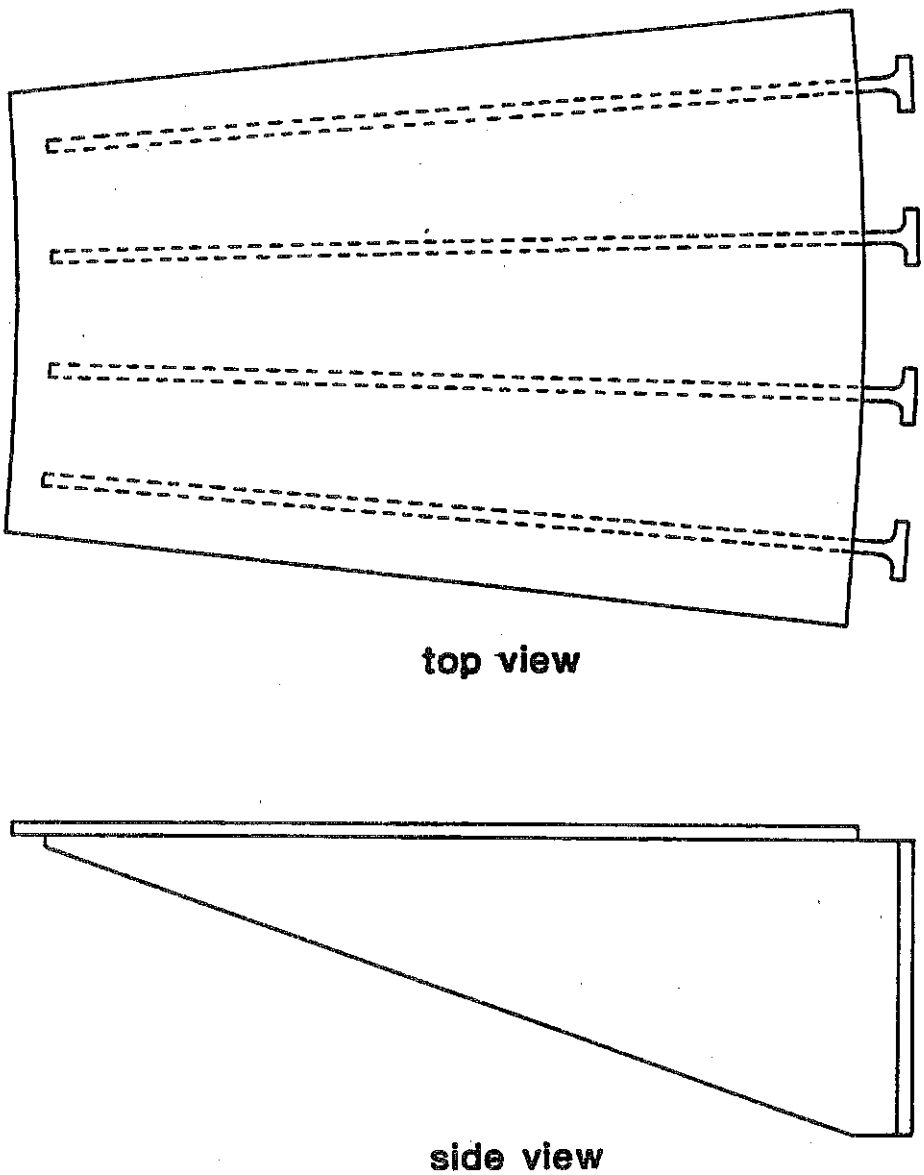

Fig. VI.2-5 Top and side views of upper support plate.

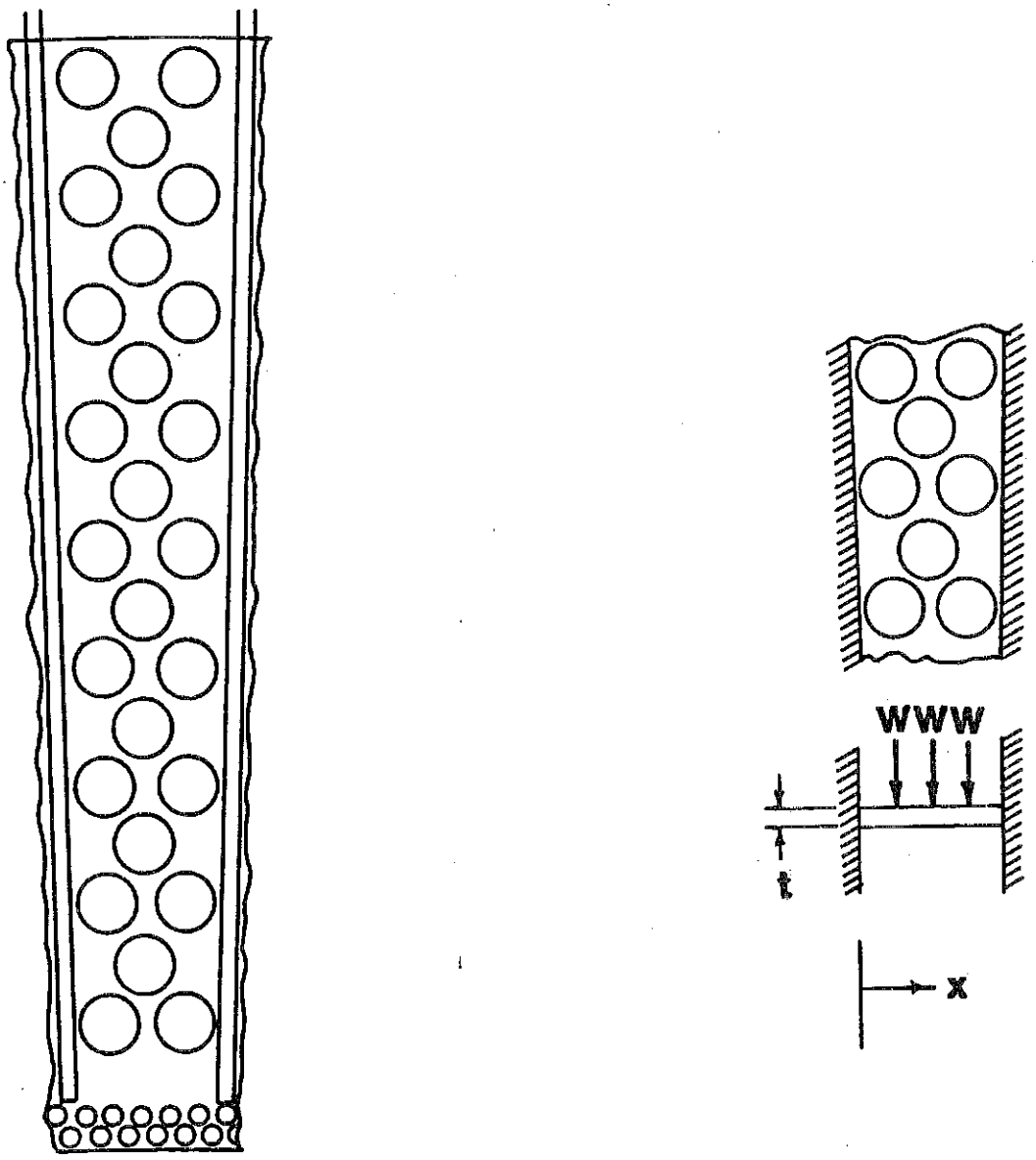

Fig. VI.2-6 (a) Tube distribution between support struts.
(b) Loads on upper support plate.

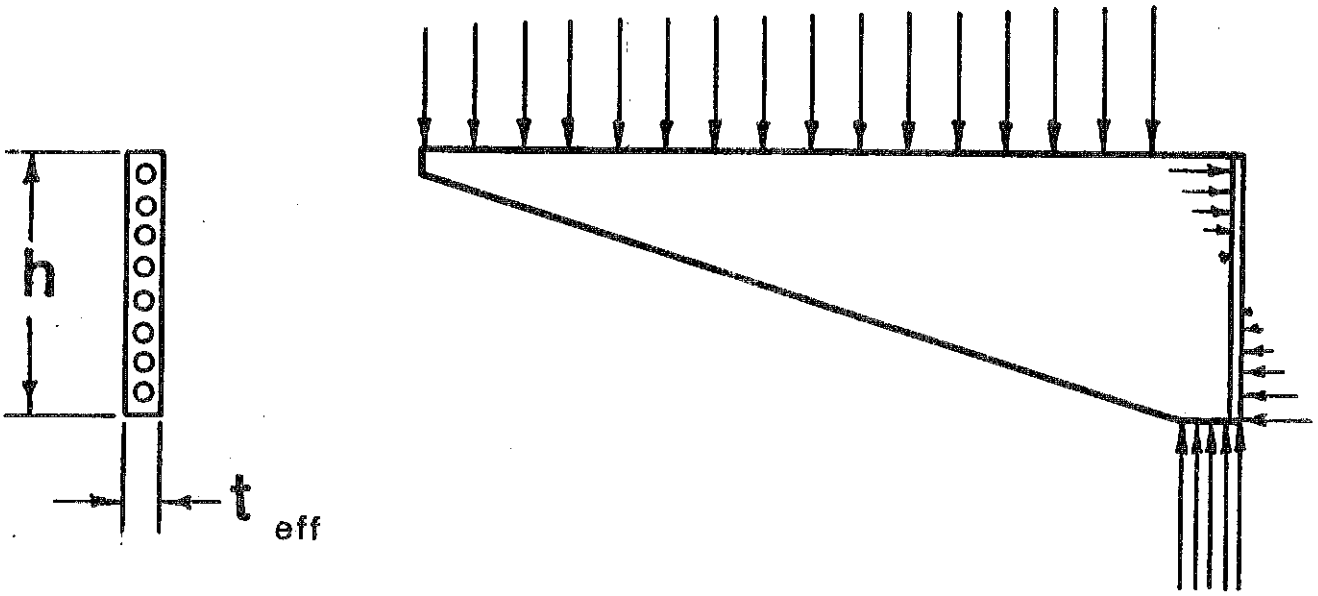

Fig. VI.2-7 Loading and reactions on support strut.

exerted by the reflector. The stress equation reduces to:

$$t_{eff.}\, h^2 = \frac{3wL^2}{\sigma_{max.}}$$

where t_{eff} is the strut effective thickness, h the depth of the strut in the back, w the loading per unit length and L = 180 cm. Substituting values we get

$$t_{eff.}\, h^2 \approx 14{,}700\ cm^3$$

and for h = 70 cm, the effective thickness of the strut is 3 cm. The maximum stress in the strut is at the point of attachment into the reflector. Table VI.7-2 summarizes the tube support parameters.

Table VI.7-2

Summary of Tube Support Parameters

Number of 3 cm tubes/module	41
Number of 10 cm tubes/module	102
Total mass/module (tonnes)	74
Max. allowable stress (MPa)	70
Number of struts/module	4
Effective strut thickness (cm)	3
Strut depth in back (cm)	70
Upper support plate thickness (cm)	3

VII Tritium

VII.1 Introduction and Overview

HIBALL is a heavy ion beam reactor composed of 4 chambers which produce a total power of 10,233 MW_t and a net electrical output of 3768 MW_e by focusing high energy Bi^{+2} ions on a cryogenic DT target. The cavity has a "wetted wall" design in which liquid metal flows down woven SiC INPORT tubes and "weeps" through the weaving, forming a layer of liquid on the tube surface. The liquid metal chosen, $Li_{17}Pb_{83}$, protects the INPORT tubes from the target explosion and serves as the coolant and breeding material. This section describes the tritium systems of HIBALL -- the tritium pathways are summarized in Fig. VII.1-1 and the inventories in the various reactor components are given in Table VII.1-1.

The reactor cavities are fueled with multilayer targets containing 4.0 mg DT, which are fired at a rate of 5 sec^{-1} per cavity. A one day fuel supply consists of 2.8 kg D and 4.1 kg T. The fraction of fuel burned is 0.29, thus 1.9 kg/d of deuterium and 2.9 kg/d of tritium are handled by the exhaust system. In addition, 2.8 kg/d of D_2, used to propel the target, and 1.5 kg/d of tritium bred by the $Li_{17}Pb_{83}$ will enter the exhaust processing system. The details of how the targets will be manufactured are unspecified, but recommendations are made on minimizing the tritium handling in target manufacture.

The chamber exhaust is pumped by compound cryopumps with on-line times of 2 hours and a tritium inventory of 0.37 kg. The pumps are regenerated so that helium is released first, then the hydrogen isotopes are released and sent to the fuel cleanup unit. The purpose of the fuel cleanup unit (T_{INV} = 0.041 kg) is to remove impurities from the hydrogen isotopes before sending them to the cryogenic distillation unit. (The distillation system consists of 4 columns (T_{INV} = 0.083) which separate the isotopes into an H stream which is vented, a

Hydrogen Isotope Pathways in HIBALL

- Flow Rates in kg/d
- All Four Reactor Cavities Included in Data

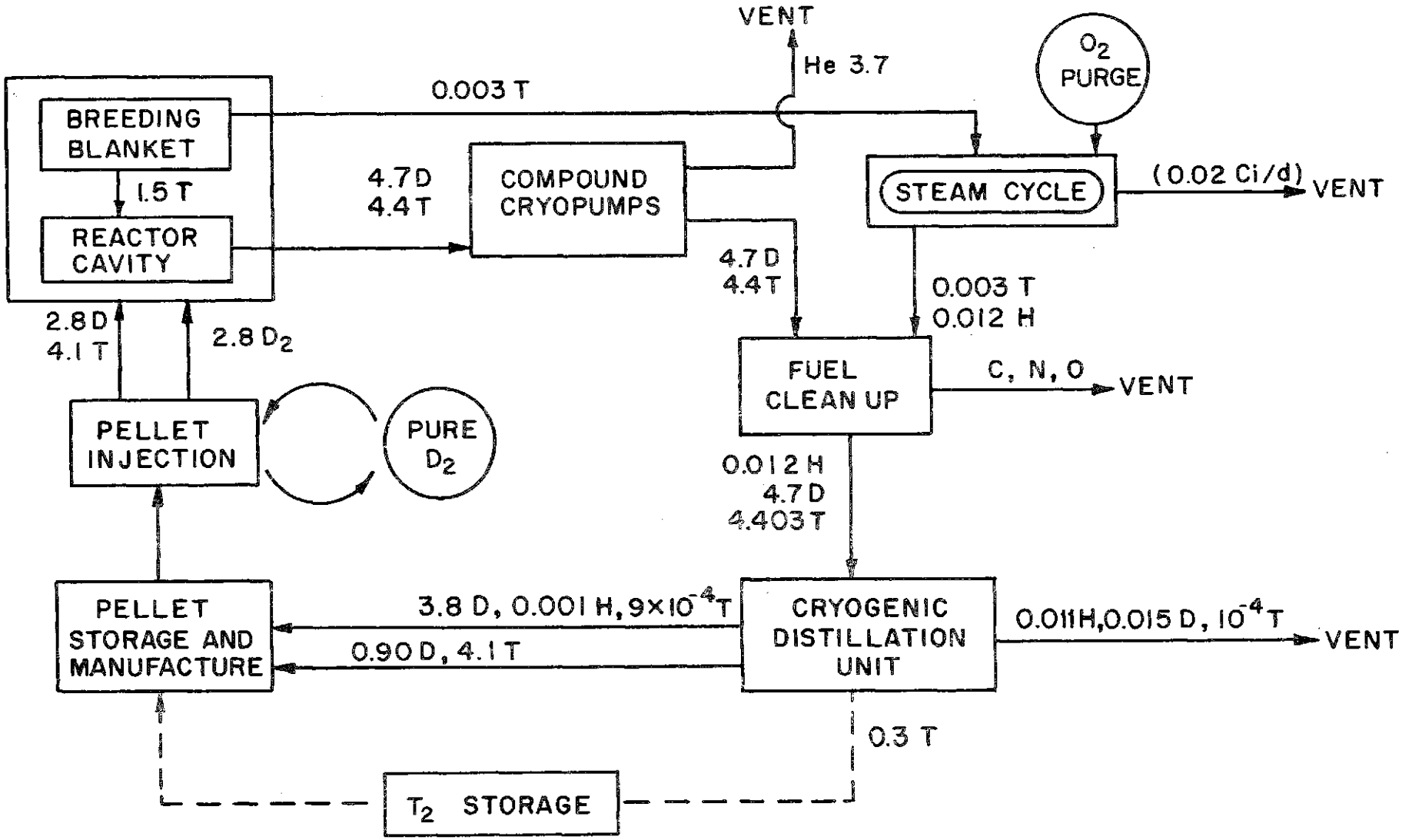

Fig. VII.1-1

Table VII.1-1 HIBALL Tritium Inventory

Fuel cycle (kg):		
Cryopumps	0.37	
Fuel cleanup	0.041	
Isotopic separation	0.083	
Subtotal		0.494
Blanket (kg):		
$Li_{17}Pb_{83}$ (cavity and reflector)	0.013	
SiC tubes	0.012	
Subtotal		0.025
Target manufacture (kg):	4.1	4.1
Storage (kg):		
Targets	4.1	
Uranium beds	4.1	
Subtotal		8.2
TOTAL INVENTORY (kg)		12.819
TOTAL ACTIVE INVENTORY (kg)		0.519

pure D_2 stream for the target injector, and a pure DT stream for the target factory and storage.

In the blanket system a low solubility of 7×10^{-2} wppm T in alloy/torr$^{1/2}$ results in an inventory of 0.013 kg T in the $Li_{17}Pb_{83}$ (1.9×10^7 kg). Tritium is bred at a rate of 4.4×10^{-6} kg/sec and extracted from the reactor chamber by pumping at pressures less than or equal to the vapor pressure of tritium above the eutectic (10^{-4} torr). The inventory in the silicon carbide tubes (1.6×10^4 kg) at 500°C is unknown, but has been approximated as 0.012 kg. Only very minimal amounts of silanes and hydrocarbons will form as the liquid metal protects the silicon carbide from interacting with hydrogen atoms.

The liquid metal is circulated into the heat exchange cycle. The tritium pressure above the eutectic is 10^{-4} torr, which causes a tritium containment problem in the steam cycle. The permeation of tritium through clean HT-9 results in a loss of 33.3 g T_2/day to the steam cycle. Oxide coatings or other tritium barriers can be used to reduce the permeation by factors of 10 to 100. With a design goal to limit tritium losses to 10 Ci/day, the steam generator is designed with double walled tubes purged with an oxygen atmosphere. This provides a very effective barrier limiting losses to less than 1 Ci/day. the tritiated water from the sweep gas is condensed and eventually merged with the reactor exhaust for reprocessing.

VII.2 Fuel Cycle

The HIBALL reactor is an inertial confinement fusion (ICF) device where the fusion reaction occurs by implosion of a cryogenic D-T target with 10 GeV Bi^{+2} ion beams. There are four reactor cavities with 20 bismuth ion beam ports per cavity. The target yield is 400 MJ at a gain of 83, with a repetition rate of 5 sec^{-1} per cavity and a total energy per fusion event of 17.6 MeV. This results in a total thermal power of 10,232 MW_t and a net electrical output of 3768 MW_e. The energy production in HIBALL is about three times higher than the energy produced from previous laser driven ICF reactor designs.[1] The fractional burnup (f_b) of the target is given by $f_b = T_b/(T_b + T_p)$, where T_b is the amount of tritium burned per day and T_p is the unburned tritium fuel that must be pumped out of the chamber per day. In the HIBALL reactor the fractional burnup is 29% which is comparable to other ICF reactor systems (20-40%).[1] At this point there has been no consideration of the possibility of misfirings.

Each reaction chamber is equipped with a target injection system and cryopumps. Exhaust from regeneration of the cryopumps from the four chambers is combined and sent into the fuel cleanup and processing system. The daily D-T fueling and exhaust characteristics of HIBALL are given in Table VII.2-1.

VII.2.1 Fueling

The HIBALL reactor is fueled by injection of a cryogenic DT target. The target consists of three shells: the equimolar DT fuel, a Li-Pb ablator (Li:Pb mole ratio 18.1:1), and a lead outer shell as the high-Z component. The target composition is given in Fig. VII.2-1. The targets are injected at a velocity of 200 m/sec with a target injection gun (section III.5) that also releases 1.6 mg of D_2 propulsion gas into the chamber per shot. The target is loaded into a plastic 2-piece carrier called a sabot. During injection,

PELLET COMPOSITION

Layer	Materials	Weight (mg)	Atoms x 10^{20}	Density g/cm^3	Thickness mm
3	Pb	288	8.34	11.3	0.245
2	Li Pb	26 41	22 1.2	1.26	0.739
1	D T	1.6 2.4	4.8 4.8	0.21	0.477

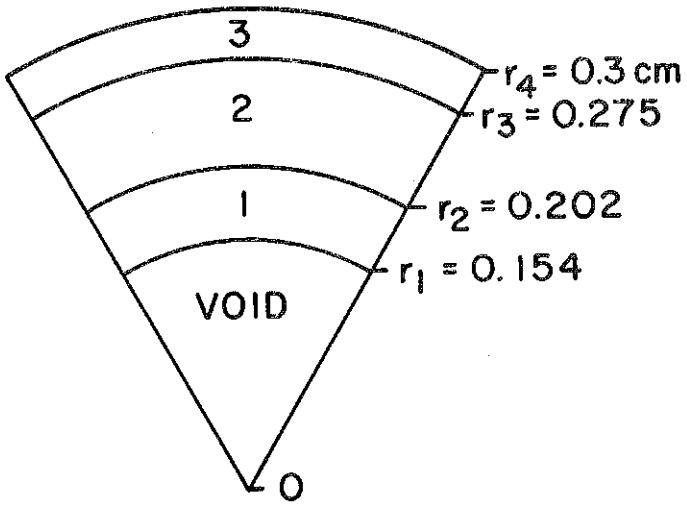

Fig. VII.2-1

Table VII.2-1 Daily Fueling and Exhaust Characteristics*

	Deuterium	Tritium
Fraction burned (%)	29	29
Fuel injected (kg/d)	2.8	4.1
Fuel burned (kg/d)	.80	1.2
Fuel exhaust pumped (kg/d) (from D-T reaction)	2.0	2.9

*For all four reactor cavities

the sabot is shed into a buffer cavity and does not enter the reactor. Deuterium propulsion gas in the buffer cavity which does not reach the reaction chamber (139.4 mg/shot) will be recycled periodically with the hydrogen isotopes.

The choice of lithium and lead for target materials is favorable because they are compatible with the $Li_{17}Pb_{83}$ liquid wall. Debris from the target shells will dissolve in the liquid wall. In Table VII.2-2 the change in blanket composition with time is shown. Since the ratio of Li:Pb in the target is greater than in the eutectic (17:83 atom%), the ratio of Li:Pb in the blanket slowly increases with time. Therefore, quantities of lead will have to be added and properly mixed to maintain the eutectic composition.

The target injection rate is 5 sec^{-1} per cavity, requiring 4.32×10^5 targets/day, corresponding to 4.1 kg T/day and 2.8 kg D/day. The details of how the targets will be manufactured have not been developed at this time in the reactor study. However, the effects of target manufacture on the tritium inventory are discussed in section VII.2.6.

Table VII.2-2 Change in $Li_{17}Pb_{83}$ Composition with Time

	Mass Changes			
	^{+}Pb (target) (kg)	^{+}Li (target) (kg)	^{-}Li $Li(n,\alpha)T$ (kg)	^{+}Li (total) (kg)
1 shot	3.29×10^{-4}	2.65×10^{-5}	2.03×10^{-6}	2.45×10^{-5}
1 day	142	11.4	.877	10.5
1 year	5.18×10^{4}	4.16×10^{3}	320	3.84×10^{3}

	Composition Changes		
	Original blanket	1 year operation	% change
Mass Li (kg)	3.26×10^{4}	3.64×10^{4}	11.8
Mass Pb (kg)	4.74×10^{6}	4.79×10^{6}	1.09
Ratio Li:Pb	0.205	0.228	
Formula	$Li_{17}Pb_{83}$	$(Li_{18.9}Pb_{83})$	

VII.2.2 Exhaust

Each fusion event will cause a pressure rise in the chamber as Li-Pb debris is ablated from the walls and gases from the D-T reaction and unburned fuel are released. The major components present in the exhaust are given in Table VII.2-3. Between fusion events, the chamber must be pumped to at least 10^{-4} torr, as higher pressures will cause interference and scattering of the ion beams. The vaporized liquid metal will recondense on the liquid wall. Any Li-Pb vapor or debris that enters the vacuum or beam ports is assumed to condense on the cold duct surfaces and will not contaminate the cryopumps.

Table VII.2-3 Exhaust Gas Composition

	mg/shot	kg/d[a]
Deuterium target (unburned)	1.1	1.9
Tritium target (unburned)	1.7	2.9
Helium (DT fusion)	.93	1.6
Helium (breeder)	1.2	2.1
Tritium (breeder)	.87	1.5
Li-Pb vapor[b]	0	0
D_2 target injection	1.6	2.8
TOTAL GASES	7.4	12.8
TOTAL TRITIUM	2.57	4.4

[a] All four cavities.

[b] Lithium and lead vapor will condense on cold surfaces before reaching cryopumps.

The amount of lithium and lead in the gas phase in the chamber that results from the equilibrium vapor pressure of lithium and lead above $Li_{17}Pb_{83}$[2,3] is given in Table VII.2-4. The vapor pressure is less than the 10^{-4} torr pressure limit at the operating temperature. The bismuth from the ion beam, is similar to lead and will dissolve completely in the wetted wall and will not be emitted in the exhaust gas. The concentration of bismuth in the chamber with time is given in Table VII.2-5. After 20 years of operation the bismuth concentration in the liquid metal is still less than 1 wppm.

Table VII.2-4 Vapor Pressure of $Li_{17}Pb_{83}$ at 500°C

	Li	Pb
Activity	1.3×10^{-4}	0.81
Pressure (pure)	2.86×10^{-3}	1.69×10^{-5}
Pressure (above eutectic)	3.7×10^{-7}	1.4×10^{-5}

Table VII.2-5 Bismuth Concentration in $Li_{17}Pb_{83}$

Time	Bi dissolved (kg)	wppm Bi in $Li_{17}Pb_{83}$
1 shot	1×10^{-9}	2.1×10^{-10}
1 day	4.3×10^{-4}	9.0×10^{-5}
1 year	1.6×10^{-1}	0.033
10 years	1.6	0.33
20 years	3.2	0.66

VIII.2.3 Cryopumps

The reactor chambers are pumped with compound cryopumps, capable of pumping both the hydrogen isotopes and helium at the high volumetric flow rates required. The separation of hydrogen isotopes from helium on the cryosorption panels is extremely sharp.(4) By controlled heating, the helium panel is regenerated first, then the hydrogen isotopes are removed and sent to the fuel cleanup unit. The on-line time for the pumps is two hours and the tritium inventory in the pumps is 0.37 kg.

VII.2.4 Fuel Cleanup

The exhaust from the cryopumps enters the fuel cleanup unit where hydrogen isotopes are separated from hydrocarbons, water, ammonia or any other impurities. The fuel cleanup unit is patterned after the Tritium Systems Test Assembly (TSTA) designs.(5) Impurities are first absorbed onto molecular sieve beds at 75°K while hydrogen isotopes flow into the distillation unit. These impurities are then recovered from the sieves and catalytically oxidized to form tritiated water and tritium free compounds. The tritiated water is condensed and electrolyzed to recover the tritium. For a 500 mole T flow rate TSTA has estimated an inventory in the fuel cleanup unit of 14 g.(6) In HIBALL the exhaust contains 1467 moles T/day giving an inventory of 41 g.

VII.2.5 Isotopic Separation Unit

Hydrogen isotopes from the fuel cleanup unit enter the crogenic distillation system in the mole ratio 12 H:2350 D:1467 T. (A stream of the deuterium from the target injection gun that does not enter the cavity will also be purified.) The goals of the separation system are to separate and vent hydrogen, to form a purified D-T stream for the target manufacturing system and storage, and to form a pure D_2 stream for the target injection

system. The separation scheme, patterned from the literature[6,7] is shown in Fig. VII.2-2. The inventory in the separation system is estimated as 83.4 g.

VII.2.6 Tritium Considerations in Target Manufacture

The details of the target manufacturing system have not been addressed at this time, thus the tritium inventory in the target manufacturing process and the inventory that must be kept in storage as targets to insure production in case of a malfunction are unknown. This inventory will be dependent on:

(1) the number of targets produced per day;

(2) the time required to make a day's quantity of targets;

(3) the process used - batch or continuous; and

(4) the amount of tritium that must enter the recycling system due to rejection of targets that do not conform to specifications.

The fusion targets for HIBALL must be produced economically at a rate of 4.32×10^5/day. Three possible pathways for target production are outlined in Fig. VII.2-3. After selected steps in the manufacturing process, the product is examined to insure it meets certain specifications,[8] and at this point a number of targets will be rejected. If the rejected targets contain D-T, the fuel must be recovered and reprocessed. To minimize the tritium handling, the filling of the targets with DT fuel should come as late in the manufacturing process as possible or at least following steps with large rejection rates.

To minimize the tritium storage for the target manufacturing system, the time required to fill the targets with DT should be as short as possible. If the DT fuel is diffused into a hollow shell, the targets will be produced in a batch process and the fill-time will be dependent on the permeation rate of DT through the shell at temperatures below the shell melting point. In SOLASE[9] two target designs were examined. Plastic targets required a 1 day fill-time resulting in a one day fuel storage, while glass targets required a five day

HIBALL Isotope Separation Unit

Flow Rates in g/d
T = Tritium Inventory (g)

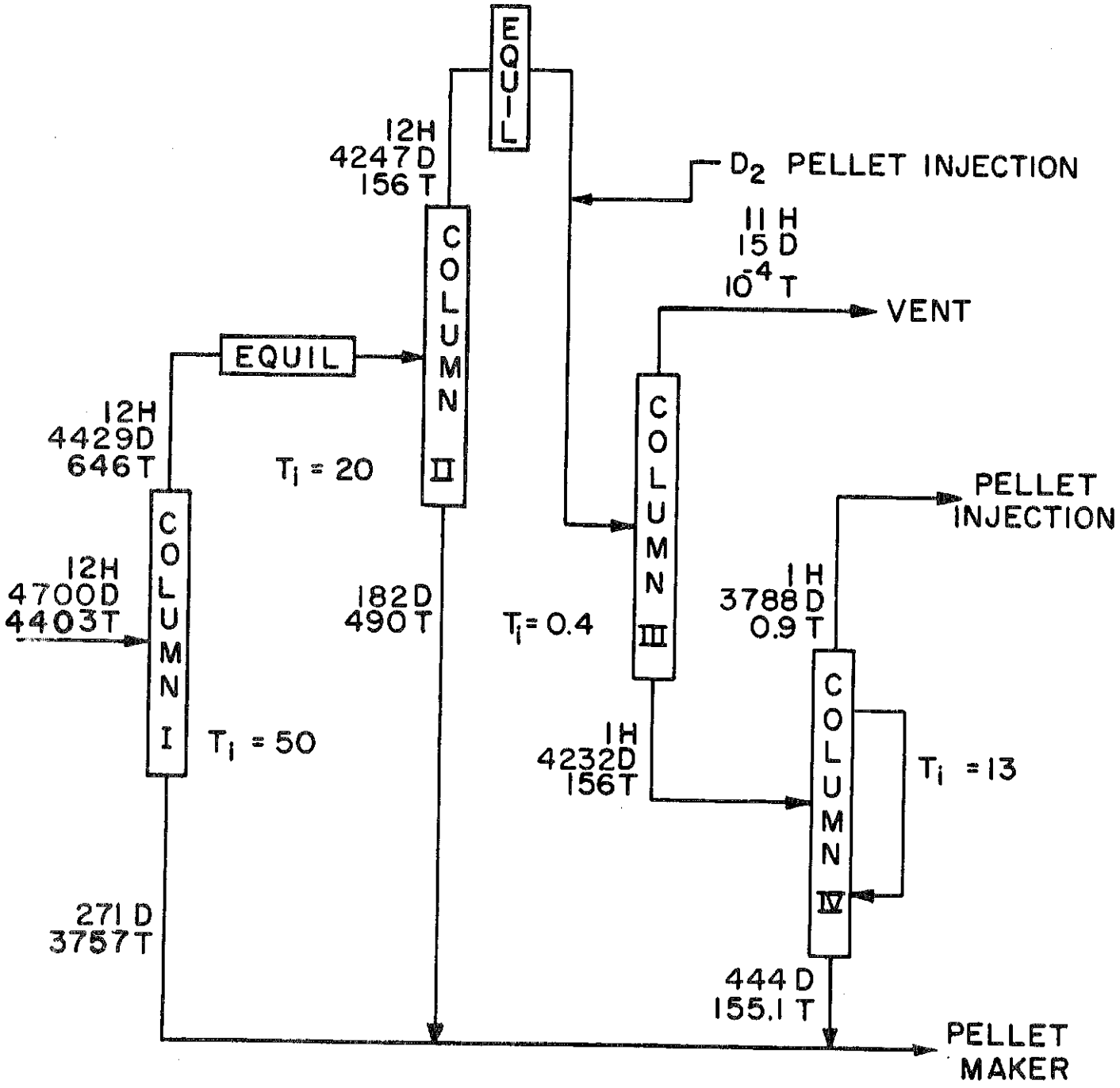

Fig. VII.2-2

POSSIBLE PELLET MANUFACTURING SCHEMES

STEP	PROCESS	TRITIUM RECYCLE?	
1	FORMATION OF Li-Pb SHELL	NO	
2	DT FILL		PATH I
	(a) BATCH GAS DIFFUSION	YES	
	(b) CONTINUOUS DRILL, FILL & SEAL	YES	
3	Pb COATING	YES	
4	CRYOGENIC PROCESS		
1	FORMATION OF CRYO. DT SHELL	YES	
2	Li — Pb COATING	YES	PATH II
3	Pb COATING	YES	
1	FORMATION OF Li-Pb SHELL	NO	
2	Pb COATING	NO	PATH III
3	DT FILL		
	(a) BATCH GAS DIFFUSION	YES	
4	CRYOGENIC PROCESS		

Fig. VII.2-3

full-time and a five day inventory in storage. Therefore, Path III in Fig. VII.2-3 is probably unreasonable because it would require diffusion of DT through two layers at fairly low temperatures (mp. Pb = 327°C; mp. $Li_{18.1}Pb \approx 450°C$), resulting in a large storage inventory.

While microdrilling of laser targets and parts has been successfully tried,[10] the filling and sealing process has not been demonstrated. Although the drill-and-fill process is continuous, requiring less tritium storage than batch processes, the high symmetry requirements of the target would probably result in a high rejection rate of improperly sealed shells and a significant amount of tritium recycle and recovery. Therefore, until this option is proven to be practical, target production by diffusion methods seems more reasonable.

In Path I the first step is the preparation and analysis of the ablation shell. Hollow glass and hydrogen shells have been prepared by introducing a stream of gas bubbles into a controlled jet producing uniform spheres.[11] The DT is then diffused into the shell. The permeability of DT through this layer of Li-Pb is unknown, so the time to fill this shell and the required DT storage are unknown. The Li-Pb shell is then coated with lead. There are four major processes that have been developed for producing metallic coatings onto microspheres[12]: magnetic sputtering, electroplating, electroless plating, and chemical vapor pyrolysis. At present the sputtering technique seems to have the most general applicability. After the coatings are applied initial cooling of the target freezes the DT non-uniformly. By vaporizing the inner coating of fuel with a laser or heat pulse and quickly refreezing the DT, a uniform layer can be produced.[13,14]

Hendricks et al. proposed a process in which cryogenic spheres are transported past sputtering guns which apply consecutive layers onto the sphere.[8]

A cold helium gas jet[15] can be used to keep the targets frozen and levitate the targets as they pass the sputtering guns and quality control apparatus. This process is outlined in Path II. This method has the disadvantage of handling tritium throughout the process; however, there is no batch diffusion step requiring a large storage inventory. While the tritium reprocessing of imperfect D-T spheres would be minimal, the processing after the coatings are applied would require more sophistication. From a comparative standpoint, Path II is probably the superior method from tritium considerations, assuming the coatings can be applied to high standards requiring minimal tritium recycling.

Until the details of the target manufacturing system are known it will be assumed that one day's fueling supply (4.1 kg) will be stored as cryogenic targets and another day's supply will be tied up in the target manufacturing system.

VII.2.7 Storage

The storage requirements for HIBALL include a one day supply of targets to fuel the reactor (4.1 kg T) and a one day supply kept on uranium beds to feed into the target manufacturing system. (This storage inventory will depend on the target manufacturing process as discussed in the preceding section.) The storage inventory of 8.2 kg T, represents a large fraction of the total inventory.

References for Section VII.2

1. M.S. Ortman, E.M. Larsen, S.I. Abdel-Khalik, "A Study of the Tritium Handling Systems in Magnetic and Inertal Confinement Fusion Reactors With and Without Tritium Breeding," Nuclear Technology/Fusion 1, 255-274 (April 1981).

2. J.L. Ballif, D.W. Jeppson, W.W. Yuan, and B.E. Chou, "Lithium Literature Review: Lithium's Properties and Interactions," (HEDL-TME-78-15, Hanford Engineering Development Laboratory (April 1978).

3. D.H. Shiu and Z.A. Munir, "The Heat of Vaporization and Vapor Pressure or Liquid Lead," Met. Trans. 2, 2953-2955 (1971).

4. J.L. Anderson, "Design and Construction of the Tritium Systems Test Assembly," Proceedings Tritium Technology in Fission, Fusion and Isotropic Applications, Dayton, Ohio, April 29 - May 1, 1980, CONF-800427, American Nuclear Society (1980), 341-346.

5. E.C. Kerr, J.R. Bartlit and R.H. Shermon, "Fuel Cleanup System for the Tritium Systems Test Assembly: Design and Experiments," Proceedings Tritium Technology in Fission, Fusion and Isotropic Applications, Dayton, Ohio, April 29 - May 1, 1980, CONF-800427, American Nuclear Society (1980), 115-118.

6. J.L. Anderson and R.H. Sherman, "Tritium Systems Test Assembly Design for Major Device Fabrication Review," LA-6855-P, Los Alamos Sci. Lab (June 1977).

7. B. Badger et al., "WITAMIR-I - A Tandem Mirror Reactor Study," University of Wisconsin Fusion Design Memo UWFDM-400, Chapter XI, (Dec. 1979).

8. C.D. Hendricks, W.L. Johnson, "Power Production of Inertial Confinement Fusion Targets," Lawrence Livermore Laboratory, UCRL-52539, February 15, 1979.

9. R.W. Conn et al., "SOLASE, A Laser Fusion Reactor Study," University of Wisconsin Fusion Design Program Memo UWFDM-220, Chapter IV, (1977).

10. B.W. Weinstein, C.D. Hendericks, J.T. Weir, "Laser Microdrilling in the Fabrication of Laser Fusion Targets," Lawrence Livermore Laboratory, UCRL-77406, October 15, 1975.

11. C.D. Hendricks, "Fabrication of Targets for Laser Fusion," Lawrence Livermore Laboratory, UCRL-76380, January 20, 1975.

12. S.F. Meyer, "Metallic Coating of Microspheres," Lawrence Livermore Laboratory, UCRL-84463, August 15, 1980.

13. R.L. Woerner and C.D. Hendricks, "Fabrication of Cryogenic Laser Fusion Targets," Lawrence Livermore Laboratory, UCRL-79442, September 27, 1977.

14. K. Kim and H. Rieger, "Fabrication and Characterization of Cryogenic Targets for Inertial Confinement Fusion," Dept. of Electrical Engineering, University of Illinois, Urbana, Report 1979, UCRL-15113 (1980).

15. W.L. Johnson, S.A. Letts, D.W. Myers, J.K. Crane, J.D. Illige, and C.W. Hatcher, "Plasma Processed Coating of Laser Fusion Targets," Lawrence Livermore Laboratory, UCRL-83000, September 19, 1979.

VII.3 Blanket System

The breeding material is the liquid lithium-lead eutectic, $Li_{17}Pb_{83}$ (.68 Li:99.32 Pb wt%). This material flows through woven SiC fixtures at the top and woven SiC tubes at the sides of the reactor providing a protective coating on the SiC surfaces and forming a pool at the bottom of the reactor. The cavity reflector also contains $Li_{17}Pb_{83}$. The liquid alloy serves as the heat exchange material and is circulated through the steam cycle. The properties of the blanket system and the tritium extraction scheme are discussed in this section.

VII.3.1 Solubility of Tritium in $Li_{17}Pb_{83}$

In order to determine the tritium inventory in the breeding material and the method of extraction, the solubility of tritium in $Li_{17}Pb_{83}$ at the reactor temperatures (300-500°C) must be known. Ihle et al.[1] has determined the deuterium solubility in Li-Pb alloys at 677 and 767°C, much higher temperatures than the reactor conditions. In NUWMAK,[2] $Li_{62}Pb_{38}$ was used as the breeding material, and a model was proposed for determining the solubility of hydrogen isotopes in lithium-lead alloys versus temperature. This model[3] assumes that the Sievert's constant for the solubility of tritium in the lithium-lead alloy ($K_{S(alloy)}$) is related to the Sievert's constant for tritium in pure lithium ($K_{S(Li)}$) by the expression:

$$K_{S(alloy)} = K_{S(Li)} \cdot \gamma_{Li(alloy)} \cdot N_{Li(alloy)} = K_{S(Li)} a_{Li(alloy)}$$

where: $a_{Li(alloy)}$ = activity of lithium in lithium-lead

$\gamma_{Li(alloy)}$ = activity coefficient for lithium in lithium-lead

$N_{Li(alloy)}$ = mole fraction of lithium in the alloy.

The Sievert's constant for hydrogen isotopes in pure lithium[4-8] (Fig.

VII.3-1) and the activity of lithium in lithium-lead[1,9-11] (Fig. VII.3-2) are well-known quantities.

The major assumptions in this model are:

(1) The manner in which tritium dissolves in the alloy is by association with the lithium only. Any lead-tritium interaction is assumed to be negligible. This behavior is expected from periodic trends[12]; lithium is capable of forming hydride bonds while lead-hydrogen interactions are weak. A comparison of the hydrogen solubility in lithium and lead to that in other metals,[4,5,14-16] (Fig. VII.3-3) shows that lithium has one of the highest hydrogen solubilities of any known metal while lead has one of the lowest hydrogen solubilities.

(2) The manner in which lead enters into the lead-lithium-tritium equilibrium is to chemically bond the lithium making it less available to interact with the tritium. The degree to which the lithium is available for bonding is related to the activity coefficient for lithium in lithium lead.

(3) The lithium activity is unaffected by ppm quantities of tritium.

A plot of the theoretical solubility constant for deuterium in lithium-lead alloys is shown in Fig. VII.3-4. This figure also contains the experimental solubility data of Ihle et al.[1] and the data for deuterium solubility in pure lithium[4,7,8] and hydrogen solubility in pure lead[13,17]. (Note in Fig. VII.3-4 the data is plotted such that the Sievert's constant is directly proportional to the solubility, rather than inversely as in Ihle's paper. Also, there is no attempt to plot the theoretical solubility in regions where solid phases occur.) If the assumptions in the theoretical model are reasonable two important conclusions can be drawn:

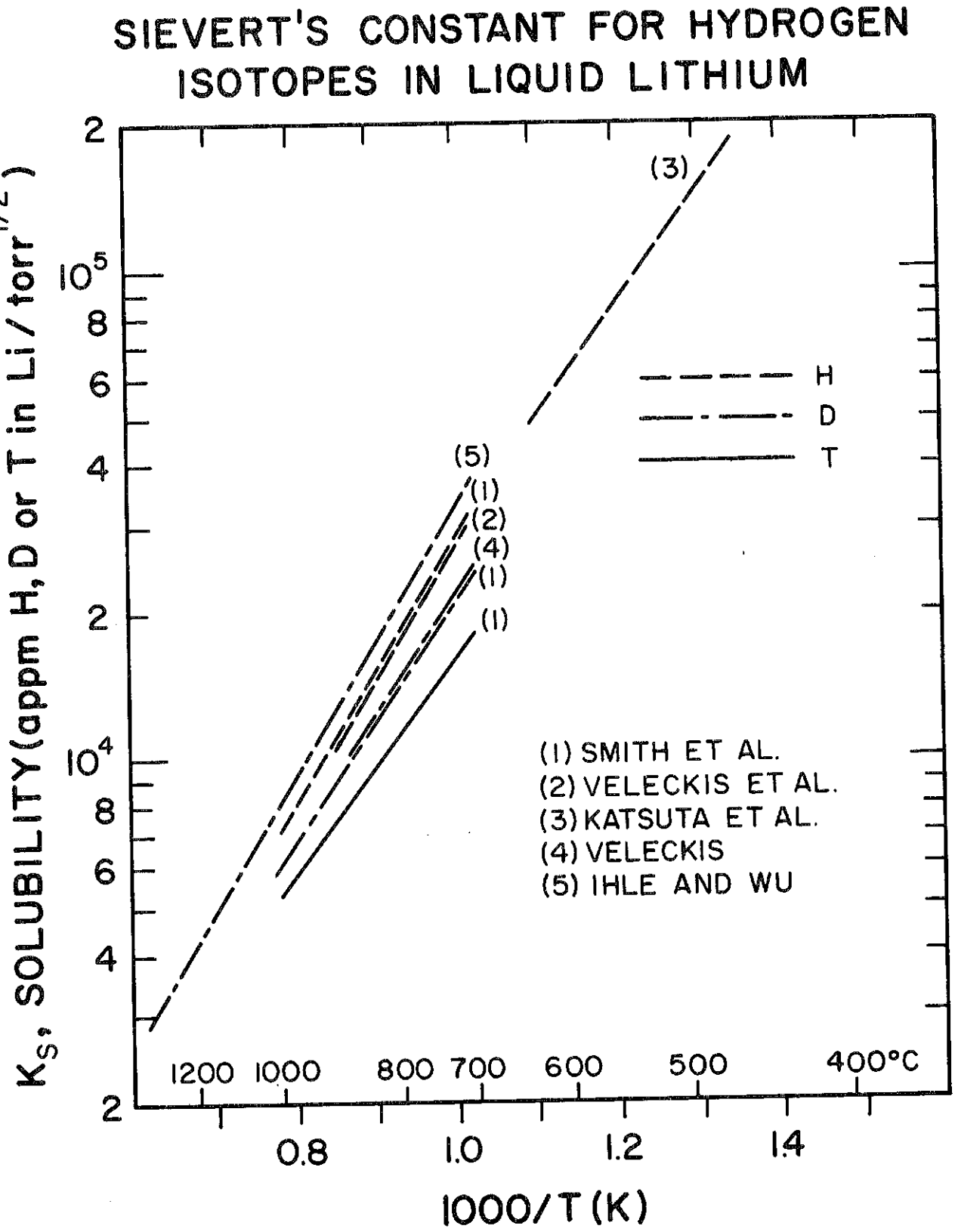
SIEVERT'S CONSTANT FOR HYDROGEN ISOTOPES IN LIQUID LITHIUM
K_S, SOLUBILITY (appm H, D or T in Li / torr$^{1/2}$)
2
10^5
8
6
4
2
10^4
8
6
4
2
(3)
(5)
(1)
(2)
(4)
(1)
(1)
H
D
T
(1) SMITH ET AL.
(2) VELECKIS ET AL.
(3) KATSUTA ET AL.
(4) VELECKIS
(5) IHLE AND WU
1200 1000 800 700 600 500 400°C
0.8 1.0 1.2 1.4
1000/T (K)

Fig. VII.3-1

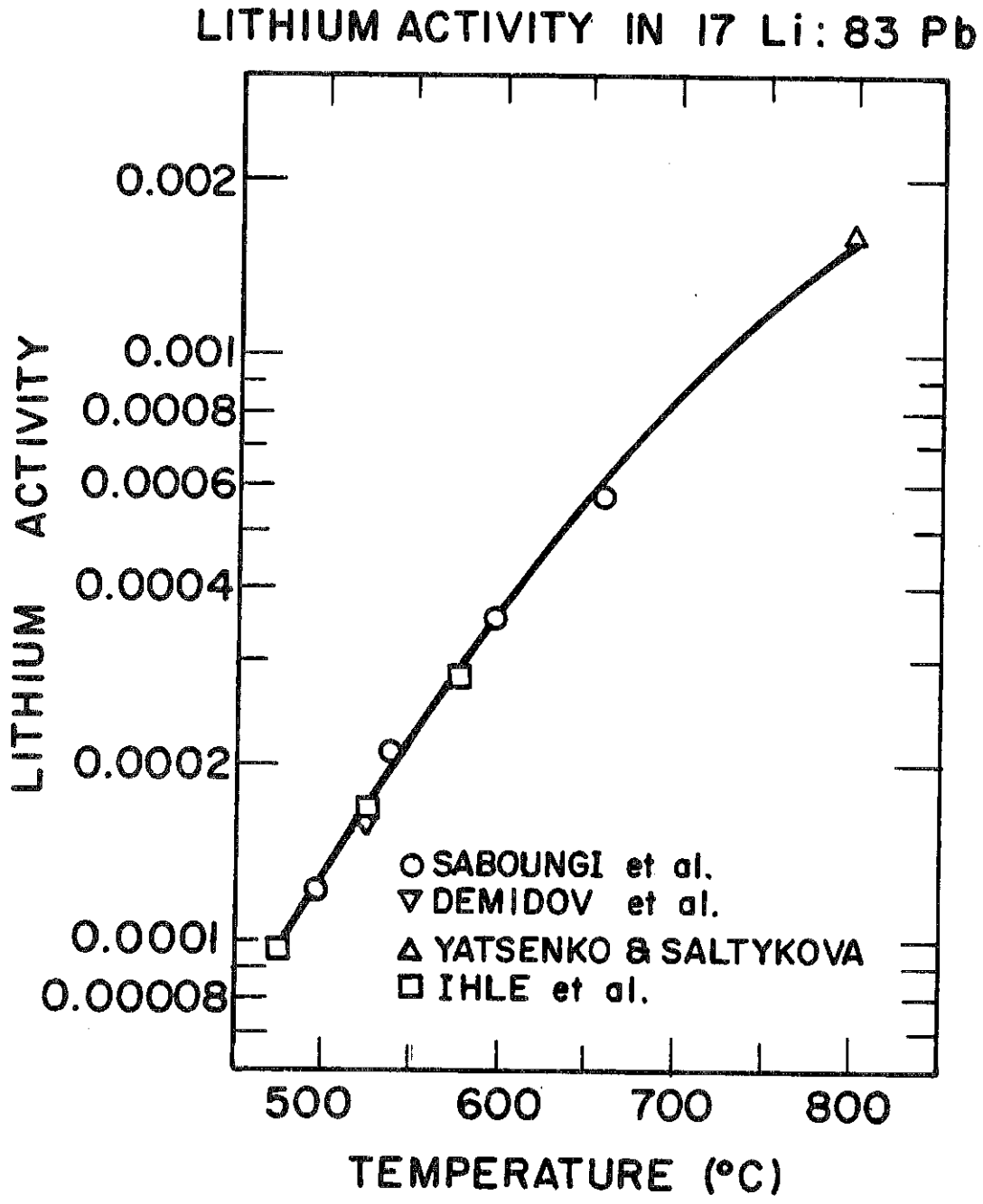
LITHIUM ACTIVITY IN 17 Li : 83 Pb
LITHIUM ACTIVITY
0.002
0.001
0.0008
0.0006
0.0004
0.0002
0.0001
0.00008
500
600
700
800
TEMPERATURE (°C)
○ SABOUNGI et al.
▽ DEMIDOV et al.
△ YATSENKO & SALTYKOVA
□ IHLE et al.

Fig. VII.3-2

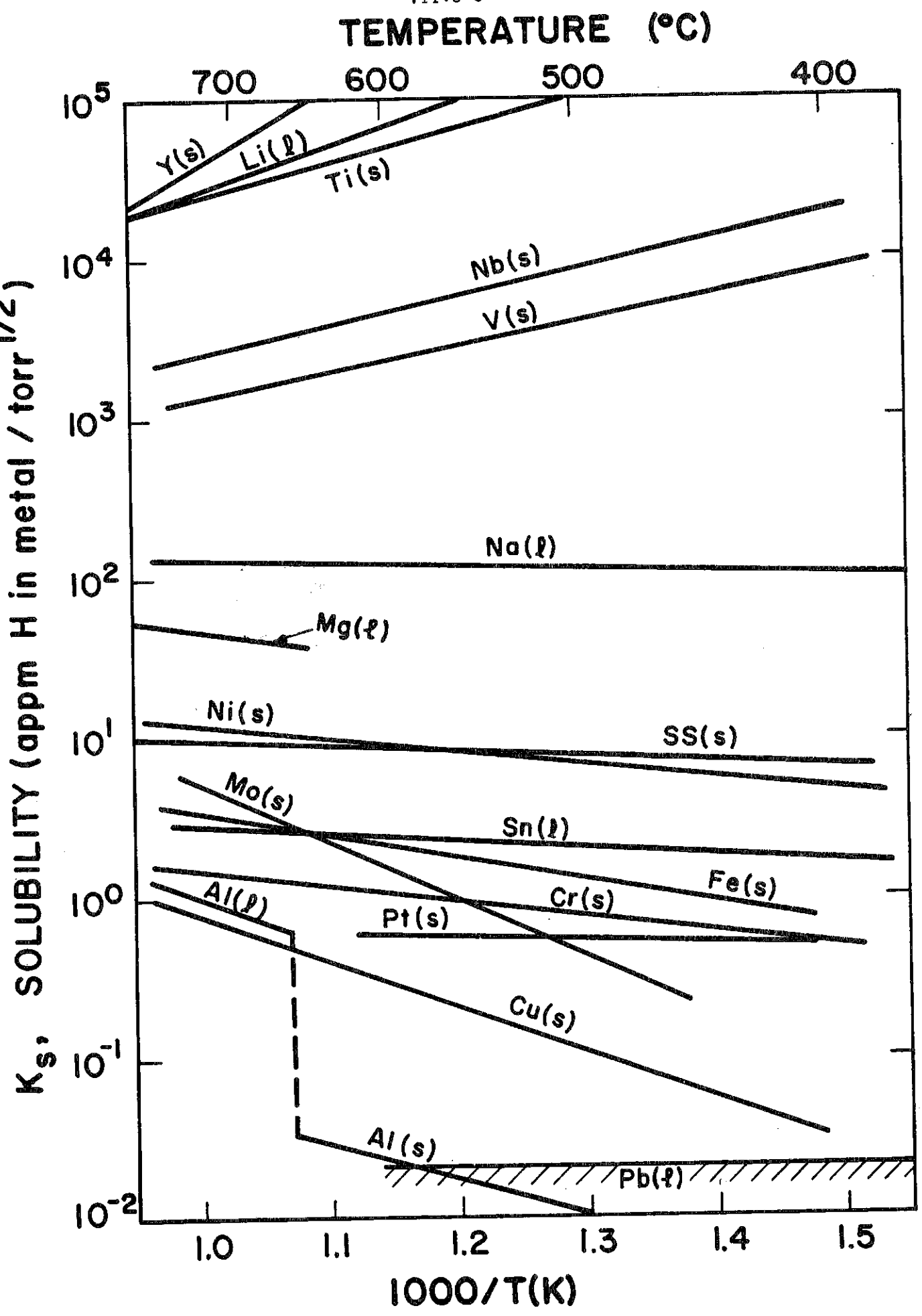

Fig. VII.3-3 Comparison of solubilities of various metals.

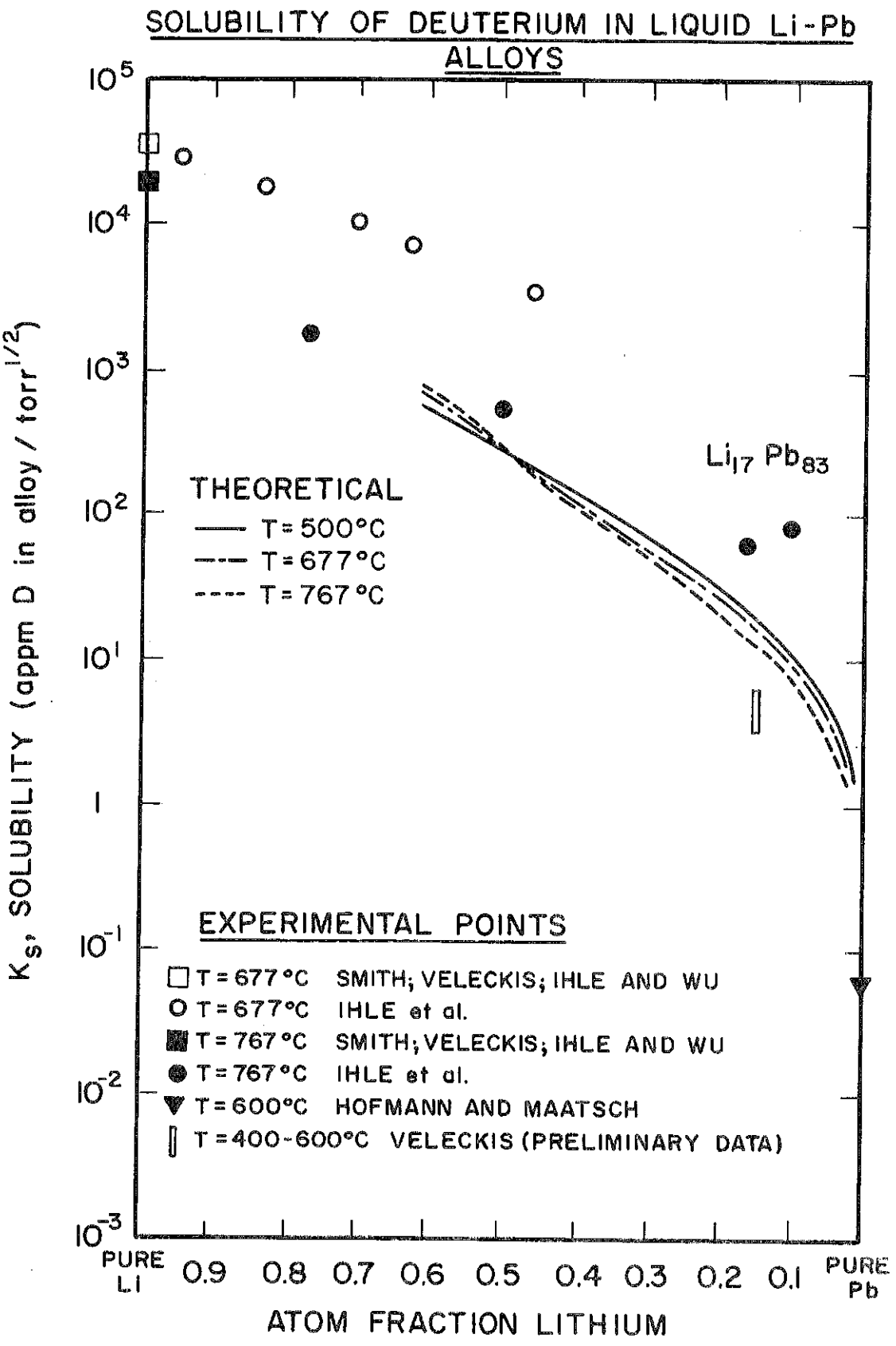
SOLUBILITY OF DEUTERIUM IN LIQUID Li-Pb ALLOYS
K_s, SOLUBILITY (appm D in alloy / torr$^{1/2}$)
10^5
10^4
10^3
10^2
10^1
1
10^{-1}
10^{-2}
10^{-3}
THEORETICAL
T = 500°C
T = 677°C
T = 767°C
$Li_{17}Pb_{83}$
EXPERIMENTAL POINTS
T = 677°C SMITH; VELECKIS; IHLE AND WU
T = 677°C IHLE et al.
T = 767°C SMITH; VELECKIS; IHLE AND WU
T = 767°C IHLE et al.
T = 600°C HOFMANN AND MAATSCH
T = 400-600°C VELECKIS (PRELIMINARY DATA)
PURE Li
0.9
0.8
0.7
0.6
0.5
0.4
0.3
0.2
0.1
PURE Pb
ATOM FRACTION LITHIUM

Fig. VII.3-4

(1) The theoretical model predicts only a slight temperature dependence. This behavior is expected from examination of Fig. VII.3-3 which shows that lithium dissolves hydrogen exothermically while metals with low hydrogen solubilities (such as lead) generally dissolve hydrogen endothermically. This probably leaves Li-Pb alloys in an intermediate category showing little temperature dependence. The temperature dependence observed in the work by Ihle et al. is greater than has been observed for any other metal or alloy system and does not agree with the model predictions.

(2) The theoretical model predicts lower solubilities than those determined by Ihle et al.

Preliminary experiments conducted by E. Veleckis[18] at Argonne National Laboratory indicate deuterium solubilities that are fairly temperature independent and lower than both the data found by Ihle et al. and the model predictions. The Sievert's constant used in this design for tritium solubility in $Li_{17}Pb_{83}$ at 500°C (based on preliminary Argonne results) is 4 appm $H/torr^{1/2}$ or 7×10^{-2} wppm $T/torr^{1/2}$ which at 10^{-4} torr gives a tritium concentration of 7×10^{-4} wppm in $Li_{17}Pb_{83}$. The mass of $Li_{17}Pb_{83}$ in the four chambers and the reflectors is 1.91×10^{7} kg, resulting in a low tritium inventory of 0.013 kg.

VII.3.2 Tritium Breeding and Recovery

The breeding ratio of $Li_{17}Pb_{83}$ is 1.25 resulting in a breeding rate of 4.4×10^{-6} kg T/sec in each chamber. The $Li_{17}Pb_{83}$ alloy (4.8×10^{6} kg/chamber) serves both as breeder and coolant and is circulated through the power cycle at a rate of 3.38×10^{8} kg/hr. Assuming the tritium solubility is 7×10^{-4} wppm, the flow rate of tritium in one reactor chamber is 6.6×10^{-5} kg T/sec.

In order to recover tritium at the breeding rate, 6.7% of the tritium must be extracted during each pass of $Li_{17}Pb_{83}$ through a chamber. The pressure of tritium above $Li_{17}Pb_{83}$ is 10^{-4} torr; therefore, the pressure that must be maintained in the reactor to allow the tritium to be released from the liquid metal is less than or equal to 10^{-4} torr.[19] The quantity of tritium that must be extracted is 7.4×10^{-4} mole T_2/sec. This is a volumetric flow rate of 3.7×10^5 ℓ/sec at 700°K and 10^{-4} torr. The high pumping rate necessary to remove the exhaust between shots, ($\sim 4 \times 10^6$ ℓ/sec at 10^{-4} torr and 700°K) is sufficient to remove the tritium at the breeding rate and a separate extraction unit will not be needed. The breeder and coolant characteristics are summarized in Table VII.3-1. Although the diffusion of tritium in $Li_{17}Pb_{83}$ is unknown, the high surface area of the flowing liquid metal in the chamber should allow easy release of tritium from the eutectic into the chamber.

Table VII.3-1 Breeder and Coolant Characteristics

Blanket temperature (°C)	
Inlet	330
Outlet	500
Tritium concentration (wppm)	7×10^{-4}
Inventory (kg)	
Tritium	.013
$Li_{17}Pb_{83}$	1.9×10^7
Tritium Breeding	
Ratio	1.25
Rate (kg/sec)	4.4×10^{-6}
Flow Rate (kg/sec)	
Tritium	6.6×10^{-5}
$Li_{17}Pb_{83}$	9.4×10^4

VII.3.3 Silicon Carbide Interactions with Hydrogen Isotopes

The silicon carbide tubes are surrounded with the alloy containing 7×10^{-4} wppm tritium at 10^{-4} torr and 500°C, resulting in some of the tritium dissolving into the silicon carbide reaching an equilibrium concentration. Experiments on deuterium solubility in SiC at 1000 to 1400°C[21] are shown in Fig. VII.3-5. The solubility is very temperature dependent; decreasing as the temperature increases. This dependence is thought to be due to chemical bond formaton between hydrogen atoms and the lattice atoms. The presence of Si-H and C-H bonds have been observed.[22] The pressure dependence on the solubility was determined to be to the 0.61 power, indicating that the hydrogen dissolves monatomically. It also can be observed that the temperature dependence differs substantially for vapor deposited β-SiC and powdered α-SiC.

Due to the large exothermicity of the dissolving process, extrapolations to lower temperatures result in large tritium inventories. At 500°C and 10^{-4} torr, the data for β-SiC extrapolates to 0.017 atoms D/atom Si or ~ 800 wppm. This seems quite unlikely. The last data point measured for β-SiC was at 1000°C, resulting in 0.05 wppm for 10^{-4} torr. It is impossible to predict where the solubility curve will begin to level off. It is also impossible to predict if the woven β-SiC will behave similarly to vapor deposited β-SiC. If it is assumed that the data can only be extrapolated for a few hundred degrees (to 800°C) before leveling off, for β-SiC a solubility of 0.76 wppm at 10^{-4} torr is obtained. This results in an inventory of 0.012 kg T in 1.6×10^4 kg SiC.

Silicon carbide can react with hydrogen to produce hydrocarbons and silanes. The thermodynamics[20] for the interactions of hydrogen atoms and hydrogen molecules with SiC are given in Table VII.3-2. Hydrogen molecule reactions are unfavorable, while hydrogen atom reactions have negative free

VII.3-10

HYDROGEN SOLUBILITY IN SiC COMPARED TO OTHER METALS

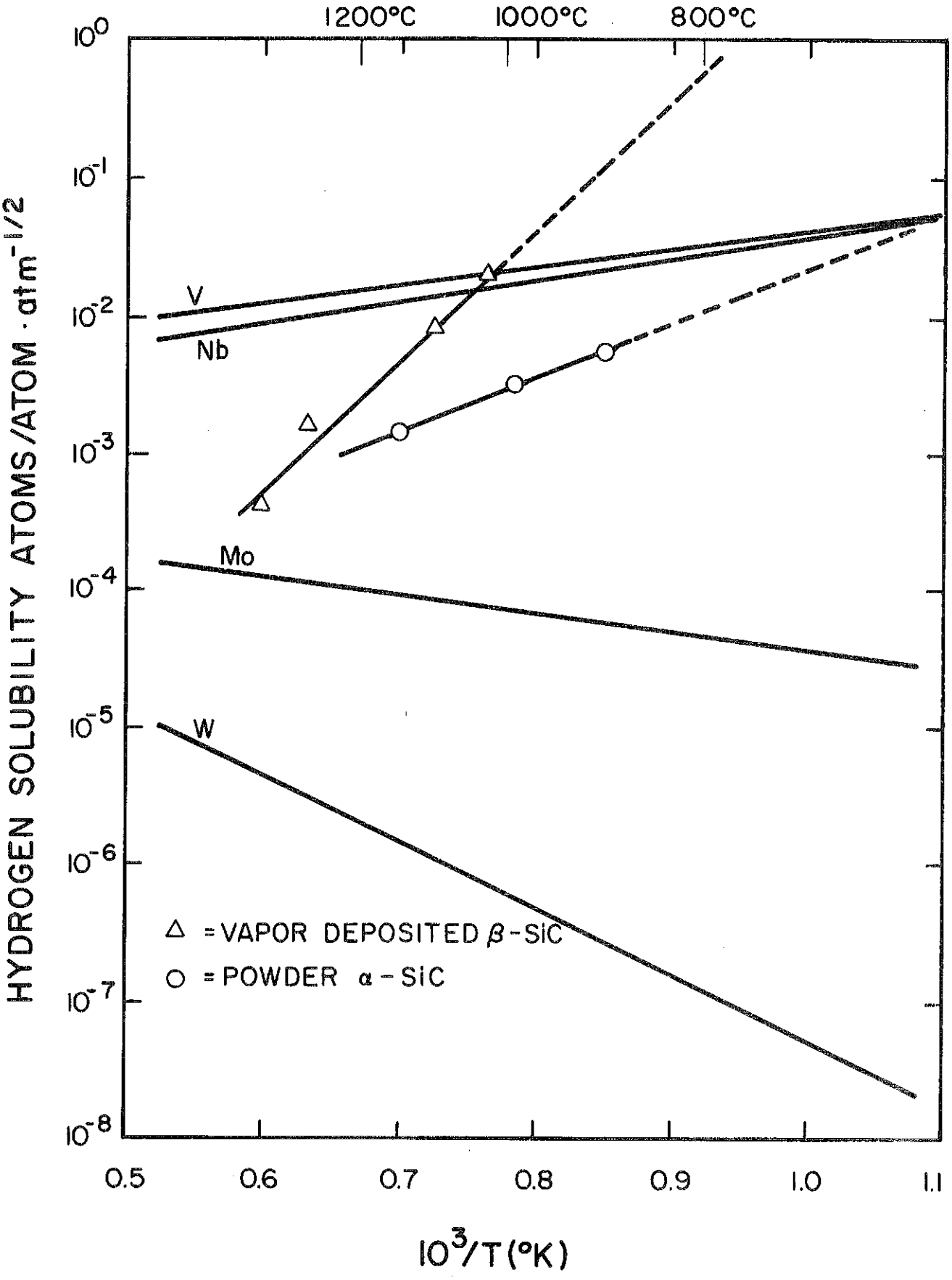

Fig. VII.3-5

energies. The SiC tubes are coated with a protecting layer of liquid metal which should absorb the hydrogen atom debris. Therefore, production of hydrocarbons and silanes should be minimal.

Table VII.3-2 Thermodynamics for Hydrogen-Silicon Carbide Interactions

Free Energy (kcal/mole)

H_2 Interactions	600°K	700°K	800°K
α-SiC(s) + 2 H_2(g) → Si(s) + CH_4(g)	10.45	12.70	15.03
α-SiC(s) + 1/2 H_2(g) → Si(s) + 1/2 C_2H_2(g)	38.85	37.98	37.13
α-SiC(s) + 2 H_2(g) → SiH_4(g) + C(s)	35.41	37.51	39.65
H Interactions			
α-SiC(s) + 4H(g) → Si(s) + CH_4(g)	-168.9	-161.5	-153.9
α-SiC(s) + 1 H(g) → Si(s) + 1/2 C_2H_2(g)	- 6.00	- 5.58	- 5.11
α-SiC(s) + 4 H(g) → SiH_4(g) + C(s)	-144.0	-136.7	-129.3

References for Section VII.3

1. H.R. Ihle, A. Neubert and C.H. Wu, "The Activity of Lithium, and the Solubility of Deuterium, in Lithium-Lead Alloys," Proc. Tenth Symp. Fusion, Padova, Italy, September 4-9, 1978, Pergamon Press, New York, 639-644 (1979).

2. B. Badger et al., "NUWMAK - A Tokamak Reactor Design Study," University of Wisconsin Fusion Design Memo UWFDM-330, March 1979.

3. E.M. Larsen, M.S. Ortman, K.E. Plute, "Comments on the Hydrogen Solubility Data for Liquid Lead, Lithium and Lithium-Lead Alloys and Review of a Tritium Solubility Model for Lithium-Lead Alloys," University of Wisconsin Fusion Design Memo UWFDM-415, to be published.

4. F.J. Smith, A.M. Batistoni, G.M. Begun, J.F. Land, "Solubility of Hydrogen Isotopes in Lithium," Report 1976, Conf. 760631-1.

5. E. Veleckis, E.H. Van Deventer and M. Blander, "The Lithium-Lithium Hydride System" J. Phys. Chem. 78, 1933-1940 (1974).

6. H. Katsuta, T. Ishigai and K. Furukawa, "Equilibrium Pressure and Solubility of Hydrogen in Liquid Lithium," Nucl. Tech. 32, 297-303 (1977).

7. E. Veleckis, "Thermodynamics of the Lithium-Lithium Deuteride System," J. Phys. Chem. 81, 526-531 (1977).

8. H.R. Ihle and C.H. Wu, "The Solubility of Deuterium In and Its Separation From Liquid Lithium by Distillation," Hydrogen in Metals, Vol. 1, Proceedings of the 2nd International Congress, Paris, France, June 6-10, 1977, Pergamon Press, New York (1977).

9. M.L. Saboungi, J. Marr, and M. Blander, "Thermodynamic Properties of a Quasi-Ionic Alloy from Electromotive Force Measurements - The Li-Pb System," J. Chem. Phys. 68, 1375-1384 (1978).

10. A.I. Demidov, A.G. Morachevskii, and L.N. Gerasimenko, "Thermodynamic Properties of Liquid Lithium-Lead Alloys," Sov. Electrochem. 9, 813-814 (1973).

11. S.P. Yatsenko and E.A. Saltykova, "Thermodynamic Properties of Liquid Lithium-Lead Alloys," Russ. J. Phys. Chem. 50, 1278 (1976).

12. F.G.A. Stone, "Hydrogen Compounds of the Group IV Elements," Prentice Hall Inc., New Jersey, 1962.

13. (a) H. Cerjak and F. Erdmann-Jesnitzer, "Increasing the Creep Strength Through Reaction Products Formed in the Melt. I. Lead-Lithium-Hydrogen Alloys," Metall. 22, 113-123 (1968)
(b) F. Erdmann-Jesnitzer, A.P. Van Peteghem and R. De Wilde, "Untersuchungen zur Verbesserung des Kriechverhaltens von Blei-Lithium-Legierungen durch Wasserstoff," Metall. 28, 449-455 (1974).

14. M. Hansen, Constitution of Binary Alloys, Second Edition, McGraw-Hill Book Co., Inc., New York, 789-790 (1958).

15. V.A. Maroni and E.H. Van Deventer, "Materials Considerations in Tritium Handling Systems," J. Nucl. Mater. 85 & 86, 257-269 (1979).

16. S.D. Clinton and J.S. Watson, "The Solubility of Tritium in Yttrium at Temperatures from 250 to 400°C," J. Less-Common Met. 66, 51-57 (1979).

17. W. Hofmann and J. Maatsch, "Loslichkeit von Wasserstoff in Aluminum, Blei-und Zinkschmelzen," Z. Metallkunde 47, 89-95 (1956).

18. E. Velekis, Argonne, Private Communication.

19. K. Ruttiger, "Vacuum Degassing in the Liquid State," Vacuum Metallurgy, O. Winkler and R. Bakish (eds.), Elsevier Publishing Company, New York (1971), 337-463.

20. JANAF Thermochemical Tables, D.R. Sull et al., The DOW Chemical Company, Midland, Michigan.

21. R.A. Causey, J.D. Fowler, C. Ravanbakht, T.S. Elleman and K. Eghese, "Hydrogen Diffusion and Solubility in Silicon Carbide," J. Amer. Cer. Soc. 61, No. 5-6, 221-225 (1975).

22. R.B. Wright, R. Varma, D.M. Gruen, "Raman Scattering and SEM Studies of Graphite and Silicon Carbide Surfaces Bombarded with Energetic Protons, Deuterons and Helium Ions," J. Nucl. Mater. 63, 415-421 (1976).

VII.4 Tritium Containment Systems

The active tritium inventory in the HIBALL reactor is 0.52 kg or 5.0 x 10^6 Ci, with an additional inventory of 12.3 kg or 1.2 x 10^8 Ci in storage and target manufacture. Tritium is being processed at a rate of 4.4 x 10^7 Ci/day (2.9 x 10^7 Ci from the exhaust and 1.5 x 10^7 Ci from the breeder). The losses of tritium to the environment must be limited to ~ 10 Ci/day. Using containment schemes similar to those found in the TSTA[1] design and in a previous reactor design,[2] losses are expected to be less than 10 Ci/day.

VII.4.1 Permeability of Tritium into Steam Cycle*

The primary containment problem which is the most difficult to control is the permeation of tritium from the $Li_{17}Pb_{83}$ breeder/coolant through the walls of the steam generator. Once in the steam cycle the tritium is generally considered lost to the environment because the tritium exchanges with protium forming HTO. Separation of HTO from the bulk of the steam is technically difficult and expensive.[3]

The steam generator composition is HT-9. Permeation data for HT-9 and chromium ferritic steels has been reviewed in WITAMIR.[2] By assuming that, Permeability = Solubility x Diffusivity, and comparing the available data, the "best fit" line in the WITAMIR study resulted in a tritium permeation through clean HT-9 of:

$$P = \frac{1.8 \times 10^3}{\sqrt{3}} \exp\left(\frac{-11100}{RT}\right) \frac{\text{mole } T_2 \cdot \text{mm}}{\text{d} \cdot \text{m}^2 \cdot \text{atm}^{1/2}} \cdot$$

For HIBALL:

Tube thickness = 1 mm Pressure above coolant = 10^{-4} torr

*Based on WITAMIR[2] steam cycle. The steam generator system has not been designed in HIBALL-I.

Area = 5.2×10^4 m^2 Temperature range = 315-490°C

In order to calculate the total loss to the steam cycle, the area of the tubing is assumed to have a linear relationship with temperature, and the permeation, in units of g $T_2 \cdot d^{-1} \cdot m^{-2}$, is plotted against area (m^2) as seen in Fig. VII.4-1. The area under the curve represents the total loss of tritium through clean HT-9; this is a permeation rate of 33 g T_2/day. Losses of this magnitude are unacceptable and must be minimized.

One factor that will reduce the permeability is the fact that the liquid metal side of the steam tubing will have clean surfaces, while the steam side will form an oxide layer. In situ formed oxide coatings are effective in reducing tritium permeability[4] as shown in Table VII.4-1. For ferritic steels at 660°C, permeabilities are reduced by factors of 100 or more due to the oxide coating. At lower temepratures (315-490°C) the ability to maintain an effective oxide coating decreases.[6] For HIBALL the permeability through HT-9 is assumed to be decreased by about a factor of 10 due to the oxide layer on the steam generator side of the tubing.

Another method of achieving lower losses of tritium to the steam cycle include formation of a permeation resistant nickel-alumide layer[6] on the liquid metal side of the tubing. This is accomplished by addition of aluminum to the liquid-metal coolant, which forms an aluminum layer on nickel alloy surfaces, reducing the permeation by a factor greater than 100 for 304 SS at 550°C. The HT-9 alloy, however, is low in nickel and thus would not be adaptable to this scheme. Using a different material in the steam cycle from the reactor material may cause enhanced corrosion through mass transfer mechanisms.

Work has been done on the development of multilayered metal composites and impurity coated refractory metals as tritium barriers.[7] Reductions of a

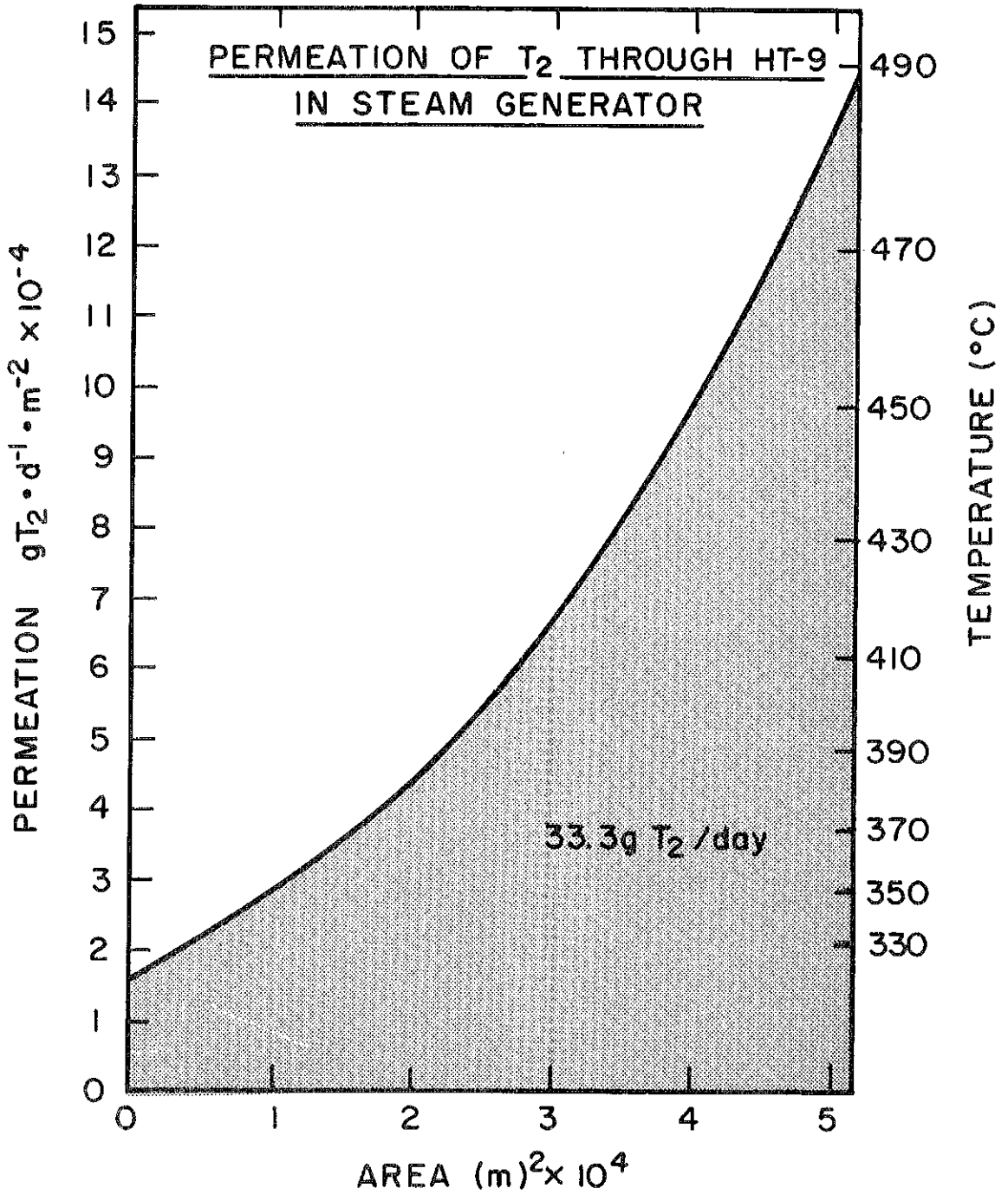
PERMEATION OF T_2 THROUGH HT-9
IN STEAM GENERATOR
33.3g T_2/day
PERMEATION $gT_2 \cdot d^{-1} \cdot m^{-2} \times 10^{-4}$
TEMPERATURE (°C)
AREA $(m)^2 \times 10^4$
0
1
2
3
4
5
6
7
8
9
10
11
12
13
14
15
330
350
370
390
410
430
450
470
490

Fig. VII.4-1

factor of 50 have been demonstrated for stainless steel structures containing an intermediate layer of Cu-Al-Fe alloy at 600°C. Metallic coatings with low hydrgen permeability coefficients would also present a barrier to the tritium. At present, the HIBALL design will utilize an oxide coating barrier, however, future designs will try to employ more effective tritum barriers.

Table VII.4-1 Permeation Barrier Factors of Ferritic and Austenitic Steels Produced by Steam Oxidation of the Downstream Side

	Ferritic	Ferritic	Austenitic
	Fe-2-1/4 Cr-1 Mo	SS 406	SS 316
Reference	5	4	4
Temperature (°C)	472	660	660
Steam Pressure (atm)	2	0.94	0.94
Factors by Which Permeabilities are Reduced			
0.33 d	10	13	---
1 d	25	72	1.6
6 d	100	144	2.8
24 d	170	291	3.8
40 d		434	4.3

VII.4.2 Containment in Steam Cycle

Assuming a factor of 10 reduction in permeation due to the oxide coating results in 3.3 g T_2/day lost to the steam cycle. In order to further reduce this quantity, the tubes in the steam generator will have a double-walled

construction, with a purge gas containing a low partial pressure of O_2 sweeping the tubing gap. Although double-walled tubing is expensive and difficult to produce,[3] this concept provides an effective tritium containment scheme. The oxygen in the purge gas helps to maintain a good oxide layer and it also converts tritium to HTO by combining it with the hydrogen that diffuses through the steamside. This significantly reduces the free tritium partial pressure, and thus reduces the diffusion driving force to the steam side.

If the oxygen partial pressure in the purge gas is assumed to be 1 torr and the maximum HTO pressure allowed in the gap is 0.1 torr, then the volumetric flow rate of the purge gas is 5.3 ℓ/sec. The HT pressure in the gap is about 10^{-16} torr, resulting in $\sim 10^{-2}$ Ci/day loss to the steam generator. The parameters for the steam cycle are given in Table VII.4-2.

The HTO that is formed in the purge flow is condensed and sent to a fuel cleanup unit where tritiated water is electrolyzed and hydrogen isotopes are then sent to the cryogenic distillation system for separation.

Secondary and tertiary containment schemes have not been addressed in detail at this time for HIBALL. However, the designs for containment in the TSTA facility will be tested in the near future, providing essential information to the fusion community on the aspects of tritium handling and containment.

Table VII.4-2 Parameters in Steam System

Tritium diffusion to LiPb side	3.3 g/day
Steam generator surface area	5.2×10^4 m^2
Tritium diffusion rate	1.5×10^{10} atoms T/cm^2 sec
O_2 pressure in purge gas	1 torr
Maximum HTO pressure	0.1 torr
Temperature range	315-490°C
Required purge gas flow rate	5.3 ℓ/sec
HT partial pressure in gap	1×10^{-16} torr
Total tritium loss to water	0.02 Ci/d

References for Section VII.4

1. R.V. Carlson and R.A. Jalbert, "Preliminary Analysis of the Safety and Environmental Impact of the Tritium System Test Assembly," Proceedings Tritium Technology in Fission, Fusion and Isotropic Applications, Dayton, Ohio, April 29 - May 1, 1980, CONF-800427, American Nuclear Society (1980), 347-352.

2. B. Badger et al., "WITAMIR-I - A Tandem Mirror Reactor Study," University of Wisconsin Fusion Design Memo UWFDM-400, Chapter XI, (Dec. 1979).

3. A.B. Johnson, Jr. and T.J. Kabele, "Tritium Containment in Fusion Reactors," Topical Meeting on Technology of Controlled Nuclear Fusion, Richland, Washington, Sept. 21, 1976, 1319-1328, CONF-760935.

4. J.T. Bell, J.D. Redman and H.F. Bittner, "Tritium Permeability of Structural Materials and Surface Effects on Permeation Rates," Proceedings Tritium Technology in Fission, Fusion and Isotropic Applications, Dayton, Ohio, April 29 - May 1, 1980, CONF-800427, American Nuclear Society (1980), 48-53.

5. T.A. Renner and D.J. Rave, "Tritium Permeation Through Fe-2-1/4 Cr-1 Mo Steam Generator Material," Nucl. Technol. 47, 312-319 (1979).

6. J.C. McGuire, "Hydrogen Permeation Resistant Layers for Liquid Metal Reactors," Proceedings Tritium Technology in Fission, Fusion and Isotropic Applications, Dayton, Ohio, April 29 - May 1, 1980, CONF-800427, American Nuclear Society (1980), 64-68.

7. V.A. Maroni, E.H. Van Deventer, T.A. Renner, R.H. Pelto, and C.J. Wierdak, "Experimental Studies of Tritium Barrier Concepts for Fusion Reactors," Proceedings Radiation Effects and Tritium Technology for Fusion Reactors, Gatlinburg, Tennessee, October 1-3, 1975, CONF-750989 Vol. IV, 329-361.

VIII Materials

VIII.1 Introduction

The materials problems in HIBALL can be categorized according to placement in the reactor and material type as shown in outline form.

1. Inside Reactor Cavity
   a. SiC
   b. HT-9 Structure
2. Reflector Region
   a. HT-9 Structure
3. Reactor Vessel Shield
   a. HT-9 Structure
   b. Pb
   c. Boron Carbide
4. Final Focussing Magnets
   a. NbTi Superconductor
   b. Cu Stabilizer
   c. Electrical Insulation

By far the most severe problems occur in the SiC INPORT units and the HT-9 structure of the reflector region and we will concentrate on these areas here. The analysis of each of these materials will be made in the following sequence:

1. Environment
   a. Thermal, Chemical, Stress
   b. Radiation
2. Comparison With Existing Data and Prediction of Expected Life in HIBALL

Obviously, a great deal of extrapolation will be necessary to arrive at meaningful lifetime predictions. The readers should recognize that we are breaking new ground in this area and the results should be viewed accordingly.

VIII.2 Materials Problems Inside Reactor Cavity

VIII.2.1 Silicon Carbide INPORT Units

VIII.2.1.1 Environment

VIII.2.1.1.1 General

The SiC woven structures are expected to operate in intimate contact with the $Pb_{83}Li_{17}$ coolant over a temperature range of 300-500°C. There is a possibility of some erosion due to the high (5 m/s) velocity of the coolant in the inner tubes. However, due to a relatively short lifetime (to be demonstrated later) of 1 to 2 years, and a capacity factor of ~ 70%, the total exposure time at temperature will be 6000 to 12,000 hours.

The stresses in the SiC tubes come from drag exerted by the flowing PbLi and amount to maximum static stresses of 130 MPa in the inner (smaller) tubes and 97 MPa in the outer (larger) tubes. The pulsed loads due to neutron heating amount to less than 1 MPa. Finally, the maximum pulsed stresses due to ablation of the front surface amount to 60 MPa-seconds at a 5 Hz rate.

VIII.2.1.1.2 Radiation Environment

It is assumed that all surfaces on the INPORT units facing the plasma are entirely covered by a liquid $Pb_{83}Li_{17}$ film which is at least 1 mm thick. The consequences of "dry" spots will be examined later. The SiC is mainly subjected to neutron damage because the target debris and most of the X-rays will be absorbed in the liquid film.

The neutron spectrum at the inner ring of tubes is shown in Fig. VIII.2-1 and the variation in displacement damage rate in the SiC is given in Fig. VIII.2-2. Figure VIII.2-3 gives the transmutation rate into gaseous elements throughout the $Pb_{83}Li_{17}$-SiC zone. The peak dpa rate in the SiC tubes is 118 per FPY and it drops to 10 dpa per FPY in the back (17th) row of INPORT units. Similarly, the peak helium and hydrogen production rate is 3705 and 1408 appm

Fig. VIII.2-1

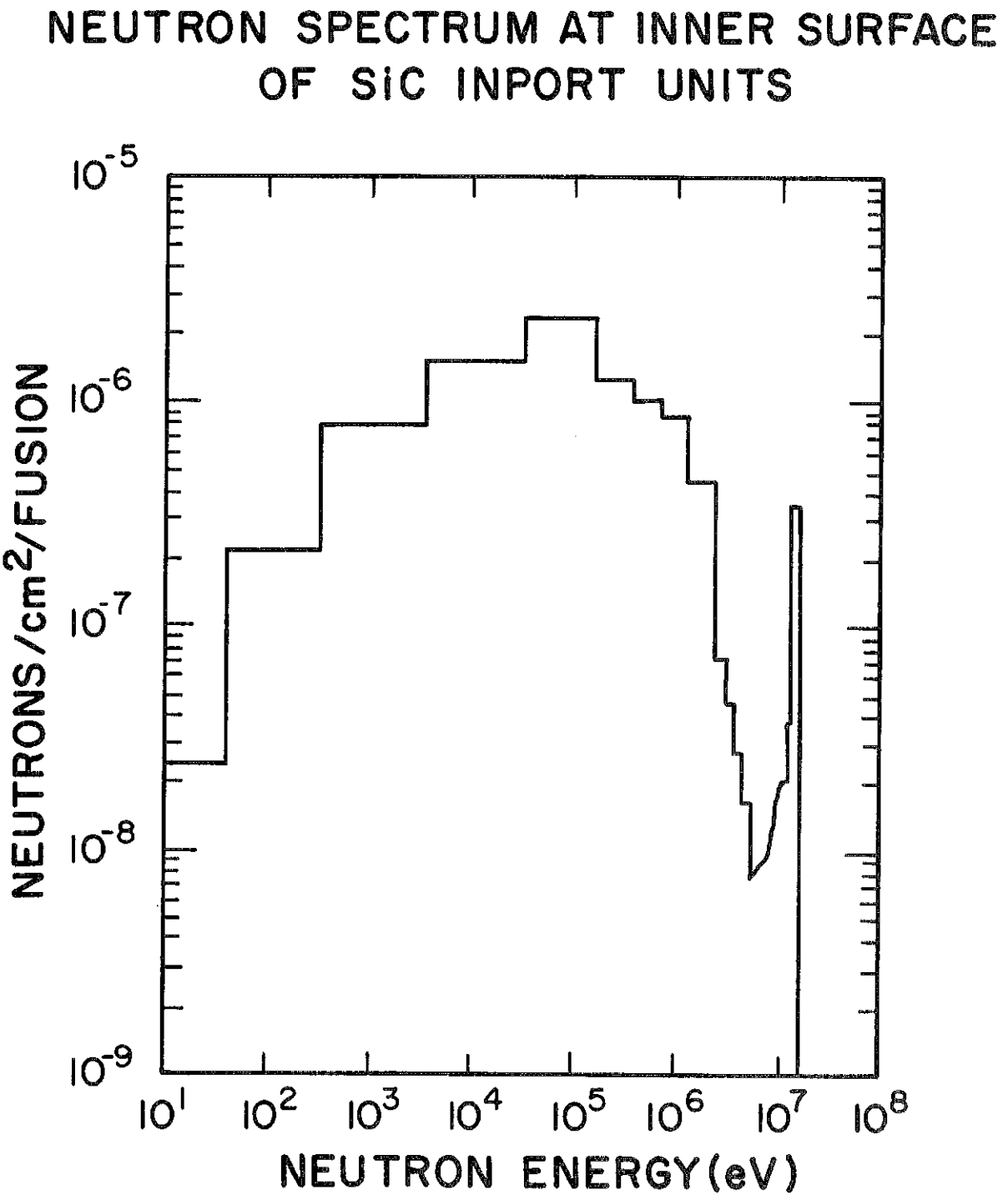
NEUTRON SPECTRUM AT INNER SURFACE OF SiC INPORT UNITS
NEUTRONS/cm2/FUSION
10-5
10-6
10-7
10-8
10-9
10¹
10²
10³
10⁴
10⁵
10⁶
10⁷
10⁸
NEUTRON ENERGY(eV)

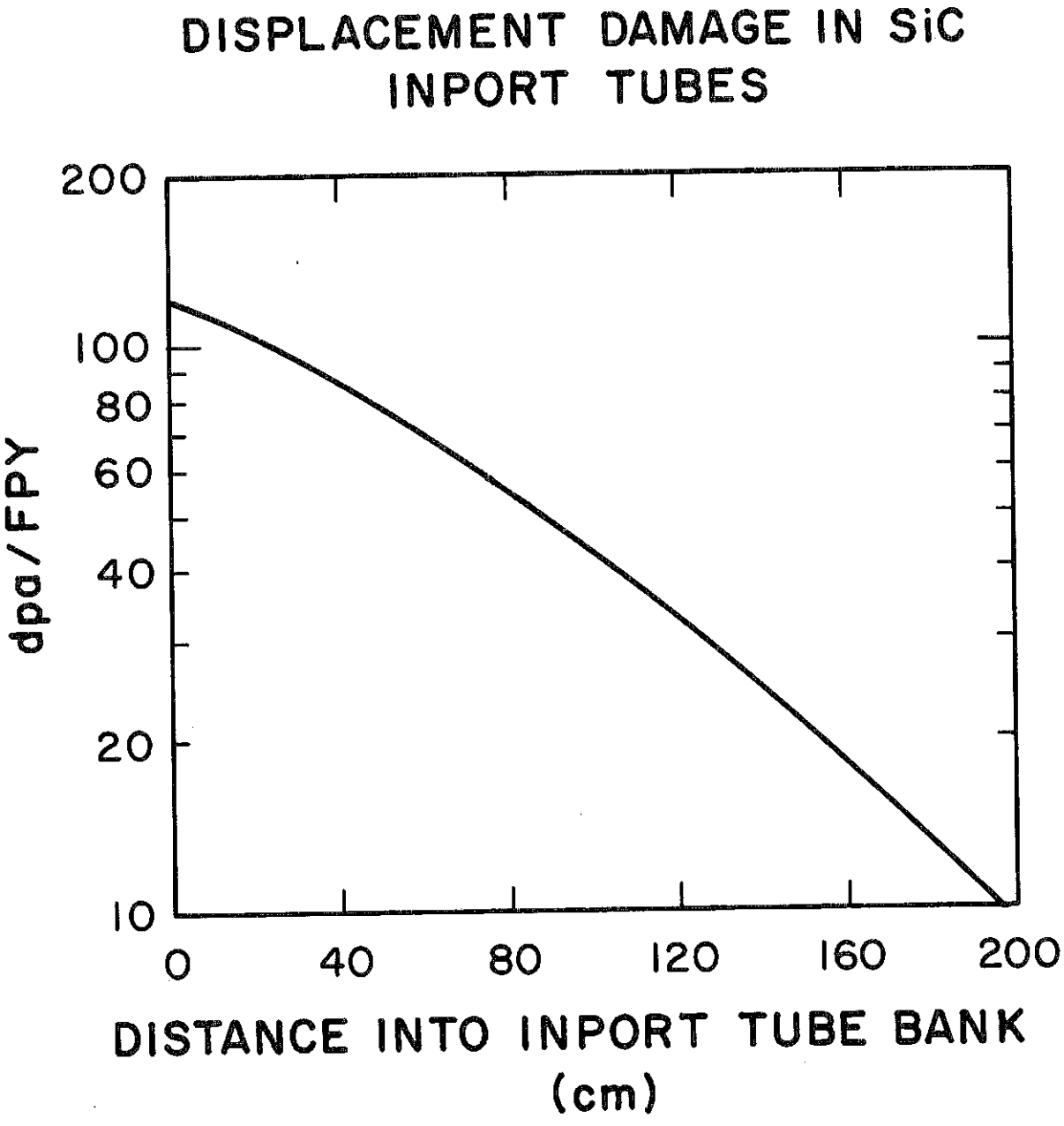
DISPLACEMENT DAMAGE IN SiC
INPORT TUBES
200
100
80
60
40
20
10
dpa/FPY
0
40
80
120
160
200
DISTANCE INTO INPORT TUBE BANK
(cm)

Fig. VIII.2-2

Figure VIII.2-3

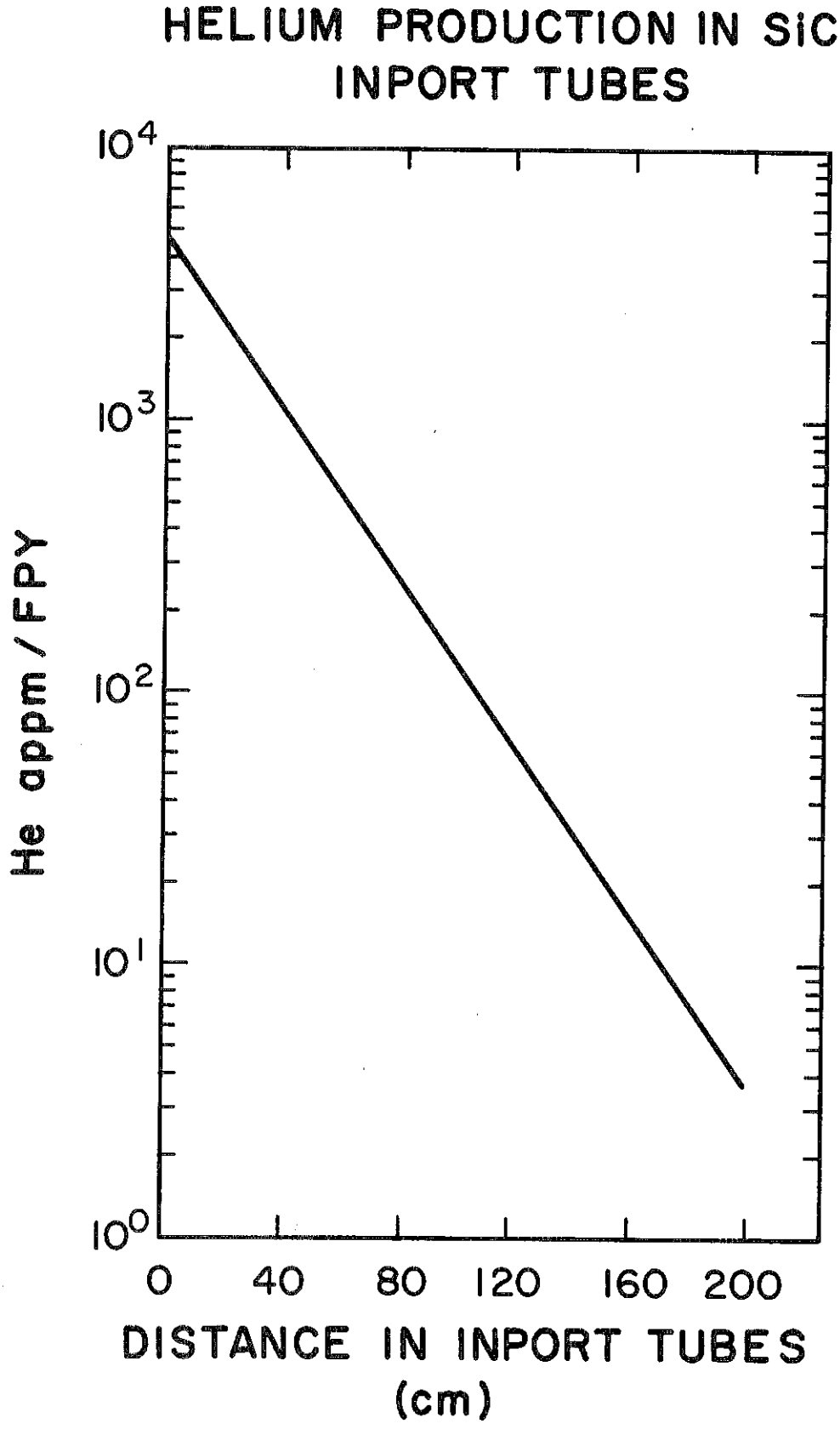

per FPY respectively and this drops to 4 appm and 1.7 appm per FPY respectively in the back row of tubes.

If the tubes become uncovered, for any reason, the SiC would be exposed to high intensity X-ray and particle debris fluxes. The X-ray flux (see Chapter III) results in a 27.9 J/cm^2 exposure to the SiC spread over 10 ns. The target debris (see Chapter III) will impact on the unexposed surface with an additional 6.6 J/cm^2 flux spread over 10 microseconds.

VIII.2.1.2 Previous Experience with SiC in Environment Typical of HIBALL

VIII.2.1.2.1 Mechanical Properties

As shown in section VI.2, the strength of SiC is entirely adequate in the 300-500°C range. However, essentially nothing is known about the effect of long term exposure to Pb or Li with respect to the tensile properties.

VIII.2.1.2.2 Chemical Compatibility of SiC with $Pb_{83}Li_{17}$

An extensive literature search revealed only one experimental reference to the compatibility of SiC with Li. W.H. Cook[1] determined that after 100 hours at 816°C, the corrosion resistance of SiC to Li was "bad". This particular rating was given to a material which suffered any one of the following physical changes:

1) a depth of attack of more than 0.076 mm,
2) more than a 6% weight change, or
3) more than a 3% dimensional change.

Obviously the testing conditions are far more severe than HIBALL conditions, but there is no reasonable way to extrapolate this experimental point to the 300-500°C operating regime at this time; therefore, continued experimental research into this topic is strongly recommended for the HIBALL conditions.

In view of the lack of pertinent experimental data, we chose to investigate the thermodynamics of Li interaction with SiC. Thermodynamic data[2] on

the formation of $Li_2C_2(s)$ as a corrosion product is given in Table VIII.2-1. Formation of lithium carbide from lithium interactions with silicon carbide is not favorable, however, there is no thermodynamic data on formation of known or other silicides or higher carbides which may be responsible for the incompatibility at higher (~ 1100°K) temperatures. Extrapolating the information for pure lithium and lead to the alloy system is difficult and more experimental work must be done. If it is assumed that the corrosive action occurs only from lithium, then because of the low percentage of lithium in the alloy (0.68 wt%) and the low activity of lithium in $Li_{17}Pb_{83}$ (~ 10^{-4} at 500°C) the compatibility should fall in the fair to good range.

Table VIII.2-1 Thermodynamic Formation of Lithium Carbide from Lithium and Various Ceramic Materials

	Free Energy (kcal/mole)		
Reaction	600°K	700°K	800°K
$Li(l) + C(s) \rightarrow 1/2\ Li_2C_2(s)$	-6.18	-5.96	-5.75
$Li(l) + \alpha\text{-}SiC(s) \rightarrow 1/2\ Li_2C_2(s) + Si(s)$	9.76	9.79	9.81
$Li(l) + \beta\text{-}SiC(s) \rightarrow 1/2\ Li_2C_2(s) - Si(s)$	10.13	10.18	10.21
$Li(l) + B_4C(s) \rightarrow 1/2\ Li_2C_2(s) + 4\ B(s)$	2.85	3.04	3.19
$Li(l) + TiC(s) \rightarrow 1/2\ Li_2C_2(s) + Ti(s)$	36.13	36.11	36.07
$Li(l) + ZrC(s) \rightarrow 1/2\ Li_2C_2(s) + Zr(s)$	39.31	39.33	39.35

VIII.2.1.2.3 Radiation Effects on SiC

The amount of fission neutron irradiation data on SiC is very limited[3-6] and, of course, there is no information on 14 MeV neutron effects at the present time. What data is available is entirely from solid SiC samples and there is no information on woven structures. However, there is some data on woven grahite fibers[7] which indicates successful operation up to ~ 10 dpa at ~ 500°C.

Traditional lifetime analyses for fusion reactor first walls cannot be used for the woven SiC INPORT units. Dimensional changes (due to voids, linear growth, etc.) can be easily accommodated, crack propagation has little meaning in a structure made up of thousands of individual strands, and thermal stress has little significance when the fibers are only microns in diameter. Ductility changes will be important and could give some indication of when the tubes (at least in the front rows) might begin to break apart under the periodic motion associated with the target debris. However, no meaningful measurements of the ductility of irradiated fibers has been conducted as of now. Ductility is notoriously sensitive to small amounts of He in metals, but helium effects in ceramics like C or SiC are far less documented. In fact, at high enough temperatures, helium is known to migrate out of carbon.[8]

What then, is a reasonable set of criteria by which to judge the lifetime of the SiC INPORT units? Because of the sparcity of data we will examine the following information

	HIBALL Limit
Linear Expansion	< 10%
Fracture Strength	> 180 MPa
Burnup of SiC	< 1%

VIII.2.1.2.3.1 Linear Length Changes in Irradiated SiC

Early work by Price[3] revealed that the linear expansion of SiC saturated at relatively low levels of irradiation (less than 3 x 10^{20} n/cm^2 which is ~ 0.3 dpa). Price found that this saturation level of expansion was inversely proportional to temperature as indicated in Fig. VIII.2-4. Such information would suggest that saturation levels of ~ 0.5% might be reasonable.

Later work by Sheldon[4] to 5 x 10^{22} n/cm^2 (~ 50 dpa) at 550°C also confirmed the saturation effect and projected that "acceptable" linear expansion could be tolerated up to 100 dpa (~ 10^{23} n/cm^2).

Even more recent work by Corelli et al.[5], Fig. VIII.2-5, showed that at $\lesssim$ 200°C, the swelling saturated at roughly 3 to 4% by 10^{22} n/cm^2 (~ 10 dpa). This corresponds to a linear expansion of ~ 1%, very close to the data of Price (Fig. VIII.2-4).

In summary, it appears that linear expansions of 0.5 to 1% might be observed after ~ 1 month of operation in HIBALL. After that time, we might expect very little additional expansion and therefore irradiation induced growth would not appear to be a life limiting feature.

This conclusion is supported by studies at BNWL where graphite clothes were irradiated to 4, 7, and 10 dpa at 470°C.[7] The dimensional changes ranged from +33% to -27%, far in excess of those observed in SiC. Despite these large dimensional changes, the two-dimensional cloth remained essentially unchanged. Such results give us more confidence in the ability of the SiC cloth structure to withstand neutron irradiation.

VIII.2.1.2.3.2 Fracture Strength of Irradiated SiC

There are two studies of significance in this area: one by Mathney et al in 1979[6] and the other by Corelli et al.[5] in 1981. Both studies used a

Figure VIII.2-4

THE NEUTRON-INDUCED EXPANSION OF SILICON CARBIDE [AFTER PRICE]

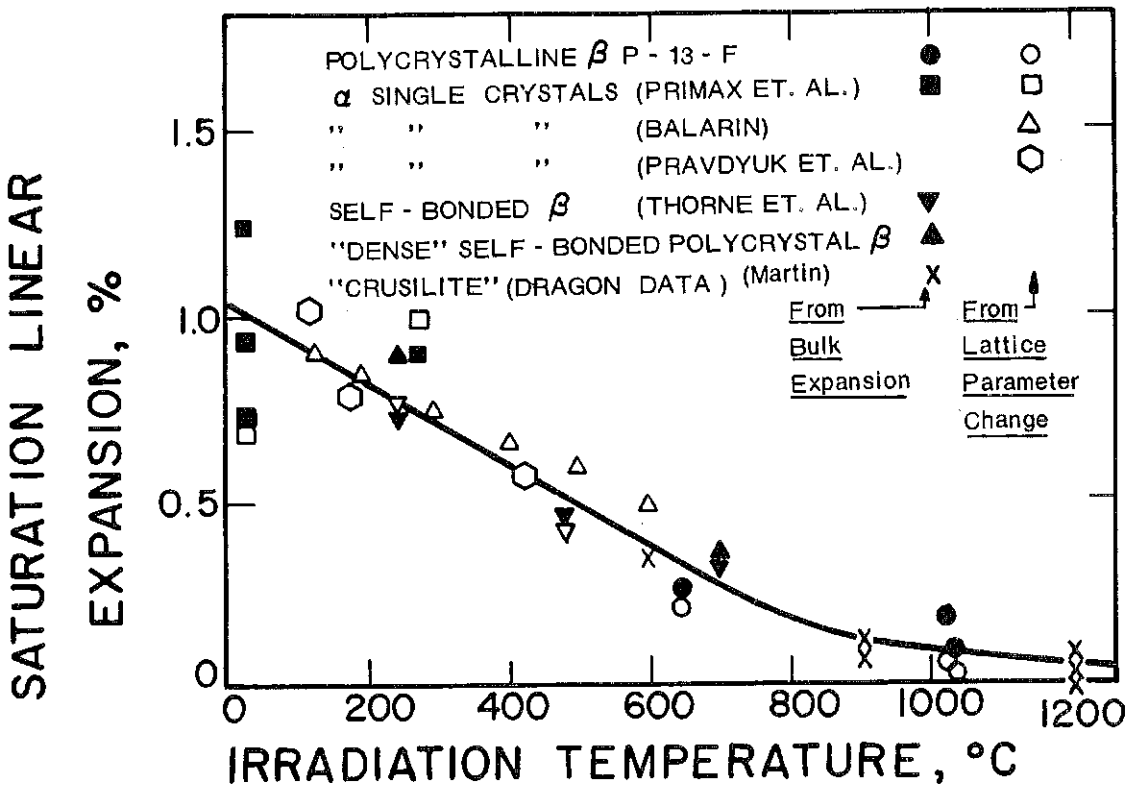

Figure VIII.2-5

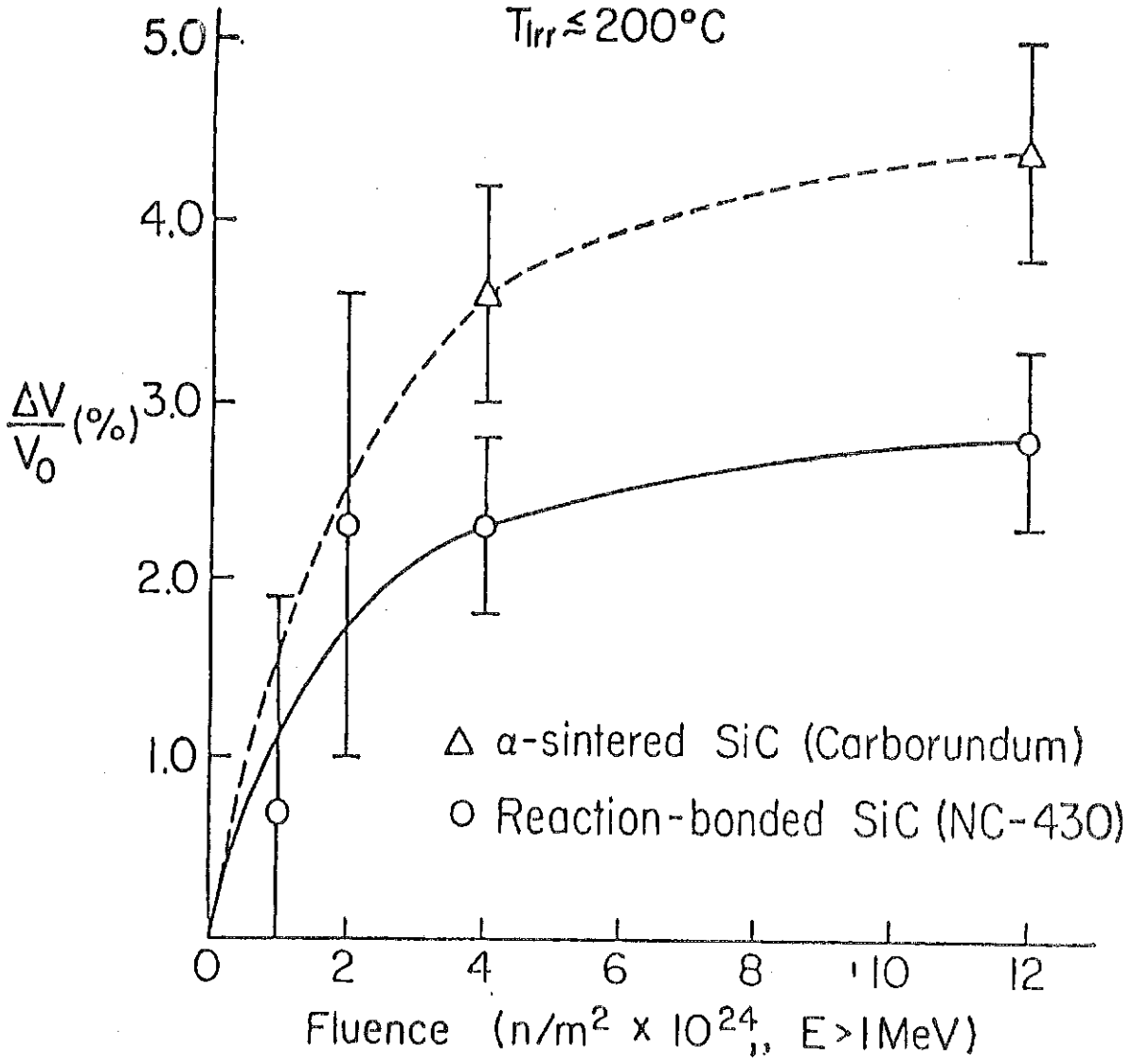

Swelling $\Delta V/V_0$, vs. fluence for NC-430 SiC and sintered α-SiC.

material labelled NC-430 which is 88.5% SiC, silicon metal of 8-10%, and minor impurities such as Fe (0.4%), Al (0.1%), and Boron (0.005%). The initial fracture strength was 230 to 270 MPa. After irradiation up to ~ 1 dpa at < 200°C the fracture strength remained unchanged when tested at 1200°C (Fig. VIII.2-6).

Irradiation of sintered α-SiC revealed much more sensitivity to irradiation. The fracture strengths of the α-SiC dropped to ~ 120 MPa at 1200°C after ~ 1 dpa damage at 200°C (Fig. VIII.2-7).

In summary, low fluence (~ 1 dpa) irradiation at < 200°C seems to have little effect on the fracture strength of NC-430 but it can reduce the fracture strength of α-SiC by a factor of 3. There is no higher fluence data on which to extrapolate to the 100 dpa level at this time.

VIII.2.1.2.3.3 Effect on Thermal Conductivity

It is well known that neutron irradiation will reduce the thermal conductivity of carbon and SiC. Recent work by Corelli et al.[5] shows that the thermal conductivity is reduced by a factor of 3 in the first dpa of damage and seems to saturate at that level (Fig. VIII.2-8). Since the majority of the heat conduction in the INPORT units is done by the Pb-Li alloy, such a drastic change has little effect on the liquid surface temperature. Therefore, we do not view such a degradation as a serious problem.

VIII.2.1.2.3.4 Burnup of SiC Atoms

The neutron spectral difference between fission and fusion systems is quite dramatic. For example, the damage rate per full power year in HIBALL is 118 dpa/FPY. At a maximum neutron wall loading of ~ 5 MW/m^2 on the tubes this translates into 24 dpa per MW-y/m^2. In a fission reactor the damage rate is ~ 10 dpa per 10^{22} n/cm^2 (E > 0.1 MeV).

Figure VIII.2-6

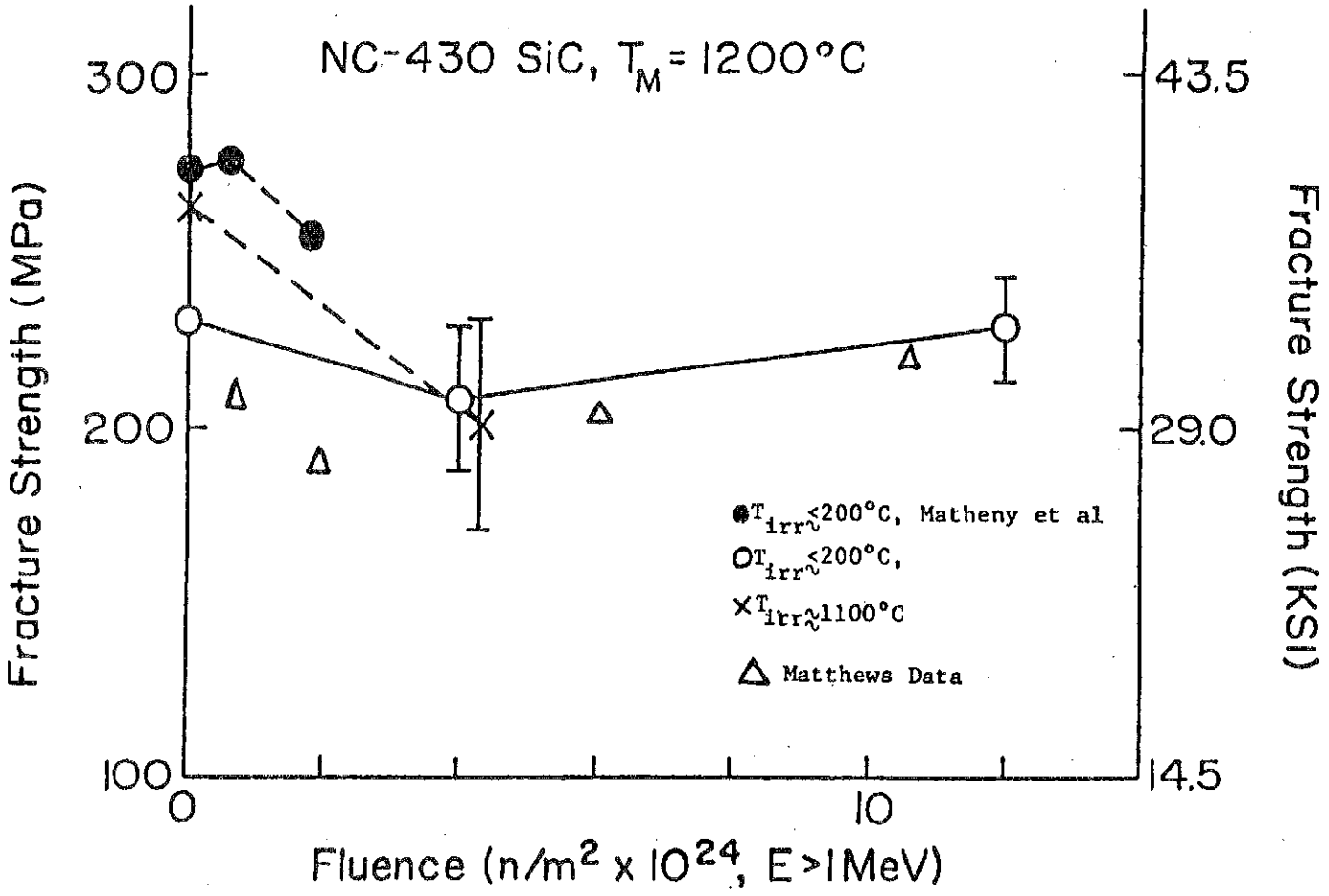

Mean fracture strength vs. fluence of NC-430 SiC at 1200°C.

VIII.2-13

Figure VIII.2-7

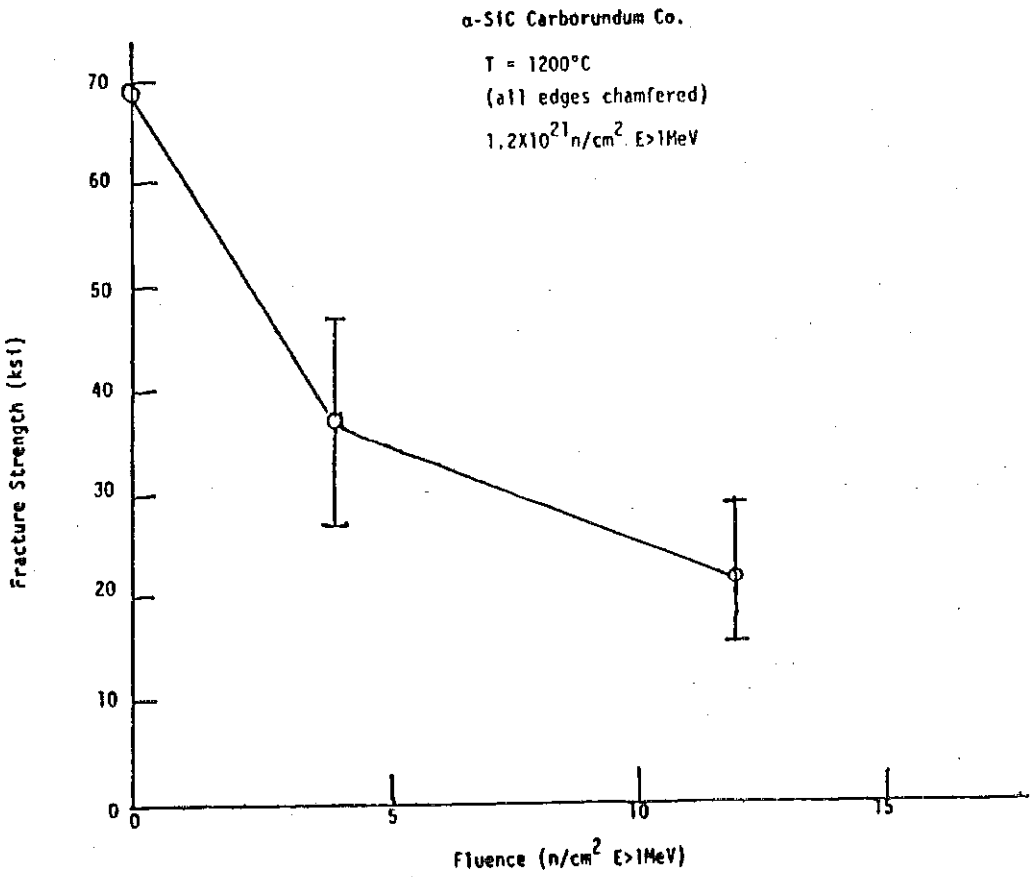

Mean fracture strength vs. fluence of sintered α-SiC at 1200 ^{o}C.

Figure VIII.2-8

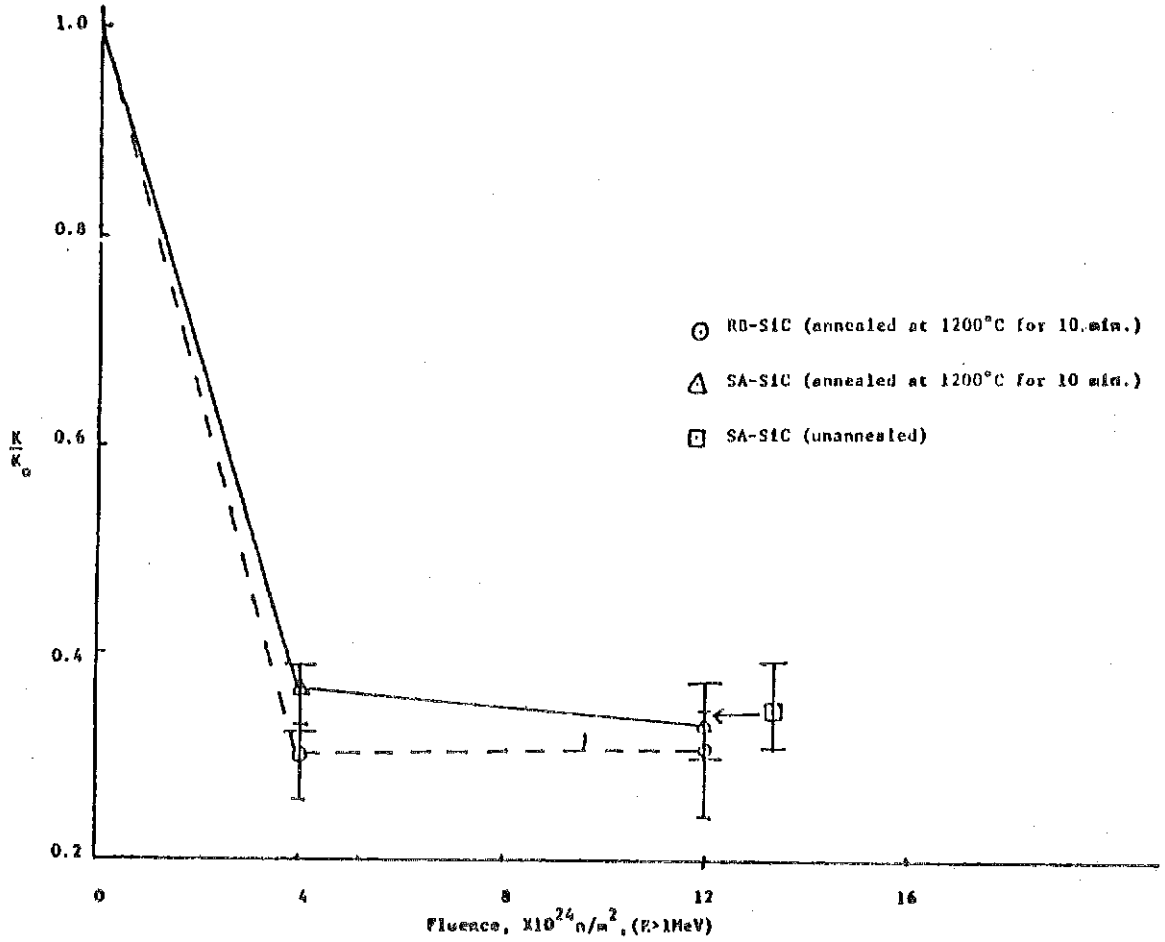

Relative thermal conductivity, K/K_0 (measured at $T \approx 23\ ^{o}C$), vs. fluence for NC-430 SiC and sintered α-SiC.

The production of helium is ~ 740 appm He per MW-y/m^2 in HIBALL but only ~ 14 appm per 10^{22} n/cm^2 in a fission reactor. Similarly the production of hydrogen is ~ 280 appm per MW-y/m^2 in HIBALL but ~ 11 appm per 10^{22} n/cm^2. A comparison of the appropriate values for fission and fusion reactors is given in Table VIII.2-2.

From the information in Table VIII.2-2 we find that roughly 0.5% of the SiC molecules lose one of its atoms per FPY. While there is no firm rule of thumb as to how much burnup can be tolerated, we think the value of 1% is reasonable. On this basis, we would limit the INPORT unit lifetime to 2 FPY in the inner units. The burnup drops off rapidly in the outer tubes such that the limit is not reached for 10 FPY in the 10th row and the last (17th) row of tubes never reaches the 1% limit in 20 FPY's.

Table VIII.2-2 Comparison of Radiation Damage Parameters in SiC

	HIBALL	HFBR(a)
Displacement damage		
dpa per MW-y/m^2	24	---
dpa per 10^{22} n/cm^2 (b)	---	10
dpa/FPY	118	16
Helium production		
appm He per MW-y/m^2	740	---
appm He per 10^{22} n/cm^2 (b)	---	14
appm He/FPY	3705	22
Hydrogen production		
appm H per MW-y/m^2	280	---
appm H per 10^{22} n/cm^2 (b)	---	10
appm H/FPY	1408	16

(a) High flux beam reactor[5].
(b) (E > 0.1 MeV).

References for Section VIII.2

1. W.H. Cook, "Corrosion Resistance of Various Ceramics and Cermets to Liquid Metals," Oak Ridge National Laboratory, June 15, 1960, ORNL-2391.

2. D.R. Sull et al., JANAF Thermochemical Tables, The DOW Chemical Company, Midland, Michigan.

3. R.J. Price, J. Nucl. Mat. 33, 17 (1969).

4. B.E. Sheldon, UKAEA-Harwell, AERE-R8025, August 1975.

5. J.C. Corelli et al., Chapter 8 in "Ceramic Materials for Fusion Reactors," EPRI-AP-1702, February 1981.

6. R.M. Matheny, J.C. Corelli, and G.G. Trantina, J. Nucl. Mat. 83, 313 (1979).

7. W.J. Gray, Battelle Northwest Laboratory, BNWL-2390, August 1977.

8. J. B. Holt et al., "Helium Generation and Diffusion in Graphite," Lawrence Livermore Laboratory Report, April 1976.

VIII.3 HIBALL Reflector Region

VIII.3.1 HT-9 Structural Material

VIII.3.1.1 General Environment

The reflector is cooled by a Pb-Li alloy which ranges in temperature from 300 to 500°C. The flow velocity is 1 m/s and the coolant pressure is 2 MPa. A relatively high vacuum ($< 10^{-5}$ torr) normally exists on the chamber-side of the reflector region, but the first wall of the reflector region is periodically covered with Pb vapor at 500°C or higher. The hydrogen partial pressure is 10^{-4} torr at 500°C.

VIII.3.1.2 Radiation Environment for HT-9

The two key measures of radiation damage, the displacement damage and amount of He produced per FPY are plotted in Fig. VIII.3-1 as a function of effective INPORT unit thickness. Because of the protection afforded by the inport units the maximum damage in the HT-9 side wall is 2.7 dpa per FPY and this drops by a factor of 100 over the 41 cm thickness (Fig. VII.3-2). Similarly, the maximum helium production is 0.4 appm He per FPY and this drops by a factor of 1000 across the reflector. The appm He/dpa ranges from 0.1 to 0.02.

The damage rate of the neutrons behind the INPORT units is given in Fig. VIII.3-3. The peak damage rate is 0.009 dpa per second and the damage rate stays above 10^{-3} dpa per second for ~ 5 microseconds and above 10^{-4} dpa sec^{-1} for 10 microseconds.

VIII.3.2 Previous Experiments Under HIBALL-Type Conditions

VIII.3.2.1 Compatibility of HT-9 with Pb-Li Alloys

As might be expected, there is no data concerning the $Pb_{83}Li_{17}$ eutectic alloy on HT-9 at temperatures of 350-500°C. There is a small amount of information on low alloy, high strength steels in pure lead[1-5], and some data on

Fig. VIII.3-1 Variation in damage parameters for HT-9 in the reflector region of HIBALL.

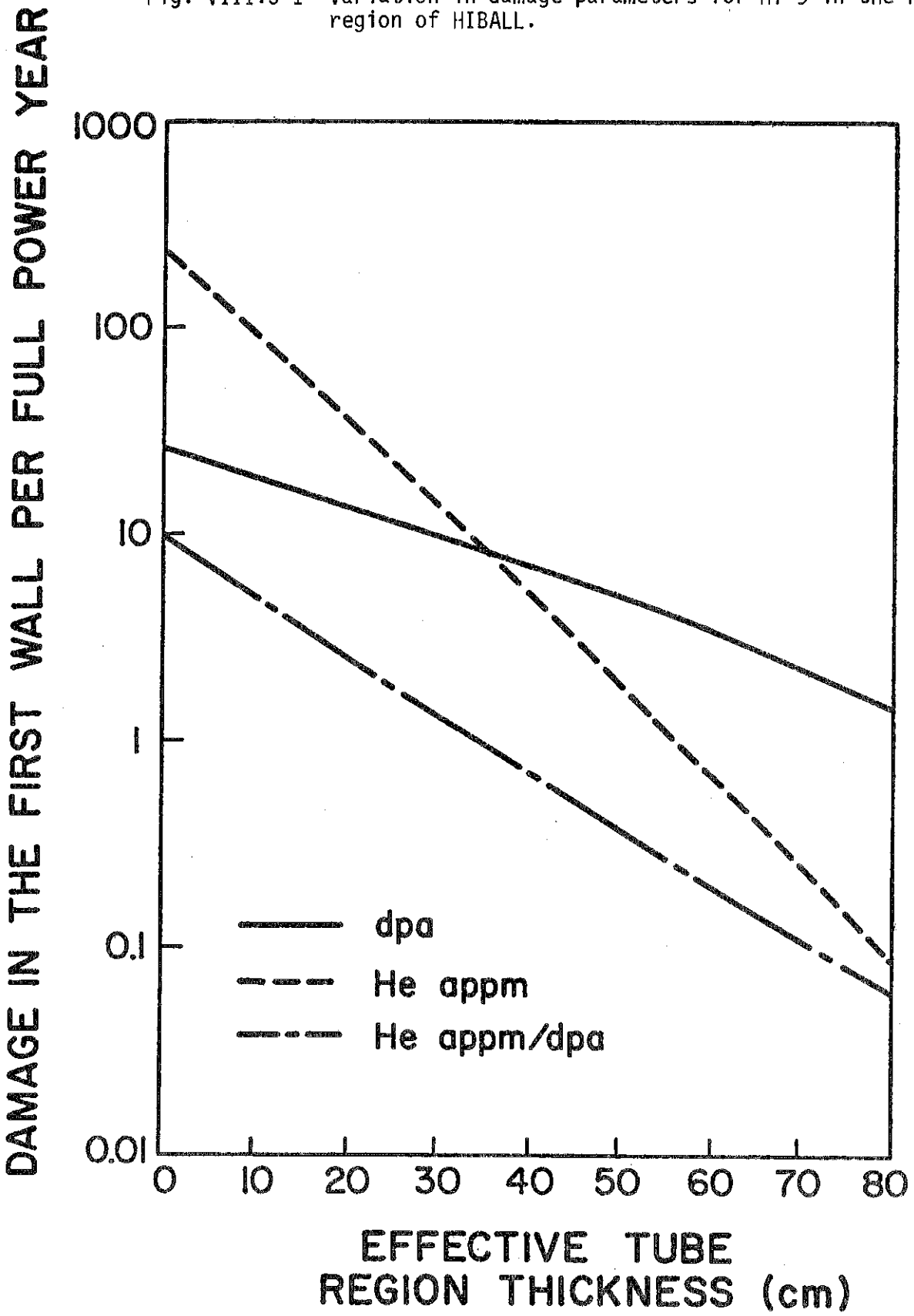

Figure VIII.3-2

Spatial variation of radiation damage in HT-9 structure of HIBALL reflector region.

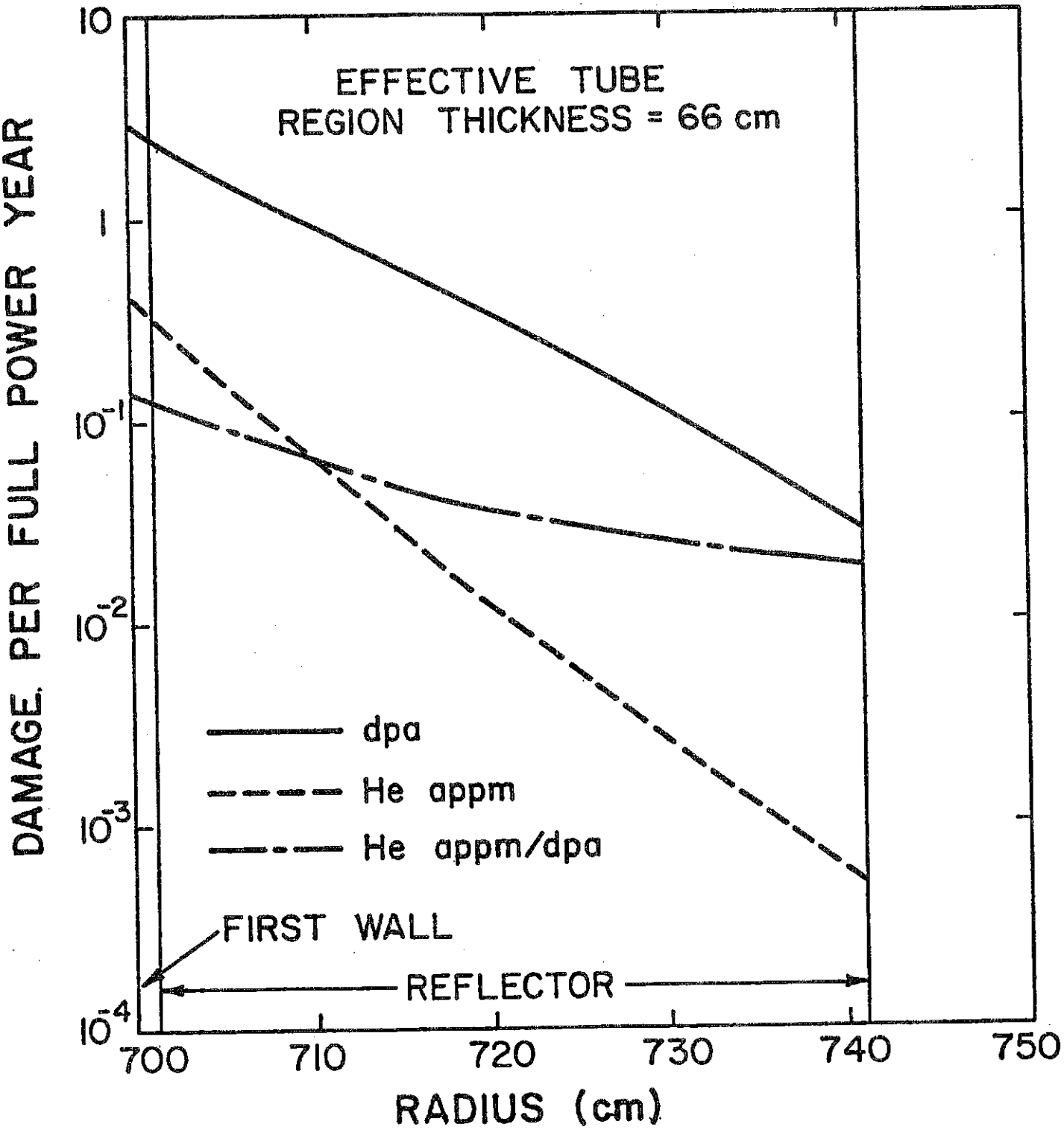

VIII.3-4

Figure VIII.3-3

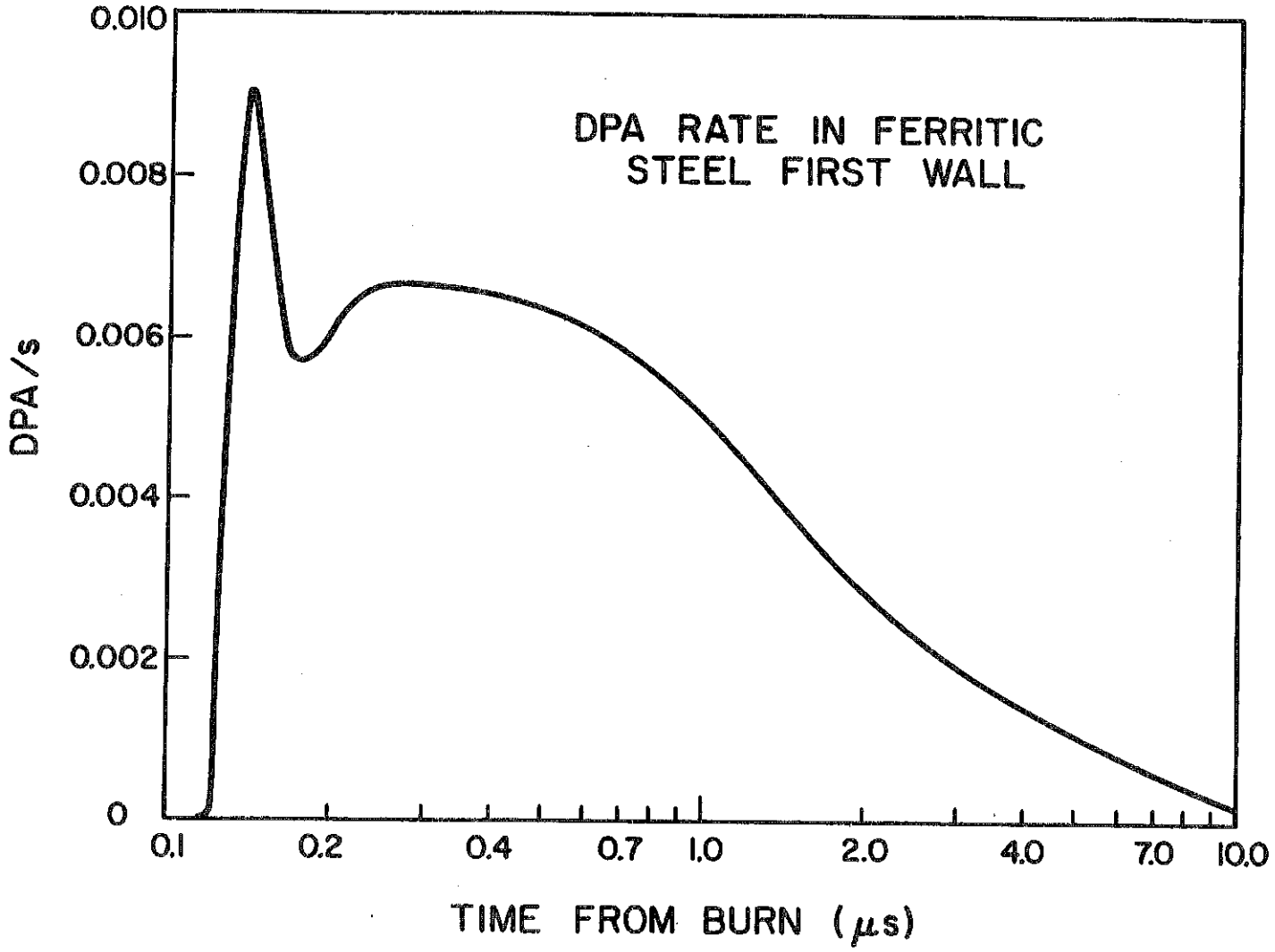

2-1/4 Cr-1 Mo alloys with a $Li_{99}Pb_1$ system at 500°C.[6] The only information on liquid metals and HT-9 is a recent study at ANL in pure lithium and lithium contaminated with nitrogen at 482°C.[7]

Despite claims in earlier studies that low alloy steels were not embrittled by pure lead, recent results showed embrittlement could occur near the melting point of the lead (327°C).[4,5] The embrittlement of the high strength 4100 series steels started at ~ 200°C and reached a maximum (lowest ductility) at ~ 320°C. Above ~ 370°C there was degradation in the ductility (see Fig. VIII.3-4). The addition of Sn increased the width of the embrittling zone.

At higher temperatures, 700°C, 2-1/4 Cr-1 Mo alloy suffered a severe attack after 300 hours of exposure to lead.[3] However, the addition of Ti to the Pb completely eliminated the corrosion under the same conditions. It has been known for a long time that the addition of Ti or Zr to Pb would inhibit corrosion by forming tightly adherring TiC and ZrC films on the steel surface.

On the other end of the spectrum, a $Li_{99}Pb_1$ alloy was shown to attack Fe_3C and Mo_2C in the welded zones of a 2-1/4 Cr-1 Mo alloy at 500°C after exposure up to 1600 hours. Figure VIII.3-5, from the paper by Anderson et al.[4], shows that the cementite and Mo_2C are unstable with respect to Li below 500°C while the chromium carbides are stable over a wide range.

Work at Harwell[8] has shown that low alloy steels can be significantly decarborized by exposure to Li even at ~ 200°C. However, higher Cr containing steels such as 2-1/2 Cr-1 Mo, or the 9 Cr-1 Mo alloys showed much greater resistance.[9] Presumably, the higher Cr content of HT-9 would help to protect that alloy from decarborization and hence embrittlement.

A recent study by Chopra and Smith[7] has shown that nitrogen can have a large effect on the fatigue life of HT-9 in flowing Li at 482°C. They found

Figure VIII.3-4

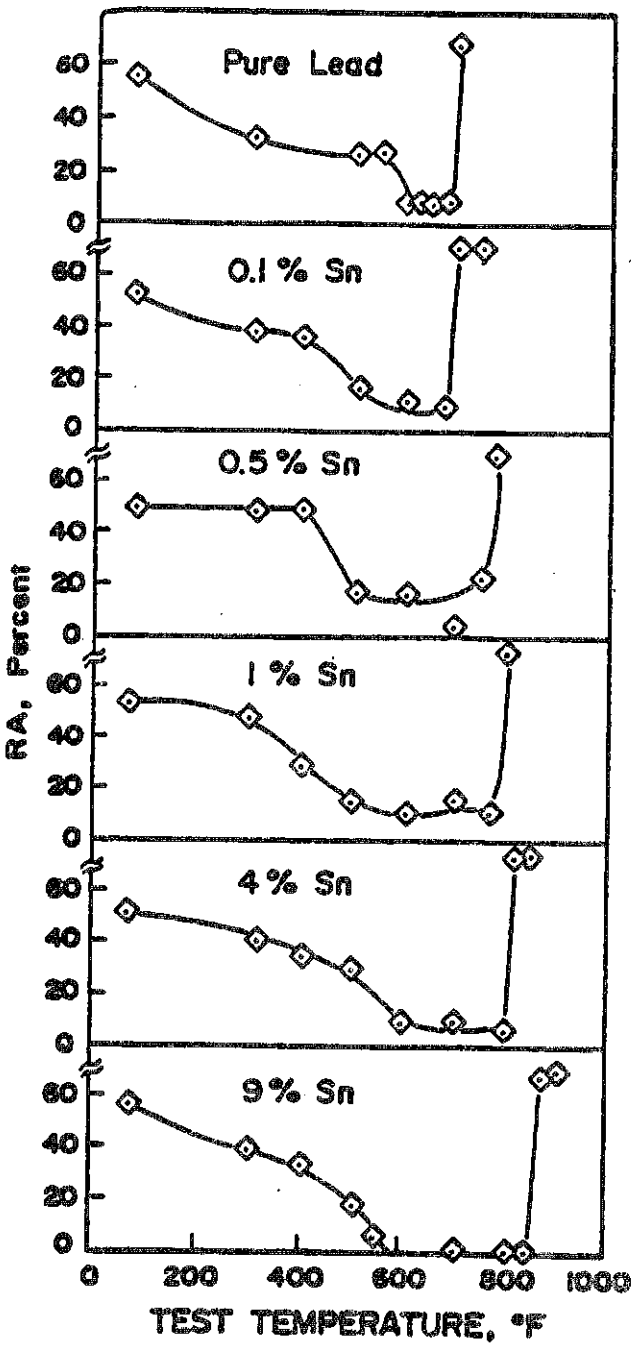

Reduction of area, RA, for 200-ksi (1379-MPa) 4145 steel, surface wetted with various Pb-Sn alloys as a function of test temperature. (4,5)

VIII.3-7

Figure VIII.3-5

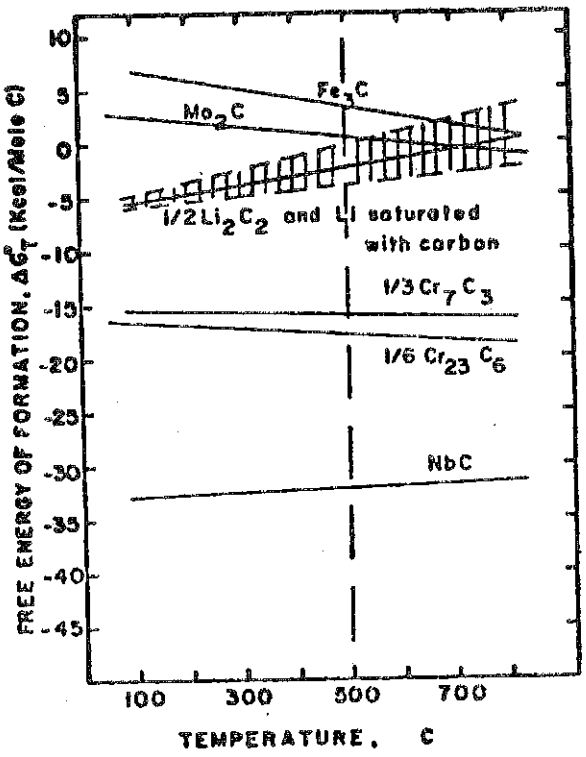

Relative thermodynamic stability of several carbides in carbon saturated lithium. (4)

that in short term fatigue tests, where the nitrogen level was between 80 and 130 ppm, the fatigue life in Li was the same as that obtained in Na. However, when the nitrogen level reached > 1000 ppm of nitrogen, there was a dramatic drop in the fatigue life (Fig. VIII.3-6) by as much as a factor of 5. This strongly suggests that close control of the nitrogen level of the HIBALL coolant will be necessary.

In summary, it appears that pure lead can have an embrittling effect on low chromium containing steels between 200 and 320°C but operation above that temperature and below 700°C should be acceptable. Ti or Zr inhibitors can be added to the Pb-Li alloy to reduce the corrosion. The higher chromium content of the HT-9 is also likely to help the weld zones to resist attack by the lithium.

VIII.3.2.2 Radiation Effects to HT-9

The response of HT-9 to neutron irradiation has been the subject of intense investigation in the LMFBR program. It has been found (by scientists at General Atomic) that HT-9 is resistant to significant void production below 100 dpa which is roughly equivalent to 40 FPY in HIBALL (see Fig. VIII.3-7). Similarly neutron damage to 5 dpa has been shown to have very little effect on the tensile properties and tensile ductility of the HT-9 alloy. However there is a modest upward shift in the ductile to brittle transition temperature (DBTT) of 100°C in 5 dpa (Fig. VIII.3-8). This DBTT shift seems to be saturated above 5 dpa and at 25 dpa it is still only ~ 100°C. Since the melting temperature of $Pb_{83}Li_{17}$ is 254°C, this is still 150°C above the DBTT. Therefore it appears that ferritic steel can last the lifetime of HIBALL without necessarily having to enter the brittle regime.

The effect of high damage rates (Fig. VIII.3-3) on the final damage state can only be a subject for speculation at this time. Theoretical analysis

VIII.3-9

Figure VIII.3-6

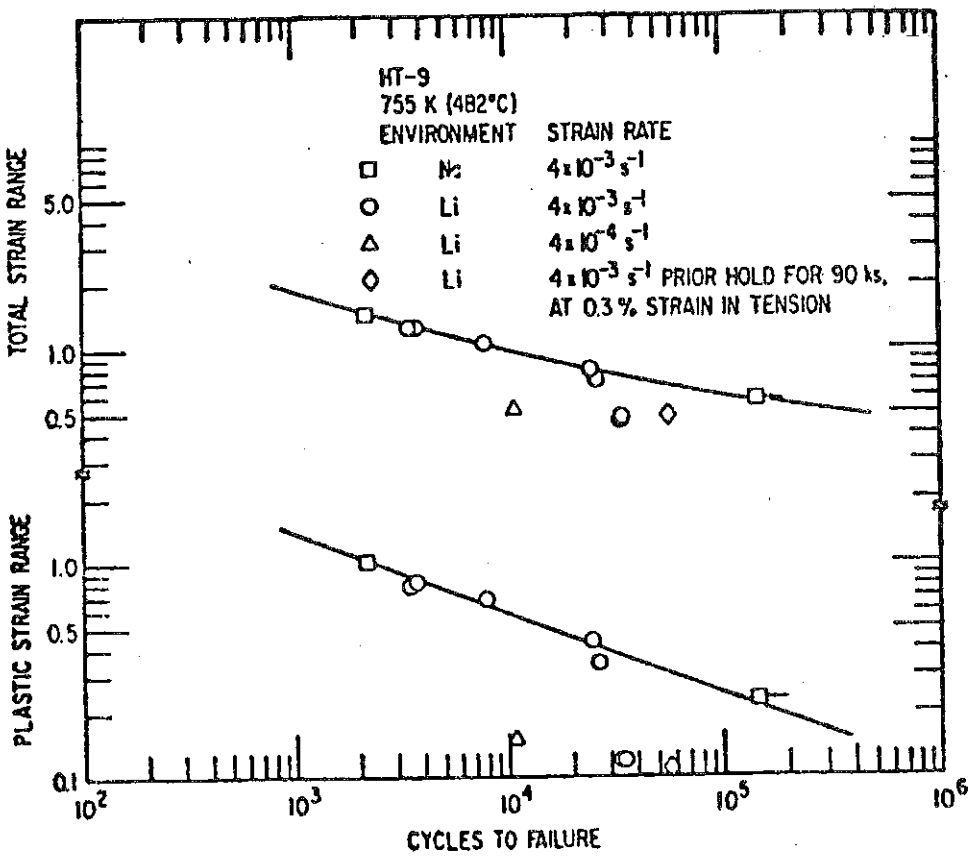

Total and plastic strain range vs. cycles to failure for HT-9 alloy tested in lithium at 755 K.(7)

Figure VIII.3-7
Swelling of candidate CTR materials during neutron irradiation.

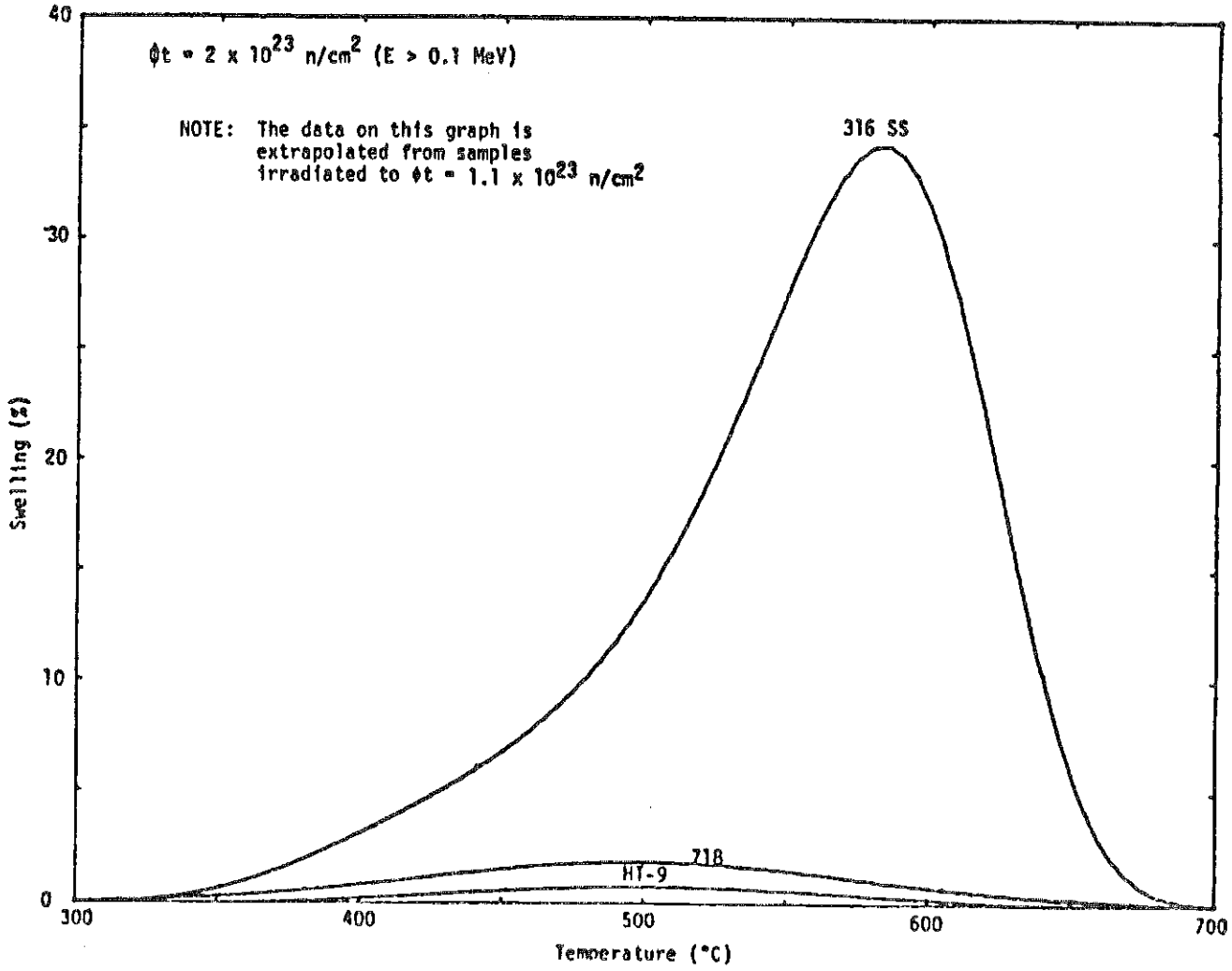

Figure VIII.3-8

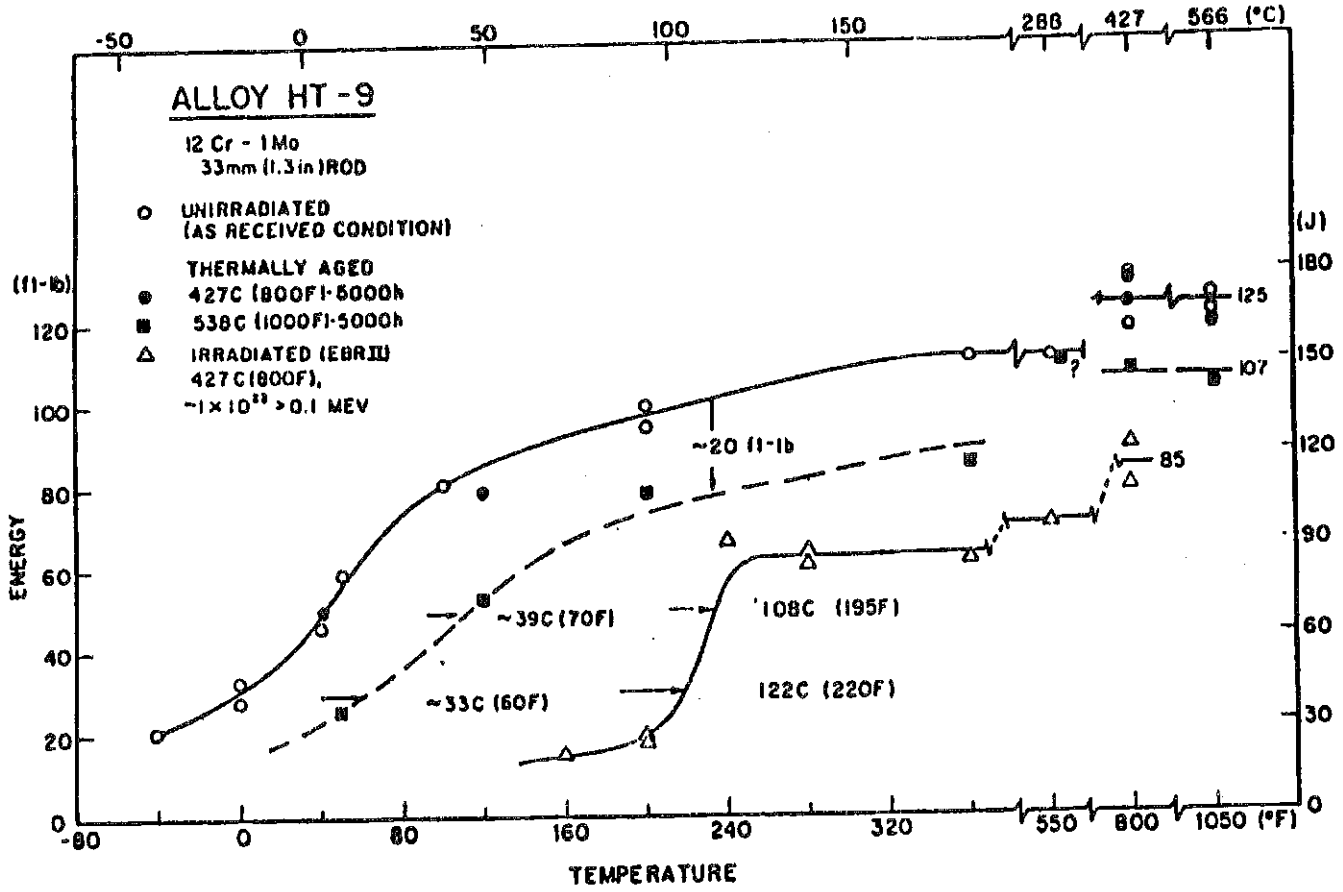

Charpy-V energy values as a function of test temperature for HT-9 in the as-received condition, after 5000 hr aging at 427°C, after 5000 hr aging at 538°C, and after irradiation to a neutron fluence of 1.1×10^{22} n/cm^2 (E > 0.1 MeV) at an irradiation temperature of 419°C ± 15°C in the EBR-II reactor From F. Smidt and scientists at Naval Research Laboratory.

reveals that the high damage rates may promote such a high supersaturation of point defects that enhanced recombination will occur and lower the residual damage. However no experimental data on pulsed data exists at this time and we will have to wait for future clarification in test facilities.

References for Section VIII.3

1. W.R. Warke and M.M. Breyer, "Effect of Steel Composition on Lead Embrittlement," J. of the Iron and Steel Institute, p. 779 (Oct. 1971).

2. C.F. Old, "Liquid Metal Embrittlement of Nuclear Materials," J. Nuclear Materials 92, (1980).

3. R.C. Asher, D. Davis, and S.A. Beethour, "Source Observations on the Compatibility of Structural Materials with Molten Lead," Corrosion Science, 17, 545 (1977).

4. J.C. Lynn, W.R. Warke, and P. Gordon, "Solid Metal-Induced Embrittlement of Steel," Mat. Sci. and Engr. 18, 51 (1975).

5. M.M. Breyer and K.L. Johnson, "Liquid Metal Embrittlement of 4145 Steel by Lead-Tin and Lead-Antimony Alloys," J. of Testing and Evaluation 2, 471 (1974).

6. T.C. Anderson et al., "Intergranular Penetration of 2-1/4 Cr-1 Mo Weldiments by a Lithium-Lead Liquid," to be published, 2nd Int. Conf. on Liquid Metal Technology in Energy Production, April 20, 1980, Richland, WA.

7. O.K. Chopra and D.L. Smith, to be published.

8. C.F. Olds and P. Trevena, AERE-R9505 (1979).

9. J.E. Cordell, in Proc. BMES Conf. on Liquid Alkali Metals, Nottingham, p. 177 (1973).

VIII.4 Helium Behavior in the HIBALL Structural Material

VIII.4.1 Introduction and Background

Fusion reactor first walls are expected to withstand severe operational environments. Aside from the detrimental effects of radiation damage, nuclear reactions produce both solid and gas transmutants in the structural materials. The generation of helium as a result of transmutation reactions arouses concern about its effects on the long-term integrity of the first wall. The presence of helium has been recognized to degrade the high temperature ductility of stainless steel.(1) More recently, void formation and swelling of metals were recognized to be strongly influenced by the presence of helium.(2)

Helium is thermodynamically insoluble in metals and tends to precipitate into bubbles if the temperature is high enough for the helium atoms to migrate. Whereas helium concentrations in steel typical of fission reactor environments are in the range of 1-10 appm,(3) the situation is expected to be much more severe for Magnetic Confinement Fusion Reactors (MCFR's) and Inertial Confinement Fusion Reactors (ICFR's) because the transmutation cross sections for the 14 MeV neutrons are much higher. Generation rates are projected to be considerably greater than fast breeder reactors with up to 644 appm/yr in a Princeton design,(4) 285 appm/yr in UWMAK-I,(5) and ~ 294 appm/yr in the INTOR design.(6) The helium generation rates in HIBALL depend on whether or not the steel is protected by the INPORT units. Components such as the inlet for the target injector or the front part of the struts holding up the INPORT units will experience helium production rates of ~ 230 appm per full power year. On the other hand, the HT-9 first wall behind the INPORT units will only experience helium production rates of ~ 0.4 appm per FPY.

The helium content and the high ratio of helium concentration to displacement damage predicted for fusion reactors has given rise to the

expectation that bubbles rather than voids may exist in many fusion reactor structural materials.[7,8] Furthermore, the synergistic effects of helium and displacement damage have been predicted to have a significant influence on the microstructural evolution.[9,10] The object of this section is to examine only the effects of helium in HIBALL on the dimensional stability of the HT-9 structure.

VIII.4.2 Helium Migration Mechanisms

The migration mechanisms of helium in metals are not well understood. Speculations for these mechanisms include substitutional, interstitial, mutual (interstitial + substitutional) diffusion, momentum transfer, diffusion by di-vacancies and various combinations of the mechanisms. It is not the intent of the present section to discuss the details and supportng evidence of all of these mechanisms. However, selected theoretical and experimental evidence for helium migration by a trapping-detrapping mechanism are briefly discussed.

An interstitial migration mechanism was inferred from computer calculations of minimum energy lattice configurations for a variety of atomic jumps by helium atoms, vacancies, and self-interstitials in face-centered cubic metals.[11] There is strong evidence that helium has a low value for the activation energy for interstitial diffusion and a high interstitial formation energy.[12]. Smidt and Pieper[13] found for stainless steel assuming 25 ppm He, a migration energy of 2.3 eV for the helium atom to reach a bubble. The value is close to the self-diffusion energy of nickel, 2.8 to 2.9 eV. This is consistent with the motion of helium as a substitutional atom to form bubbles.

The model considered in the present study is substantiated by experiments and explains helium migration[12-14] reasonably well. Helium forms in an interstitial position and moves rapidly as an interstitial until it encounters a vacancy, void, or other helium trap, or is lost to the surface. The gas

atom moves to a vacancy and its jump distance is best represented by the distance between available vacancies. The time spent in a vacancy or other trap is large compared with the time the gas atoms spend in an interstitial position. The trap sites fill rapidly because they offer a large sink to diffusing gas atoms. Following this model, Reed[12] gave the following diffusion coefficient

$$D^{He} = \nu_o \frac{\lambda^2}{6} C_v^{-2/3} \exp\{-E^D_{He}/kT\} \qquad \text{(VIII.4-1)}$$

where ν_o is the frequency factor for the detrapping of helium, λ is the jump distance, and E^D_{He} is approximately the detrapping energy of helium in ferritic steel.

VIII.4.3 A Simplified Theory for Helium Swelling

VIII.4.3.1 Assumptions and Equations

Ideally, one would like to formulate a theory in which all possible atomistic interactions are accounted for. However, there are two major difficulties with such a notion. The detailed description of the atomistic processes can be computationally burdensome,[15,16] with a very limited chance of correlating to experiments. On the other hand, basic material parameters such as binding and migration energies of defect complexes are not very well determined. In view of these difficulties, theorists have attempted to envoke convenient approximations. The validity of such approximations can only be tested by detailed and careful correlations with experiments. In this section we develop a simplified conceptual rate theory in which many complicating features have been neglected. Only those details that are believed to play dominant roles are retained. A qualitative description of the present model is given below.

Helium is assumed to migrate by an interstitial mechanism in between vacancy traps. There is no distinction in the theory between interstitial and substitutional helium. Once two helium atoms collide, they form a di-helium gas atom cluster for which vacancies are readily available. Because of the possibilities of thermal dissociation and radiation re-solution, this cluster is unstable. Once a tri-helium gas atom cluster is formed, it can attract few more vacancies and form the critical nucleus size for small gas-filled cavities. Nucleation is therefore dictated by the behavior of gas atoms rather than by vacancies. It has been recently discussed by Meyer et al.[17] that experimental evidence supports this assumption. The nucleation rate of cavities is the rate at which they cross this boundary in size space. The density of cavities will therefore increase as the density of single and di-helium species increase. After a certain irradiation time, it becomes more probable for single helium to collide with larger size cavities than with the small nuclei. Thus a gradual shift from the nucleation stage to the growth stage is achieved. The large size cavities are assumed to start growing from the nucleus site at only one average speed. The size distribution is therefore approximated by a delta function and by keeping track of vacancy, interstitial and helium atom flows in and out of the average cavity, we can determine its size and nature (void or bubble) at any time. Since interstitial loops nucleate rapidly during irradiation[15,16], their number density is assumed to be constant and they are only at a state of growth.

Such a simplified description is obviously not complete but it will provide an order-of-magnitude comparison with the experiment. The roles of vacancy loops, divacancies, precipitates, dislocation dynamics, cavity migration and coal essence, and matrix chemical changes in complex alloys are all neglected. Under these restrictive assumptions, the following rate

equations describe swelling under conditions of simultaneous helium gas and displacement damage production.

$$\frac{dC_{He}}{dt} = P - 2K_{11}C_{He}^2 - k_{12}C_{He}C_{2He} - \bar{K}C_{He}N + 2(2C_{2He})b + mNb - Z_{He}\rho_d D_{He}C_{He} - 6D_{He}\frac{\sqrt{Z_{He}\rho_d}}{d}C_{He} + 2\gamma_h(2)C_{2He} \quad \text{(VIII.4-2)}$$

$$\frac{dC_{2He}}{dt} = K_{11}C_{He}^2 - K_{12}C_{He}C_{2He} - 2C_{2He}b + 3C_{3He}b - \gamma_h(2)C_{2He} \quad \text{(VIII.4-3)}$$

$$\frac{dC_{3He}}{dt} = K_{12}C_{He}C_{2He} - K_{13}C_{He}C_{3He} - 3C_{3He} + 4C_{4He}b \quad \text{(VIII.4-4)}$$

$$\frac{dN}{dt} = K_{12}C_{He}C_{2He} - 3C_{3He}b \quad \text{(VIII.4-5)}$$

$$\frac{dC_v}{dt} = P_d - Z_v\rho_d D_v C_v - K_{vi}C_v C_i \quad \text{(VIII.4-6)}$$

$$\frac{dC_i}{dt} = P_d - Z_i\rho_d D_i C_i - K_{vi}C_v C_i \quad \text{(VIII.4-7)}$$

$$\frac{dm}{dt} = 4\pi R_c D_{He}C_{He} - bm \quad \text{(VIII.4-8)}$$

$$\frac{dR_c}{dt} = \frac{1}{R_c}\{D_v C_v - D_i C_i - D_v C_v^e\left[\exp\frac{\Omega}{kT}\left(\frac{2\gamma}{R_c} - p\right) - 1\right]\} \quad \text{(VIII.4-9)}$$

$$\frac{dR_{i\ell}}{dt} = \frac{1}{b}\{Z_i D_i C_i - Z_v D_v C_v + D_v C_v^e \exp\frac{-(\gamma_{sf} + F_{e\ell})b_v^2}{kT}\} \quad \text{(VIII.4-10)}$$

where the concentrations are expressed in atoms per atom (apa) and the radii are in meters. Some of the terms in the above equations are defined in Table VIII.4-1 and the numerical values used in the present calculations are included in Table VIII.4-2 (ref. 20). The first three equations describe the concentrations of single gas atoms, diatomic clusters and triatomic clusters. The fourth equation describes the total cavity number density.

The vacancy and interstitial concentrations are represented by two coupled rate equations. The last three equations describe the gas atom concentration in a cavity, the average radius of the cavity, and the average interstitial loop radius.[18]

The quantities K_{mn} are defined as follows:

$$K_{mn} = \frac{z_{mn}\Omega D_{He}}{a_o^2} \qquad \text{(VIII.4-11)}$$

where z_{mn} is the combinatorial number, Ω is the atomic volume, a_o is the lattice parameters, and D_{He} is the helium diffusion coefficient given by Eq. VIII.4-1.

The thermal dissociation parameter for di-gas atom clusters[19] is

$$\gamma_h(2) = \frac{D_{He}}{a_o^2} \exp\left(-\frac{E^B_{2He}}{kT}\right) \qquad \text{(VIII.4-12)}$$

where E^B_{2He} is the di-helium binding energy.

The elastic energy of a dislocation loop of radius $R_{i\ell}$ is given by[31]

$$F_{e\ell} = \frac{\mu b_v^2}{(1-\nu)4\pi(R_{i\ell}+b_v)} \ln\left(\frac{R_{i\ell}+b_v}{b_v}\right) \qquad \text{(VIII.4-13)}$$

where π is the shear modulus, ν is the Poisson's ratio, and b_v is Burger's

vector. Details of the derivation of the previous set of equations are given in reference 20.

Table VIII.4-1 Terms and Processes in the Rate Equations

Term/Process	Description
P	Production of helium gas atoms.
$2K_{11}C_{He}^2$	Rate at which helium gas atoms disappear by formation of diatomic clusters (two gas atoms are consumed for each diatomic cluster).
$K_{12}C_{He}C_{2He}$	Rate of formation of triatomic clusters from di-gas atoms and single gas atoms.
$K_{13}C_{He}C_{3He}$	Rate of formation of four-atom clusters from tri-gas atoms and single gas atoms.
$K_{14}C_{He}C_{4He}$	Rate of formation of five-atom clusters from four-gas atoms and single gas atoms.
$2(2C_{2He})b$	Rate at which single atoms are returned to the matrix by resolution of diatomic clusters.
$3C_{3He}b, 4C_{4He}b$	Resolution rates.
$Z_{He}\rho_d D_{He} C_{He}$	Rate of diffusion-controlled absorption of helium gas atoms by dislocations.
$6D_{He}\sqrt{\frac{Z_{He}\rho_d}{d}}\,C_{He}$	Removal rate of helium gas atoms by grain boundaries.
$\gamma_h(2)C_{2He}$	Thermal dissociation rate of diatomic clusters into single gas atoms.
P_d	Production of rate defects.
$Z_{v,i}\rho_d D_{v,i} C_{v,i}$	Rate of diffusion-controlled absorption of vacancies/interstitials by dislocations.
$K_{vi}C_vC_i$	Rate of homogeneous point defect recombination.
$C_v^e \exp\frac{-(\gamma_{sf} + F_{e\ell})b^2}{kT}$	Equilibrium vacancy concentration at the edge of an interstitial dislocaiton loop of radius $R_{i\ell}$ with a stacking fault energy, γ_{sf}.

Table VIII.4-2 Material Parameters used in the Calculations[20]

Parameter	Definition	Numerical Value
a_o	lattice parameter	3.63 Å
k	Boltzmann's constant	8.617×10^{-5} eV/K
b	Burger's vector	2.5668×10^{-8} cm
c_{vi}	recombination combinatorial number	48
c_{11}	combinatorial number for He-He	84
c_{12}	combinatorial number for He-$2He_2$	20
c_{13}	combinatorial number for He-He_3	12
d	grain diameter	3.0×10^{-3} cm
ρ_o	initial value of dislocation density	10^8 cm/cm^3
E^B_{2He}	binding energy of di-helium	0.79 eV
E^D_H	detrapping energy of helium	3.16 eV
E^F_i	formation energy of an interstitial	4.08 eV
E^M_i	migration energy of single-interstitial	0.20 eV
E^F_v	formation energy of a vacancy	1.60 eV
E^M_v	migration energy of single vacancy	1.40 eV
γ	surface energy	6.24×10^{14} eV/c,^{2}
Ω	atomic volume	1.1958×10^{-23} cm^3
ν	Poisson's ratio	0.291
$R_c(0)$	initial value of the cavity radius	20 Å
$R^c_{i\ell}$	initial value of the interstitial loop radius	5 Å
γ_{sf}	stacking fault energy	9.2×10^{12} eV/cm^2
π	shear modulus	1.7665×10^{23} eV/cm^3
B	Van der Waal's constant	1.75×10^{-23}
ν_H	helium vibrational frequency	5.0×10^{14}/sec
ν_i	interstitial vibrational frequency	5.0×10^{12}/sec
ν_v	vacancy vibrational frequency	5.0×10^{13}/sec
Z_{He}	bias factor of helium gas atoms	1.00
Z_i	bias factor of interstitials	1.01
Z_v	bias factor of vacancies	1.00

VIII.4.4 The EXPRESS Computer Code

In order to solve the previous set of rate equations (VIII.4-2 to VIII.2-10) for Inertial Confinement Fusion conditions, a special computational technique was developed. The EXPRESS computer code (Integration/EXtrapolation Method for Pulsed Rate Equations of Stiff Systems) solves time dependent rate equations describing the evolution of the space-averaged damage state of an ICFR first wall. As such, it represents an extension of the HEGBUF code[20], developed by M. Takata to describe the damage-state evolution in steady-state and slowly pulsed fusion machines.

The equations describing this system possess the property of stiffness; that is, the time scales characterizing the various elements of the system span a large range of values. The integration of such a system requires the use of specialized numerical techniques. Many of these techniques have been incorporated into a set of subroutines called the GEAR package.[21] When the pulse frequency is high, as in the case of ICFR's, even the methods of GEAR become prohibitively expensive.

To alleviate this difficulty, we have developed an integration/extrapolation method which allows us to obtain the solution of the equations without integrating each pulse. A detailed description of this method is contained in a UCLA report.[22] A flow diagram is shown in Fig. VIII.4-1.

VIII.4.5 Results

In all of our calculations, the displacement and helium production rates were idealized by square waves of definite pulse lengths (T_{on}). The peak displacement damage and helium production rates are determined by conserving the total number of displacements and helium within one pulse. The magnitude of the on-time is determined as the "full width at half maximum (FWHM)" from the nuclear analysis of the wall response. It was also found that under our

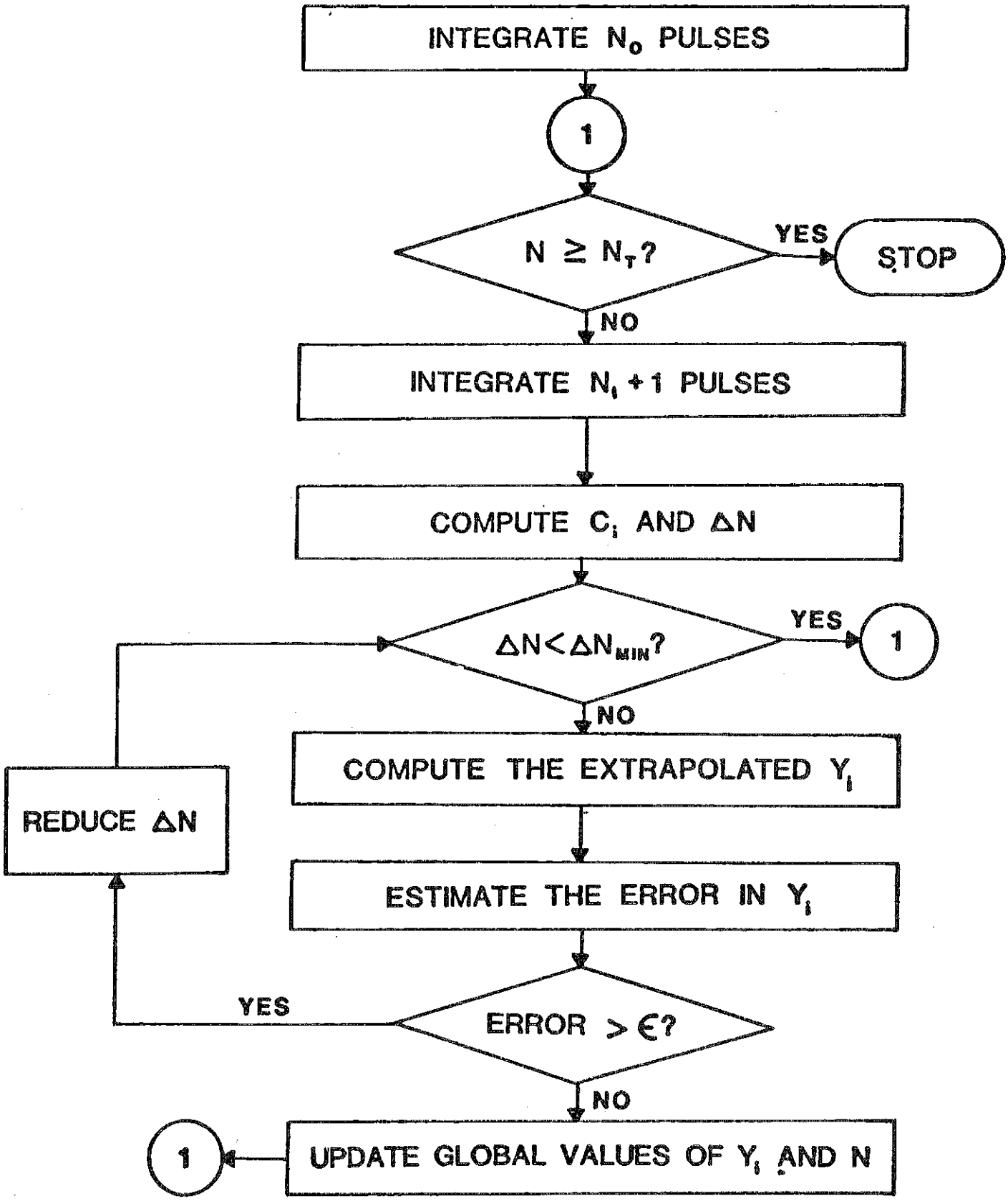

Fig. VIII.4-1 Flow diagram of integration/extrapolation method of solution developed.

specific conditions, the helium mean-lifetime is much longer than the on-time. No helium diffusion is therefore expected during the short on-time, and the helium on-time can be approximated by the displacement damage on-time.

The following conditions apply:

$$\tau_i < T_{on} < \tau_v < \tau_{He} \qquad \text{(VIII.4-14)}$$

and

$$T_{on}(He) \simeq T_{on}(dpa) \qquad \text{(VIII.4-15)}$$

We will here analyze the following two cases.

VIII.4.5.1 Unprotected Ferritic Steel First Wall

Based upon the previous assumptions, and the results of the nuclear analysis, we use as input to the computer code EXPRESS the following:

T_{on} = 5 ns

T_{cycle} = 0.2 s

instantaneous dpa/s = 32.12 dpa/s

instantaneous He/s = 2.89×10^{-4} at/at/s

dpa/FPY = 25.36 dpa/FPY

He/FPY = 227.6 appm/FPY

He/dpa ratio $\hat{=}$ 9 appm/dpa

Figure VIII.4-2 shows the concentration of single helium atoms in the ferritic steel matrix, as a function of irradiation time. The calculations for this case (500°C) were performed up to ~ 80,000 pulses. The helium is mainly trapped in vacancies and has a very little chance for diffusion. The cavity concentration is shown in Fig. VIII.4-3 where the solid lines are for equivalent continuous-irradiation, and the dotted are for the actual pulsed case. By ~ 80,000 pulses, the cavity density in the pulsed case is already

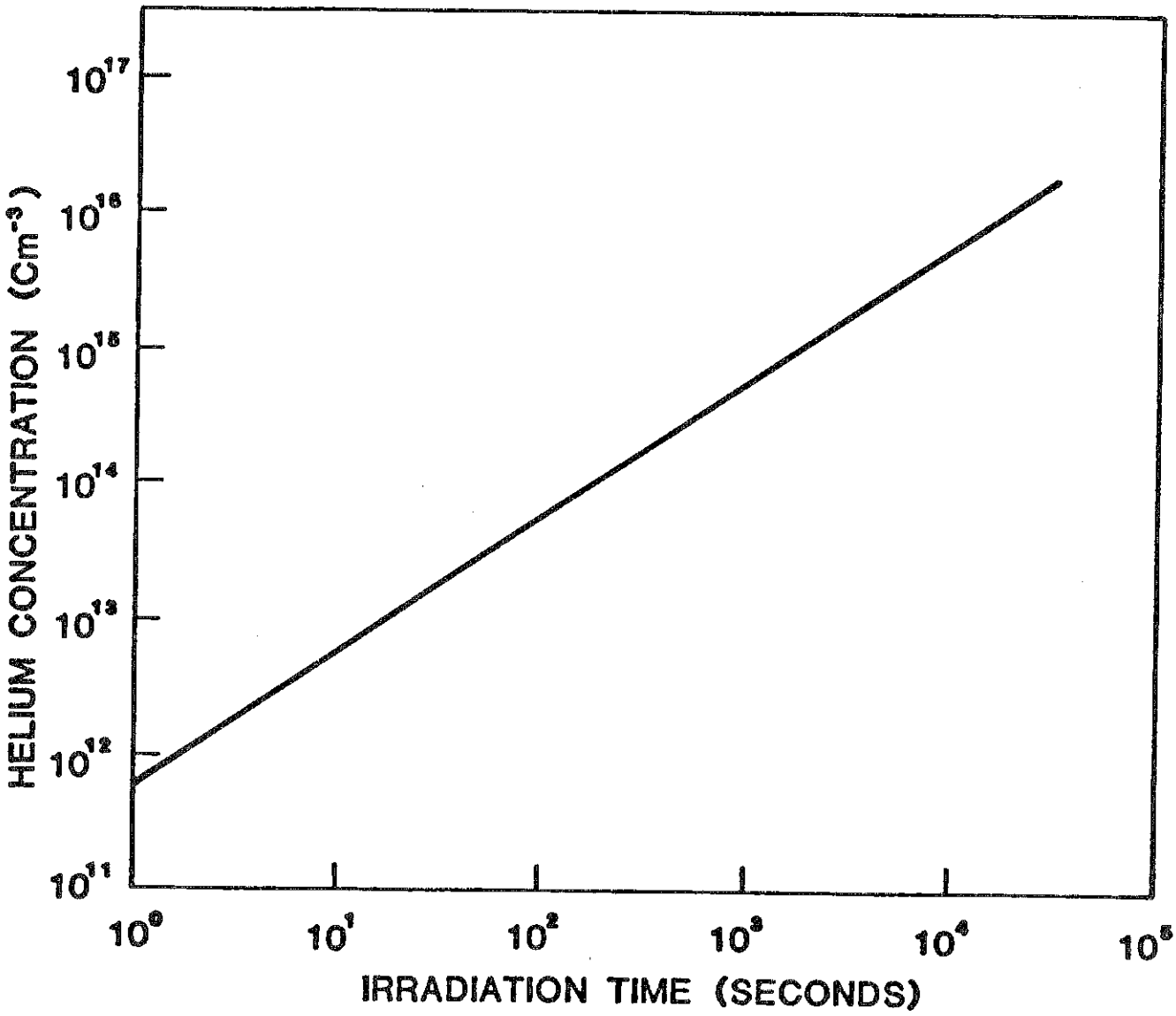

Fig. VIII.4-2 Concentration of single He atoms in ferritic steel matrix, as a function of irradiation time.

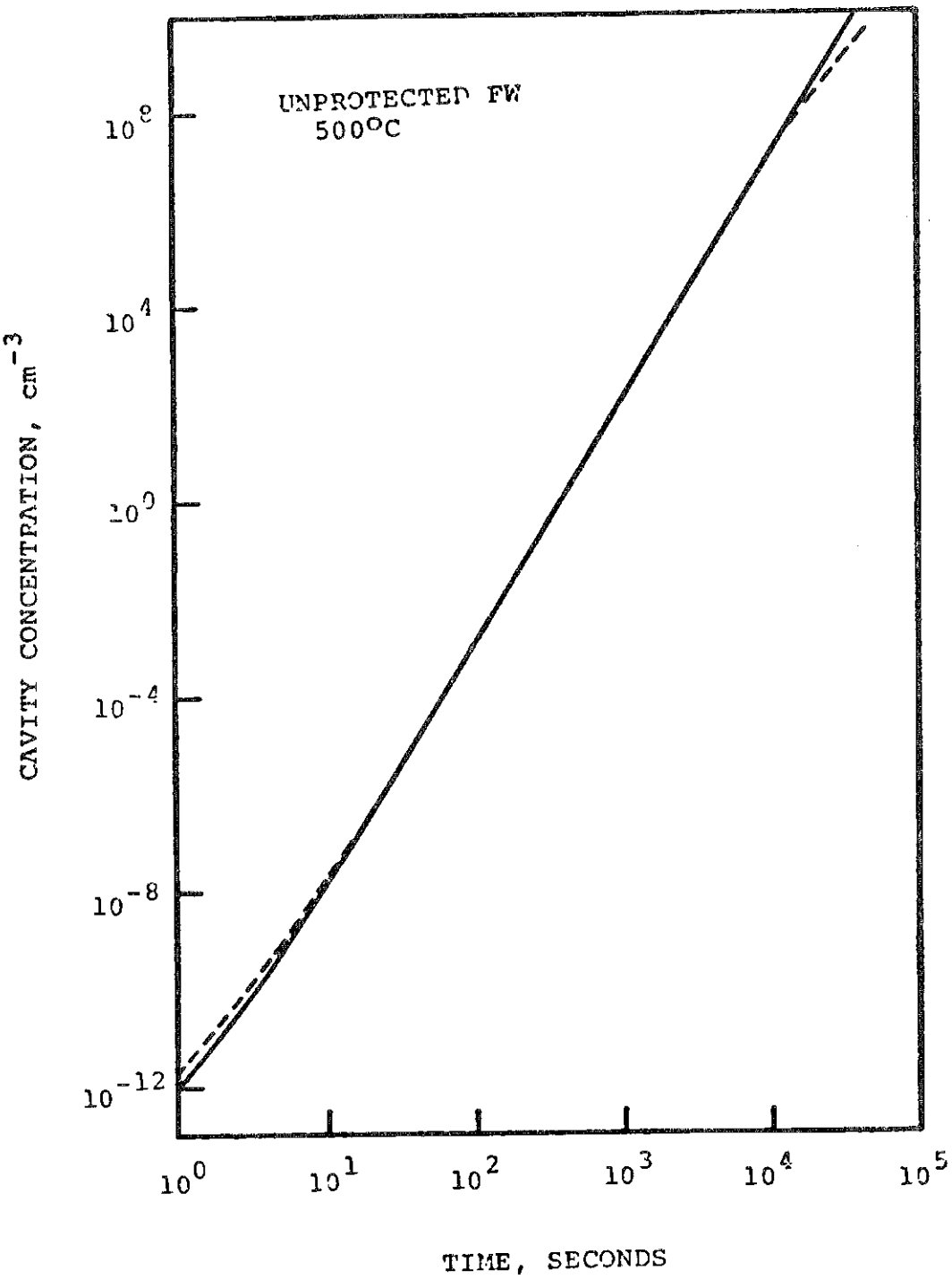

Fig. VIII.4-3 Cavity concentration; solid lines are for equivalent continuous irradiation, dotted are for pulsed case.

smaller than the corresponding continuous irradiation. The concentrations of both vacancies and interstitials for the first 300 pulses are shown on Fig. VIII.4-4 and up to 80,000 pulses on Fig. VIII.4-5. The solid lines are for the continuous irradiation equivalent, while the dotted lines represent the envelope of the fluctuations in these components. The increase in the average radius of the cavity is shown in Fig. VIII.4-6 where it is evident that pulsing of irradiation results in a smaller cavity radius. This is mainly due to the enhanced vacancy-interstitial recombination brought about by the fluctuations shown on the previous figure. It is concluded therefore that under pulsed irradiation, a lower amount of swelling is observed than that observed under the equivalent continuous irradiation. This conclusion is unique to the HIBALL conditions and caution should be used in extrapolating to other conditions.

A comparison of the cost of the new integration/extrapolation method, and the straight numerical integration of the previous equations is shown in Fig. VIII.4-7. A gain of over a factor of 20 in the cost of integration is achieved using our new method. This is extremely important in studies of pulsed effects that include ratcheting (build-up) phenomena.

VIII.4.5.2 Protected Ferritic Steel First Metallic Wall

A summary of radiation damage parameters in the first metallic wall, and in the reflector, is given in Table VIII.4-3 below.

Figure VIII.4-8 shows the concentrations of the primary components of damage: vacancies, interstitials, and helium atoms, during the first pulse and pulse 615. The vacancy and interstitial concentrations are shown to be higher than the helium concentration during the first pulse where the helium is relatively mobile. As damage accumulates, the concentration of helium increases due to its decreased mobility. It is also shown that the self-

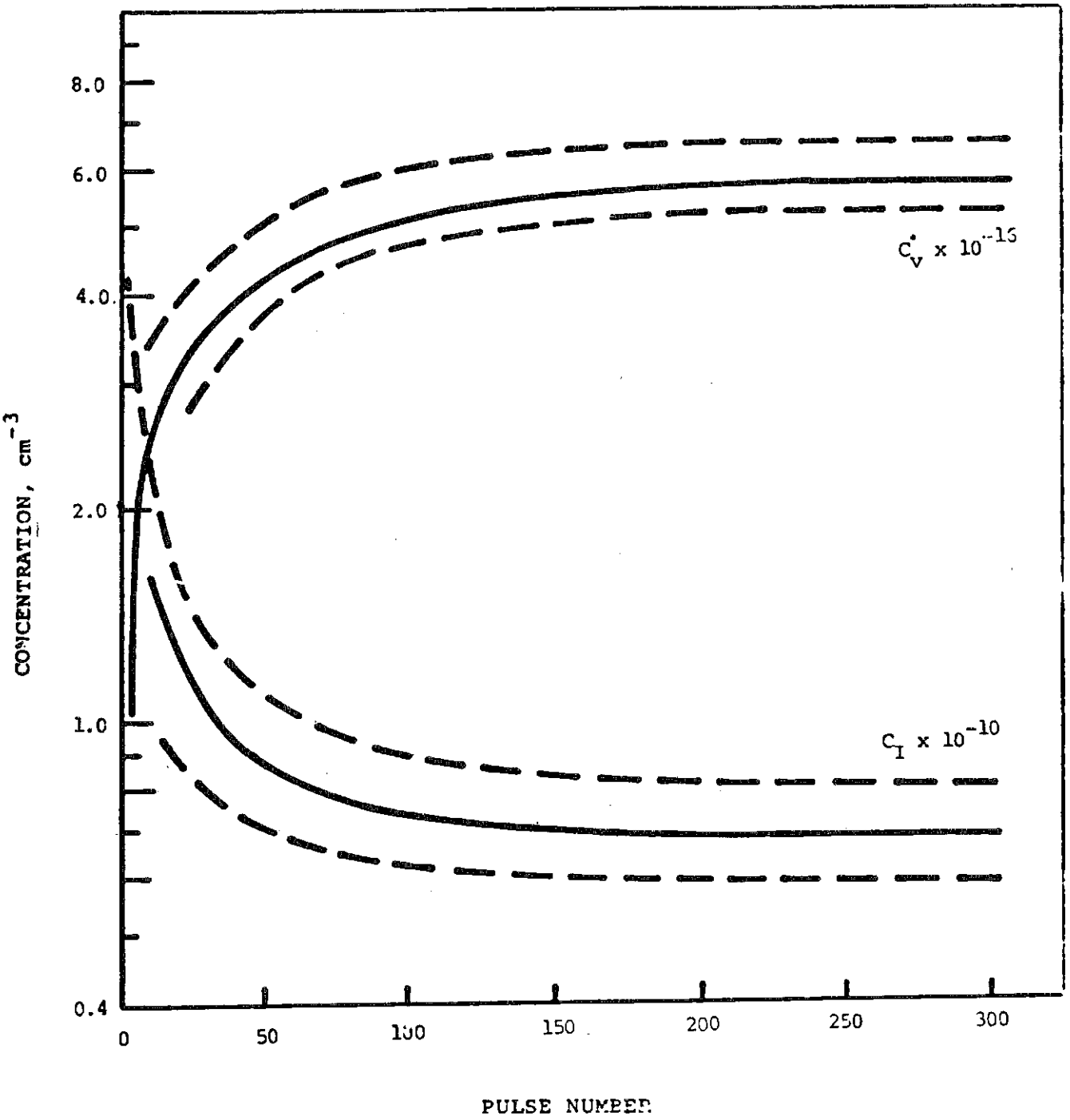

Fig. VIII.4-4 Concentrations of vacancies and interstitials for the first 300 pulses.

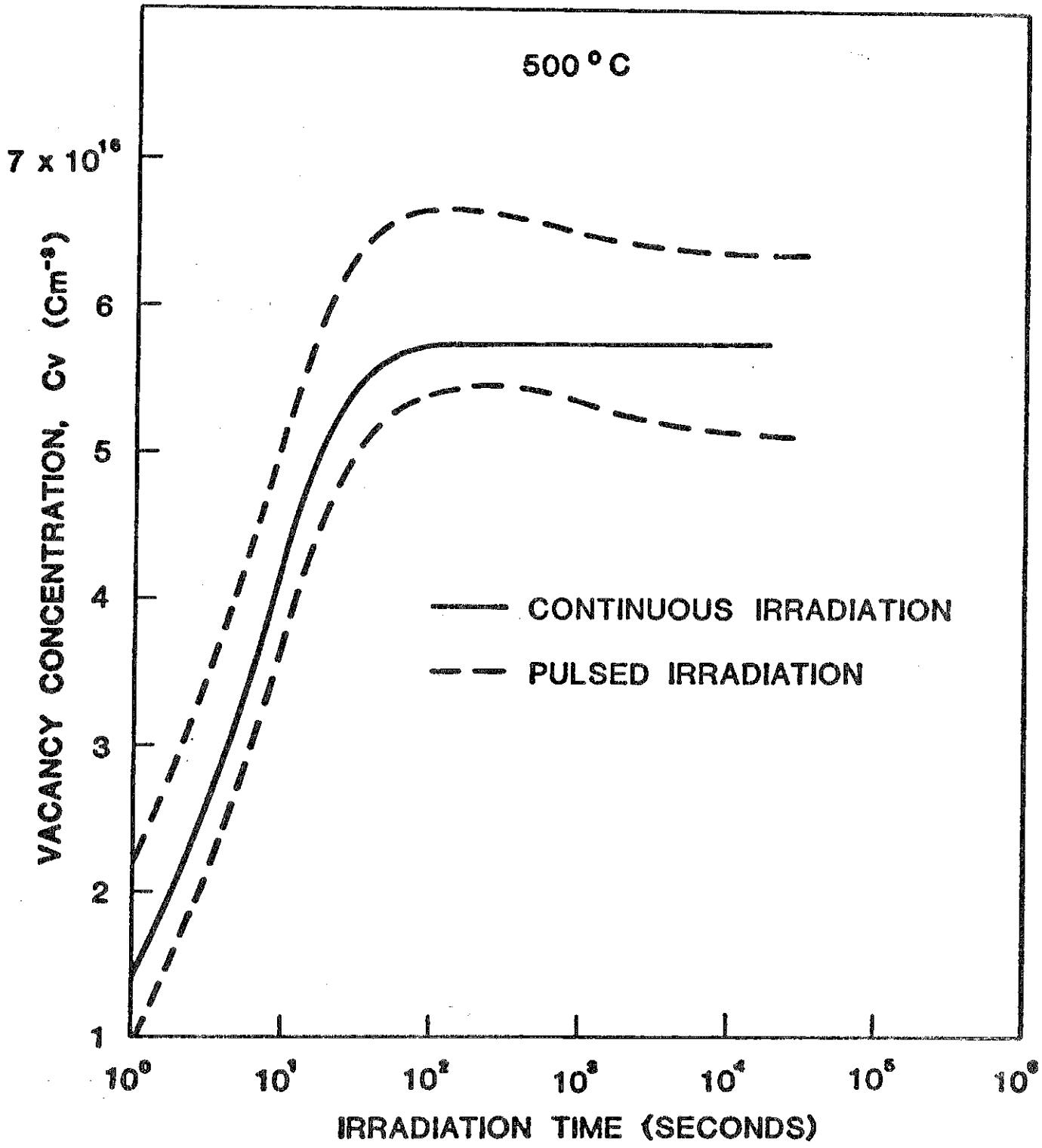

Fig. VIII.4-5 Concentration of vacancies up to 80000 pulses.

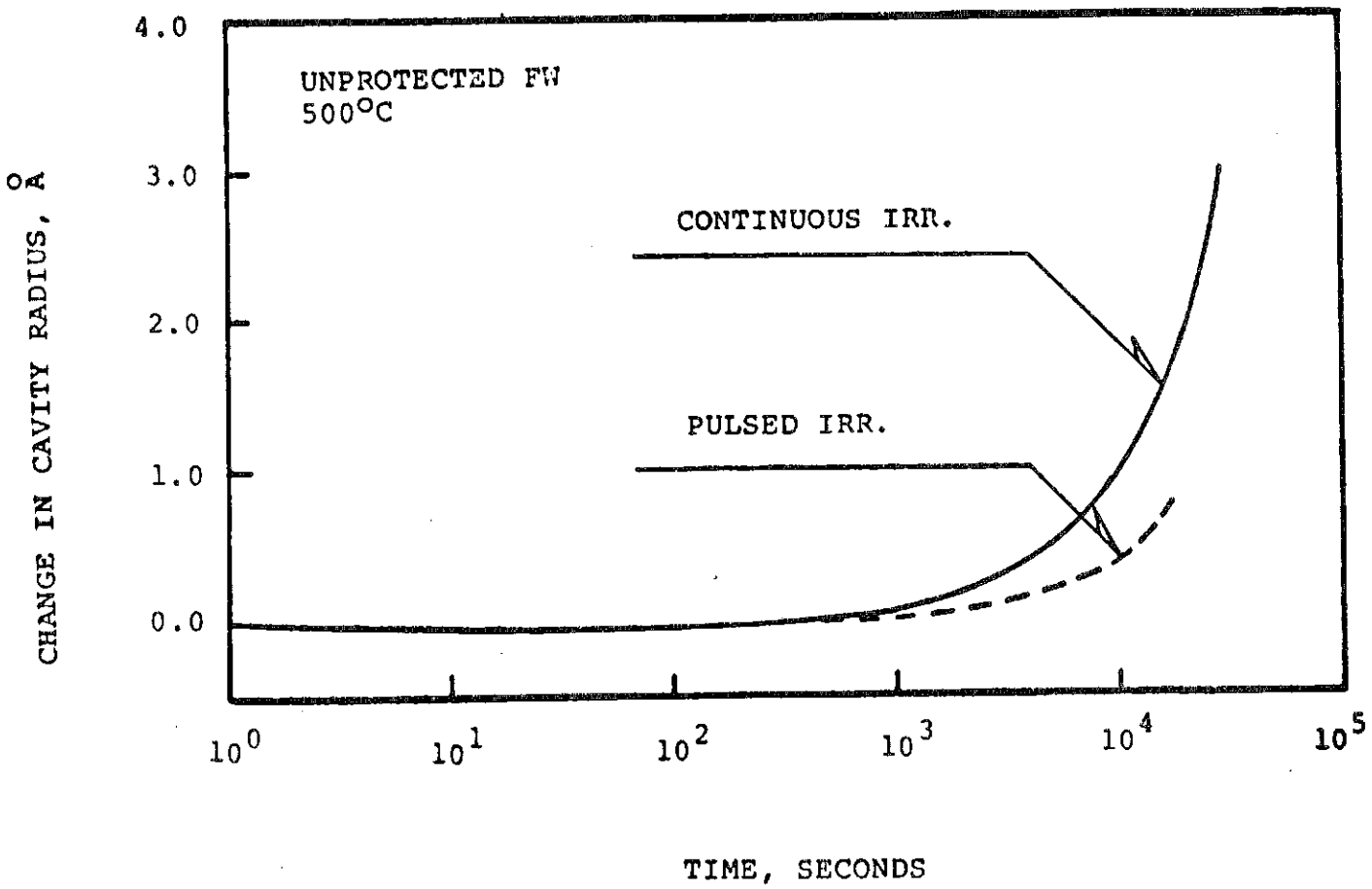

Fig. VIII.4-6 Change in cavity radius vs. time of irradiation.

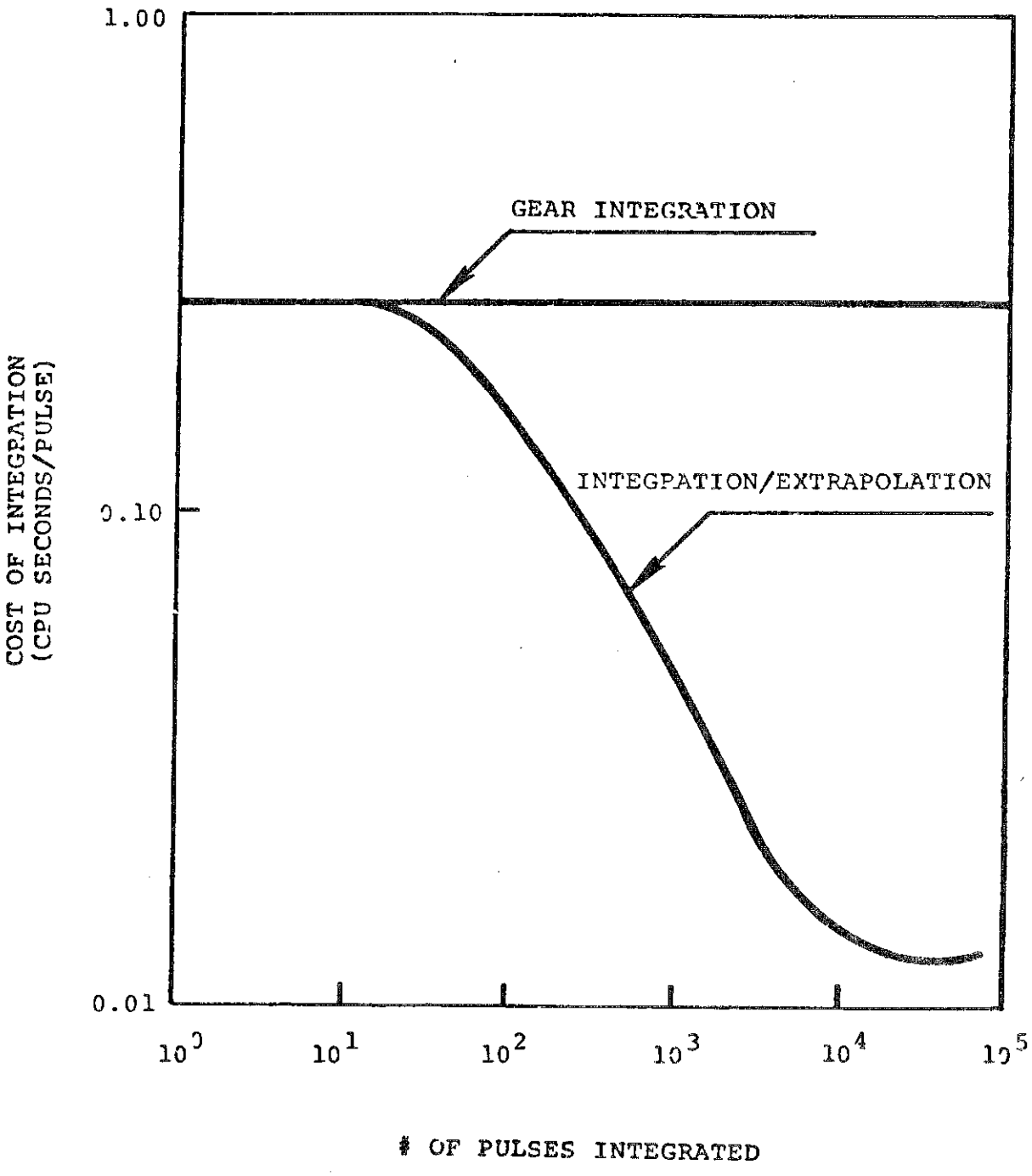

Fig. VIII.4-7 Cost comparison for two computational methods used.

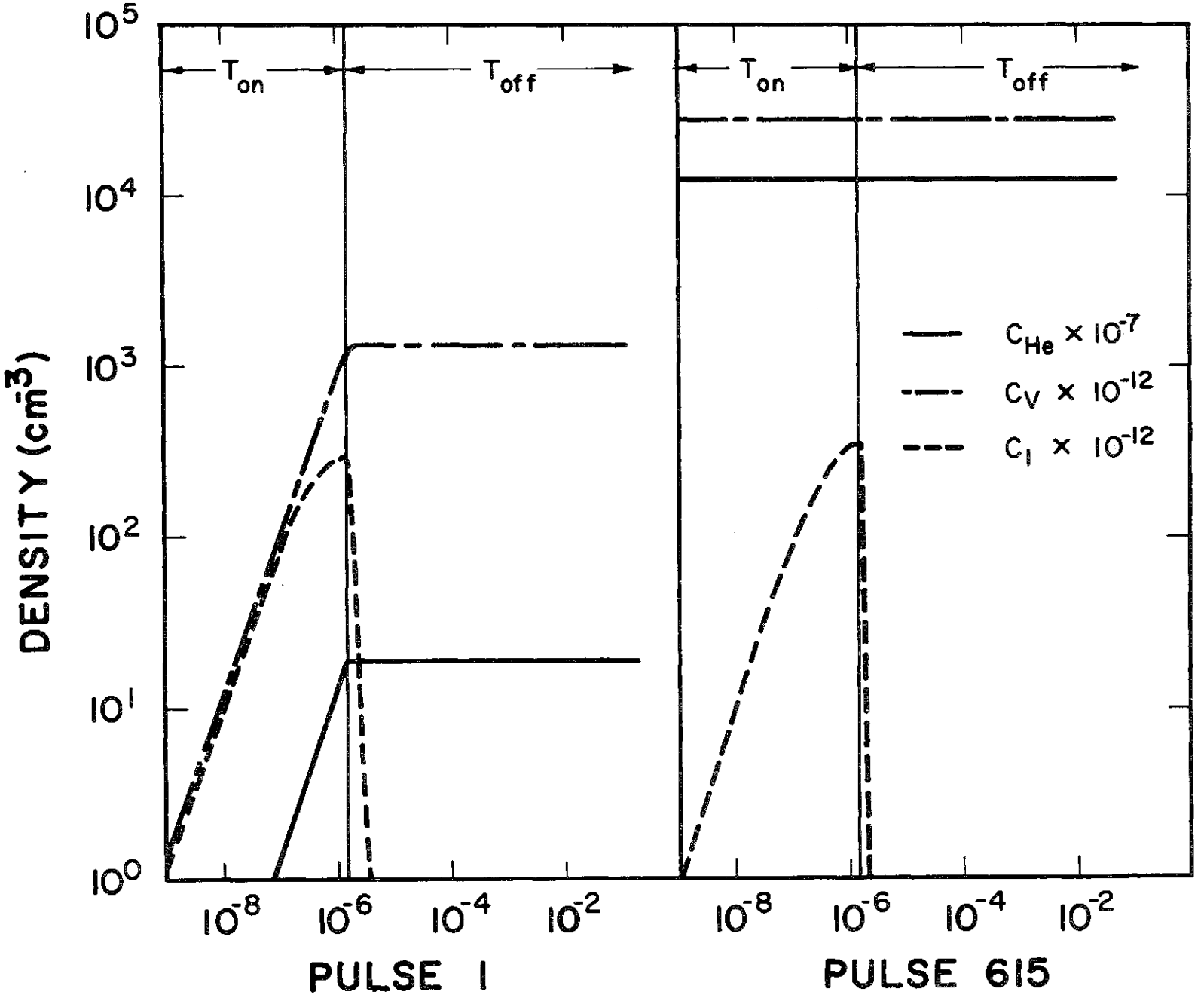

Fig. VIII.4-8 Concentration of vacancies, interstitials, and He atoms, during the first pulse and pulse 615.

Table VIII.4-3 Radiation Damage Parameters for the Protected First Metallic Wall

	First Wall	Half Ref. Thickness	Full Ref. Thickness
T_{on}, πs	1.5	2.0	2.4
T_{cycle}, s	0.2	0.2	0.2
dpa/yr	2.7	0.32	0.028
appm He/yr	0.364	0.0112	5.4×10^{-4}
He/dpa	0.135	0.035	0.019
$dpa/s_{inst.}$	1.14×10^{-2}	1.02×10^{-3}	7.4×10^{-5}
$He/s_{inst.}$	1.54×10^{-9}	3.56×10^{-11}	1.4×10^{-12}

interstitials diffuse significantly during the pulse on-time, while both vacancies and helium remain in the matrix during this short period. The helium diffusion coefficient is shown in Fig. VIII.4-9 as a function of the pulse number.

Equivalent steady state calculations were made for the peak damage position in the first wall. Figure VIII.4-10 shows the results of these calculations where $\frac{\Delta V}{V}$, the cavity average radius, and the concentration are shown as functions of irradiation time. The maximum swelling is shown to be insignificant over the first wall lifetime at 450°C ($< 10^{-3}\%$).

In order to understand this low value of swelling, we developed a simplified model for the partitioning of gas atoms in cavities. The model assumptions are:

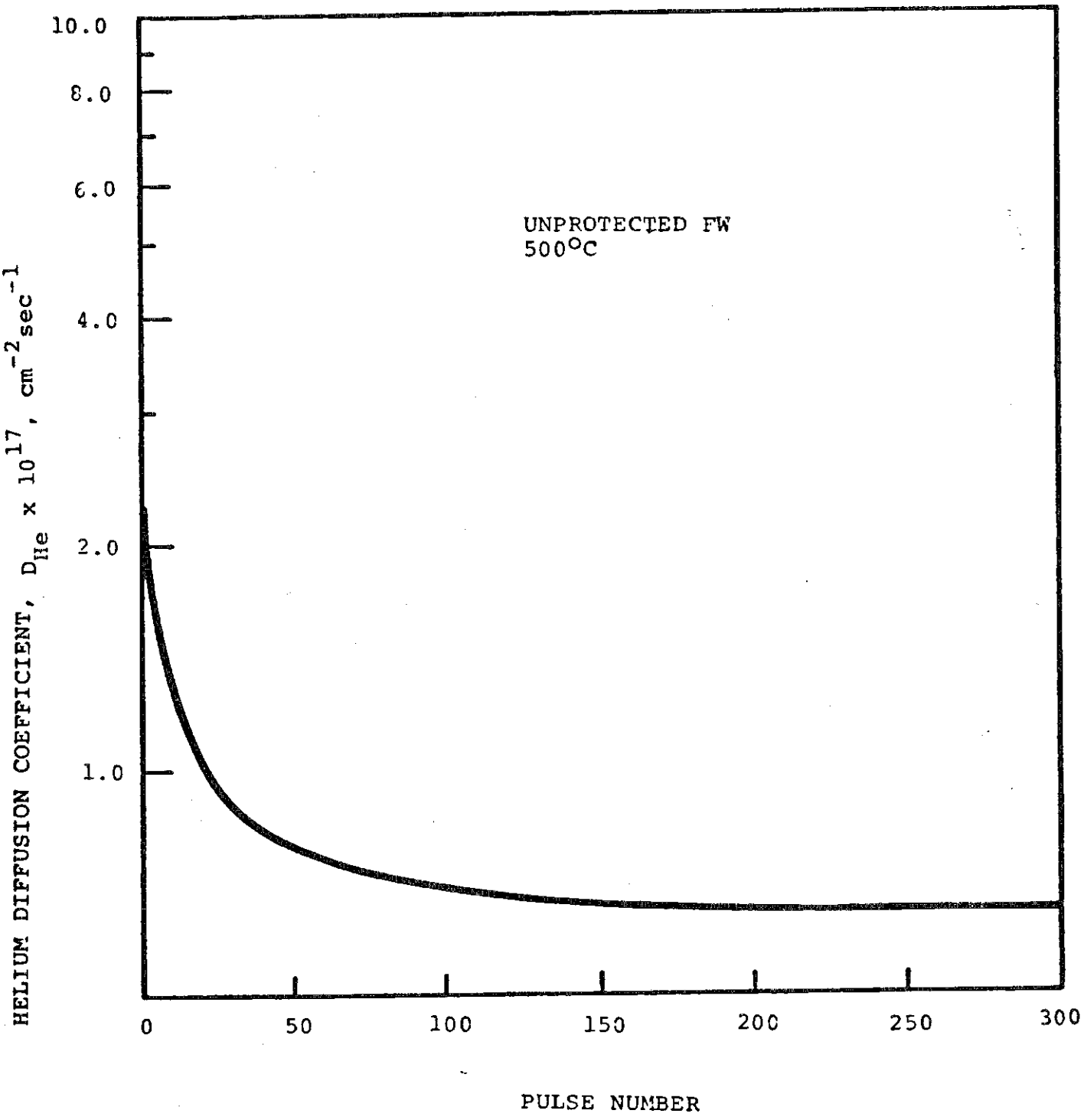

Fig. VIII.4-9 He diffusion coefficient as a function of pulse number.

VIII.4-22

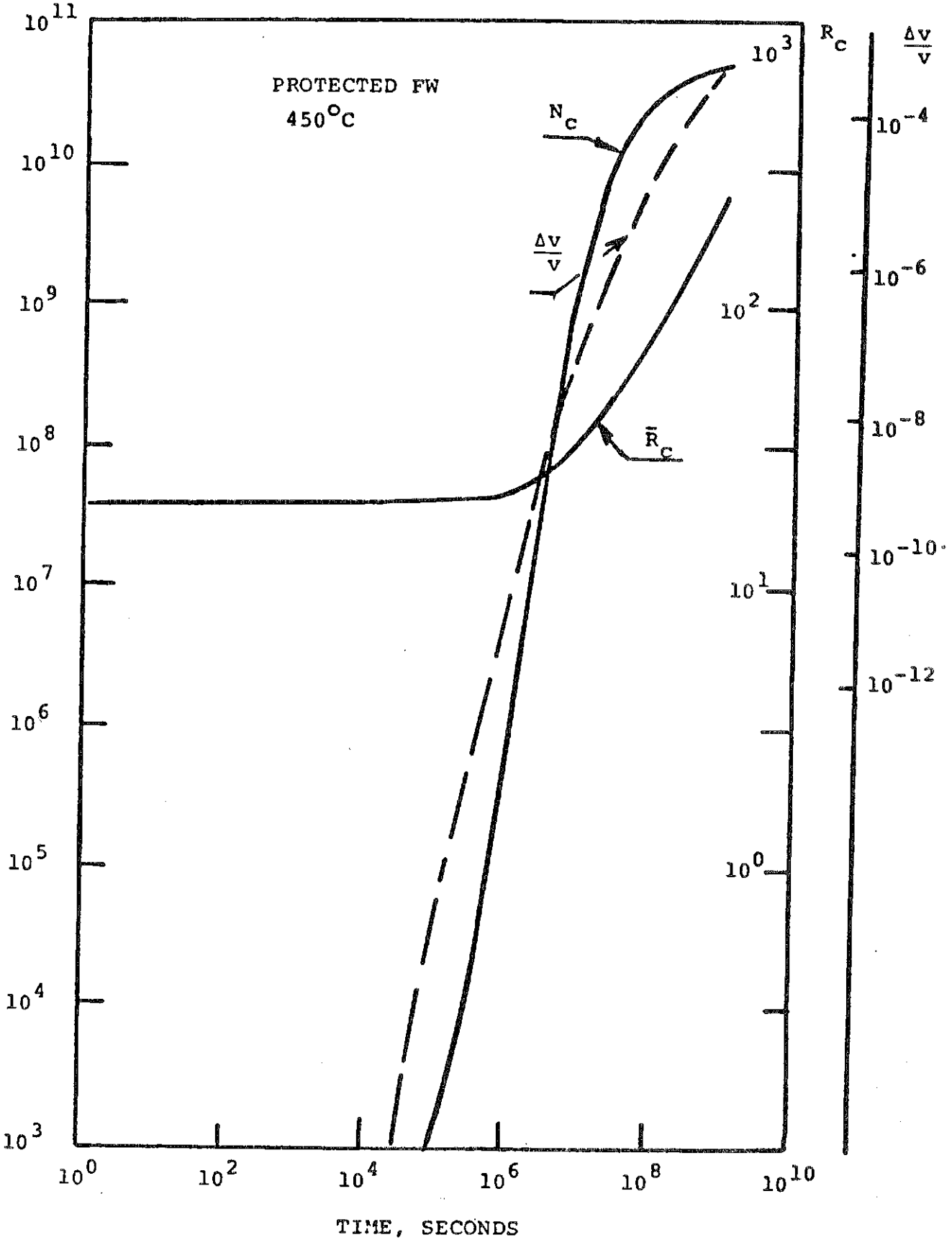

Fig. VIII.4-10 Δv/v, cavity average radius, and concentration as function of irradiation time.

(1) Continuous irradiation.

(2) HFIR cavity density for 316 SS

$$N_C = 6.642 \times 10^{22} \exp(-0.023\ T(K))$$

(3) Cavities are equilibrium bubbles.

(4) Van der Wall's equation of state.

(5) All gas is in cavities.

The calculated swelling, based on this model is shown in Table VIII.4-4. These simplified calculations indicate that the maximum amount of swelling will again be small over the lifetime of the wall. It is concluded therefore the swelling is not a major design problem, and lifetime will be more limited by other considerations (such as embrittlement at low temperature and creep rupture at high temperature).

Table VIII.4-4 Percent Swelling for the Protected First Wall

T, °C	1 yr	10 yrs	30 yrs
300	0	6.4×10^{-4}	1.93×10^{-3}
400	6.42×10^{-5}	6.6×10^{-4}	1.97×10^{-3}
500	6.6×10^{-5}	3.0×10^{-4}	1.58×10^{-3}
600	3.04×10^{-5}	9.7×10^{-4}	5.0×10^{-3}

VIII.4.6 Conclusions

From our study of helium behavior in the HIBALL design, we conclude the following:

(1) Helium migrates interstitially by a trapping/detrapping mechanism.

(2) The He/dpa ratio is the parameter that significantly affects cavity nucleation.

(3) Maximum nucleation will be in the first wall.

(4) A successful new integration/extrapolation technique has been developed for pulsed systems:

CPU time → down by ~ 20

Error → up by ~ 1-4%

(5) The cavity density in pulsed irradiation is higher than continuous irradiation only before significant helium diffusion occurs.

(6) Fluctuations in point defect concentrations due to pulsing lead to a smaller growth rate of cavities.

(7) Overall swelling due to pulsing will be smaller than corresponding continuous irradiation.

(8) Swelling will not be a life-determining factor for the HIBALL design.

References for Section VIII.4

1. D. Kramer, H.R. Brager, C.G. Rhodes, and H.G. Park, J. Nucl. Mat. 26, 121 (1968).

2. E.E. Bloom, Radiation-Induced Voids in Metals, ed. by J.W. Corbett and L.C. Ianniello, CONF-71061, U.S. Atomic Energy Commission, Washington, D.C., 1972, p. 1.

3. G.L. Kulcinski, D.G. Doran, and M. Abdou, Properties of Reactor Structural Alloys After Neutron or Particle Irradiation, ASTM-STP-570, American Society for Testing and Materials, Philadelphia, PA, 1975, p. 329.

4. R.G. Mills, "A Fusion Power Plant," Princeton University, MATT-1050, 1974, p. 292.

5. B. Badger et al., "UWMAK-I," University of Wisconsin Fusion Design Memo UWFDM-68, Vol. I, (1973).

6. International Tokamak Reactor Zero Phase, R.S. Pease, Chairman, International Atomic Energy Agency, Vienna, available from UNIPUB, new York, 1980, p. 384.

7. G.R. Odette and S.C. Langley, Radiation Effects and Tritium Technology for Fusion Reactors, ed. by J.S. Watson and F.W. Wiffen, Vol. I, CONF-750989, National Technical Information Service, Springfield, VA, 1976, p. 395.

8. F.V. Nolfi, Jr., A. Taylor, D.I. Potter, S.C. Agarwal, and B. Okray Hall, Trans. Am. Nucl. Soc. 26, 190 (1970).

9. F.V. Nolfi, Jr., and Che-Yu Li, Nucl. Technol. 38, 405 (1978).

10. K. Farrell, M.B. Lewis and N.H. Packan, Scripta met. 12, 1121 (1977).

11. W.D. Wilson and C.L. Bisson, Phys. Rev. B1, 3510 (1970).

12. R.J. Reed, Rad. Effects 31, 129 (1977).

13. F.A. Smidt, Jr., and A.G. Pieper, Properties of Reactor Structural Alloys After Neutron or Particle Irradiation, ASTM-STP-570, American Society for Testing and materials, Philadelphia, PA, 1975, p. 352.

14. W.D. Wilson and C.L. Bison, Rad. Effects 19, 53 (1973).

15. M.R. Hayns, J. Nucl. Mat. 59, 195 (1976).

16. N.M. Ghoniem and D.D. Cho, Phys. Stat. Solidi 54, 171 (1979).

17. Mayer et al., to be published, J. Nucl. Mat.

18. N.M. Ghoniem and G.L. Kulcinski, Rad. Effects 39, 47 (1978).

19. D.D. Cho and N.M. Ghoniem, "The Initial Stages of Point Defect Clustering in Fusion Reactor First Wall," Univ. of California-Los Angeles, UCLA-ENG-7935, 1979.

20. N.M. Ghoniem and M.L. Takata, "A Theory for the Interaction of Helium and Displacement Damage in Fusion Reactor Structural Materials," submitted to J. Nucl. Mat.

21. A.C. Hindmarch, Lawrence Livermore Laboratory Report, UCID-3001, (1974) rev. 3.

22. R. Schafer and N.M. Ghoniem, "EXPRESS: A Computer Code for the Integration/Extrapolation of Pulsed Rate Equations for Stiff Systems," UCLA report, 1981.

IX Maintenance

IX.1 Radiation Environment

The calculations presented in section VI.3 showed that the dose outside the shield was acceptable during and following operation. However, the calculations presented in section VI.3.5 indicated that very high levels of activity will be associated with the structure in the INPORT region and the first wall and reflector. In addition, neutron streaming will produce activity in the vacuum lines and pumps, the beam ports, and the beam dump. The activity generated in those parts of the system that are struck by heavy ions must also be considered. The consequences of this for maintenance is that dose levels will be so high that remote maintenance will be required for all major tasks such as replacement of INPORT tubes, service of vacuum systems, coolant lines, magnets, etc. The following sections indicate, at least in a schematic fashion, the features of the design that have been incorporated to carry out these tasks and how they might be performed.

IX.2 Cavity Components

IX.2.1 Introduction and Maintenance Philosophy

A mechanical description of the cavity was given in Section VI.1.2. In this section we will outline the procedures and maintenance philosophy for the internal cavity components.

There are essentially only two kinds of cavity components which will require periodic replacement due to radiation damage; they are the radial blanket modules and the upper blanket modules. These blanket modules were designed with maintainability as a prime consideration.

Figure IX.2-1 shows a cross section of the cavity. The upper blanket covers the top of the cavity and is divided into 30 identical modules. Each module has one supply header connected to it at the upper outer periphery. The coolant circulates through the blanket and exits through a tube which connects with the radial blanket. The coolant from the upper blanket then drains through the back tubes of the radial blanket.

During operation when the upper blanket is filled with $Li_{17}Pb_{83}$, the upper blanket modules are supported on the reflector by means of studs. These studs fit in milled slots in the reflector and are locked to it by means of a latching mechanism. When the upper blanket modules are drained, the latching mechanism can be deactivated and then the reflector and shield is free to rotate about the central axis while the blanket modules remain in place. At this time the modules are supported on the outer edge and on a central hub. Figure IX.2-2 is a view of the upper blanket from inside the reactor cavity showing the coolant drain tubes and the vacuum system ducts. In Fig. IX.2-3 are several views of an upper blanket module. Support studs are shown only at one location but in principle there can be more of them along the length of the module. The cross sections show details of the structural frame and the

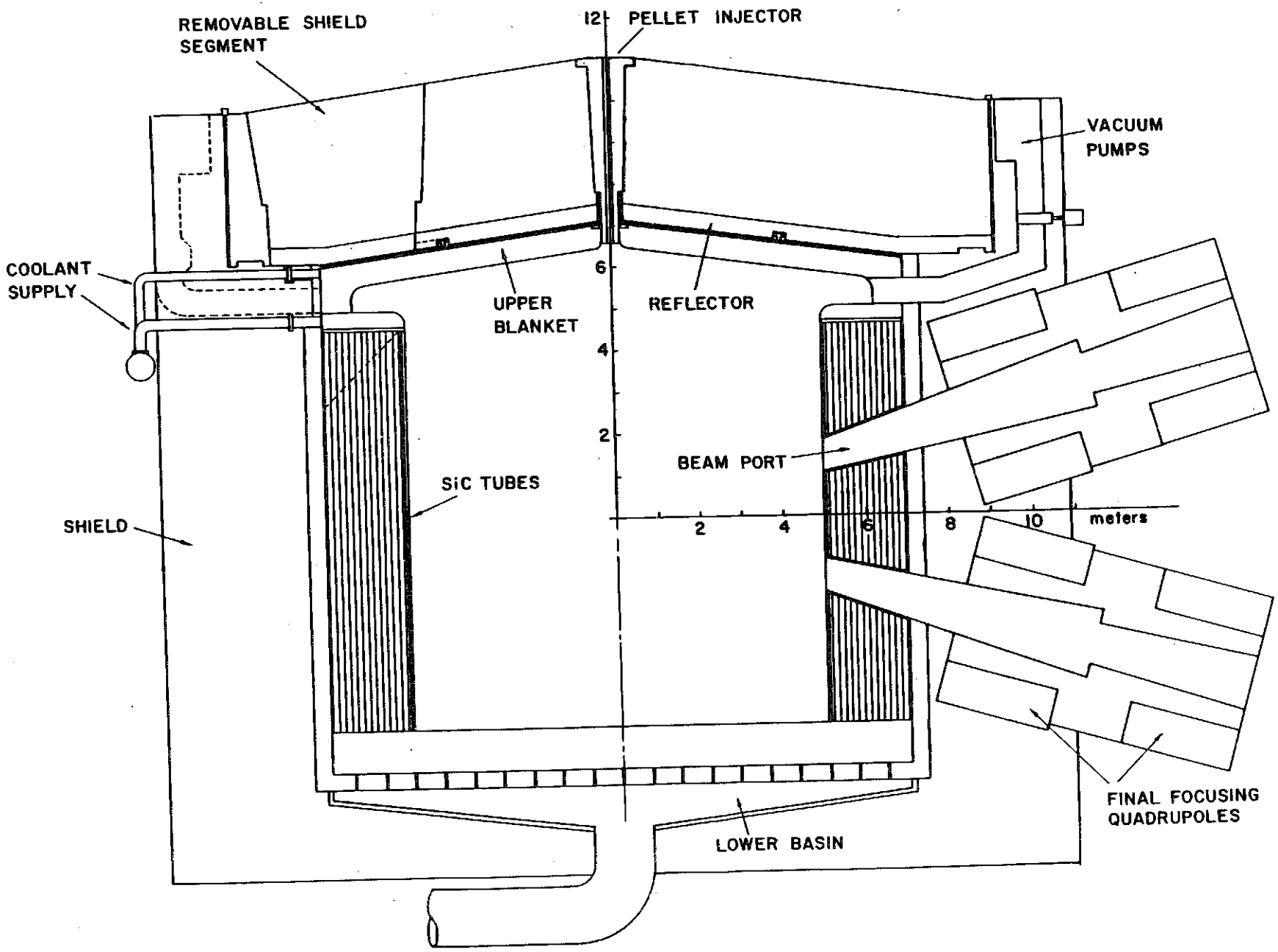

Fig. IX.2-1 Cross section of reactor cavity.

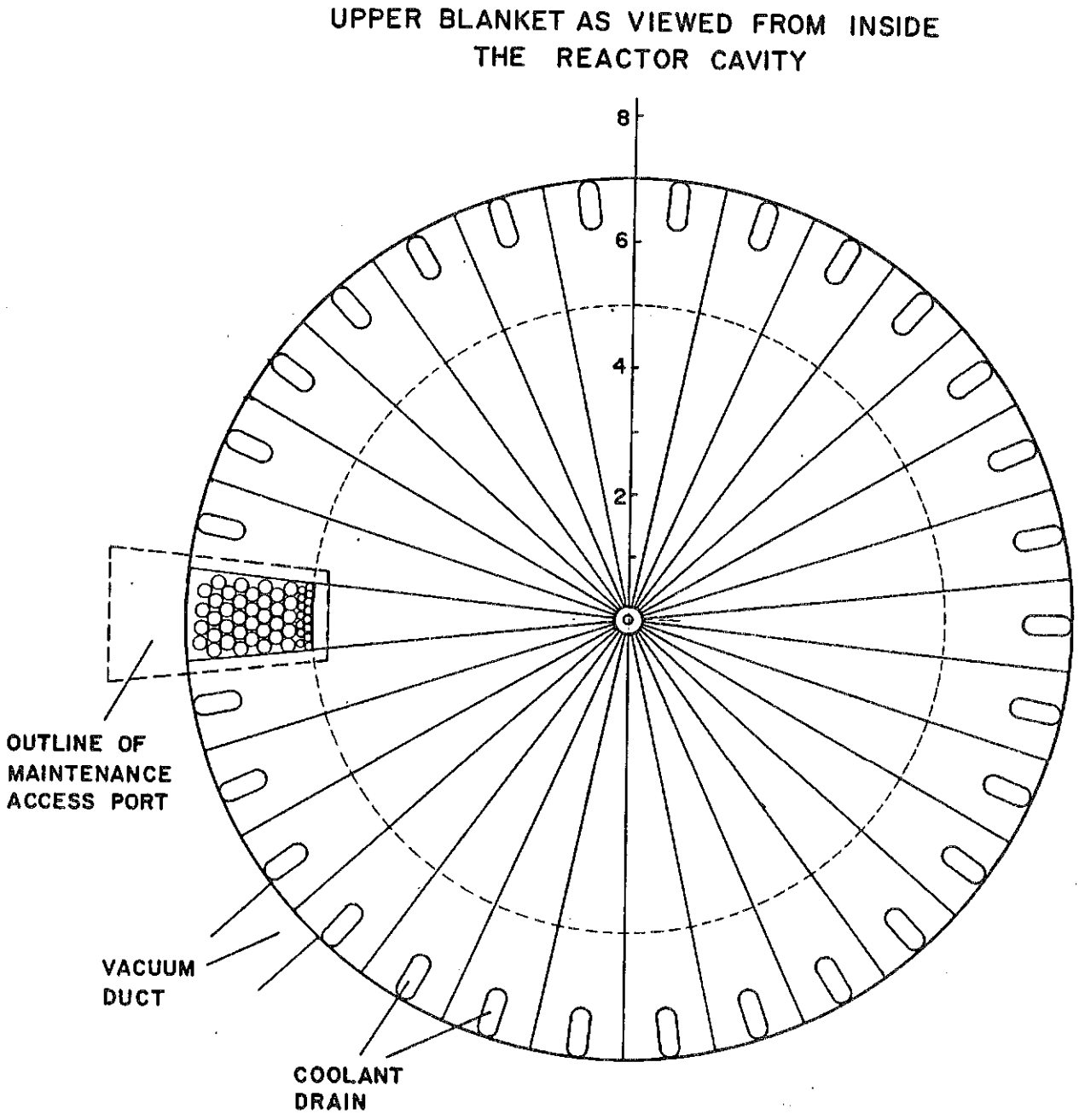

Fig. IX.2-2 Upper blanket as viewed from inside the reactor cavity.

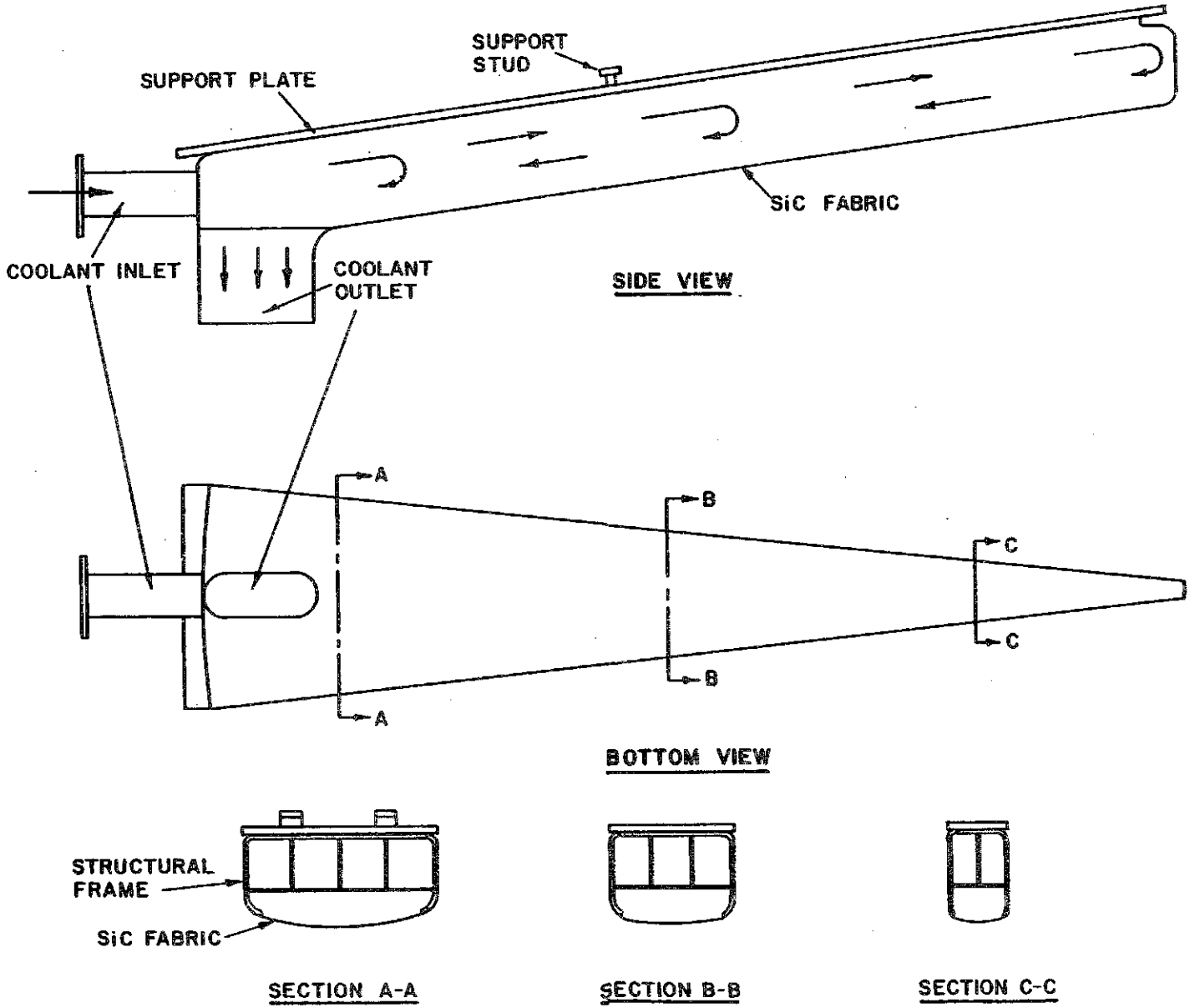

Fig. IX.2-3 Design of an upper blanket module.

SiC fabric which surrounds the frame entirely. Arrows in the side view indicate the direction of coolant flow.

The radial blanket is also divided into 30 equal modules. An outline of a single module and its SiC tubes is superimposed on Fig. IX.2-2 where the dotted line indicates the first surface. Each module consists of a distribution manifold which is a part of the upper tube support plate, the SiC tubes and the lower restraining plate. Ten out of the thirty modules have two beam ports built in. Each module is attached to the 40 cm thick reflector by means of 4 equally distributed struts welded to the HT-9 support plate. The struts have tees machined on the ends which fit into milled slots in the reflector. Pulling up on a module retracts the struts from the slots in the reflector and disengages them.

The maintenance philosophy that has been adopted for the HIBALL cavities depends on five key features. They are:

1. The reactor cavity is built below grade such that the maintenance hall essentially sits on top of it as shown in Fig. IX.2-4.
2. The upper reflector and shield are designed to rotate about the central axis while the upper blanket remains stationary.
3. Upper and radial blanket modules can be removed into the maintenance hall through an access port in the upper shield. A shielded plug is placed in the port during reactor operation.
4. The unprotected central hub of the target injector can be pulled out from the outside for replacement.
5. Remote viewing devices (TV camera, etc.) can be inserted through the central aperture devoted to the target injector. The target injector unit can be removed vertically into the maintenance hall.

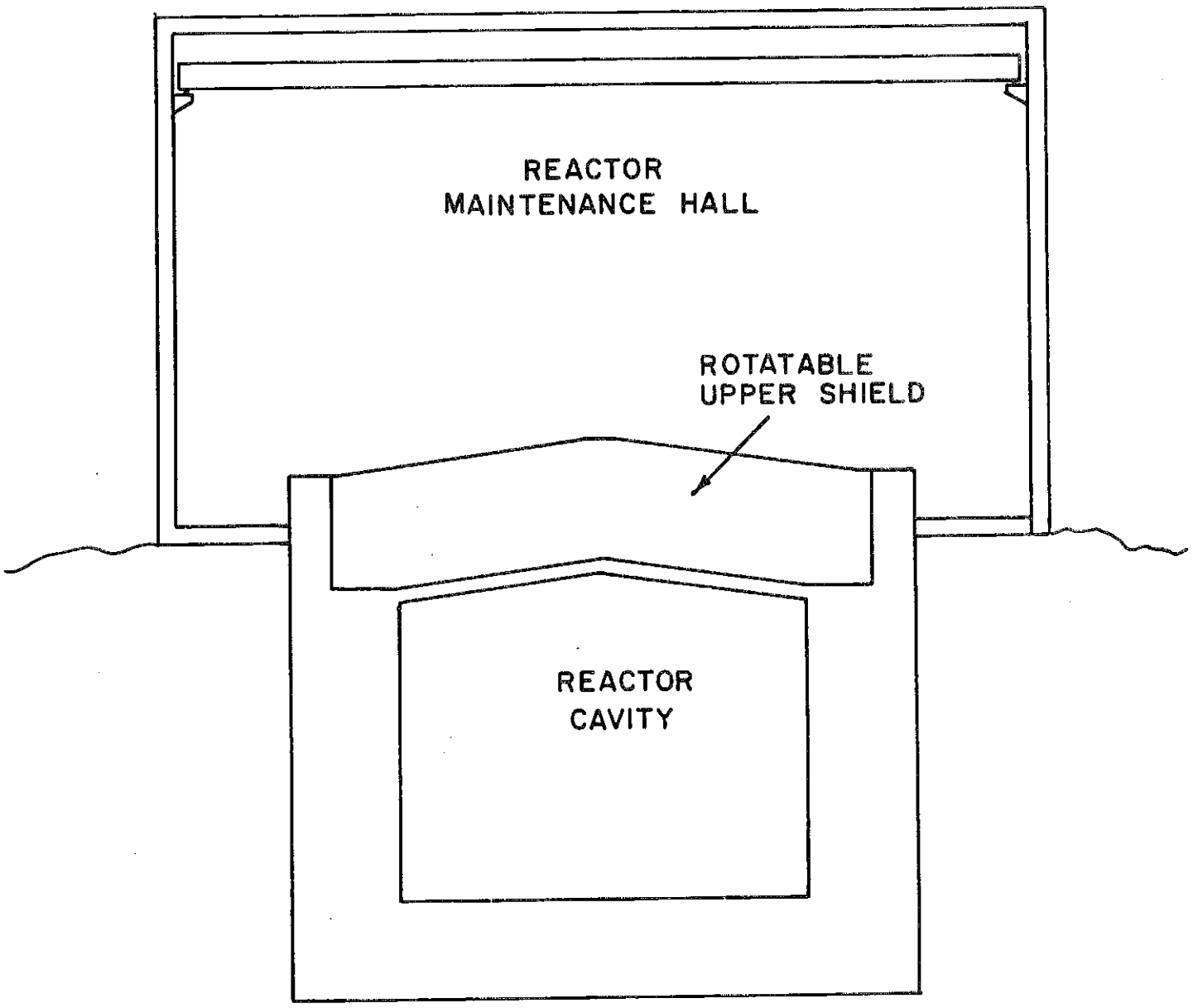

Fig. IX.2-4 Cross section showing reactor cavity below grade with maintenance hall above.

In the following sections we will address specific aspects of blanket maintainability, namely, preparation for blanket replacement, remote disconnection and connection of coolant lines and removal and replacement of blanket modules.

IX.2.2 Preparation for Blanket Maintenance

In preparing the cavity for blanket replacement many preliminary operations have to be carried out. The list below enumerates the key operations that can be performed during a 24 hour period after shutdown while the short lived radio-isotopes, in particular Mn-56, are decaying.

- Vacuum ports are valved off to prevent contamination of the cryopumps with undesirable gasses and the cryosurfaces are warmed up.
- Beam lines are isolated from the cavity by valves.
- The $Li_{17}Pb_{83}$ is drained from the cavity entirely.
- The $Li_{17}Pb_{83}$ coolant is drained from the reflector and the reflector is hooked up to an auxiliary cooling system, perhaps of helium gas. The reflector is cooled sufficiently to maintain its temperature above the ductile-brittle transition level. This will also keep whatever residual $Li_{17}Pb_{83}$ molten and will prevent freezeup of the blanket support systems.
- The cavity is brought up to atmospheric pressure with air.
- The upper shield seal between the rotatable and stationary shield components is disconnected.
- The plug in the upper shield access port is unsealed and removed.
- The target injector is removed and remote viewing devices are inserted in its place.
- The mechanical latch which locks the upper blanket modules to the reflector is deactivated making it possible to rotate the reflector/shield.

IX.2.3 Disconnecting and Connecting Coolant Lines

The breeding/cooling material selected for HIBALL, $Li_{17}Pb_{83}$ is an excellent solder. We feel we should take advantage of this fact in designing the means for connecting and disconnecting the coolant lines. The idea shown in Fig. IX.2-5 is to make a coupling with a wide enough flange such that the $Li_{17}Pb_{83}$ forms a frozen barrier at the outer periphery. A mechanical latch is used to apply pressure between the flanges and provide restraint against displacement. A heater must be provided to melt the connection during disassembly. On the other hand, because of the high temperature surroundings in the vicinity of the joint, it may be necesary to actively cool the edges of the stationary flange. The coolant is turned off to melt the joint. This is truly a remotely maintainable self-healing coupling which is relatively easy to manipulate.

In a practical sense, for this scheme to work entirely automatically, the following sequence must be followed:

Disconnecting a Coolant Joint

- The breeding/cooling material is drained out.
- The heater on the flange is turned on, or alternatively, the coolant on the flange edge is turned off.
- The mechanical latch is deactuated to release the pressure between the flanges.
- The stationary half of the joint is retracted to provide clearance for uncoupling the joint.

Connecting a Coolant Joint

- The flanges are aligned and the conical surfaces are mated. The newly inserted blanket module will have a flange which has been appropriately fluxed.

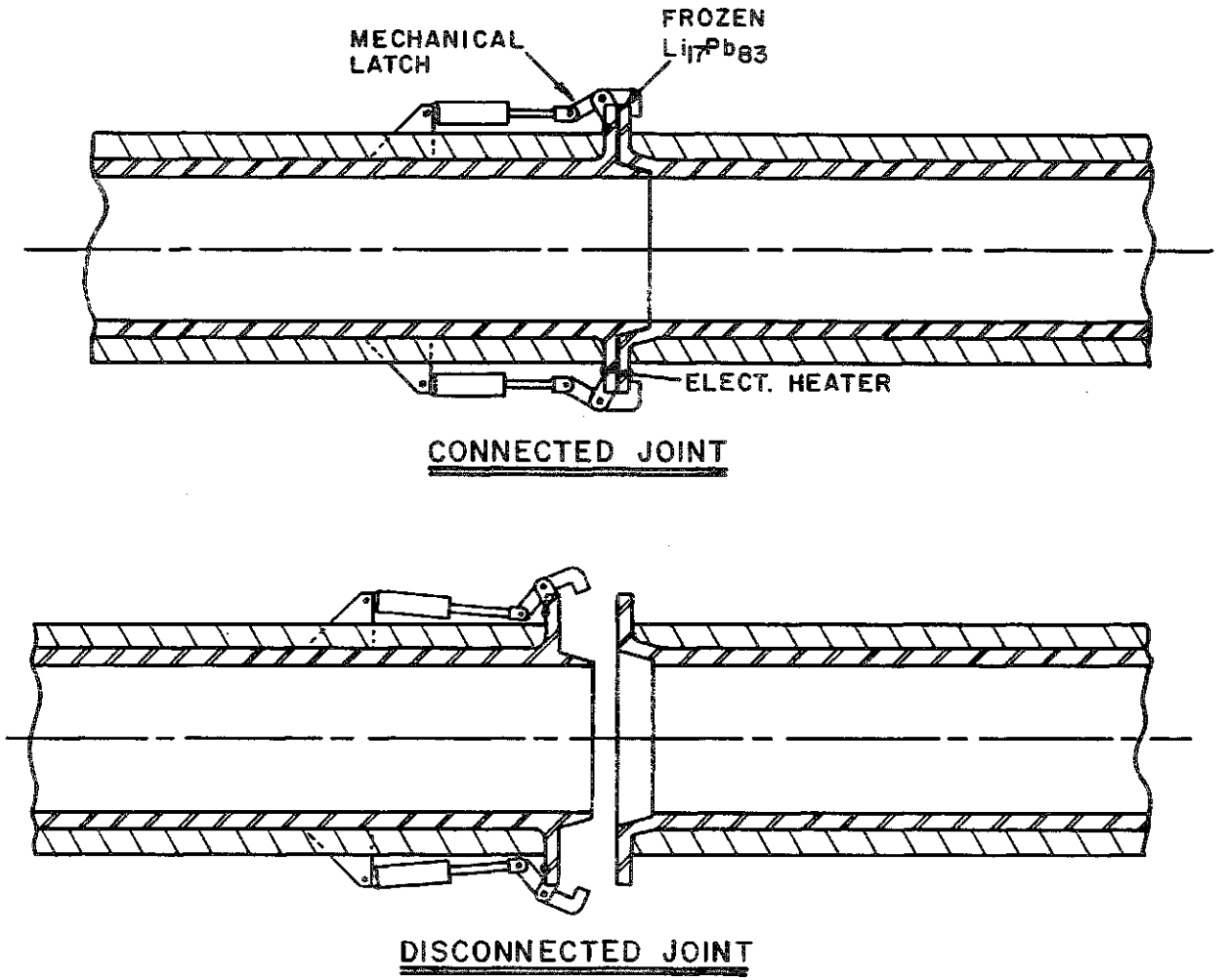

Fig. IX.2-5 Coolant tube remote joining concept.

- The mechanical latch is actuated and the joint is immobilized.
- As the breeding material is admitted into the header it forms a frozen seal on the edge between the flanges.

IX.2.4 Replacing Blanket Modules

Figure IX.2-2 shows the outline of the maintenance access port superimposed on a view of the upper blanket and Fig. IX.2-6 shows an upper blanket module being removed through the access port.

Following the preparation outlined in section XI.2-2, the upper shield/reflector is rotated and made to index onto the blanket module to be replaced. Once the coolant line is disconnected, an overhead crane in the maintenance hall equipped with a special fixture is attached to the upper blanket module. In order to decouple the module from its supports, it has to be lifted up in the back and then pulled radially outwards. When the support studs clear the slots in the reflector, the blanket module is tilted forward as shown in Fig. IX.2-6 and is lifted out of the cavity into the reactor hall.

With an upper blanket module removed, the radial blanket module immediately below it is now visible through the access port. Another special fixture is attached to it and is used to extract it vertically through the access hatch as shown in Fig. IX.2-7. After the coolant line is disconnected, an upward pull on the module disengages the tee sections on the upper support plate struts from the milled slots in the reflector. Once engaged, the whole module is free to be removed from the cavity.

Replacing the spent modules with new ones entails reversing the process outlined above. A new radial blanket module is inserted into the cavity, attached to the reflector and the coolant line. It is followed by a vertical blanket module which is also inserted and the appropriate attachments

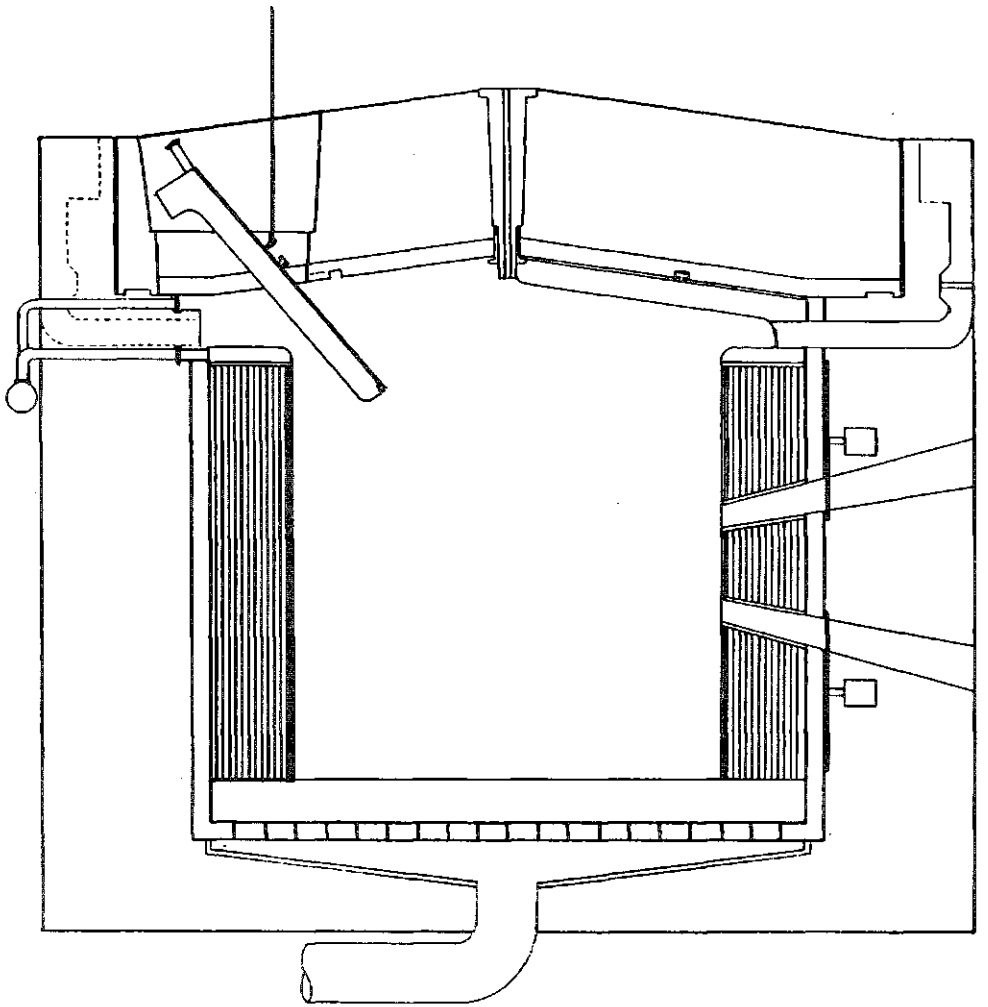

Fig. IX.2-6 Cross section showing removal of an upper blanket module.

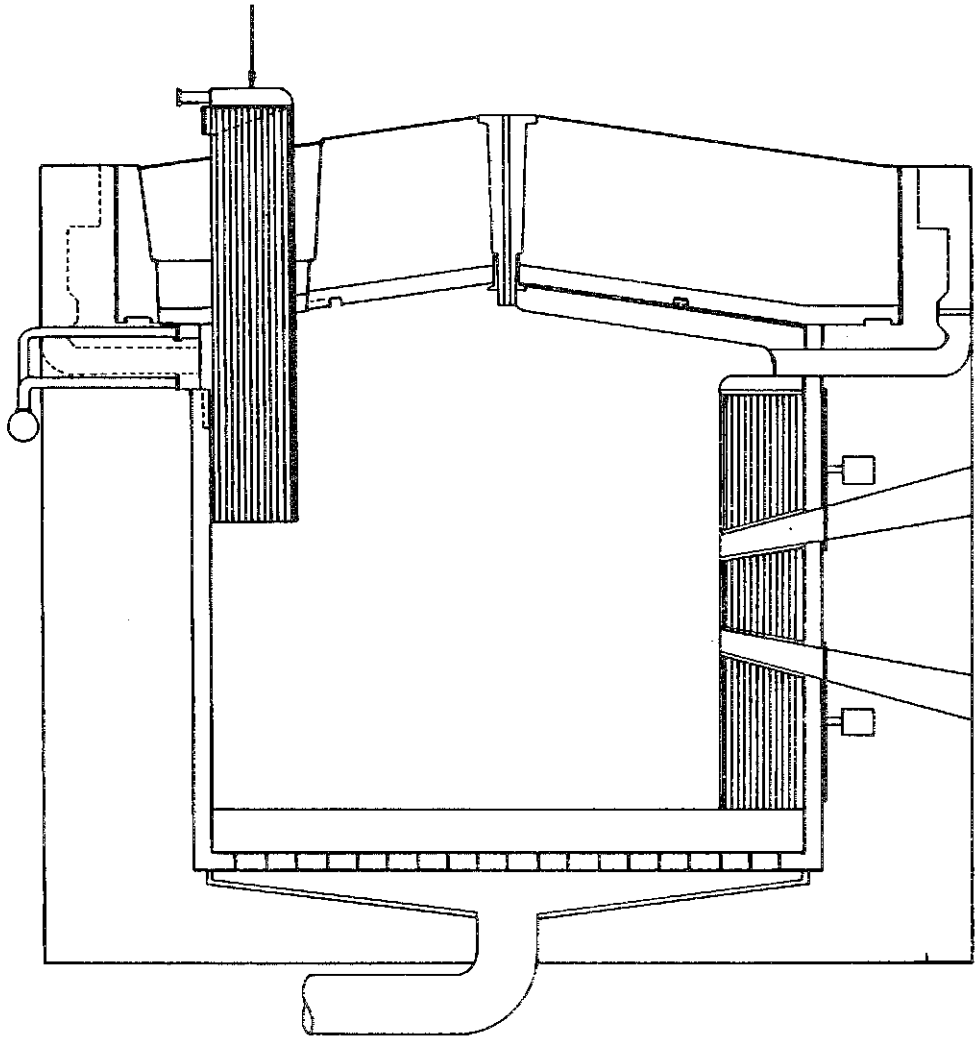

Fig. IX.2-7 Cross section showing removal of a radial blanket module.

performed. The upper reflector/shield is then rotated to the next location and the same procedure repeated.

Although the blanket modules are large and bulky, they are quite light once the breeding material has been drained from them. For example, the mass of an upper blanket module is ~ 1.5 tonnes and a radial module ~ 1.8 tonnes. The mass of the shield plug is ~ 150 tonnes, well within the capacity of the overhead crane in the maintenance hall.

When blanket replacement is completed, the cavity must be returned to operational status. The upper shield is rotated to a designated location, the access port is plugged, the seals are secured and the support mechanism which locks the upper blanket modules to the reflector is actuated. The cavity is now ready for evacuation and initiation of startup procedures.

A summary of the attractive features of this maintenance concept is given below:

Summary

- Preassembled blanket modules with integral support manifolds and beam tubes minimize "in reactor" manipulation.
- Coolant headers, vacuum pumps and ducts remain undisturbed.
- Number of coolant connections is minimized and the designed joints can be disconnected remotely with relative ease.
- Although bulky, the blanket modules are light.
- Operations are limited to simple linear translation and vertical lifting.
- The unprotected central hub of the target injector can be easily removed for servicing.

X Preliminary Cost Estimates

X.1 Basis for Costing

The following list enumerates the basis for the costing:

a. Methodology adopted from the US-DOE "Fusion Reactor Design Studies - Standard Accounts for Cost Estimates," PNL 2648,

b. Unit costs for the cavities taken from the US-INTOR study,

c. Driver and beam transport costs by GSI-Darmstadt,

d. Constant dollars used - no escalation due to inflation, and

e. Cost of target factory amortized over 30 years and accounted for in the target costs.

X.2 Driver and Beam Transport

The cost estimate for the HIBALL driver and beam transport system is of a preliminary nature and in many cases does not include development costs or redundancy of critical elements.

For the driver and beam lines, the most costly items have been derived from current projects which are comparable in size or magnitude. The linac costs are based on the German SNQ project and the superconducting element, on the HERA proposal which relied mainly on magnet fabrication at FNAL. The costs of the induction modules linac were based on available data from the LBL fusion linac study. Assembly and testing has been included for the major cost items but not for the many smaller systems. It should be mentioned that these costs do not reflect any optimization or simplification which may result from more detailed analysis.

Table X.2-1 gives the linac costs and Table X.2-2 the costs of the transfer ring, the five condenser rings, the ten storage rings and all the associated beam lines. These costs were compiled at GSI-Darmstadt (FRG) and are given in DM with the gross values converted to dollars at the present conversion rate of 2.5 DM per U.S. dollar.

Table X.2-1 Linac Costs

in MDM

		($DM \times 10^6$)		($\$ \times 10^6$)
Source and injection	8 x 3.0	24		
RFQ linac	0.2 MDM/m x 160 m	32		
27 MHz Widerøe	0.15 MDM/m x 120 m	18		
54 MHz Widerøe	0.15 MDM/m x 208 m	31		
108 MHz Alvarez	0.1 MDM/m x 320 m	32		
324 MHz Alvarez	0.06 MDM/m x 2500 m	150		
Funnel section	1.2 MDM x 7	8		
Debuncher, energy + emitt. meas., beam dump		5		
			300	
RF < 108 MHz	1.75 MDM/MW x (20 + 26)	81		
RF 108 MHz	1 MDM/MW x (23 + 72)	95		
RF 324 MHz	0.7 MDM/MW x (250 + 653)	632		
			808	
Controls		19		
Software		25		
			44	
Cooling		130		
Air condition		33		
El. power distribution		50		
Safety + communications		8		
			221	
Injection building	200 DM/m^3x60x60x20 m^3	14		
Linac low energy	9 kDM/m x 530 m	5		
Linac high energy	13 kDM/m_3x 2500 m	33		
Equipment building	130 DM/m^3 x 15x15x3000 m^3	88		
Operation building		28		
Workshop and stores		40		
			208	
			1581	632.4

Table X.2-2 Rings and Beam Transport Costs

		(DMx10^6)		(x10^6$)
Length of superconducting elements	31.4 km			
Cost per m incl. vacuum, controls, power supplies, refrigerator	38.5 kDM			
Total beam line and ring cost		1209		
Kickers and septa	1.5 MDM x 42	63		
Switching magnets	0.3 MDM x 36	11		
Beam rotator		4		
Beam combiner		6		
RF syst. in storage rings	5 MDM x 10	50		
Induction linacs		876		
Timing and controls		35		
Correction dipoles	0.7 x 80	56		
Final focusing	3.5 x 80	280		
Remote handling equipment		10		
Cooling plant + distribution		130		
			2730	
Ring tunnels	10 kDM/m x 14.7 km	147		
Transport tunnels	5 kDM/m x 24 km	120		
Utility buildings for rings	10 MDM x 4	40		
Refrigerator + power supply buildings	3 MDM x 20	60		
Maintenance building		40		
			407	
			3137	1254.8

X.3 Cavities

In the reactor cavities at the present level of design, the costing procedure consists simply of calculating the masses of materials used in the cavity and applying a unit cost which is based on a completely fabricated product. In places where such a method is impractical, for example in the area of cryopumps or cryogenerators, algorithms are used which relate the cost to the capacity of the system.

The unit costs and cost algorithms used in this study are derived from the guidelines adopted for INTOR. Prices given reflect only the material and fabrication costs. Engineering, assembly and contingency are assessed as a percentage of the direct costs.

Table X.3-1 gives the unit costs used in the cavities and Table X.3-2 summarizes these costs.

Table X.3-1 Unit Costs Used in HIBALL Cavity

		$ (1981)
1. Blanket		
Fabricated SiC		
10 cm diam. INPORT tubes	$/unit	5660
3 cm diam. INPORT tubes	$/unit	865.4
Upper blanket modules	$/kg	1500
Beam ports	$/kg	1500
HT-9 Structure	$/kg	45
$Li_{17}Pb_{83}$	$/kg	4.5
2. Reflector and Liner		
HT-9	$/kg	20
3. Shield		
Structure	$/kg	10
Concrete	$/m^3	250
4. Vacuum System		
Valves	$/unit	70,000
Cryopanels (algorithm used)		
Root blowers (algorithm used)		
5. Pipes and Headers		
36 cm diam. inlet pipes,	$/m	10,000
1.0 m diam. header	$/m	20,000

Table X.3-2 Summary of Cavity Costs

		$ x 10^6 (1981)	$ x 10^6 (1981)
Blanket			
SiC	INPORT tubes	18.384	
	Upper blanket	7.155	
	Beam tubes	2.777	
HT-9	Radial blanket	1.758	
	Upper blanket	1.882	
$Li_{17}Pb_{83}$		20.205	52.161
Reflector and Liner			
HT-9	Reflector	47.438	
	Other liner	1.883	
	Bottom drain	2.400	
	Upper latching mechanism	1.500	53.221
Shield			
Structure		73.000	
Concrete		4.471	77.471
Vacuum System			
Valves (30 + 2 spares)		2.240	
Cryopumps (He)		2.800	
Cryopanels (D_2T_2)		2.880	
Roots blowers		0.800	8.720
Pipes and Headers			
Coolant lines and flanges		2.520	
Headers		2.108	4.628
TOTAL/CAVITY			196.201

X.4 Remaining Direct Costs

The remaining major cost item in the reactor plant is the main heat transfer and transport system. This account is estimated at $560 x 10^6 and is broken down in the following manner:

Liquid metal pumps	225×10^6
Steam generators	175×10^6
Pipes/dump tanks/cleanup system	160×10^6

In the balance of plant, it was assumed that a 1000 acre site will be required at $5000/acre. The structures and site facilities take into account that the buildings for the linac, rings and beam line tunnels are already included in section X.2.

For the turbine plant equipment, the electric plant equipment and the miscellaneous plant equipment, we have used the guidelines provided by PNL-2987 "Fusion Reactor Design Studies Standard Cost Estimating Rules" prepared for the US DOE by Battelle Northwest. Table X.4-1 lists the direct costs for the reactor plant and the balance of plant.

Table X.4-1 Breakdown of Direct Costs

	$ x 10^6 (1981)	
Reactor Plant		
Reactor cavities (4)	785	
Pellet injectors (4)	12	
Main heat transfer system	560	
RF linac	632	
Transfer ring (1)		
Condenser rings (5)		
Storage rings (10)	1255	
Induction linac (20)		
Beam lines		3244
Balance of Plant		
Land and land rights	5	
Structures and site facilities	280	
Turbine plant and heat rejection	430	
Electric plant equipment	275	
Miscellaneous plant equipment	50	1040
		4284

X.5 Indirect Costs and Interest During Construction

As mentioned in section X.1, the guidelines given in PNL 2648 were used in arriving at the indirect costs.

Since this economic analysis is in constant dollars, the interest during construction is based on a 5% annual deflated cost of capital. An 8 year construction period was used on the assumption that the driver, reactor plant and balance of plant construction could be ongoing simultaneously. With the capital disbursed according to the classical S curve biased to the right, the interest during construction factor is 0.17 (PNL 2648). Table X.5-1 gives the breakdown of the indirect cost and the interest during construction.

Table X.5-1. Indirect Costs and Interest During Construction

		$ x 10^6 (1981)
Total Direct Costs		4284
Indirect Costs		
Construction Facilities (15% of TDC)	642	
Engineering & Cost Management (15% of TDC)	642	
Owners Costs (5% of TDC)	214	1498
Interest During Construction	983	983
5%/Annum Deflated Interest		
8 year Construction Period		
Grand Total Cost		6765

The net electric power output of HIBALL is 3768 MWe. Thus the capital cost is:

$$\text{Capital Cost} = \frac{\$6765 \times 10^6}{3768 \times 10^3 \text{ kW}} = \$1795/\text{kWe} \quad .$$

This can be compared with other recent fusion designs:

STARFIRE	2000
NUWMAK	2227
WITAMIR	2130

X.6 Busbar Costs

X.6.1 Target Costs

The cost of the target factory was amortized in the target costs and thus does not appear as a direct cost. We assumed a \$200 x 10^6 target factory cost which, after the indirect costs and interest during construction were added became \$316 x 10^6. Thus the target cost breakdown is as follows:

	cents/target
30 year amortization of target factory	2.4
Operation and maintenance (2% of capital cost)	1.4
Interest on capital (10% annual)	7.2
Material (D_2, plastic, etc.)	2.0
Profit	2.0
	15.00

At a 70% availability, the number of targets needed for all four cavities is 4.4 x 10^8/annum. The annual target cost is thus \$66 x 10^6.

X.6.2 Operation and Maintenance

As provided in PNL 2648, the operation and maintenance was taken as 2% of the total capital cost, or \$135 x 10^6.

X.6.3 Component Replacement

A two year lifetime was taken for the INPORT tubes and the upper blanket modules. The annual component replacement cost is thus \$64 x 10^6.

X.6.4 Interest on Capital

A straight 10% annual interest on capital was used. Table X.6-1 gives the busbar cost.

Table X.6-1. HIBALL Busbar Costs

Assumptions: 70% availability

10% interest on capital

3768 MWe net power output = 2.31×10^{10} kWh/yr

$$\text{Busbar Cost} = \$ \frac{(66 \times 10^6 + 135 \times 10^6 + 64 \times 10^6 + 676.5 \times 10^6)\ 1000\ \text{mills/\$}}{2.31 \times 10^{10}\ \text{kWh}}$$

$$= 40.8\ \text{mills/kWh}.$$

Some of the other recently designed fusion power systems have the following busbar costs:

STARFIRE	35.1
NUWMAK	37.5
WITAMIR	36.1

APPENDIX

HIBALL PARAMETER LISTING #6

I. GENERAL PARAMETERS

	4/29/81	5/8/81	6/30/81
Average DT power - 17.6 MeV/fusion (MW)	8000	8000	8000
Target power (MW)	7873.6	7920	7920
Target multiplication	0.984	0.99	0.99
Target yield (MJ)	400	400	396
Ion beam pulse energy (MJ)	4.8	4.8	4.8
Overall driver efficiency (%)	26.5	26.5	26.7
Target gain	83	83	83
Fusion gain ηG	18.5	18.5	22
Blanket multiplication	1.27	1.274	1.274
Total nuclear thermal power (MW)	10149	10193	10193
Gross power		10233	10233
Gross thermal efficiency (%)	42	42	42
Gross electrical output (MW)	4168	4278	4298
Recirculating power fraction	0.2	0.2	0.123
Net electrical output (MW)	3309	3309	3768
# of chambers	4	4	4
Chamber repetition rate (Hz)	5	5	5
Chamber geometry	cylindrical	cylindrical	cylindrical
Chamber diameter (m)	14	14	14
Chamber height (m) (at vacuum wall)	10	10	10
Chamber alloy	HT-9	HT-9	HT-9
# of beam ports per chamber	20	20	20
Breeding material	$Pb_{83}Li_{17}$	$Pb_{83}Li_{17}$	$Pb_{83}Li_{17}$
Breeding ratio	1.25	1.25	1.25

II. TARGET PARAMETERS

	4/29/81	5/8/81	6/30/81
Composition			
D (mg)	1.61	1.6	1.6
T (mg)	2.42	2.4	2.4
DT load (mg)	4.0 (2.0)	4.0 (2.0)	4.0 (2.0)
Material #1 (mg)	PbLi 67.1	PbLi 67.1	PbLi 67.1
Material #2 (mg)	Pb 288	Pb 288	Pb 288
Burnup (%)	30 (60)	30 (60)	30 (60)
Total mass (mg)	359	359	359
Configuration (# of shells)	3	3	3
Target diameter (cm)	0.6	0.6	0.6
Absorbed ion energy (MJ)	4.8	4.8	4.8
No burn ignition temperature (keV)	5	5	5
Fuel ρR at ignition (g/cm^2)	2	2	2
Hot spot ρR at ignition (g/cm^2)	0.4	0.4	0.4
Pusher ρR at ignition (g/cm^2)	1	1	1
DT yield (MJ)	400	400	400
Target yield (MJ)	393.67	396	396
Target energy multiplication	0.984	0.99	0.99
Average DT power (MW)	8000	8000	8000
Target power (MW)	7873.6	7920	7920
Target gain	83	83	83
Neutron yield (MJ)	284.8	284.8	284.8
Neutron spectrum, $\bar{E}$ (MeV)	11.98	11.98	11.98
Neutron multiplication	1.046	1.046	1.046
Stopping Power (MeV-cm/mg)			
10 GeV Bi → Pb_{cold}		40	40
Bi → PbLi		65	65
Gamma yield (MJ)	0.6	0.6	0.6

	4/29/81	5/8/81	6/30/81
Gamma spectrum, $\bar{E}$ (MeV)	1.53	1.53	1.53
X-ray yield (MJ)	87.6	89.5	89.5
X-ray spectrum - blackbody (keV)	see histo-gram	see histo-gram	see histo-gram
Debris yield (MJ)	20.6	21.0	21.0
Debris spectrum (keV/amu)	0.6	0.6	0.6
Radioactivity production (Ci/target @ t = 0)	1.2×10^6	1.2×10^6	1.2×10^6 ?
Radioactivity production (Ci/target @ t = 0.2 sec)			?
Target injection velocity (m/s)	1000	200	200
Target injector type	gas gun	gas gun	gas gun

III. TARGET MANUFACTURE AND DELIVERY PARAMETERS

	4/29/81	5/8/81	6/30/81
Target manufacture			
Production rate (#/s)			
Material stored within target factory (kg)			
Deuterium			
Tritium			
Material #1			
Material #2			
Cost/target (cents)			
Target storage			
# of targets in storage			
Average target storage time (hr)			
Target delivery			
Longitudinal positioning tolerance (mm)			0.5
Lateral positioning tolerance (mm)			0.7
Target velocity (m/s)			200
Repetition Frequency (Hz)			5
Injection:			
Type			gas gun
Projectile (sabot+target) mass (g)			2
Propellant gas amount (Torr liters/shot)			608
Propellant gas			D_2
Total prop. gas handled (mg/shot)			141
Buffer cavity pressure, min, (Torr)			1
max, (Torr)			2
Buffer cavity volume (m^3)			0.88

	4/29/81	5/8/81	6/30/81
Injection channel diameter (mm)			10
Prop. gas entering reactor cavity (mg/shot)			1.6
Gas gun total efficiency			0.5
Gun barrel diameter (mm)			10
Pressure of prop. gas reservior (Bar)			5
Acceleration distance (m)			2
Acceleration (m/s^2)			10^4
Acceleration time (ms)			20
Total target travel time (ms)			80
Tolerance on total travel time (ms)			±5
Distance muzzle to focus (m)			12
Tracking:			
Lateral tracking			none
Longitudinal tracking, type			light-beam interception
Tracking position 1, distance from focus (m)			5.5
Tracking position 2, distance from focus (m)			3.0
Light beam diameter (mm)			0.2
Precision of arrival time prediction (μs)			±1
Duration of processing tracking results (ms)			1

IV. DRIVER PARAMETERS

	4/29/81	5/8/81	6/30/81
Ion			
Type	Bi	Bi	Bi
Charge state	+2	+2	+2
Energy (GeV)	10	10	10
Velocity v (m/s)	9.25×10^7	9.25×10^7	9.25×10^7
Beta, $\beta = v/c$	0.309	0.30875	0.30875
Gamma, $\gamma = (1 - \beta^2)^{-1/2}$	1.051	1.051	1.051
Magnetic stiffness (Tesla • meters)		105.4	107.7
Mass number	209	209	209
Source	Elsire	"Elsire" (reflex)	"Elsire" (reflex)
Accelerator			
Type	RF	RF Linac	RF Linac
Efficiency (%)	33.5	33.5	33.3
Length (km)	3.0	3.0	3.0
Effective voltage drop, U_Σ (GV)	5	5	5
Beam current during single pulse (mA)	147	155	160
Single pulse length (ms)			
Length of macro pulse train containing 450 single pulses (ms)	7.5	7.5	7.5
Repetition rate of pulse trains (Hz)	20	20	20
RF duty cycle	0.16	0.16	0.16
Momentum width, $\Delta p/p$	$\pm 5 \times 10^{-5}$	$\pm 3 \times 10^{-5}$	5×10^{-5}
Source emittance, normalized, ϵ_N (m)	2×10^{-7}	2×10^{-7}	2×10^{-7}
Linac emittance, normalized, ϵ_N (m)	4×10^{-7}	6×10^{-7}	6×10^{-7}
Micro-bunch frequency (MHz)	108.4	108.4	108.4
Pulse length (μs)	700	15	15
bunch spacing (μs)	35	see figure	see figure
gap between bunches (μs)	1	1 (16)	1 (16)

	4/29/81	5/8/81	6/30/81
Transfer Ring			
Injection, radial stacking			
# turns	20	3	3
Maximum dilution factor	5	2	2
Beam emittance			
horizontal (mm-mrad)		12	12
vertical (mm-mrad)		2	2
Average dipole field, $\bar{B}$ (Tesla)	?	0.159	0.159
Average radius (m)	?	663.4	663.4
Circumference (m)	?	4168	4168
Revolution frequency (kHz)	?	22.22	22.22
Revolution time (μs)	35	45	45
Coasting beam current (A)	3.4	0.46	0.46
# lattice periods	?	240 (?)	240 (?)
ν_{Ho}	?	59.85 (?)	59.85 (?)
ν_{Vo}	?	59.85 (?)	59.85 (?)
Beam full width (cm)			
horizontal	?	2.2 (?)	2.2 (?)
vertical	?	0.9 (?)	0.9 (2)
Vacuum pressure (Torr)	$< 10^{-10}$	(10^{-9} ?)	(10^{-9} ?)
Ejection kicker			
Flat top time (μs)	35	45	45
Rise time (μs)	< 1	< 1	< 1
Reset time (μs)		< 15	< 15
Kicking angle (mrad)		2.5	2.5
Stored energy per shot (kJ)	?	0.05	0.05
Average frequency of shots (sec^{-1})		200	200
Power (kW) (n = 0.2)	?	50	50
Beam rotator $\int$ Bdz (Tesla-m)	330	330	330
Condenser rings			
# of rings		5	5

	4/29/81	5/8/81	6/30/81
Injection radial stacking			
# of turns		3	3
Maximum dilution factor		1.67	1.67
Beam emittance			
horizontal (mm-mrad)		10	10
vertical (mm-mrad)		12	12
Average dipole field, $\bar{B}$ (Tesla)		0.477	0.477
Average radius (m)		221.1	221.1
Circumference (m)		1389.4	1389.4
Revolution frequency (kHz)		66.67	66.67
Revolution time (μs)		15	15
Coasting beam current (a)		1.38	1.38
# lattice periods		80 (?)	80 (?)
ν_H		19.85 (?)	19.85 (?)
ν_V		19.85 (?)	19.85 (?)
Beam full width (cm)			
horizontal		2.0 (?)	2.0 (?)
vertical		2.2 (?)	2.2 (?)
Vacuum pressure (Torr)		$< 10^{-10}$	$< 10^{-10}$
Ejection kickers (1 per ring)			
Flat top time (μs)		> 15	> 15
Rise time (μs)		< 1	< 1
Reset time (μs)		< 100	< 100
Kicking angle (mrad)		2.5	2.5
Stored energy per shot (kJ)		0.1	0.1
Average frequency of shots (sec^{-1})		40	40
Power per CR, η = 0.2 (kW)		20	20
Storage rings			
# of rings	10	10	10
Injection, radial stacking			
# of turns	7	3	3
Maximum dilution factor	4	1.5	1.5

	4/29/81	5/8/81	6/30/81
Beam emittance			
horizontal (mm-mrad)		45	45
vertical (mm-mrad)		90	90
Average dipole field, $\bar{B}$ (Tesla)	?	1.431	1.431
Average radius (m)	?	73.7	73.7
Circumference (m)	?	463.1	463.1
Revolution frequency (MHz)	0.2	0.2	0.2
Revolution time (μs)	5	5	5
Coasting beam current (A)	24	21	21
# of lattice periods	?	40 (?)	40 (?)
ν_{Ho}	?	9.85 (?)	9.85 (?)
ν_{Vo}	ν_H	ν_H	$\leq\nu_H$
Beam full width (cm)			
horizontal	6(or 4)	3.7 (?)	3.7 (?)
vertical	12(or 8)	5.2 (?)	5.2 (?)
Vacuum pressure (Torr)	10^{-10} - 10^{-11}	10^{-10} - 10^{-11}	10^{-10} - 10^{-11}
Adiabatic compression			
RF (MHz)	0.4	0.4	0.4
Harmonic number	2	2	2
Initial volts per turn (kV)	2	2	0.1
Final volts per turn (kV)	200	200	76
Rise time (ms)	< 0.1	10	10
Initial $\Delta p/p$	5×10^{-5}	$\pm 3 \times 10^{-5}$	$\pm 5 \times 10^{-5}$
Final $\Delta p/p$	5×10^{-4}	$\pm 5 \times 10^{-4}$	$\pm 5 \times 10^{-4}$
Final $\Delta\Phi$	$\pm 15°$	$\pm 15°$	$\pm 15°$
Final Δt (ns)	± 100	± 100	± 100
Separatrix $\Delta p/p$	$\pm 3 \times 10^{-3}$	$\pm 3 \times 10^{-3}$	$\pm 3 \times 10^{-3}$
Synchrotron freq/revolution freq.	1/350	1/350	1/350
Fast extraction kickers			
# of kickers per ring		2	2

	4/29/81	5/8/81	6/30/81
Kicking angle (mrad)	20	6*	6*
Rise time (μs)	1.5	1.5	1.5
Flat top time (ns)	> 500	> 500	> 500
Stored energy per shot (kJ)		2	2
Average frequency of shots (s^{-1})		4	20
Power per kicker, η = 0.2 (kW)		40	40
Fast Compression: induction linac			
(space charge effects included)			
Length (m)	100-200	200	200
Voltage (MV)	160	300	±150
Pulse shape	sawtooth	sawtooth	sawtooth
Pulse length (ns)	200	200	200
Focal length (km)	< 1.16	0.8	0.8
Δp/p	$>\pm 8 \times 10^{-3}$	$\pm 5 \times 10^{-3}$	$\pm 5 \times 10^{-3}$
Beam lines			
Total number-long	20	20	20
Length (km) per long beam line	1.2	1.2	1.2
# into each chamber (short)	80	20	20
Length (km)	0.3	0.3	0.3
Total length of all beam lines (km)	48	48	48
Lattice period (m)	?	> 2.8	> 2.8
Phase advance	π/3	π/3	π/3
Beam tube inner diameter (cm)	10	8	8
Beam chamber entry			
Final focusing magnets	triplet	quadrupoles	quadrupoles
Distance from FFM to target (m)	8.5	8.5	8.5
Clearance for cavity-beam line vacuum pump (m)	2	2	2

*For 4 cm hor. beam width (space charge).

		4/29/81	5/8/81	6/30/81
Cavity pump down time between shots (ms)		150	150	150
Beam port dimensions (cm)				
vertical		85	103	103
horizontal		25	34.3	34.3
Distance from beam port to target (m)		7	7.28	7.27
Final Beams				
# of beams	Step 1	---	---	---
	Step 2	20	20	20
Pulse length (ns),	Step 1	---	---	---
	Step 2	20	20	20
Particle Current/beam (kA) (Electric current = 2x particle current)	Step 1	---	---	---
	Step 2	1.2	1.25	1.25
Pulse energy (MJ)		5	4.8	5.0
Maximum power (TW)		250	250	250
Pulse repetition rate (Hz)		20	20	20
Focused spot diameter (mm)		6	6	6
Focused spot area (mm^2)		28.3	28.3	28.3
Unnormalized emittance per beam (mm-mrad)				
vertical		120π	90π	$90\pi(120\pi)$
horizontal		30π	45π	$45\pi(30\pi)$
Normalized emittance per beam (mm-mrad)				
vertical		58π	29π	29π
horizontal		17.4π	15π	15π

V. "CAVITY" REGION PARAMETERS

	4/29/81	5/8/81	6/30/81
Coolant and breeding material	$Pb_{83}Li_{17}$	$Pb_{83}Li_{17}$	$Pb_{83}Li_{17}$
Li-6 enrichment, %	natural	natural	natural
Tube Region			
Inport tube structural material	HT9-0.7	HT9-0.7	HT9-0.7
and v/o	SiC-2	SiC-2	SiC-2
Inport tube coolant v/o	97.3	97.3	97.3
Tube region support structure v/o	HT9-0.7	HT9-0.7	HT9-0.7
First surface radius (m)	5	5	5
Region thickness (m)	2	2	2
Region density factor	0.33	0.33	0.33
Effective coolant thickness (m)	0.66	0.66	0.66
Mass of coolant in tubes/cavity (tonnes)	2295	2295	2295
Tubes			
Length (m)	10	10	10
Diameter (cm)			
First two rows	3	3	3
Wall thickness (mm)		0.8	0.8
Remainder	10	10	10
Wall thickness (mm)		2	2
Number			
First two rows	1230	1230	1230
Remainder	3060	3060	3060
Number of penetrations in region	20	20	20
Total area of beam penetrations at first surface (m^2)	3.6	3.6	3.6
Pb at. density - $x10^{-10}$ atom/cm^3*	4	4	4

*Just before shot.

	4/29/81	5/8/81	6/30/81
Noncondensible at. density @ 500°C - x 10^{-10} atoms/cm^3	0.13	0.13	0.13
Pressure - Torr	< 10^{-4}	< 10^{-4}	< 10^{-4}
Chamber top			
Structural material and v/o	HT-9 1 SiC 2	HT-9 1 SiC 2	HT-9 1 SiC 2
Coolant v/o	97	97	97
Height at chamber centerline (m)	6.5	6.5	6.5
Region thickness (m)	0.5	0.5	0.5
Mass of coolant in top cavity (tonnes)	717	717	717
Number of penetrations in top region	1	1	1
Total area of penetrations at chamber inner surface (m^2)	small	"small"	"small"
Chamber bottom pool			
Structural material and v/o	---	---	---
Coolant v/o	100	100	100
Height at chamber centerline (m)	5	5	5
Region thickness (m)	1.0	1.0	1.0
Mass of coolant in bottom pool/ cavity (tonnes)	1448	1448	1448
Maximum 1st surface neutron energy current - at chamber midplane (MW/m^2)	4.54	4.54	4.54
Neutrons passing through each beam line penetration per shot	8.14×10^{16}	8.14×10^{16}	8.14×10^{16}
Maximum total 1st surface X-ray and debris heat flux (J/cm^2)	34.5	34.5	34.5
DT power per cavity (MW)	2000	2000	2000
Total n & γ power in cavity (MW)	1667.4	1667.4	1667.4
Tube region	1097.1	1097.1	1097.1
Cavity top	293.1	293.1	293.1
Cavity bottom	277.2	277.2	277.2

	4/29/81	5/8/81	6/30/81
Total power in cavity, including X-rays and debris (MW)	2208.7	2208.7	2208.7
Energy multiplication(1)	1.1	1.1	1.1
n & γ energy multiplication(2)	1.17	1.17	1.17
Average power density (W/cm^3)	3.44	3.44	3.44
Tube region	4.41	4.41	4.41
neutron	2.20	2.20	2.20
gamma	2.21	2.21	2.21
Top region	3.51	3.51	3.51
neutron	1.89	1.89	1.89
gamma	1.62	1.62	1.62
Bottom region	1.80	1.80	1.80
neutron	1.06	1.06	1.06
gamma	0.74	0.74	0.74
Peak/average spatial power density in tube region	4.87	4.87	4.87
Impulse on first row of tubes ($dyne\text{-}sec/cm^2$)	600	600	600
Amount of coolant blown off per shot (kg)	13	13	13
Maximum DPA/FPY in SiC			
Tube region	118	118	118
Top region	70	70	70
Bottom region	---	---	---
Average DPA/FPY in SiC			
Tube region	33.5	33.5	33.5
Top region	29.6	29.6	29.6
Bottom region	---	---	---

(1) Total energy deposited in region/Dt yield

(2) Total n & γ energy deposited in region/n & γ energy incident on 1st surface.

	4/29/81	5/8/81	6/30/81
Maximum H production in SiC (appm/FPY)			
Tube region	1408	1408	1408
Top region	833	833	833
Bottom region	---	---	---
Average H production in SiC (appm/FPY)			
Tube region	273	273	273
Top region	216	216	216
Bottom region	---	---	---
Maximum He production in SiC (appm/FPY)			
Tube region	3705	3705	3705
Top region	2192	2192	2192
Bottom region	---	---	---
Average He production in SiC (appm/FPY)			
Tube region	353	353	353
Top region	274	274	274
Bottom region	---	---	---
Tritium breeding ratio	1.216	1.216	1.216
^{6}Li	1.190	1.190	1.190
Tube region	0.729	0.729	0.729
Top region	0.226	0.226	0.226
Bottom region	0.235	0.235	0.235
^{7}Li	0.026	0.026	0.026
Tube region	0.081	0.081	0.081
Top region	0.004	0.004	0.004
Bottom region	0.004	0.004	0.004
Coolant			
Inlet temperature (°C)	330	330	330
Outlet temperature (°C)	500	500	500
Flow rate/cavity (kg/hr)	2.7×10^{8}	2.94×10^{8}	2.94×10^{8}
Maximum velocity within tubes in first two rows (m/s)	5	5	5

	4/29/81	5/8/81	6/30/81
Maximum velocity within tubes not in the first two rows (m/s)	1.3	1.3	1.3
Pressure (MPa)	0.2	0.2	0.2
ΔP for entire loop (MPa)	2.0	2.0	2.0
Pumping power delivered to coolant per cavity (MW)	17.7	17.9	17.9

VI. "NON-CAVITY" REGION PARAMETERS

	4/29/81	5/8/81	6/30/81
A. Vacuum Boundary Wall			
Structural material	HT-9	HT-9	HT-9
Side wall			
Inside diameter (m)	14	14	14
Thickness (m)	0.01	0.01	0.01
Height (m)	12.0	12.0	12.0
Top liner			
Height above midplane (m)			
at centerline	7.0	7.0	7.0
at side wall	6.0	6.0	6.0
Thickness	0.01	0.01	0.01
Maximum neutron wall loading (MW/m^2)			
- side wall at midplane	0.032	0.032	0.032
Average power density (W/cm^3)	1.65	1.65	1.65
Side wall	1.22	1.22	1.22
neutron	0.097	0.097	0.097
gamma	1.13	1.13	1.13
Top liner	3.07	3.07	3.07
neutron	0.20	0.20	0.20
gamma	2.87	2.87	2.87
n & γ energy multiplication	0.008	0.008	0.008
Power deposited in vacuum wall/			
cavity (MW)	11.0	11.0	11.0
Side wall	6.2	6.2	6.2
Top liner	4.8	4.8	4.8
Maximum DPA/FPY			
Side wall	2.69	2.69	2.69
Top liner	4.98	4.98	4.98

	4/29/81	5/8/81	6/30/81
Peak instantaneous DPA rate (DPA/s)			
- side wall at midplane	0.009	0.009	0.009
Maximum H production (appm/FPY)			
Side wall	1.38	1.38	1.38
Top liner	3.20	3.20	3.20
Maximum He production (appm/FPY)			
Side wall	0.364	0.364	0.364
Top liner	0.862	0.862	0.862
Peak instantaneous He production rate			
(appm/s) - side wall at midplane	0.11	0.11	0.11
Maximum temperature (°C)	?	1520	1520
Expected lifetime (FPY)	?	20	20
Radioactivity at shutdown (Ci)	?	?	?
B. Reflector			
Structural material	HT-9	HT-9	HT-9
Coolant	$Pb_{83}Li_{17}$	$Pb_{83}Li_{17}$	$Pb_{83}Li_{17}$
Side reflector			
Inside diameter (m)	14.02	14.02	14.02
Thickness (m)	0.4	0.4	0.4
Mass of structure (tonnes)	1530	1530	1530
Mass of coolant (tonnes)	205	205	205
v/o of structure	90	90	90
v/o of coolant	10	10	10
Top reflector			
Thickness (m)	0.4	0.4	0.4
Mass of structure (tonnes)	432	432	432
Mass of coolant (tonnes)	58	58	58
v/o of structure	90	90	90
v/o of coolant	10	10	10
Bottom of reflector (splash plate)			
Thickness (m)	0.4	0.4	0.4
Mass of structure (tonnes)	484	484	484

	4/29/81	5/8/81	6/30/81
Mass of coolant (tonnes)	65	65	65
v/o of structure	90	90	90
v/o of coolant	10	10	10
Total mass of structural material in reflector/cavity (tonnes)	2446	2446	2446
Total mass of coolant in reflector/cavity (tonnes)	328	328	328
n & γ energy multiplication	0.223	0.223	0.223
Average power density (W/cm^3)	0.941	0.941	0.941
Side reflector	0.939	0.939	0.939
neutron	0.082	0.082	0.082
gamma	0.857	0.857	0.857
Top reflector	1.465	1.465	1.465
neutron	0.127	0.127	0.127
gamma	1.338	1.338	1.338
Bottom reflector (splash plate)	0.257	0.257	0.257
neutron	0.023	0.023	0.023
gamma	0.234	0.234	0.234
Peak/average spatial power density - in side reflector	4.577	4.577	4.577
Power deposited in reflector/cavity (MW)	318.3	318.3	318.3
Side	211.1	211.1	211.1
Top	91.4	91.4	91.4
Bottom	15.8	15.8	15.8
Maximum DPA/FPY			
Side reflector	2.43	2.43	2.43
Top reflector	4.50	4.50	4.50
Bottom reflector	1.36	1.36	1.36
Average DPA/FPY			
Side reflector	0.41	0.41	0.41
Top reflector	0.73	0.73	0.73
Bottom reflector	0.125	0.125	0.125

A-20

	4/29/81	5/8/81	6/30/81
Maximum H production in structural material (appm/FPY)			
Side reflector	1.15	1.15	1.15
Top reflector	2.68	2.68	2.68
Bottom reflector	0.026	0.026	0.026
Average H production in structural material (appm/FPY)			
Side reflector	0.17	0.17	0.17
Top reflector	0.41	0.41	0.41
Bottom reflector	0.004	0.004	0.004
Maximum He production in structural material (appm/FPY)			
Side reflector	0.300	0.300	0.300
Top reflector	0.715	0.715	0.715
Bottom reflector	0.006	0.006	0.006
Average He production in structural material (appm/FPY)			
Side reflector	0.032	0.032	0.032
Top reflector	0.96	0.96	0.96
Bottom reflector	0.006	0.006	0.006
Tritium breeding ratio	0.034	0.034	0.034
^{6}Li	0.034	0.034	0.034
Side	0.022	0.022	0.022
Top	0.010	0.010	0.010
Bottom	0.002	0.002	0.002
^{7}Li	4×10^{-6}	4×10^{-6}	4×10^{-6}
Side	2×10^{-6}	2×10^{-6}	2×10^{-6}
Top	2×10^{-6}	2×10^{-6}	2×10^{-6}
Bottom	0	0	0
Coolant			
Mass of coolant within reflector per cavity (tonnes)	328	328	328

	4/29/81	5/8/81	6/30/81
Flow rate/cavity (kg/hr)	3.7×10^7	4.4×10^7	4.4×10^7
Inlet temperature (°C)	330	330	330
Outlet temperature (°C)	500	500	500
Maximum coolant velocity (m/s)	1	1	1
Pressure (MPa)	2	2	2
ΔP for entire loop (MPa)	0.7	0.7	0.7
Pumping power delivered to coolant per cavity (MW)	1	1	1
Maximum structure temperature (°C)	550	550	550
C. Shield			
Structural material and v/o	concrete	concrete	concrete
	95	95	95
Coolant and v/o	H_2O 5	H_2O 5	H_2O 5
Side shield			
Inside diameter (m)	14.82	14.82	14.82
Thickness (m)	3.5	3.5	3.5
Top shield			
Height above midplane at centerline (m)	7.41	7.41	7.41
Thickness (m)	3.5	3.5	3.5
Bottom shield			
Height below midplane (m)	6.40	6.40	6.40
Thickness (m)	3.5	3.5	3.5
Maximum power density at midplane (W/cm^3)	0.045	0.045	0.045
Average power density (W/cm^3)	0.0018	0.0018	0.0018
Power deposited in shield/cavity (MW)	6.82	6.82	6.82
Power deposited in neutron & debris dump per beam line (MW)	?	?	?
Energy flux at outer surface of shield at midplane (W/cm^2)			
neutron	1.52×10^{-17}	1.52×10^{17}	1.52×10^{17}

	4/29/81	5/8/81	6/30/81
gamma	2.38×10^{-10}	2.38×10^{-10}	2.38×10^{-10}
Dose rate at outer surface of shield at midplane (mrem/hr)	2.64	2.64	2.64
neutron	1.4×10^{-5}	1.4×10^{-5}	1.4×10^{-5}
gamma	2.64	2.64	2.64
Peak DPA rate in F.F. magnet stabilizer (DPA/FPY)	4.48×10^{-6}	4.48×10^{-6}	4.48×10^{-6}
Peak radiation dose rate in F.F. insulator magnets (Rad/FPY)	7.2×10^{6}	7.2×10^{6}	7.2×10^{6}
Peak power density in F.F. magnets (W/cm^3)	5.35×10^{-7}	5.35×10^{-7}	5.35×10^{-7}
Coolant			
Inlet temperature (°C)	45	45	45
Outlet temperature (°C)	60	60	60
Flow rate per cavity (kg/hr)	3.25×10^{5}	3.6×10^{5}	3.6×10^{5}
Maximum velocity (m/s)	1	1	
Pressure (MPa)	0.5	0.5	0.5
ΔP in entire loop (MPa)	0.2	0.2	0.2
Pumping power delivered to coolant/ cavity (MW)	1.25	1.4	1.4
Peak structure temperature (°C)	60	60	60

VII. BALANCE OF PLANT

	4/29/81	5/8/81	6/30/81
Steam temperature (°C)	482	482	482
Steam pressure (MPa)	15.5	15.5	15.5
Steam flow rate (kg/hr)	1.9×10^7	1.8×10^7	1.8×10^7
Feedwater temperature (°C)	300	300	300
Reheat temperature (°C)	482	482	482
Steam generator surface area (m^2)	5.2×10^4	5.2×10^4	5.2×10^4

VIII. SYSTEM PARAMETERS

	4/29/81	5/8/81	6/30/81
Average DT power per cavity (MW)	2000	2000	2000
Total power recoverable per cavity (MW)	2538.2	2548	2548
System energy multiplication	1.27	1.274	1.274
Total pumping power delivered to coolant per cavity (MW)	20	20	20
Gross power per cavity (MW)	2558.2	2558.2	2558
Gross power per 4 cavities (MW)	10233	10233	10233
Gross thermal efficiency (%)	42	42	42
Gross plant output (MWe)	4298	4298	4298
Recirculating power (MWe)	827	827	530
Driver system	467	467	375
Linac	313	313	300
Storage rings			
Beam handling	154	154	75
Final focusing			
Target manufacture and delivery (MW)	?	?	?
Coolant pumps	160	110	110
Vacuum pumps			5
Plant auxiliaries			40
Net plant output (MWe)	?	?	3768
Net plant efficiency (%)	?	?	36.8

IX. TRITIUM PARAMETERS (FOR 29% BURNUP)

	4/29/81	5/8/81	6/30/81
Material inserted per shot			
D - target (mg)	1.61	1.6	1.6
(# of atoms)	4.856×10^{20}	4.8×10^{20}	4.8×10^{20}
T - target (mg)	2.42	2.4	2.4
(# of atoms)	4.856×10^{20}	4.8×10^{20}	4.8×10^{20}
Li - target (mg)	26.5	26.5	26.5
(# of atoms)	2.30×10^{21}	2.30×10^{21}	2.30×10^{-21}
Pb - target (mg)	329	329	329
(# of atoms)	9.56×10^{20}	9.56×10^{20}	9.56×10^{20}
Bi - ion beam (mg)	1.0×10^{-3}	1.0×10^{-3}	1.0×10^{-3}
(# of atoms)	3.0×10^{15}	3.0×10^{15}	3.0×10^{15}
Li - INPORT (g)	79	79	79
(# of atoms)	6.85×10^{24}	6.85×10^{24}	6.85×10^{24}
Pb - INPORT (g)	13200	13000	13000
(# of atoms)	3.8×10^{25}	3.8×10^{25}	3.8×10^{25}
Nonvolatiles (mg)	1.36×10^{4}	1.4×10^{4}	1.4×10^{4}
(# of atoms)	4.52×10^{25}	4.52×10^{25}	4.52×10^{25}
Total (mg)	1.36×10^{4}	1.36×10^{4}	1.36×10^{4}
Total # of atoms	4.52×10^{25}	4.52×10^{25}	4.52×10^{25}
D_2 (target injector) mg/shot	.940	1.6	1.6
# of atoms	2.83×10^{20}	4.8×10^{20}	4.8×10^{20}
Total D, T, D_2 (mg)	2.888	5.6	5.6
(# of atoms)	7.52×10^{20}	1.44×10^{21}	1.44×10^{21}
Fractional burnup, $f_b = T_b/(T_b + T_p)$	.29	.29	.29
Material pumped per shot			
D - target, unburned (mg)	1.146	1.1	1.1
(# of atoms)	3.44×10^{20}	3.4×10^{20}	3.4×10^{20}
T - target, unburned (mg)	1.719	1.7	1.7

	4/29/81	5/8/81	6/30/81
(# of atoms)	3.44×10^{20}	3.4×10^{20}	3.4×10^{20}
D_2 (target injector) - mg/shot	.940	1.6	1.6
- # atoms	2.83×10^{20}	4.8×10^{20}	4.8×10^{20}
T - lost from coolant (mg)	.877	.88	.88
(# of atoms)	1.76×10^{20}	1.76×10^{20}	1.76×10^{10}
He-DT fusion reaction (mg)	.942	.94	.94
(# of atoms)	1.41×10^{20}	1.4×10^{20}	1.4×10^{20}
He-T decay (mg)	1.3×10^{-9}	1.3×10^{-9}	1.3×10^{-9}
(# of atoms)	1.9×10^{11}	1.9×10^{11}	1.9×10^{11}
He-T production (mg)	1.17	1.17	1.17
(# of atoms)	1.76×10^{20}	1.76×10^{20}	1.76×10^{20}
He - total (mg)	2.11	2.11	2.11
(# of atoms)	3.17×10^{20}	3.17×10^{20}	3.17×10^{20}
Bi - ion beam (mg)	1.0×10^{-3}	1.0×10^{-3}	1.0×10^{-3}
(# of atoms)	3.0×10^{15}	3.0×10^{15}	3.0×10^{15}
Li - not condensed (mg)	0	0	0
(# of atoms)	0	0	0
Pb - not condensed (mg)	0	0	0
(# of atoms)	0	0	0
Nonvolatiles (mg)	0	0	0
(# of atoms)	0	0	0
Total (D, T, He, D_2 Target inj.)	6.79	7.39	7.39
Total # of atoms	1.46×10^{21}	1.65×10^{21}	1.65×10^{21}
# of shots per chamber per second	5	5	5
# of chambers	4	4	4
Total condensibles pump rate/chamber (g/s)	0	0	0
Total noncondensibles pump rate/chamber (g/s)	3.4×10^{-2}	.037	.037
Cavity pressure (Torr @ 0°C)	10^{-4}	10^{-4}	10^{-4}
Coolant breeding region			
Breeding material	$Pb_{83}Li_{17}$	$Pb_{83}Li_{17}$	$Pb_{83}Li_{17}$

	4/29/81	5/8/81	6/30/81
Flow rate for one chamber (kg/hr)	2.7×10^8	3.38×10^8	3.38×10^8
Breeder mass within one chamber (kg)	4.78×10^6	4.46×10^6	4.46×10^6
Total breeder mass for all chambers (kg)	1.91×10^7	1.78×10^7	1.78×10^7
Inlet temperature (°C)	330	330	330
Outlet temperature (°C)	500	500	500
Breeding ratio	1.25	1.25	1.25
Steady state tritium concentration (wppm)	6.1×10^{-4}	6.1×10^{-4}	6.1×10^{-4}
Tritium pressure (Torr @ 0°C)	10^{-4}	10^{-4}	10^{-4}
Weep rate (kg/hr)			
Extractor			
Inlet temperature (°C)			
Outlet temperature (°C)			
Inlet concentration (wppm)			
Outlet concentration (wppm)			
Extraction method	In situ extraction	In situ extraction	In situ extraction
Size of extractor			
Mass of breeding material within extractor (kg)			
% of total breeding material within extractor			
Steam generator			
Material composition		HT-9	HT-9
Wall thickness (mm)		1.0	1.0
Primary inlet temperature (°C)		330	330
Primary outlet temperature (°C)		500	500
Secondary inlet temperature (°C)		315	315
Secondary outlet temperature (°C)		490	490
Secondary pressure (MPa)		15.5	15.5
Surface area (m^2)		5.2×10^4	5.2×10^4

	4/29/81	5/8/81	6/30/81
Tritium permeation rate to H_2O (Ci/s)		.38	.38
Tritum inventory - steady state			
Breeding material - 4 cavities			
Reactor chamber - kg	.011	0.11	0.11
Reflector - kg	7.9×10^{-4}	7.9×10^{-4}	7.9×10^{-4}
Cryopumps (2 hr on-line) - kg	.374	.37	.37
Cryogenic distillation columns (kg)	.157	.16	.16
Fuel cleanup (kg)	.042	.042	.042
Structural material and piping (kg)			
Steam generator piping (kg)			
Storage - 3 days fuel supply (kg)	12.5	12.5	12.5
Total (kg)	13.08	13.1	13.1
Total (Ci)	1.3×10^8	1.3×10^8	1.3×10^8
Containment			
Total building volume (m^3)			
Volume of reactor & auxiliaries (m^3)			
Cleanup volume (m^3)			
Containment pressure (Torr @ 0°C)			
Time for tritium cleanup (hr)			